

Design of Horizontal Axis Tidal Turbines for Less Energetic Currents

A thesis submitted for the
Degree of Doctor of Philosophy

Job Immanuel Biares Encarnacion
Energy Systems Research Unit
Department of Mechanical and Aerospace Engineering
University of Strathclyde, Glasgow

April 12, 2024

Declaration of Authenticity and Author's rights

This thesis is the result of the author's original research. It has been composed by the author and has not been previously submitted for examination which has led to the award of a degree.

The copyright of this thesis belongs to the author under the terms of the United Kingdom Copyright Acts as qualified by University of Strathclyde Regulation 3.50. Due acknowledgement must always be made of the use of any material contained in, or derived from, this thesis.

Signed:

Date: 12 April 2024

I dedicate this thesis to Maru, Yuki, Lulu, Tutu, Waffle, and Mister Momo.
May they reach places and bring joy to everyone they encounter.

*Hope is the thing with feathers
That perches in the soul
And sings the tune without the words
And never stops at all*

Hope is the thing with feathers - Emily Dickinson (Stanza 1/3)

Acknowledgements

I would like to earnestly thank my supervisor Cameron Johnstone for supporting and providing guidance in my research while also allowing for utmost freedom in what I want to achieve.

I would like to thank the Marine Energy Group of ESRU: Song, Manuel, Gavin, Stephanie, Rodrigo, and Katie. They have supported me by providing feedback in my work and companionship in a once alien city to me that is Glasgow.

I would like to thank my collaborators from the Philippines and Mexico that have provided me the opportunity to do research while also obtaining data for my own research.

I would like to acknowledge DOST-ERDT for providing me the opportunity to study my PhD in the University of Strathclyde Glasgow. This opportunity not only has provided me an opportunity to grow in my professional and academic career but as well as a person.

I would like to thank my new found friends in the office where all we talked about is food. It was a refuge from the everyday toils of a PhD student. There is also the University of Strathclyde Ultimate Frisbee Club - Dark Horses. Ultimate has been a way for me to experience Scotland and the sport has allowed me to meet beautiful people from all over the world.

Finally, I would like to thank my old time friends, close friends, and family, that have supported me in my endeavour. There is much to say that one page cannot possibly capture. Throughout this thesis, friends have come and go. And some ultimately stayed. Nonetheless, all these experiences with them are already part of me and I will forever be grateful.

Abstract

Much of the growth in the tidal turbine industry is concentrated in energetic current sites within current magnitudes exceeding 2m/s. Less energetic sites with $U_\infty < 2\text{m/s}$ are not tapped since there is no perceived economic benefit.

This thesis explores the benefits of designing higher tip-speed ratio (TSR) rotors that operate in less energetic currents with the hypothesis that such rotors are can increase the viability of tidal turbines in less energetic sites. A parametric blade design methodology is developed to push the optimal TSR of rotors towards higher values. The performance of the blades is simulated using a BEM code with wave-current interaction. The blade designs are then evaluated according to three objectives: power, TSR, and thrust. A general cost model is also developed to evaluate the economic feasibility of the resulting blade designs.

High-TSR rotors were found to reduce the cost associated with the generator, which then drives other cost components of a turbine although this is only significant up to a threshold rotational speed of 50RPM. Higher TSR rotors have better LCOE values but utility scale feasibility is yet to be seen. The lowest LCOE value of the resulting turbine with a high-TSR rotor is at 0.6 EUR/kWh which is still higher than the current strike price of current tidal stream energy projects. However, these turbines may still be beneficial for off-grid sites that rely on unsustainable diesel-fired generation.

While cost is an issue, high-TSR rotors overcome the issues when operating in less energetic currents - load variability as result of low magnitude current velocities that are more susceptible to wave-induced variations. High-TSR rotors lessen the variation in load in addition to reducing the load due to lower torque and thrust loads since high-TSR rotors tend to have low solidity.

Contents

Acknowledgements	iii
Abstract	iv
List of Figures	xi
List of Tables	xix
1 Introduction	1
1.1 Marine energy technologies: the drive towards the oceans	1
1.2 State of the art technology for horizontal axis tidal turbines	2
The cost of horizontal axis tidal turbine technology	3
1.3 Capturing energy in less energetic tidal current sites	3
Less energetic currents in the UK and Europe	4
Less Energetic Currents in South East Asia	4
Continuous Oceanic Currents	5
Alternative Technologies to Horizontal Axis Tidal Turbine	6
Reducing the cost of TSTs for less energetic currents	7
1.3.1 Research Needs	8
1.3.2 Research Aims	8
1.3.3 Research Objectives	8
1.3.4 Research Scope and Limitations	9
1.4 Contributions to body of knowledge	10
1.5 Thesis Overview	11

Contents

1.6	Relevant publications	12
1.6.1	Journal Publications	12
1.6.2	Conference Papers and Posters	12
2	Background on Tidal Stream Turbines	14
2.1	Overview on tidal energy converters	14
2.1.1	Hydrodynamics of horizontal axis tidal turbine blades	16
	Blade design parameters	16
	Lift and Drag characteristics	17
2.1.2	Hydrodynamic performance	19
2.1.3	Solidity	21
2.2	Blade Element Momentum Theory	22
2.2.1	Linear Momentum and the Betz Limit	22
2.2.2	Angular Momentum	25
2.2.3	Blade Element Theory	28
2.2.4	Correction Factors	29
	Tip and Hub Loss Factors	30
	High induction Factors	30
	Post-Stall	31
2.2.5	Single parameter BEM	31
2.3	Turbines operating under non-uniform flow	34
2.3.1	Modelling a sheared tidal velocity profile	34
2.3.2	Effects of a sheared velocity profile on turbine loading	36
2.3.3	Incorporation of flow profile in BEM	37
2.4	Wave-Current Interactions	38
2.4.1	Observations and modelling of wave-current interactions	39
2.4.2	Effects of wave-current interactions	41
2.4.3	Incorporating wave-current interactions in BEM	44
	Superposition method	44
	Linear and Stokes waves	45
	Kinematic stretching	48

Contents

2.5	Summary	49
3	Tidal turbine blade design	50
3.1	Methods on blade design	50
3.1.1	Considerations in Turbine Design Optimisation	50
	From wind turbines to tidal turbines	50
3.2	The Design Problem	58
3.2.1	Existing design tools and methods	58
3.2.2	Design framework	60
3.3	Rapid blade generation for evaluation	63
3.3.1	Parametric blade modifications	63
	Physical representations	67
3.3.2	Limiting possible values of Γ and defining the design space	68
3.3.3	Additional Parameters	69
3.4	Summary	70
4	Verification of Blade Design and Analysis Methods with Preliminary Design Evaluation	71
4.1	Comparison with GA and control point optimisation	71
4.1.1	Conic Fits	72
	Performance Fits	76
4.2	Establishing a baseline	77
4.2.1	Steady-State Verification	78
4.2.2	Implication of C_L/C_D to operational speed	82
4.3	Decision Modelling	82
4.3.1	Pareto Optimal Solutions	83
4.3.2	Weighted Decision Matrix	84
4.3.3	Simulations in a limited design space	85
	Two-round blade design process	86
	Blade Geometries and Performance	87
4.4	Summary	92

5	Experimental Validation and Simulation adjustments	93
5.1	Small-scale testing of high-TSR rotor	93
5.1.1	Rotor Setup	94
5.1.2	Experimental Setup	95
5.1.3	Experimental Results	97
5.2	Adjusting aerofoil trailing edges	99
5.2.1	Trailing edge alterations	99
5.2.2	CFD Setup	100
5.3	Resulting Aerofoil characteristics	102
5.3.1	Comparing CFD and XFOIL ideal aerofoils	102
5.3.2	Lift and Drag Results	104
5.3.3	Relative Differences	106
5.3.4	Rotor performance of altered aerofoils	109
	Quantifying Blade Deflections	112
5.4	Increasing Blade Length	114
5.5	Summary	116
6	Parametric investigation using full design space	118
6.1	Simulations with Full Design Space	118
6.1.1	NACA 63-8xx Rotor	118
6.1.2	Wortmann FX63137 Rotor	122
6.1.3	Finalising candidate blades	126
	Sensitivity to Decision Weights	126
	Issues on Cavitation	127
6.2	Parameter Sensitivity	133
6.2.1	Sobol and Morris Methods of Sensitivity Analysis	133
	Elementary Effects by Morris	134
	Variance-based Sobol	136
6.2.2	Setup and Results of Sensitivity Analysis	138
	Sobol Results	140
	Morris Results	146

Contents

Thresholds for high TSR	149
6.3 Summary	155
7 Technical Performance of Designed Blades in Characteristic Sites	157
7.1 Characteristic sites: Country Profiles	157
7.1.1 Mexico	157
7.1.2 Philippines	159
7.2 Velocity Profile Modelling	162
7.2.1 Data Processing	162
Mexico	162
Philippines	164
7.2.2 Power Law Fit	165
7.3 Performance under a less energetic current profile	167
7.3.1 Hydrodynamic performance in characteristic sites	168
7.3.2 Wave Loading	175
7.3.3 Annual Energy Production with Theoretical Power Curve	179
7.4 Summary	182
8 Economic Evaluation of Designed Blades	183
8.1 Cost Modelling	183
8.1.1 Generator Configuration	184
8.1.2 Energy Loss	186
8.1.3 Availability and Capacity Factor	187
8.1.4 Power Scaling	188
8.2 Costs considering different inflow and diameter	189
8.2.1 Costs due to the generator	189
8.2.2 Turbine Sizing	191
Power Output	191
Energy Cost associated with generator only	192
8.3 Levelised Cost of Energy	193
8.3.1 CAPEX Estimates	194

Contents

Changes in CAPEX	195
CAPEX trends	197
8.3.2 OPEX Estimates	198
8.3.3 Calculated LCOE of tidal turbine with designed blades	199
OPEX at 4% CAPEX	199
OPEX at 6.25%+ of CAPEX	200
8.3.4 LCOE Sensitivity with respect to array size	201
8.4 Summary	209
9 Conclusions and Future Work	210
9.1 Development of rapid blade design methodology	210
9.2 Performance in representative sites	211
9.3 Economics of high-TSR rotors	211
9.4 Design considerations for high-TSR rotors operating in less energetic currents	212
9.5 Future Work	214
9.5.1 Improvements in blade design methodology	214
9.5.2 Data from representative sites	215
9.5.3 Improvements in load simulation	215
9.5.4 Improvement on the cost model	216
9.5.5 Small-scale testing	216
Bibliography	217
Appendix A Sample Calculation on Conic Fitting for existing blade design	244
Appendix B Second Order Sobol Indices	248
Appendix C PDFs of Wortmann FX63-137	252
Appendix D Complete Statistical Results for Velocity Profile Fitting	254

Contents

Appendix E	Sample Calculation for LCOE	256
E.1	CAPEX	256
E.1.1	Foundations	257
E.1.2	Rotor	257
E.1.3	Nacelle and Systems	257
E.1.4	Cabling	257
	Nacelle and device cables	258
	Transformer Platform	258
	Electric connections at the base of the turbine	258
	Umbilical, Submarine, and Ground connection	258
E.1.5	Installation	259
E.1.6	Concept	259
E.2	OPEX	259
E.3	LCOE	259
Appendix F	LCOE Sensitivity for 4% OPEX	261
Appendix G	AEP Calculation	264
Appendix H	Single Blade Loading under Waves	266

List of Figures

1.1	Tidal Kite	6
1.2	Oscillating Hydrofoil	6
2.1	Types and motions of tidal turbines	15
2.2	A tidal turbine blade with aerofoil sections	16
2.3	Airflow streamlines and pressure variation around a NACA 63-812 aerofoil. Angle of attack, $\alpha = 8^\circ$, generated from Javafoil	17
2.4	Aerodynamic characteristics for NACA 63-824	18
2.5	Aerofoil Inflow Angles	19
2.6	Caption for LOF	19
2.7	Coefficient of Power, C_P	20
2.8	Coefficient of Thrust, C_T	20
2.9	Shaded area for Local Rotor Solidity	21
2.10	A stream tube control volume over the turbine and flow domain	23
2.11	Pressure and velocity variation within the stream tube	23
2.12	Increase of tangential velocity within the wake	26
2.13	Geometric relation of inflow velocity vectors	28
2.14	Region of validity for values of κ	32
2.15	Sheared inflow profile due to seabed friction	35
2.16	Velocity variation for 4m diameter rotor operating at $TSR = 6$ under linear shear with $U_{ave} = 6$ with period of 2π	37
2.17	Transformation of global $y-z$ axis to azimuthal $y-z'$ axis	38

List of Figures

2.18	Wave propagation and particle motion along the water column under the presence of waves	39
2.19	Profiles with concurrent waves from Klopman, Kemp and Simons, and Umeyama	40
2.20	Profiles with counter-current waves from Klopman, Kemp and Simons, and Umeyama	40
2.21	Relative Current Number and deviations in Turbine Loads	43
2.22	Applicability of wave theories	46
2.23	Wave types	46
2.24	Simulated results using Fenton vs simulated results using Kishida and Sobey	48
2.25	Inflow mapping of z -axis as a result of the stretched water column as the free surface is displaced by η	49
3.1	Average capital expenditure for onshore wind turbines	56
3.2	Average capital expenditure for offshore wind turbines	57
3.4	Documented capital expenditure for a tidal turbine in Alderney Race	57
3.3	Average capital expenditure for floating wind turbines	58
3.5	Design approach derived from Fuglsang	61
3.6	Oblique conics within the first quadrant	65
3.7	Pitfalls in applying scaling coefficients	66
3.8	Sample post-processed data with different levels (discrete) of Γ for twist alterations	68
4.1	Conic Fits for Kenway and Martins	73
4.2	Conic Fits for Liu	73
4.3	Conic Fits for Xudong	74
4.4	Conic Fits for Sale	74
4.5	Conic Fits for Zhu	75
4.6	Conic Fits for Sun	75
4.7	C_P -TSR for Zhu	76

List of Figures

4.8	C_P -TSR for Liu	76
4.9	C_P -TSR for Sun	77
4.10	C_P and C_T verification for base blade geometries used for alteration	79
4.11	C_P and C_T for blade geometries used for verification	80
4.12	Frequency of flow angles per TSR for Gracie-Orr NREL S814	80
4.13	C_L/C_D for select aerofoils used in further case studies	82
4.14	Pareto optimal solutions and Pareto frontier	83
4.15	Design process for initial investigation.	87
4.16	Round 1 Blade Geometry Distributions	88
4.17	Performance of Round 1 blade geometries	89
4.18	Round 2 Chord Distribution.	90
4.19	Performance of Round 2 blade geometries	91
5.1	NACA 63-8xx mounted for testing at Inha University flume tank ($Re = 3.43 \times 10^4$)	95
5.2	Acoustic Doppler Velocimeter measurement points	96
5.3	Flume tank and mounted experimental setup at Inha University	97
5.4	Results of Flume Tank Test with $U_\infty = 1.0\text{m/s}$	98
5.5	Ideal and Shifted Case of NACA 63-812 (turbine tip) for a 1m blade (magnified version for a 219mm small-scale blade)	98
5.6	Trailing edge for Blunt case	100
5.7	Trailing edge for Extended case	100
5.8	CFD mesh for ideal and shifted cases.	101
5.9	XFOIL vs CFD coefficient of pressure for ideal aerofoils ($Re = 5 \times 10^5$)	103
5.10	XFOIL vs CFD aerodynamic characteristics for ideal aerofoils ($Re = 5 \times 10^5$)	103
5.11	Aerodynamic characteristics for NACA 63-824 aerofoils ($Re = 5 \times 10^5$)	104
5.12	Aerodynamic characteristics for NACA 63-812 aerofoils ($Re = 5 \times 10^5$)	105
5.13	% change for Lift	106
5.14	% change for Drag	106
5.15	NACA 63-812 Ideal and Blunt Case	109

List of Figures

5.16	Turbine Performance for NACA 63-8xx ideal, and 219mm blades with altered trailing edges	111
5.17	Blade deflection at $TSR = 8$	113
5.18	Blade deflection at $TSR = 10$	113
5.19	Aerodynamic characteristics for NACA 63-824 ideal, 219mm, and 400mm shifted cases ($Re = 5 \times 10^5$	114
5.20	Aerodynamic characteristics for NACA 63-812 ideal, 219mm, and 400mm shifted cases ($Re = 5 \times 10^5$	114
5.21	XFOIL vs CFD coefficient of pressure for ideal aerofoils	114
5.22	Turbine Performance for NACA 63-8xx ideal, 219mm, and 400mm shifted aerofoil blades	115
6.1	NACA results grouped by Chord Distribution	119
6.2	NACA results grouped by Twist Distribution	119
6.3	NACA results grouped by Chord Reduction	120
6.4	NACA results grouped by Pitch	120
6.5	NACA results grouped by Blade Number	121
6.6	Summary effects of design variables on NACA rotor performance	121
6.7	Wortmann results grouped by Chord Distribution	123
6.8	Wortmann results grouped by Twist Distribution	123
6.9	Wortmann results grouped by Chord Reduction	124
6.10	Wortmann results grouped by Pitch	124
6.11	Wortmann results grouped by blade number	125
6.12	Summary effects of design variables on Wortmann rotor performance	125
6.13	Decision Scenarios	127
6.14	TSR cuts for different TSR operating points	129
6.15	Optimal NACA 63-8xx for full the TSR range	129
6.16	Optimal NACA 63-8xx for $TSR \leq 10$	130
6.17	Optimal NACA 63-8xx for $TSR \leq 8$	130
6.18	Optimal Wortmann FX63137	131
6.19	Morris Method input space for 3 variables	135

List of Figures

6.20 Comparison between significant (right) and less significant (left) variable according to Sobol sensitivity.	136
6.21 Comparison of Independent Random Sampling and Sobol Sequence Sampling	139
6.22 1 st order Sobol Indices for NACA	142
6.23 Total Sobol Indices for NACA	143
6.24 1 st order Sobol Indices for Wortmann	144
6.25 Total Sobol Indices for Wortmann	145
6.26 Morris Indices for NACA blades	147
6.27 Morris Indices for Wortmann blades	148
6.28 Probability Distribution for NACA $C_{P_{max}}$ according to different design variables	151
6.29 Probability Distribution for NACA $TSR_{C_{P_{max}}}$ according to different design variables	152
7.1 Power mix of Mexico in terms of kilotonne of oil equivalent (2017).	158
7.2 Location and potential of the Yucatan Peninsula	159
7.3 Power mix of the Philippines in MW (2017).	160
7.4 Location of each transect in the Cozumel Channel	163
7.5 Velocity variation in each transect and location of each 10m window	163
7.6 Turbine performance for Mexico Transect A	168
7.7 Turbine performance for Mexico Transect B	169
7.8 Turbine performance for Mexico Transect C	170
7.9 Turbine performance for Mexico Transect D	171
7.10 Turbine performance for Philippines Median Case	172
7.11 Turbine performance for Philippines Max Case	173
7.12 Relative Current Numbers for different current magnitudes at blade root	176
7.13 Variation in Thrust for NACA Blades given under wave loading ($H_s = 0.4909m, T_p = 5.993s, h = 10m, U = 0.98m/s$)	176
7.14 Variation in Torque for NACA Blades under wave loading ($H_s = 0.4909m, T_p = 5.993s, h = 10m, U = 0.98m/s$)	177

List of Figures

7.15	Variation in Thrust for Wortmann Blades given under wave loading ($H_s = 0.4909m$, $T_p = 5.993s$, $h = 10m$, $U = 0.98m/s$)	177
7.16	Variation in Torque for Wortmann Blades given under wave loading ($H_s = 0.4909m$, $T_p = 5.993s$, $h = 10m$, $U = 0.98m/s$)	178
7.17	Trend in Coefficient of Determination for NACA Blades (left axis, *: thrust; right axis. \diamond : torque)	178
7.18	Trend in Coefficient of Determination for Wortmann Blades(left axis, *: thrust; right axis. \diamond : torque)	179
7.19	Histogram of Velocities	180
7.20	Annual Energy Production	181
8.1	Direct-drive configuration for cost modelling	184
8.2	Fit for Material Weight (tons) vs RPM	185
8.3	Fit for Iron Losses (%) vs RPM	186
8.4	Fit for Copper Loss (MWh) vs Torque (kNm)	187
8.5	Scaling of Weight (tons) with respect to Power (MW)	189
8.6	Scatter plot of total generator weight (tonne) vs RPM	190
8.7	Scatter plot of generator power (kW) vs RPM	190
8.8	Scatter plot of total generator cost (EUR) vs RPM	190
8.9	Scatter plot of cost of power (EUR/kW, generator only) vs RPM	191
8.10	Comparison of Power considering multiple diameter rotors	192
8.11	Comparison of cost of power (COP EUR/kW, generator only) considering multiple diameter rotors	193
8.12	Average CAPEX share of components and activities for tidal turbine installation	197
8.13	Estimated CAPEX (EUR) considering multiple diameter rotors	198
8.14	Estimated LCOE (EUR/kWh) considering multiple diameter rotors with OPEX at 4% of CAPEX	200
8.15	Estimated LCOE (EUR/kWh) considering multiple diameter rotors with OPEX at 6.25% of CAPEX	200

List of Figures

8.16	Sensitivity of LCOE for varying turbine number for arrays operating at 1.0m/s	202
8.17	Sensitivity of LCOE for varying turbine number for arrays operating at 1.5m/s	203
8.18	Sensitivity of LCOE for varying turbine number for arrays operating at 2.0m/s	204
8.19	Normalised LCOE values against Diesel LCOE of 0.37EUR/kWh	208
B.1	Second Sobol Significance indices for NACA (left) and Wortmann (right)	248
B.2	Legend for Second Order Sobol Indices for one aerofoil	249
B.3	Legend for First and Total Order Sobol Indices including aerofoil	249
B.4	Legend for Second Order Sobol Indices including	249
B.5	First and Total Order Sobol Significance indices including aerofoil as a parameter	250
B.6	Second Order Sobol Significance indices including aerofoil as a parameter	251
F.1	Sensitivity of LCOE for varying turbine number for arrays operating at 1.0m/s	261
F.2	Sensitivity of LCOE for varying turbine number for arrays operating at 1.5m/s	262
F.3	Sensitivity of LCOE for varying turbine number for arrays operating at 2.0m/s	263
H.1	Thrust Variation for the Wortmann Base Rotor (TSR = 3.75)	266
H.2	Thrust Variation for the Wortmann TSR5.75 Rotor	267
H.3	Thrust Variation for the NACA Base Rotor (TSR = 5.75)	267
H.4	Thrust Variation for the NACA TSR7.75 Rotor	268
H.5	Thrust Variation for the NACA TSR9.75 Rotor	268
H.6	Thrust Variation for the NACA TSR12 Rotor	269
H.7	Torque Variation for the Wortmann Base Rotor (TSR = 3.75)	269
H.8	Torque Variation for the Wortmann TSR5.75 Rotor	270
H.9	Torque Variation for the NACA Base Rotor (TSR = 5.75)	270

List of Figures

H.10 Torque Variation for the NACA TSR7.75 Rotor	271
H.11 Torque Variation for the NACA TSR9.75 Rotor	271
H.12 Torque Variation for the NACA TSR12 Rotor	272

List of Tables

3.1	NACA 63-8xx Base Case Blade [1]	65
3.2	Physical Variables	67
3.3	Design Space	68
3.4	Extended Physical Variables	69
4.1	GA-generated optimised blade designs and corresponding Γ values for conic fitting	72
4.2	Blade geometries used for alteration and verification	78
4.3	Wortmann FX63137 Base Case Blade [2]	81
4.4	NACA 63-8xx Base Case Blade [1]	81
4.5	Alterations and expected observations for each round	86
4.6	Blade geometry specifications for Round 1 NACA blades.	88
4.7	Round 1: Averaged maximum C_P and $TSR_{C_{Pmax}}$ according to twist distribution.	89
4.8	Blade geometry specifications for Round 2 low-solidity NACA blades (37.5% reduced chord length) with base twist distribution.	90
4.9	Weighted Decision Matrix for the NACA 63-8xx	91
5.1	Change in thickness for each blade section of the NACA 63-8xx blade	94
5.2	Median and Average % change for all cases with respect to ideal C_L and C_D	106
6.1	Summary NACA optimisation (Chord and Twist Distribution)	131
6.2	Wortmann optimisation (Chord and Twist Distribution)	132

List of Tables

6.3	Summary of optimisation (Design Variables and TSR)	132
7.1	Potential and Installed Capacity of renewable energy power plants in the Philippines according to resource (2017)	160
7.2	Awarded Ocean Energy Projects in the Philippines (2019)	161
7.3	Location and mean depth of 10m windows within each transect	162
7.4	Direction of wave propagation with respect to dominant tidal direction (both flood and ebb)	165
7.5	Mean Power Law Coefficients for each transect	165
7.6	Median Power Law Coefficients for each transect	166
7.7	Mean Power Law Coefficients for each wave-tidal direction	166
7.8	Median Power Law Coefficients for each wave-tidal direction	167
8.1	Drive train configurations and material weight	185
8.2	Maximum Design TSR points considering Rotor Diameter and Inflow Velocity	191
8.3	Power production in kW for 1, 10, and 20 devices given different current magnitudes and diameter	205
A.2	Values after normalising using R_{tip}	245
A.1	Captured data points using PlotDigitizer	245
A.3	Values after subtracted twist and chord values at the tip	246
A.4	Values after normalising using the twist and chord values at the root	246
A.5	Computed λ_{tip} and Γ after using MS Excel GRG Nonlinear solver.	247
D.1	Descriptive Statistics for U_o , α , and β for Philippines: Unfiltered and complete dataset	254
D.2	Descriptive Statistics for U_o , α , and β for Philippines: Filtered for $\alpha < 10 $	254
D.3	Descriptive Statistics for U_o , α , and β for Mexico Transect A	255
D.4	Descriptive Statistics for U_o , α , and β for Mexico Transect B	255
D.5	Descriptive Statistics for U_o , α , and β for Mexico Transect C	255
D.6	Descriptive Statistics for U_o , α , and β for Mexico Transect D	255

Chapter 1

Introduction

1.1 Marine energy technologies: the drive towards the oceans

An increasing concern over a climate crisis has been discussed throughout the recent decade. Thus, scientists and engineers alike have been trying to come up with alternative ways to provide the necessary systems needed to sustain human lifestyle. Providing power or electricity is one of the main focus of such efforts as powered tools and devices are adopted into every day life - from consumer devices to heavy powered machinery needed for manufacturing of products for human consumption.

Renewable energy technologies provide an alternative way to produce the necessary power for such activities. These are wind turbines, hydropower dams, geothermal plants, and solar photovoltaic farms to name a few. Marine energy has also been explored over the recent years. It provides a more reliable form of power generation since driving forces such as the moon's gravitation that affect the tides is very much predictable among others.

Marine energy has one of the largest potentials amongst all renewable energy technologies although much of the resource remains untapped either due to the unavailability of the technology given current conditions i.e. low flow velocity, or probable site limitations given depth, distance to shore, presence of trade routes, etc. Nonetheless, this type of renewable energy technology presents numerous benefits not limited to power generation but also on the stimulation of economic growth in coastal

areas, as well as island regions [3].

1.2 State of the art technology for horizontal axis tidal turbines

Tides are caused by the combined gravitational interaction of the sun and moon, and affect local sea levels as the earth rotates. This rise and fall of sea levels around the globe cause seawater to flow from one point to another. Geographical features, both lands near the shore and underwater, determine the velocities of the flow. This movement of seawater is more commonly known as tidal flow or current.

This current can be used to drive tidal stream turbines (TSTs) to produce power. TSTs are similar to wind turbines with the dominant technology being horizontal axis tidal turbines (HATTs)¹ [4]. Development in the field has been steady over the past years although cost remains to be a huge concern [5]. Today, HATTs remain to be one of the more expensive renewable energy technologies available, second only to wave energy converters.

The European Marine Energy Center (EMEC) in Orkney houses several HATTs ranging from developmental to commercial-ready technology. Multiple companies such as Orbital Marine Power formerly known as Scotrenewables, Atlantis, Nautricity, Alstom, Andritz, Magallanes, and Voith, have utilised the site for testing and development of their TSTs.

The largest commercially available HATT as of the time of writing is the 2MW SR2000 developed by Orbital Marine Power [6]. The two 16m rotors are rated at 3m/s to produce 1MW of power each. Atlantis has also been developing a 2MW single-rotor turbine, AR2000, rated at the same 3m/s flow [7]. The device is set to have a 20-24m diameter rotor. Another project of Atlantis, Meygen, is the largest planned commercial-scale tidal turbine array with four 1.5MW AR1500 single-rotor turbines [8].

The waters around Shetland islands further north of the EMEC site also have

¹Horizontal Axis Wind Turbines or HAWTs for the wind turbine industry.

Introduction

favourable conditions for HATTs. The region is home to three 100 kW M100D turbines by Nova Innovation [9]. These are smaller 9m turbines rated at 2 m/s and are the world's first grid-connected tidal turbine array.

The cost of horizontal axis tidal turbine technology

The levelised cost of energy (LCOE, See Chapter 8 for discussion of LCOE calculation) for tidal energy remains to be high compared to other renewable energy technologies and conventional power plants. Reduction in cost remains a challenge for the industry although future projects show some promise with current LCOE of 400 EUR/MWh dropping to less than 100 EUR/MWh by 2050 [10].

The Contracts for Difference Allocations Round 4 (CFD AR4) also shows how much higher the price of tidal energy technologies, particularly Horizontal Axis Tidal Turbines (HATTs), are compared to other renewable energy technologies [11]. Still, LCOE trajectory for HATTs remain positive as long as it is continually developed at relatively high learning rates of 20%. This seems to be achievable as the current (2025) strike price is below the 20% learning rate LCOE given by Zeyringer et al. [12].

Future cost of the technology is highly dependent on the learning rate, which may even rival floating off-shore wind [13] provided that the development continues since current trends in the market show no competitive edge of HATTs (LCOE of 177-507 USD/MWh, strike price of 178 GBP/MWh) over floating offshore wind (LCOE of 103-175 USD/MWh, strike price of 37.35-87.30 GBP/MWh) [11].

1.3 Capturing energy in less energetic tidal current sites

The devices in Section 1.2 are just a few of the successful innovations. However, the development is highly concentrated in highly energetic tidal current sites with tidal velocities greater than 2m/s [14, 15].

Extractable power significantly drops in less energetic currents due to the cubic relationship of power to velocity ($P \propto U^3$). Nonetheless, the number of suitable sites for tidal stream energy extraction should increase considerably if technology for less

Introduction

energetic currents is developed. Lower structural loading is expected, which translates to lower cost of manufacturing, materials, operation and maintenance.

All of the turbines mentioned in Section 1.2, except for the Nova M100D turbines [9], have an optimum tip-speed ratio (TSR) of less than six ($TSR < 6$), These are considered as low-TSR rotors and all of the examples operate at flow speeds of greater than 2m/s. The Nova M100 turbine is designed at $TSR \approx 6$, which is skirting the considered high-TSR in this thesis as $TSR > 6$. The same Nova M100D operates at flows that skirts the definition of less energetic current in this thesis with $U_\infty < 2\text{m/s}$.

Less energetic currents in the UK and Europe

Much of the UK is also surrounded by less energetic tidal currents of velocities less than 2m/s. This includes the south, west, and east coasts of the UK with few patches having short peaks of greater than 2m/s [16–18]. Robins [19] analysed the M2, S2, K1, O1, and M4 tidal constituents to simulate the available resource around the UK and Ireland and showed that while a few sites may exceed 2m/s during peak spring conditions, majority of the waters around the UK and Ireland still fall within the category of less energetic currents.

Carballo [20] modelled a potential tidal stream energy resource in Ria de Muros, Spain and found peak current magnitudes of 2m/s throughout a 14-day spring-neap cycle. Tidal stream devices were also planned for Ria Formosa, Portugal. However, initial deployment of an Evopod turbine [21] showed a maximum output of below 25% rated output [22], which is presumably due to the current magnitude of 1.4m/s.

Less Energetic Currents in South East Asia

The interest in ocean energy technologies has increased in South East Asia over the past years. Tidal stream energy has also gained attention with research being focused on resource assessment. One of the main challenges now is addressing low tidal current magnitudes of less than 2m/s that dominate much of the region [23, 24].

Resource assessment in the Malacca strait in Malaysia by [25] showed a total time-averaged potential of 112.6MW. However, much of this available potential is

Introduction

modelled with less energetic currents with peaks at 1.5m/s [25, 26] and an average speed of 1m/s [27].

Firdaus [28] summarised different resource assessments performed in Indonesian waters. The Indonesian archipelago has numerous straits that are ideal for tidal stream turbines. Of the tens sites identified, Alas Strait had the greatest current magnitude that reached up to a peak of 2.9m/s. However, it is uncertain where such speed occurs along the strait [29]. The same was observed in Pantar Strait [30]. The rest of the sites are characterised by less energetic currents of less than 2m/s with several being even less than 1.5m/s.

Behera [31] modelled the straits of Singapore and the simulations showed a few regions with current magnitudes of 2.5m/s although majority is still under 1.5m/s.

Similar to Indonesia, the Philippines has numerous sites for tidal stream energy owing to the archipelagic nature of the country. Of these, the San Bernardino Strait has gained much attention with current magnitudes reaching up to 4.5 m/s [32] near the southern tip of Capul islands. The site has been the focus of a new project by Sabella who aims to install a 3MW tidal stream array [33]. However, much of the country's straits are characterised by currents of less than 2m/s [34, 35]. Bosch [36] studied the waters around Talampulan island in the Philippines, near the main island of Palawan. ADCP readings with peaks of more than 3m/s were obtained with most velocities falling under 2m/s. A 70kW turbine was then used to further model the energy demand and capacity for Panlaitan, the only town in Talampulan.

Continuous Oceanic Currents

Tidal stream turbines are not limited to tidal currents that follow a cyclic pattern of ebb and flow. TSTs can also harness the energy of continuous oceanic currents. Examples of these are the Yucatan current in Mexico and the Kuroshio in Taiwan.

The Yucatan current that flows through the passageway of mainland Mexico and the island of Cozumel has current magnitudes that reach up to 2m/s [37, 38], although the average current within the channel is at 1.4m/s [39]. The Kuroshio current has also been identified to be a tidal energy resource and development of a floating Kuroshio turbine

Introduction

has been in the works for as early as 2013 [40–42]. The average current magnitude was found to be 1.5 m/s [43]. This may pose a problem since the turbine being developed is still rated to have maximum output at low tip-speed ratios (TSRs) ($TSR \approx 4$) with peak generation of 400W for a 2m diameter turbine [42]. This may require large generators and a complex power take-off mechanism, which increases the cost.

Alternative Technologies to Horizontal Axis Tidal Turbine

New technologies to capture tidal stream energy have been proposed through the years [3]. Examples of these are tidal kites (Figure 1.1) and oscillating hydrofoils (Figure 1.2). These technologies solve different problems of the existing technologies e.g. HATTs.

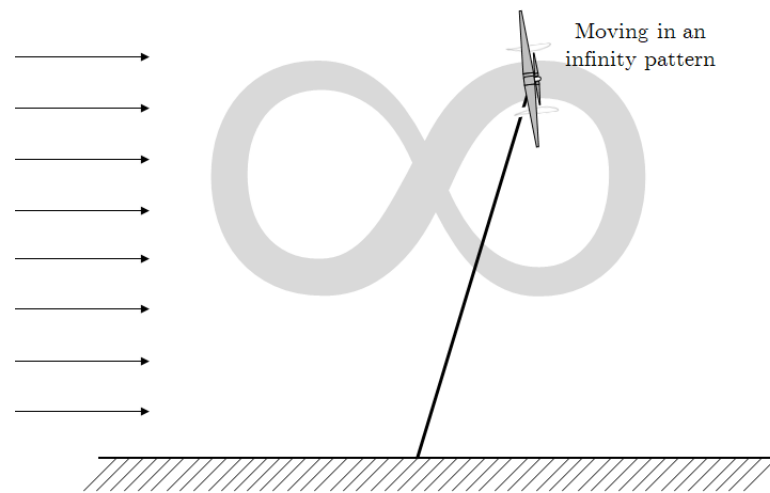


Figure 1.1: Tidal Kite

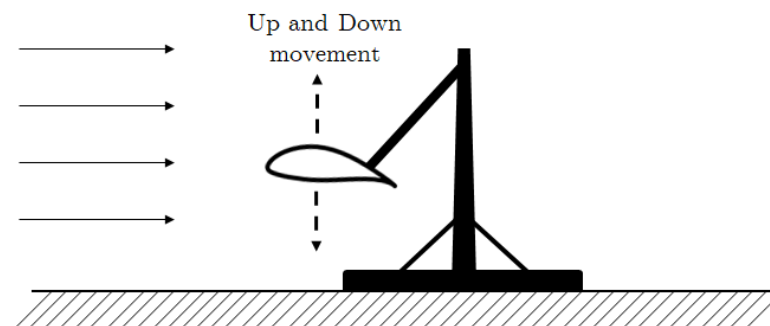


Figure 1.2: Oscillating Hydrofoil

Introduction

Tidal kites employ a wing-like structure attached to a small ducted turbine. The kite is made to move in an infinity (∞) shaped path. The wing then generates lift as it is subjected to tidal flow, pushing the kite forward and resulting in relative velocity being ten times greater than the tidal flow. Minesto has installed such system with a cut-in speed of 1.2m/s capable of producing 100 kW of power [3].

Oscillating Hydrofoils are submerged hydrofoil wings that are connected to an arm. The arm is free to move up and down about a fulcrum as the wing is subjected to tidal flow. As the wing moves, its angle of attack changes with angles of attack producing lift allowing the wing to move up, and angles of attack producing negative lift allowing the wing to move down. Most designs of oscillating hydrofoils are at their preliminary stages consisting of theoretical and numerical studies of the performance of such device [3].

While development for all kinds of technologies are continuous, horizontal axis tidal turbine still remain the most mature technology, which can serve as a proper baseline for the purpose of this thesis.

Additionally, life cycle emissions of these alternative technologies remain higher compared to the more mature HATT [13]. Thus, additional research on the technological and industrial underpinnings of the technology is needed for both technologies in both energetic and less energetic flow regimes.

Reducing the cost of TSTs for less energetic currents

Reducing cost can be achieved in ways other than downsizing and using cheaper materials. 'Conventional' slowly rotating rotors with optimum TSR less than 6 would require large torque production, which is not possible in less energetic currents. Faster rotating blades with optimal $TSR > 6$ may offset the effect of the reduced torque and produce better power output as $P = T\omega$.

Faster rotational speeds also allow for direct-drive or at least a simpler power take-off system with less step-up gear mechanisms. This not only enables for less capital cost due to generator down-sizing but also reduces cost in needed turbine support, installation and commissioning, and decommissioning.

This thesis investigates the dynamics of faster rotating blades to evaluate their

Introduction

suitability in less energetic currents. The optimal operating point of tidal turbine rotors is pushed towards the high TSRs while weighing the cost and benefits of such design from a techno-economic perspective.

1.3.1 Research Needs

Tidal energy is present all over the globe but much of this potential is untapped due to the relatively high cost of tidal turbine technology, which makes it impractical to use in less energetic environments that dominate the global resource. There is a need to explore a different approach in designing turbines to capture these less energetic tidal currents. This benefits not only the communities that may have access to sustainable energy but also to the tidal energy industry as a whole.

1.3.2 Research Aims

This thesis aims to design a technically and economically feasible horizontal axis turbine rotor for application in less energetic tidal environments. Technical feasibility is evaluated through the quantification of hydrodynamic loads and general rotor performance. Economic feasibility is evaluated through the estimation of levelised cost of energy of the resulting designs.

1.3.3 Research Objectives

The following objectives are identified to aid in achieving the aims of this thesis.

- Investigate blade design parameters that affect the location of the maximum C_p point within the range of TSRs and determine an optimum blade design using the determined parameters.
- Develop a blade design methodology to rapidly generate and evaluate blade designs using Blade Element Momentum Theory (BEM) as a primary tool for rotor performance evaluation. BEM is used in this thesis due to its capability to accurately determine performance characteristics without the need for massive computational power.

Introduction

- Identify representative sites with less energetic tidal currents to evaluate the hydrodynamic performance of the rotors.
- Determine the effect of current and waves loads in less energetic environments.
- Develop a general cost model to quantify the capital and, operation and maintenance cost of turbines operating in less energetic flows.
- Evaluate the benefits and drawbacks of running a high-TSR rotor vis-a-vis a conventional rotor.

1.3.4 Research Scope and Limitations

The design methodology is focused on multi-objective optimisation with C_P and TSR as primary parameters, and C_T as a secondary parameter. This is mainly due to the $C_P \propto U^3$ and $C_T \propto U^2$ relationships of performance and inflow velocity.

Cost is an important consideration and is one of the main drivers for the need of innovation. It is mainly used to evaluate the benefits of the proposed rotor designs against conventional rotors used in energetic flow. Ultimately, there is a need to assess if operation in less energetic flow is technically feasible before economics is evaluated. Hence, much of the work is focused on characterising hydrodynamic performance. A comprehensive cost model is not developed although system cost including the power train is considered. All other costs are derived using the cost computed from the power train, its relative share in existing literature, and other published literature that give cost values while also noting that costs are site-specific.

The study is also limited to the design of horizontal axis tidal turbines (HATTs) with the hypothesis that running at higher TSRs is beneficial for less energetic flow. Alternative turbine architecture i.e. tidal kites, vertical axis tidal turbines, and ducted tidal turbines, oscillating hydrofoils are not explored. HATTs are the most mature TST technology and they provide a good design foundation, both numerically and experimentally. Comparison between predicted performance in energetic and less energetic flow regimes can be more readily performed, and resulting designs

Introduction

may also be more readily deployed with consideration to a likely lengthy design and implementation cycle.

This also limits the design space and nevertheless, the hypothesis may still apply to the alternative architectures except for vertical axis tidal turbines, which functions differently from an aerodynamic perspective.

The study also defines high-TSR rotors as rotors with maximum C_P occurring at $TSR > 6$.

1.4 Contributions to body of knowledge

This thesis has contributed to research and of tidal stream technology through:

- Blade designs that operate in higher tip-speed regions allowing for faster rotating speeds, which decreases generator torque requirements and allows for smaller turbine nacelles, cheaper turbine support infrastructure, and smaller installation and maintenance vessels.
- A simplified design methodology that employs a reduced number of design variables that can perform similarly to computationally heavy machine learning methodologies used in current design methodologies.
- Characterisation of tidal stream sites representative of less energetic flow showing highly sheared flow as opposed to general $\beta = 7$ frequently used to model current velocity profiles in regions of energetic flow. This presents an opportunity for further research as data for potential tidal stream energy sites are continuously being obtained.

A secondary contribution of this thesis is the improvement of an unsteady blade element momentum code that now employs object-oriented programming, which aids in the simultaneous generation and analysis of new blade designs. This was originally intended to be used for a genetic algorithm approach in design although a simpler and more efficient methodology has been developed. Further work to employ GA on other parameters, especially in exploring new aerofoil profiles, using OOP may be done.

1.5 Thesis Overview

Chapter 2 discusses the physics governing the operation of tidal turbines in actual sea conditions. The chapter provides an overview of different tidal turbine architecture and describes the loads that turbines are subjected to during operation. It then proceeds to describe flow conditions that cause the said loads. This includes a discussion on wave-current interaction and the process of modelling inflow phenomena before blade element momentum theory (BEMT) can be used.

Chapter 3 discusses the blade design methodology developed and utilised for blade generation and performance optimisation. It provides additional literature on existing blade design methodologies and gives a discussion on the advantage of the proposed methodology.

Chapter 4 discusses the applicability of the blade design methodology. It provides verification of the BEM implementation with a preliminary multi-objective optimisation process. Results of the steady-state optimisation for the generated blade designs are presented.

Chapter 5 presents the results of the preliminary experiments and adjustments in the BEM inputs. Possible sources of error are identified before moving on to recommendations on small-scale testing of low solidity blades.

Chapter 6 discusses the effect of the different parameters varied in the blade design process. Global sensitivity analysis is employed to explore the significance of each parameter on the desired objectives. An expanded decision model is introduced and used to select the *optimised* blade designs.

Chapter 7 presents an investigation of the blade designs when subjected to loads in less energetic current sites. The chapter provides an economic background of the countries and the benefits that tidal stream technology may give to the respective local communities. Simulations of performance under data-derived sea-states are then presented.

Chapter 8 presents the cost model used to compare conventional rotors in energetic current sites to the blade designs developed in the study. The chapter also provides

Introduction

levelised cost of energy calculations and comparison to existing diesel-fired generators that dominate off-grid settlements.

Chapter 9 provides a synthesis of the findings from the previous chapters. The chapter reviews the applicability of the results in relation to the scope of the thesis. It also explores the more general applications that have not been tackled in-depth and presents suggestions for future work.

1.6 Relevant publications

1.6.1 Journal Publications

1. **Encarnacion, J.I.**; Johnstone, C.M. "Design of a Horizontal Axis Tidal Turbine for Less Energetic Currents." *J. Mar. Sci. Eng.*, 2019, 7, 197 .
2. Alcérreca-Huerta, J.C.; **Encarnacion, J.I.**; Ordoñez-Sanchez, S. Callejas-Jiménez, M.; Gallegos Diez Barrosa, G.; Allmark, M.; Mariño-Tapia, I.; Silva-Casarín, R.; O'Doherty, T.; Johnstone, C. "Energy Yield Assessment from Ocean Currents in the Insular Shelf of Cozumel Island." *J. Mar. Sci. Eng.*, 20129, 7, 147.

1.6.2 Conference Papers and Posters

1. Martinez, R.; **Encarnacion, J.**; Ordoñez-Sanchez, S.; Lavery, G.; O'Doherty, T.; Johnstone, C. "Aerodynamic characteristics of airfoils used in high tip-speed-ratio tidal rotors for less energetic foils." *14th European Wave and Tidal Energy Conference*, 5-9 September 2021. (*Abstract Accepted*)
2. **Encarnacion, J.**; and Johnstone, C. "Economic feasibility of high tip-speed ratio blades operating in less energetic currents." *14th European Wave and Tidal Energy Conference*, 5-9 September 2021. (*Abstract Accepted*)
3. **Encarnacion, J.I.B.**; Johnstone, C.M. "Effects of an Unsteady sea-state on the Performance of a Horizontal Axis Tidal Turbine designed for Lower Velocity Tidal Flows." *13th European Wave and Tidal Energy Conference*, 1-6 September 2019.

Introduction

4. **Encarnacion, J.I.B.;**Johnstone, C.M. ” A Preliminary Investigation on the Benefits of High-TSR Blades for Less Energetic Currents.” *INORE European Symposium*, 25-31 August 2019. *Poster*
5. **Encarnacion, J.I.B.;** Lavery, G.; Ordoñez-Sanchez, S.;Johnstone, C.M. ” Effects of Trailing Edge Alterations on the Performance of a Small-Scale, Low-Solidity Tidal Turbine Blade Design for Less Energetic Flows.” *13th ASME International Conference on Energy Sustainability*, ES2019-3891, 15-17 July 2019.
6. **Encarnacion, J.I.B.;** Johnstone, C.M. ” Preliminary Design of a Horizontal Axis Tidal Turbine for Low-Speed Tidal Flow.” *4th Asian Wave and Tidal Energy Conference*, AWTEC2018-257, 9-13 September 2018
7. **Encarnacion, J.I.B.;** Johnstone, C.M. ” Optimisation of Tidal Turbine Blades or Low Velocity Flow. *6th Oxford Tidal Energy Workshop*, 26-27 March 2018.

Chapter 2

Background on Tidal Stream Turbines

2.1 Overview on tidal energy converters

The European Marine Energy Centre (EMEC) [44] categorises tidal energy converters (TECs) into six types: (a) horizontal axis tidal turbines, (b) vertical axis tidal turbines, (c) venturi or ducted tidal turbines, (d) oscillating hydrofoils, (e) Archimedes screw, and f) tidal kite. Tidal stream turbines is a sub-category of TECs composed of the first three (a,b, and c) types mentioned. These are devices that have blades that move around an axis. Each blade is made up of a series of hydrofoils that interact with the flow, producing lift and drag forces that rotate the blade by producing torque, which may then drive a generator to produce power.

Horizontal axis tidal turbines (HATTs) are also referred to as axial flow turbines as the axis of rotation is parallel to the incoming tidal flow. This is in contrast to vertical axis tidal turbines (VATTs) where the axis of rotation is perpendicular to the incoming tidal flow. The preference for HATTs is attributed to their higher efficiency [44] and the smoother operation since VATTs are subjected to cyclic loading even at uniform flow as the blades may be situated along the shadow of another blade [15]. Figure 2.1b also shows that each VATT blade is only effective for approximately half of its range of motion compared to HATT blades being able to utilise the full 360° [45] due to half of the VATT blade motion going against the flow.

Venturi, or ducted, turbines are essentially HATTs that have increased power

Hydrodynamics of Tidal Stream Turbines

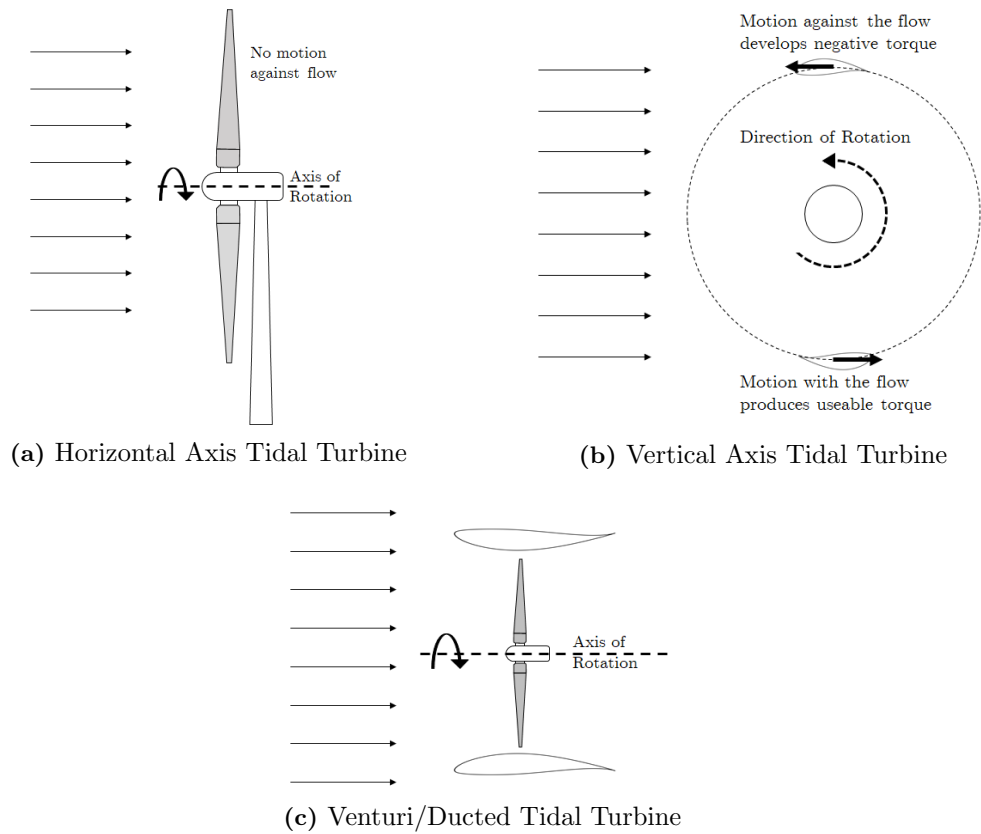


Figure 2.1: Types and motions of tidal turbines

capture as a result of the augmented flow allowed by the duct positioned around the rotor [15]. These turbines are able to produce more power for the same rotor size in less energetic flows as the duct allows for an increased fluid mass flow even at slower speeds. However, this does not come without problems as most developers are able to install ducted tidal turbines near the seabed, within the bottom boundary layer with highly sheared flow. Shives and Crawford [46] have found that ducted turbines may not necessarily be the best for tidal energy conversion when considering arrays since the overall power lost within the fluid for a given turbine power is significantly greater than open-flow turbines e.g. HATTs and VATTs. That is, for a given rotor area, ducted turbines are able to produce more power than open-flow turbines but more energy is lost as the flow is being accelerated within the duct.

This thesis is focused on the design of HATTs, which accounts for 41 of the 96 tidal devices [47] in the market. This shows the versatility of HATTs i.e. having a smoother

operation compared to VATTs and are more scalable to arrays compared to ducted turbines. From this point on, HATTs and tidal turbines will be used interchangeably unless a specific turbine type is mentioned.

2.1.1 Hydrodynamics of horizontal axis tidal turbine blades

Tidal turbine blades are constructed as a series of continuous aerofoils with each infinitesimal section producing torque, Q , and thrust, F_n , that drives the blade around its axis. The performance of a tidal turbine blade is dependent both on the aerofoil profile used to construct each section and how each is sized and oriented along the blade.

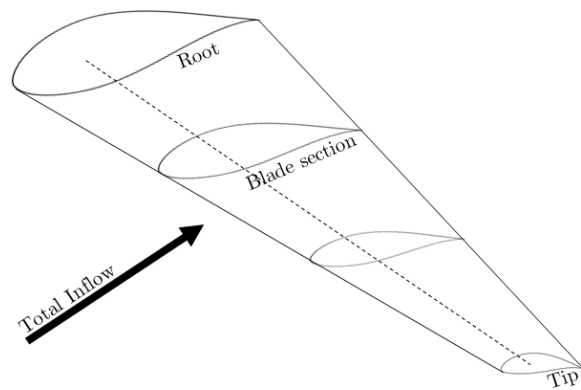


Figure 2.2: A tidal turbine blade with aerofoil sections

Blade design parameters

Chapters 4 and 6 give a more detailed analysis of the effects of different blade parameters on the performance of a tidal turbine. This section provides a brief overview of the blade parameters, some of which are self-explanatory, that this thesis analyses.

1. Blade number, B
2. Rotor radius, R

3. Blade pitch, θ_{root} , is the angle at which the root of the blade is oriented with respect to the inflow.
4. Twist, θ_{section} , is the angle at which each aerofoil section is oriented along the inflow with θ_{root} as a zero-reference point. The twist distribution, $\theta(r)$, is the collection of twist angles for all sections.
5. Chord, c , uses the same definition with chord length in aerofoils and is defined for each aerofoil section. Chord distribution, $c(r)$, is the collection of all chord lengths for all sections. This distribution is made to be dimensionless by getting the ratio of each chord length and the overall blade radius, $c(r)/R$.

Lift and Drag characteristics

The lift and drag characteristics are governed by the geometry of the aerofoil. A pressure differential is developed between the upper(suction) and lower(pressure) edges of the aerofoil as it alters the flow of the fluid passing around it as shown in Figure 2.3. Lift is then generated when higher pressure is developed at the lower edge, compared to the upper edge, of the foil.

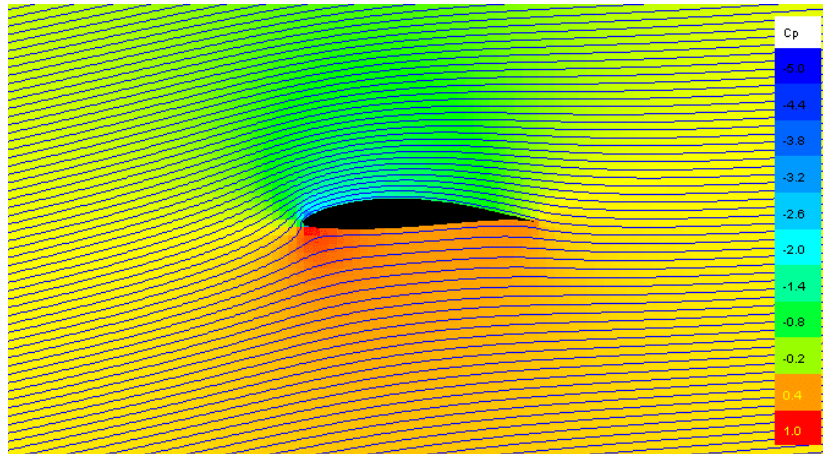


Figure 2.3: Airflow streamlines and pressure variation around a NACA 63-812 aerofoil. Angle of attack, $\alpha = 8^\circ$, generated from Javafoil [48]

Aerofoils can come in a variety of profiles such as the NACA series aerofoils [1, 49], Wortmann [50], NREL [51], etc. Each is designed to produce specific lift and drag as

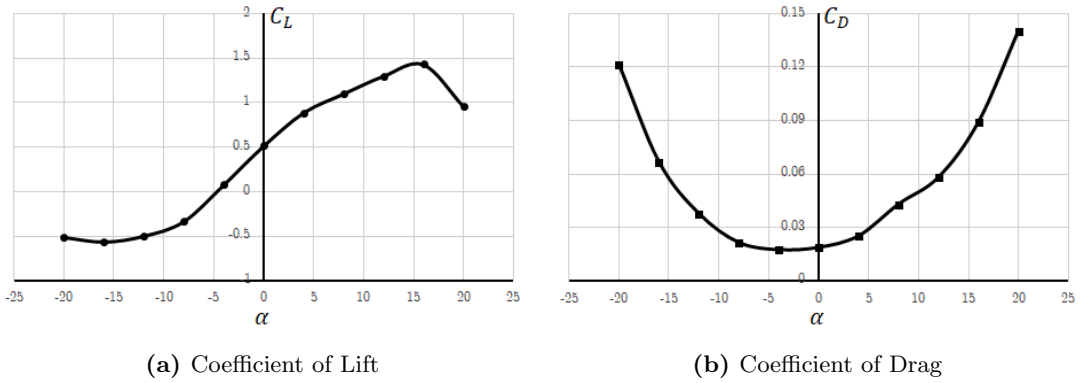


Figure 2.4: Aerodynamic characteristics for NACA 63-824

a function of α . However, aerodynamic characteristics needed to calculate for lift and drag are reported as dimensionless coefficients, C_L and C_D . These characteristics are usually determined through wind tunnel experiments although numerical simulations through XFOIL and CFD may also be used. Figure 2.4 shows plots of C_L and C_D as a function of α .

$$C_L(\alpha) = \frac{L(\alpha)}{\frac{1}{2}\rho U^2 c} \quad (2.1)$$

$$C_D(\alpha) = \frac{D(\alpha)}{\frac{1}{2}\rho U^2 c} \quad (2.2)$$

These aerodynamic characteristics play a significant role in the performance of HATTs as forces developed within the rotor are functions of the C_L and C_D as shown in Equations 2.3 and 2.4. Corollary to this, the accuracy of analytical simulations that rely on aerodynamic characteristics as inputs is very much dependent on the accuracy of the aerofoil data used in the simulations. The fundamentals of aerodynamic theory are thoroughly discussed in [52, 53].

Figure 2.5 shows the inflow vectors and angles needed to resolve forces within the aerofoil section. Figure 2.6 shows that the F_Q and F_n are the tangential and normal components of the sum of lift, L , and drag, D forces, given as a function of the angle of attack, α of the fluid on the aerofoil section. Equations 2.3 and 2.4 are given in elemental forms for each section in a singular blade.

$$\delta F_n = \delta L(\alpha) \cos \phi + \delta D(\alpha) \sin \phi \quad (2.3)$$

$$\delta F_Q = \delta L(\alpha) \sin \phi - \delta D(\alpha) \cos \phi \quad (2.4)$$

where ϕ is total section pitch equal to the sum of the blade pitch and the section twist.

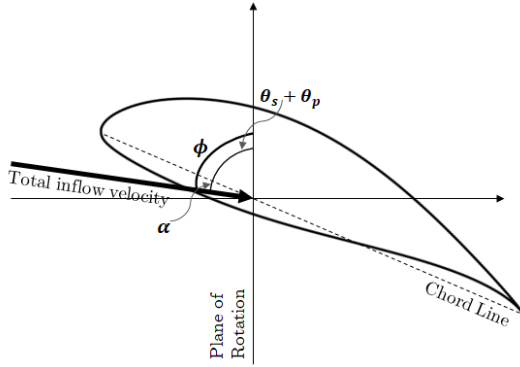


Figure 2.5: Aerofoil Inflow Angles

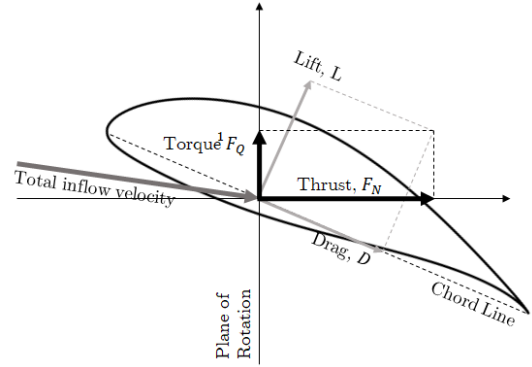


Figure 2.6: Forces¹ in an aerofoil section

Equation 2.4 relates the resulting torque F_Q to the lift and drag developed in an aerofoil. From Figure 2.6, the total inflow velocity vector makes an angle ϕ with respect to the plane of rotation. This inflow angle is the sum of the blade pitch at the given section θ and the angle of attack α . An increase in rotational speed reduces ϕ leading to an increase α . However, maximum torque occurs at the angle of attack that corresponds to $C_L/C_{D_{\max}}$; moving away from this α leads to a loss in power. Thus, it is imperative to adjust the blade and section pitch to accommodate the change in angle of attack. This is incorporated in any design process.

2.1.2 Hydrodynamic performance

Dimensionless aerodynamic characteristics are essential in tidal turbine design because turbines can be built in varying sizes such as the ones described in Section 1.2. Similarly, dimensionless quantities are used to describe the turbine performance.

¹Torque in the figure is a *torque producing* force in Newtons

Hydrodynamics of Tidal Stream Turbines

The tip-speed ratio, TSR or λ , is a common dimensionless quantity used to describe a turbine state and is given by:

$$TSR \equiv \lambda = \frac{\Omega_r R}{U_\infty} \quad (2.5)$$

where Ω_r is the angular velocity of the rotor, R is the rotor radius, and U_∞ is the inflow velocity.

The performance of any rotor can then be given as a function of TSR . The coefficient of power, C_P , and coefficient of thrust, C_T , are non-dimensionalised power and thrust developed as the turbine rotates.

$$C_P = \frac{\Omega_r Q}{\frac{1}{2} \rho U_\infty^3 A} \quad (2.6)$$

$$C_T = \frac{F_n}{\frac{1}{2} \rho U_\infty^2 A} \quad (2.7)$$

where Q and F_n are the overall torque and thrust developed on the rotor respectively, ρ is the density of the ocean water, and A is the swept area of the rotor. Physically, C_P is the ratio power captured by the rotor and the total available power of the incoming flow for a specific area A . C_T , on the other hand, is the ratio of the developed normal force on the rotor over the total dynamic force in the flow.

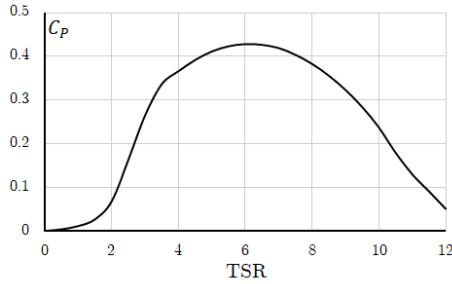


Figure 2.7: Coefficient of Power, C_P

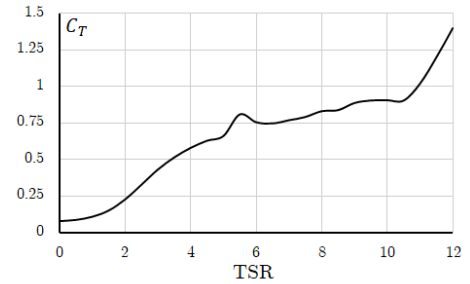


Figure 2.8: Coefficient of Thrust, C_T

C_P can be loosely used as the efficiency of the tidal turbine as it can be taken as the ratio of the power developed in the rotor and the power available in the free stream. However, recall from the discussion on ducted tidal turbines that such turbines are able to produce more power for a given rotor area but are not necessarily more efficient as

more energy is lost in the fluid flow. For ducted turbines, C_P and efficiency cannot be used interchangeably since C_P is generally a function of rotor area while efficiency is solely a function of energy. Equation 2.6 cannot be directly applied for ducted turbine efficiency since the fluid velocity acting on the rotor is significantly higher than the free-stream velocity U_∞ as the duct accelerates the flow [46].

2.1.3 Solidity

Solidity is a derived quantity using the blade number and the chord length. It is a ratio of the total area of the blades and the area of the rotor disc.

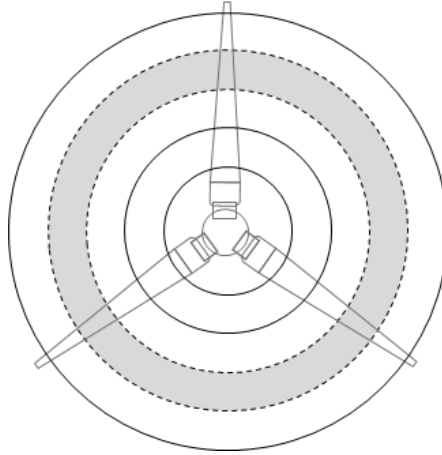


Figure 2.9: Shaded area for Local Rotor Solidity (σ_r). Overall solidity is the ratio of the area of the rotor blade over the circular swept area. It is also the integral of all local solidity values taken from the hub to the tip of the rotor.

Figure 2.9 shows an annular section wherein portions of the rotor overlap with the shaded annular area. The solidity within this shaded portion is defined as the local solidity and is given by Equation 2.8.

$$\sigma_r = \frac{Bc(r)}{2\pi r} \quad (2.8)$$

$$\sigma_s = \sum \sigma_r = \frac{\sum Bc(r)dr}{\pi r^2} \quad (2.9)$$

Note that the denominator is the circumference of the circle, usually taken at the midpoint of the two circles bounding the annulus. The total solidity is then taken as

the sum of all local solidity values, which is the same as taking the integral of all local solidities over the whole radius.²

Solidity is an important consideration in the design of blades as greater solidity allows for more area of interaction between the fluid and the rotor. Thus, it should allow for better power capture subject to other parameters. Schubel [54] showed that more slender blade (lower solidity) is actually preferred for better power capture when operating at higher TSRs.

2.2 Blade Element Momentum Theory

The Blade Element Momentum (BEM) Theory was originally used for the analysis of marine propellers. BEM is a combination of the actuator disc theory developed by Froude [55] and the blade element theory [53]. The inclusion of the blade element theory allows for the analysis of blade sections with C_L and C_D as inputs for Equations 2.3 and 2.4. The Betz limit [56] which is the limit coefficient of power for wind turbines ($C_{P_{\text{Betz}}}$), which is approximately equal to 0.593 can be proven using the Blade Element Momentum Theory.

2.2.1 Linear Momentum and the Betz Limit

In linear momentum theory, the fluid passing through the rotor is assumed to behave within a control volume in the form of a *stream tube* as shown in Figure 2.10. The *actuator disc* bounded by sections **a** and **b** extracts power from the fluid by acting as a momentum sink i.e. the momentum lost by the fluid is absorbed by the actuator disc and converted into power.

Figure 2.10 also shows that the cross-sectional area of the stream tube expands as the fluid flows downstream. This allows for mass to be conserved throughout the stream tube wherein the expansion is due to the loss in fluid velocity [57] consistent with the mass continuity equation.

$$\dot{m} = \rho A_\infty U_\infty = \rho A_d U_d = \rho A_w U_w \quad (2.10)$$

²The integral of the circumference of a circle gives the area of the circle.

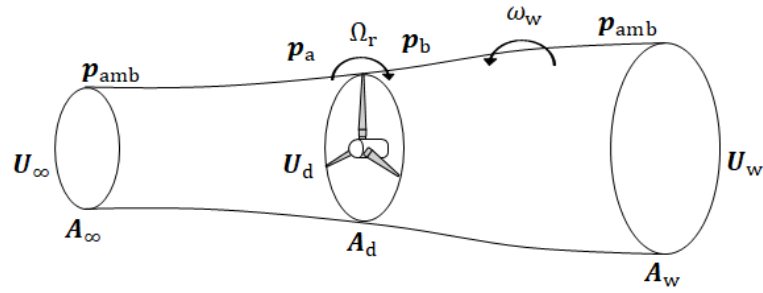


Figure 2.10: A stream tube control volume over the turbine and flow domain

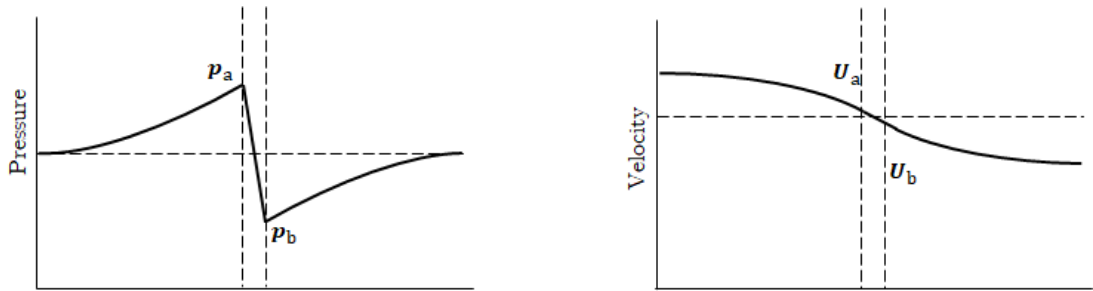


Figure 2.11: Pressure and velocity variation within the stream tube

The axial force on the rotor can be written as the change in momentum $F = \frac{d}{dt}(mU)$ with the velocity drop being the component for U .

$$F_n = \dot{m}(U_\infty - U_w) \quad (2.11)$$

The axial induction factor is defined as the ratio of the velocity drop on the rotor and the free-stream velocity.

$$a = \frac{U_\infty - U_d}{U_\infty} \quad (2.12a)$$

$$U_d = U_\infty(1 - a) \quad (2.12b)$$

A value of $a = 1$ would imply that the fluid comes to a stop as it interacts with the rotor. In terms of power capture, this would mean that all the energy in the flow is captured by the rotor resulting in a power coefficient equal to unity. This is physically impossible but also denotes that C_P can be solved through a .

The axial force on the rotor given by Equation 2.11 can now be written as

$$F_{n,1} = \rho A_d U_\infty (1 - a)(U_\infty - U_w) \quad (2.13)$$

This gives the force on the rotor derived from the change in linear momentum. However, we are left with one equation and two unknowns, a and U_w . Deriving from the conservation of energy, we start with the Bernoulli equation

$$\frac{1}{2}\rho U_\infty^2 + p_\infty = \frac{1}{2}\rho U_d^2 + p_a \quad (2.14a)$$

$$\frac{1}{2}\rho U_w^2 + p_w = \frac{1}{2}\rho U_d^2 + p_b \quad (2.14b)$$

It is reasonable to assume that the p_∞ and p_w are equal as the fluid in the *far* wake recovers lost pressure as it interacts with the ambient fluid. However, this only occurs after the fluid has travelled some distance downstream the turbine. For wind turbines, this is equal to 3-10 turbine diameters downstream [58] and even so, momentum recovery can be hampered leading to decreased performance. Wind turbine spacing is also dependent on land use and cost; the same applies to tidal turbines albeit having a harsher environment and bathymetry limitations.

Subtracting Equation 2.14b from Equation 2.14a

$$p_a - p_b = \frac{1}{2}\rho(U_\infty^2 - U_w^2) \quad (2.15)$$

The axial force on the rotor is the differential pressure from Equation 2.15 multiplied by the rotor area.

$$F_{n,2} = A_d(p_a - p_b) = \frac{1}{2}\rho A_d(U_\infty^2 - U_w^2) \quad (2.16)$$

Equating the expressions for $F_{n,1}$ and $F_{n,2}$, we get an expression for U_w

$$\rho A_d U_\infty (1 - a)(U_\infty - U_w) = \frac{1}{2}\rho A_d(U_\infty^2 - U_w^2) \quad (2.17a)$$

$$U_w = U_\infty(1 - 2a) \quad (2.17b)$$

Substituting Equation 2.17b to Equation 2.13 gives the final expression for the axial force on the rotor

$$F_n = 2\rho A_d U_\infty^2 a(1 - a) \quad (2.18)$$

Note that this equation is different from Equation 2.3, which gives the force on a blade element as a function of the aerodynamic characteristics. This is discussed in detail in the next section.

Equation 2.6 refers to the efficiency of power capture of the rotor. Solving for the power using Equation 2.18 and substituting to the numerator of Equation 2.6,

$$P_{mech} = F_n \frac{dx}{dt} = F_n U_d = 2\rho A_d U_\infty^3 a(1 - a)^2 \quad (2.19a)$$

$$C_P = 4a(1 - a)^2 \quad (2.19b)$$

Taking the derivative of C_P with respect to a gives an expression used to obtain the maximum theoretical power that can be extracted from the free stream.

$$\frac{dC_P}{da} = 4(1 - a)(1 - 3a) = 0 \quad (2.20)$$

A value of $a = 1/3$ is obtained when solving Equation 2.20. Substituting this to Equation 2.19b gives the Betz limit.

$$C_{P,Betz} = 16/27 \approx 0.593 \quad (2.21)$$

Similarly, the equation for C_T given by Equation 2.7 can be expressed in terms of a by using Equation 2.18 as the numerator for the thrust developed on the rotor.

$$C_T = 4a(1 - a) \quad (2.22)$$

2.2.2 Angular Momentum

The previous section only takes into account linear momentum. However, the fluid starts to rotate with the rotor, gaining angular momentum. This can be solved and

used to derive the torque developed by the rotor [57].

Similar to the derivation of linear momentum, it is useful to define a variable to describe the effects of the rotor on the fluid. The tangential induction factor is then defined as

$$a' = \frac{\omega_w}{2\Omega_r} \quad (2.23)$$

where ω_w is the angular velocity of the fluid immediately after the rotor.

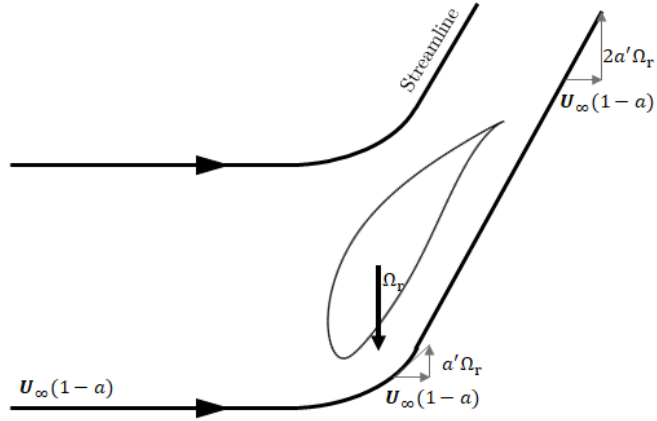


Figure 2.12: Increase of tangential velocity within the wake

Figure 2.12 shows the relative position of V_d and V_w as defined by Burton [57]. Here, the tangential velocity within the wake grows across the disc thickness. The relationship of V_d and V_w with respect to Ω_r is

$$V_d = \Omega_r a' r \quad (2.24)$$

$$V_w = 2\Omega_r a' r \quad (2.25)$$

This relationship holds true due to the absence of rotational momentum at the inlet of the disk such that V_d can be defined as $V_d = \frac{0+V_w}{2}$.

The tangential motion of the fluid has an opposite sense with respect to the rotation

of the rotor. The relative motion of the fluid is then given by

$$V_{d,\text{rel}} = (1 + a')\Omega_r r \quad (2.26)$$

Torque varies from the root to tip as the moment arm increases. This variation is taken into account by assuming an annular control volume with thickness dr positioned at a radial distance, r , from the axis of rotation. The annular control volume rotates with the rotor's angular velocity, Ω_r .

The torque developed on each annular control volume is given by

$$dQ = \dot{m}V_w dr \quad (2.27)$$

Recall from the continuity equation that $\dot{m} = \rho A_d U_d$. Also, the velocity on the rotor disc is $U_d = U_\infty(1 - a)$. Hence, the torque can then be written as

$$dQ = (\rho A_d U_d)(2\Omega_r a' r) dr \quad (2.28a)$$

$$dQ = 4\pi\rho U_\infty(1 - a)\Omega_r a' r^3 dr \quad (2.28b)$$

The inclusion of rotational momentum increases the kinetic energy in the wake. This increase in energy is balanced by a loss in static pressure [57] given by

$$\Delta p = \frac{1}{2}\rho(2\Omega_r a' r)^2 \quad (2.29)$$

Equation 2.29 multiplied by the cross-sectional area of the annular control volume, $dA = 2\pi r dr$, is added to Equation 2.18 to give the axial force

$$dF_n = 2\rho(U_\infty^2 a(1 - a)2\pi r dr) + (\rho(2\Omega_r a' r)\pi r dr) \quad (2.30a)$$

$$dF_n = 4\pi\rho(U_\infty^2 a(1 - a) + (\Omega_r a' r)^2)r dr \quad (2.30b)$$

Equations 2.28b and 2.30b can now be used to calculate the performance of the turbine for any value of a and a' . However, these induction factors are unknown values.

Thus, the momentum equations need to be complemented. Equations 2.3 and 2.4 provide a starting point but cannot be used without deriving the inflow angle, ϕ .

2.2.3 Blade Element Theory

Blade Element theory divides the blade into equally spaced *elements*. Each element is characterised by an aerofoil that generates lift and drag as mentioned in Section 2.1.1. The aerodynamic characteristics of each section are obtained via a lookup table of 2-D C_L and C_D values obtained from experiments, XFOIL, and other published sources, for a specific Reynold's number range.

In Section 2.1.1 the twist, θ_{section} , was defined as the angle at which each aerofoil section is oriented along the inflow. As the blade rotates, it induces tangential flow within the plane of rotation. The actual flow, W , into a section is then a combination of the inflow, U_∞ , assumed to be perfectly aligned with the rotor axis, and the tangential velocity developed, at an angle ϕ onto the said section. It is useful to define the component velocity vectors in terms of the axial and tangential induction factors as from Equations 2.12b and 2.26. The resultant flow can then be solved as

$$\phi = \tan^{-1} \left(\frac{U_\infty(1-a)}{\Omega_r(1+a')r} \right) \quad (2.31a)$$

$$W = \sqrt{(U_\infty(1-a))^2 + (\Omega_r(1+a')r)^2} \quad (2.31b)$$

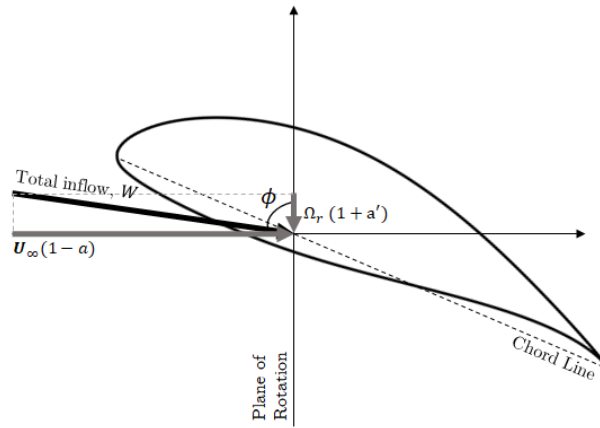


Figure 2.13: Geometric relation of inflow velocity vectors

Equations 2.3 and 2.4 can now be solved with the angle of attack, α , given as

$$\alpha = \phi - (\theta_{\text{section}} + \theta_{\text{root}}) \quad (2.32)$$

$$dF_n = B\rho\frac{1}{2}W^2c(C_L(\alpha)\cos\phi + C_D(\alpha)\sin\phi)dr \quad (2.33)$$

$$dQ = B\rho\frac{1}{2}W^2c(C_L(\alpha)\sin\phi - C_D(\alpha)\cos\phi)rdr \quad (2.34)$$

It is also convenient to define the axial and tangential force coefficients. These are simply the grouped terms in Equations 2.33 and 2.34. These terms are used for clarity in coding and discussion.

$$C_{\text{axial}}(\alpha) = C_L(\alpha)\cos\phi + C_D(\alpha)\sin\phi \quad (2.35)$$

$$C_{\text{tangential}}(\alpha) = C_L(\alpha)\sin\phi - C_D(\alpha)\cos\phi \quad (2.36)$$

The Blade Element Momentum theory is solved by equating the two momentum equations, Equations 2.30b and 2.28b, with their respective blade element counterparts. Each equation is only dependent on a and a' , which can be solved iteratively as developed in the University of Strathclyde [59] based on the work of Masters and Orme [60], implemented in Matlab. However, the two-parameter optimisation presents a problem as it is prone to non-convergence as presented by Ning [61]. Thus, Ning developed a root-finding method that is only dependent on one parameter and will be discussed in Section 2.2.5.

2.2.4 Correction Factors

BEM assumes a non-turbulent, steady-state environment, wherein turbulent vortices developed from the rotation of the rotor is not taken into account [57]. The blade sections are also made to be independent of each other wherein radial flow is neglected. At higher TSRs, a may also exceed its theoretical limit of 0.5 [62] implying flow reversal downstream the turbine. Correction factors are used to account for these effects without sacrificing the computational simplicity of BEM.

Tip and Hub Loss Factors

Similar to aircraft wings, the tip of the blade is prone to radial flow as vortices develop at the end of the blade due to the pressure difference of the suction and pressure side. This decreases hydrodynamic performance [63]. The Prandtl tip loss correction factor, F_{tip} , accounts for the drop in efficiency near the tip where the value of F_{tip} approaches zero. Radial flow also occurs near the root due to the hub geometry [60]. The hub loss correction factor, F_{hub} , is defined similar to F_{tip} wherein the value approaches zero near the root. The product of these two factors is the combined tip and hub loss factor, F .

$$F_{tip} = \frac{2}{\pi} \cos^{-1} \exp \left(-\frac{N}{2} \frac{1-r/R}{(r/R) \sin \phi} \right) \quad (2.37a)$$

$$F_{hub} = \frac{2}{\pi} \cos^{-1} \exp \left(-\frac{N}{2} \frac{r - R_{hub}}{r \sin \phi} \right) \quad (2.37b)$$

$$F = F_{tip} F_{hub} \quad (2.37c)$$

The combined correction factor is incorporated into the momentum equations.

$$dF_n = 4F\pi\rho U_\infty^2 a(1-a) + (\Omega_r a' r)^2 r dr \quad (2.38)$$

$$dQ = 4F\pi\rho U_\infty (1-a)\Omega_r a' r^3 dr \quad (2.39)$$

High induction Factors

The axial induction factor is more likely to be greater than the theoretical limit at higher TSRs, decreasing the calculated coefficient of thrust due to dF_N being a function of $a(1-a)$. This underprediction has been observed and corrected by Glauert [62] and Buhl [64]. Ning [61] noted that gradient optimisation may not be used using the Glauert high induction factor as there is a need to parametrise the correction factors. Thus, the Buhl high induction factor is used.

$$C_{T'r} = \frac{4C_{T,r}}{9} + \left(4F - \frac{20C_{T,r}}{9} \right) a + \left(\frac{25C_{T,r}}{9} - 4F \right) a^2 \quad (2.40)$$

Post-Stall

Turbine rotors can be fixed or variable pitch depending on the intended operational regime by the developer or designer. For simplicity, and to isolate the effects of the intended modifications on the blade design, a fixed-pitch rotor is adopted. This means that the blade section will be operating across the full regime of flow regimes - from (a) attached to (b) stall. It can be difficult to capture the flow phenomena at post-stall using both due to the lack of available C_L and C_D data, as well as the BEM not capturing the complex dynamics during these flow regimes.

Spera [65] presented a post-stall model that modifies the numerical call-up table of lift and drag to tackle post-stall effects. The model assumes that the torque does not decrease with increasing angle of attack and that the blade is a 3D flat plate with the dominant parameter being the maximum drag coefficient occurring at $90^\circ\alpha$. The equations used for the post-stall model for any given blade section at an angle of attack greater than the stall angle of the aerofoil used in the section are given as

$$C_L = C_{D,max} \sin 2\alpha + K_L \frac{\cos^2 \alpha}{\sin \alpha} \quad (2.41a)$$

$$C_D = C_{D,max} \sin^2 \alpha + K_D \cos \alpha \quad (2.41b)$$

$$K_L = (C_{L,s} - C_{D,max} \sin \alpha_s \cos \alpha_s) \frac{\sin \alpha_s}{\cos^2 \alpha_s} \quad (2.41c)$$

$$K_D = \frac{C_{D,s} - C_{D,max} \sin^2 \alpha_s}{\cos^2 \alpha_s} \quad (2.41d)$$

$$C_{D,max} = \begin{cases} 1.11 + 0.018\mu & \mu \leq 50 \\ 2.01 & \mu > 50 \end{cases} \quad (2.41e)$$

where $C_{L,s}$ and $C_{D,s}$ are the lift and drag coefficients at the stall angle.

2.2.5 Single parameter BEM

BEM is usually solved through numerical optimisation by minimising the sum of square errors in the induction factors as presented by Masters [60]. The approach is robust as it incorporates an initial Monte Carlo simulation with sequential quadratic programming,

minimising the risk of non-convergence within small ranges of a and a' . However, the method is still not guaranteed to converge. Ning [61] presented a solution that claims guaranteed convergence while also minimising function calls, thus improving the total time to analyse blades. This is especially important in the design process discussed in Chapters 3 and 4 with multiple blade designs being generated and analysed simultaneously.

The method implemented in this thesis solves BEM through the convergence of ϕ . The first few steps are similar to the Masters [60] with an initial guess of a and a' both usually set to zero. This dictates the initial value for ϕ for each blade section. Two convenience variables κ and κ' are then defined as functions of ϕ .

$$\kappa(\phi) = \frac{\sigma_r C_{\text{axial}}(\phi)}{4F(\phi) \sin^2 \phi} \quad (2.42a)$$

$$a(\phi) = \frac{\kappa(\phi)}{1 + \kappa(\phi)} \quad (2.42b)$$

$$\kappa'(\phi) = \frac{\sigma_r C_{\text{tangential}}(\phi)}{4F(\phi) \sin \phi \cos \phi} \quad (2.43a)$$

$$a'(\phi) = \frac{\kappa'(\phi)}{1 - \kappa'(\phi)} \quad (2.43b)$$

Note that all variables are dependent on ϕ including C_{axial} and $C_{\text{tangential}}$ as given by Equations 2.35 and 2.36. This dependence on ϕ is applied to all succeeding equations involving a and a' .

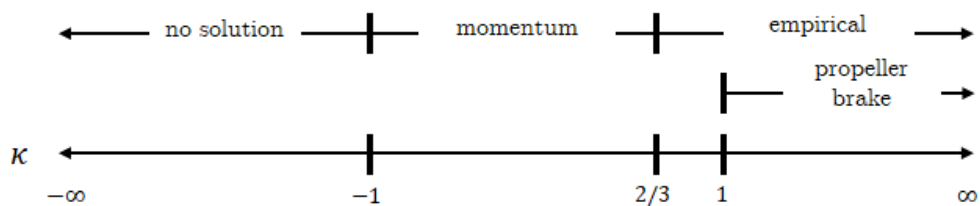


Figure 2.14: Region of validity for values of κ

Figure 2.14 shows the ranges of a where momentum theory is valid and where empirical correction needs to be performed. Induction factors in the propeller break region, which usually happen at higher TSRs, are greater than 1. In conventional BEM, it is typical to limit the solution space of a to avoid this region. However, convergence

via ϕ does not limit a and handles it by a slightly different expression. This is also important as it is possible that blades generated may reach the propeller brake region for all simulated operating points.

For the momentum region, C_T can be calculated directly

$$C_T = 4a(1 - a)F \quad (2.44)$$

For the empirical region, the Buhl high induction correction is simplified for ranges of $-1 < \kappa \leq \beta/(1 - \beta)$ where $\beta = 0.4$. It is incorporated in the solution by altering the function $a(\phi)$ and is applied for values of $\kappa \geq 2/3$.

$$C_T = \left(\frac{50}{9} - 4F\right) a^2 - \left(\frac{40}{9} - 4F\right) a + \frac{8}{9} \quad (2.45)$$

$$a = \frac{\gamma_1 - \sqrt{\gamma_2}}{\gamma_3} \quad (2.46)$$

$$\gamma_1 = 2F\kappa - \left(\frac{10}{9} - F\right) \quad (2.47a)$$

$$\gamma_2 = 2F\kappa - F\left(\frac{4}{3} - F\right) \quad (2.47b)$$

$$\gamma_3 = 2F\kappa - \left(\frac{25}{9} - 2F\right) \quad (2.47c)$$

Equation 2.46 can be undefined when γ_3 is exactly zero. Incidentally, the numerator is also exactly zero when $\gamma_3 = 0$, leading to an indeterminate value and may break the simulation. Adding a small number, $\epsilon = 1e^{-5}$ prevents this without introducing a significant amount of error.

The final region involving propeller brake with $a > 1$ introduces a change in sign for C_T and is valid for $\kappa > 1$.

$$C_T = 4a(a - 1)F \quad (2.48)$$

Solving for a using sectional theory then changes the expression to

$$a(\phi) = \frac{\kappa(\phi)}{\kappa(\phi) - 1} \quad (2.49)$$

Equation 2.31a showed the geometric relationship between a , a' , and ϕ . This relationship is used to form the residual equation subject to the solution regions shown in Figure 2.14. The residual equation $f(\phi)$ for the momentum region and f_{PB} for the propeller brake region are

$$f(\phi) = \frac{\sin \phi}{1 - a} - \frac{\cos \phi}{\lambda_r(1 + a')} = 0 \quad (2.50)$$

$$f_{\text{PB}}(\phi) = \sin \phi(1 - \kappa) - \frac{1}{\lambda_r} \cos \phi(1 - \kappa') \quad (2.51)$$

which is just the difference between the corresponding numerators and denominators i.e. $\sin \phi = 1 - a$ and $\cos \phi = \lambda_r(1 + a')$.

2.3 Turbines operating under non-uniform flow

It is convenient to assume a steady-state and uniform velocity profile for the entire water column. However, to simulate real-world sites, there is a need to understand how the velocity varies from the surface to the seabed. The bottom boundary layer leads to a sheared velocity field across the water column. This introduces a variation in load that induces fluctuations in power production and fatigue not only in the blades but also in the turbine components.

An understanding of how the flow profile is modelled is needed before presenting its implications on rotor performance. Existing studies on the effects of sheared flow include these model profiles derived from real-world data.

2.3.1 Modelling a sheared tidal velocity profile

The typical velocity profile used by oceanographers [66] adopts a power law profile incorporating seabed friction.

$$U(z) = \bar{U} \left(\frac{z}{\beta_{\text{seabed}} h} \right)^{1/\alpha_{\text{prof}}} \quad (2.52)$$

Hydrodynamics of Tidal Stream Turbines

where \bar{U} is the depth-averaged velocity, β_{seabed} is the seabed friction coefficient, z is the position along the water column with depth h being analysed. The value of α_{prof} describes the power law; $\alpha_{\text{prof}} = 7$ pertains to the commonly used 1/7th power law. Alternatively, a simpler version is provided from the wind turbine industry [67] given as

$$U(z) = U_s \left(\frac{z}{h} \right)^{1/\alpha_{\text{prof}}} \quad (2.53)$$

where U_s is the surface velocity.

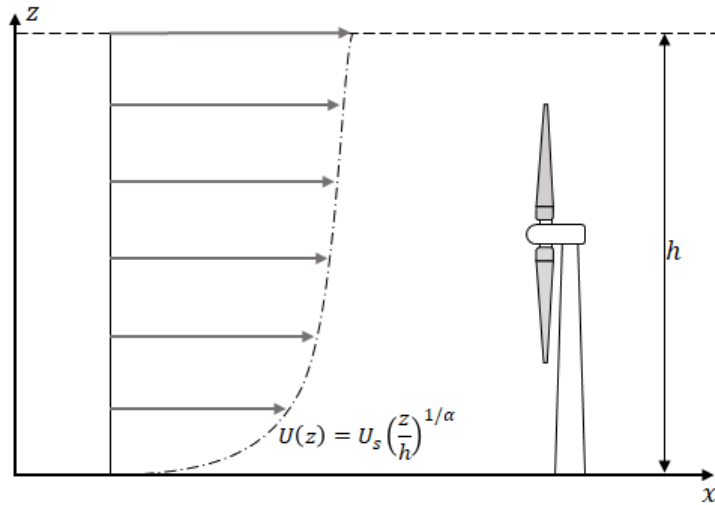


Figure 2.15: Sheared inflow profile due to seabed friction

The 1/7th power law has been observed in potential tidal sites in France and the UK. Furgerot [68] used acoustic-doppler current profilers (ADCP) and obtained a 100-day series of velocity readings in the Alderney Race, France. The results show that $\alpha_{\text{prof}} \approx 6.6$ with a maximum value of 15 at 0.2m/s and a minimum of 5.9 at 1.5m/s. There remains to be no significant trend within the range of 0.5-1.5m/s although an increasing α is observed for values beyond 1.5m/s with the faster speeds fitting better to $\alpha \approx 7$.

Lewis [69] deployed ADCP for two months in two sites within the Irish sea and observed similar results with a mean of $\alpha_{\text{prof}} = 7.1$ and $\beta_{\text{seabed}} = 0.4$. While the mean profile is similar for two sites, the observed increase and decrease in α_{prof} for accelerating or decelerating flow is inconsistent.

The ReDAPT project [70] obtained multi-year measurements of tidal velocity

profiles in EMEC. Flood tides followed $\alpha_{\text{prof}} = 7$ quite closely although the same was not observed for ebb tides wherein the velocity profiles observed were consistent with the observations of [71–74], which are discussed in Section 2.4.1.

In the absence of data, the use of the $1/7^{\text{th}}$ power law will better capture real-world conditions compared to uniform inflow. However, there is no reason to assume that the $\alpha_{\text{prof}} = 7$ is representative of all sites, especially for less energetic sites that have not been thoroughly characterised. This thesis uses a mix of real-world data and the $1/7^{\text{th}}$ power law for design and analysis.

2.3.2 Effects of a sheared velocity profile on turbine loading

The effects of a sheared velocity profile are not only present in tidal turbines. As previously discussed, the wind turbine industry has been using the power law to model the flow in wind turbine sites. Wagner [75] illustrated the inflow velocity for a given section on a turbine varies as it rotates along the rotor axis. This changes the angle of attack, which also changes the lift and drag characteristics of the aerofoil used in the blade section. However, from Section 2.2.3, it is not only the free stream velocity that is taken into account for the total inflow velocity - the angular velocity also influences the total inflow velocity. Assuming constant angular speed, higher TSRs would result in less variation in the relative speed as shown in Figure 2.16. Since wind turbines generally operate at high TSRs of greater than 7, a decrease of less than 1% in power production is observed.

Mason-Jones [76] studied the effects of sheared flow to a Wortmann FX63-137 tidal turbine using the $1/7^{\text{th}}$ power law and observed a drop of up to 70% in power when compared to a turbine operating in uniform inflow. However, it was noted that there is difficulty in the comparison as using \bar{U} instead of U_S in Equation 2.6 decreased the impact of the sheared flow to only a 15% decrease. Wagner [75] used the kinetic energy flux and thus reported a small variation in power output in addition to high TSR operation among other factors.

Hafeez [77] reported a 12% reduction in C_P for an SG06342 turbine operating at optimum TSR. A structural analysis was conducted using ANSYS CFX and ANSYS

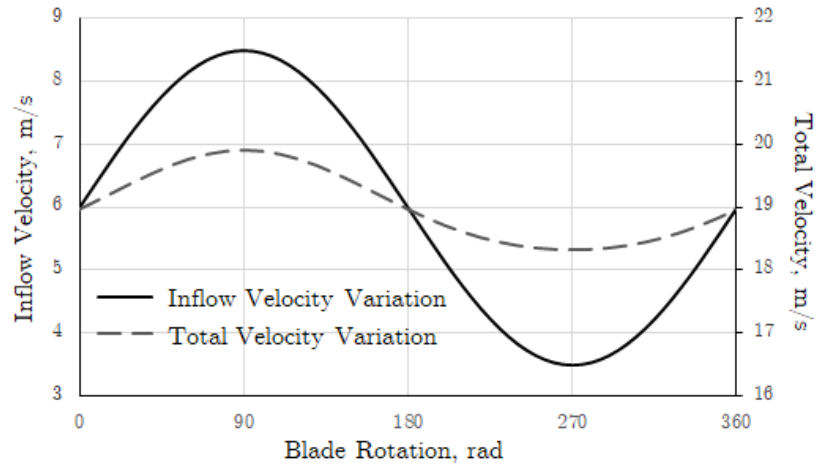


Figure 2.16: Velocity variation for 4m diameter rotor operating at $TSR = 6$ under linear shear with $U_{ave} = 6$ with period of 2π . Note the smaller amplitude of the total velocity inflow as a result of the tip-speed of 18m/s.

static structural analysis to observe changes in fatigue life. In sheared flow, total deformation decreased and had little to no effect on design fatigue life, which was attributed to the small diameter of the simulated turbine at 0.28m.

As presented, a sheared inflow profile significantly affects the performance of tidal turbine blades. While the goal of the design process is to obtain maximum performance towards higher TSRs, as is the case for wind turbines, and may result in reduced impact of sheared profile flow, it is still paramount to quantify these effects to make the case for high-TSR blades compared to traditional low-TSR blades.

2.3.3 Incorporation of flow profile in BEM

Incorporating a profiled flow in BEM involves passing of a table of tidal velocities and a time-domain simulation. This changes U_∞ in Equation 2.31a to $U_\infty(t)$ and the tracking of the coordinates of each blade section within the rotor plane. Nevalainen [59] proposed a simple way of implementing this by using a rotating coordinate system and a transformation matrix for each time step.

Figure 2.17 shows a coordinate system that using the radial and tangential vectors of each blade section along the blade as opposed to the global coordinate system that is used in traditional steady-state uniform flow BEM. Matching the velocities of each

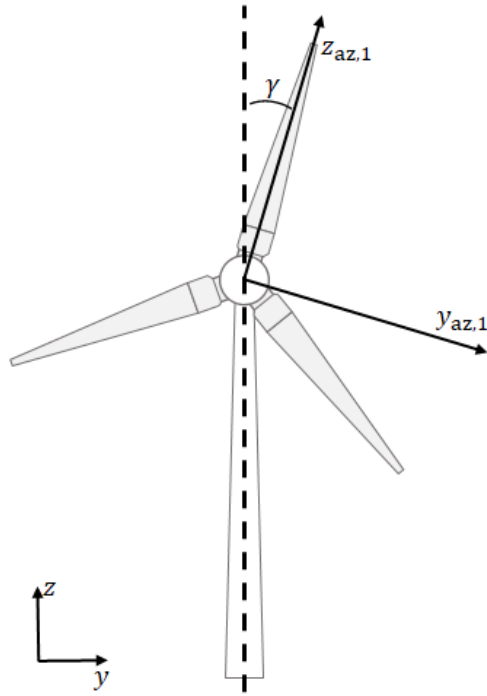


Figure 2.17: Transformation of global y - z axis to azimuthal y - z' axis

blade section to the respective tidal inflow from Equation 2.53, which is in terms of the global coordinate system, require the use of the transformation matrix

$$R = \begin{bmatrix} 1 & 0 & 0 \\ 0 & \cos \gamma & -\sin \gamma \\ 0 & \sin \gamma & \cos \gamma \end{bmatrix}$$

2.4 Wave-Current Interactions

The tidal velocity profile discussed in the previous section is distorted by the motion of the particles and this has been observed and analysed by numerous researchers. The effect of waves on the current profile differs depending on the direction of wave propagation: concurrent, counter-current, or yawed.

2.4.1 Observations and modelling of wave-current interactions

Waves in the sea are a combination of longitudinal and transverse wave motions with water particles travelling clockwise as shown in Figure 2.18. Particle motion is greatest along the surface and diminishes as it reaches the bottom [78]. Norris and Droniou [79] observed that waves penetrate up to 15m down the water column for a depth of 45m, leading to fluctuations in the current-only velocity profile. This is particularly important to tidal turbines as the particle motions add to the inflow velocity not only along the dominant tidal inflow direction but also impart a vertical velocity component.

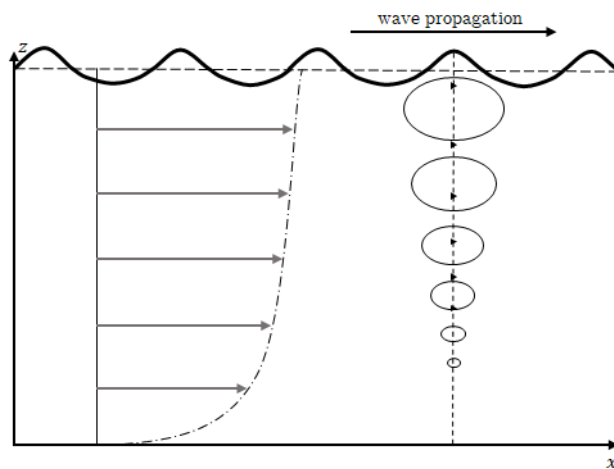


Figure 2.18: Wave propagation and particle motion along the water column under the presence of waves

For concurrent waves, Kemp and Simons [71], observed water waves following a current travelling along a smooth bed. Mean current velocities directly below the surface are reduced while the near-bottom current velocities are increased. The effect becomes more significant as wave height increases. The same observation was made by Klopman [73] for a current travelling along a bed with a roughness of 1.2mm. Umeyama [74] expanded the discussion to include the effects of increasing wave period. It was observed that wave periods counteract the effects of wave height i.e. the reduction of the near-surface current velocity and the increase in the near-bottom current velocity are both lessened at greater wave periods.

Hydrodynamics of Tidal Stream Turbines

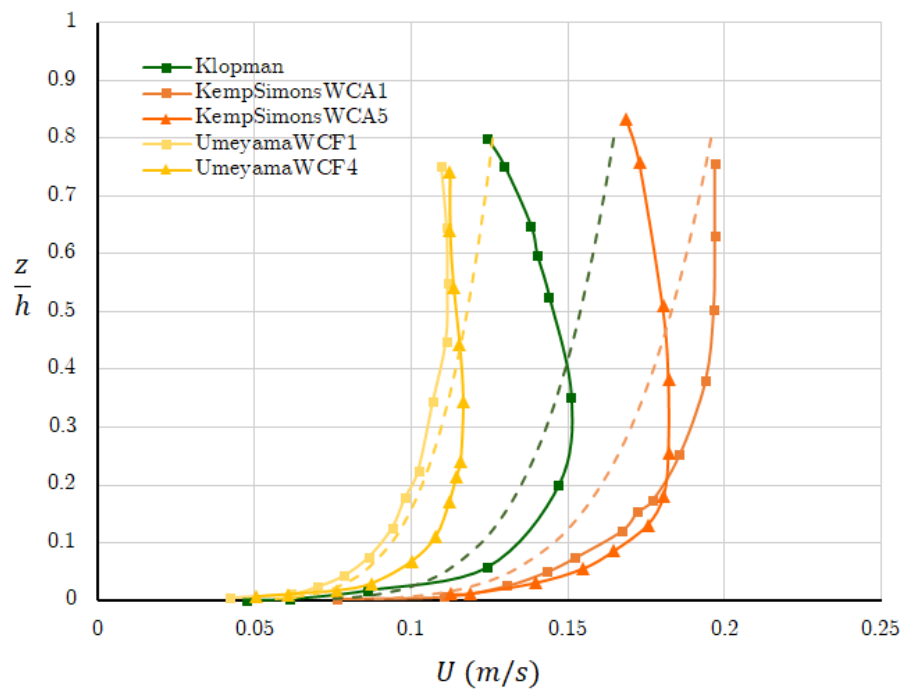


Figure 2.19: Profiles with concurrent waves from Klopman [73], Kemp and Simons [71], and Umeyama [74]

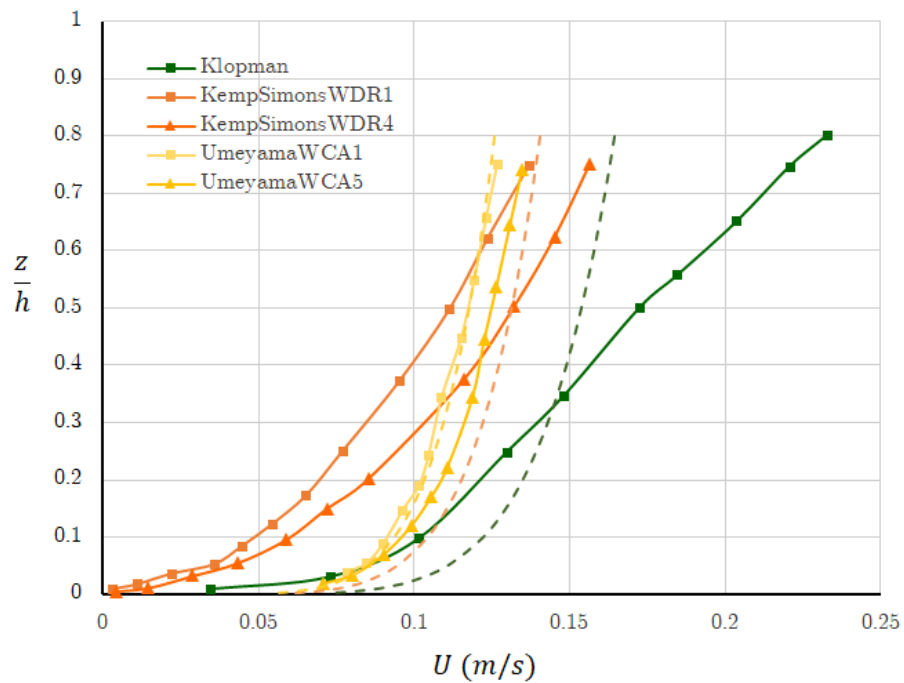


Figure 2.20: Profiles with counter-current waves from Klopman [73], Kemp and Simons [72], and Umeyama [74]

For counter-current waves, the opposite was observed. Kemp and Simons [72] and Klopman [73] observed similar results for the mean velocities; near-surface velocities are increased accompanied by a decrease in near-bottom velocities. Umeyama [74] reported a similar result although the increase in the near-surface velocities are as pronounced. Figures 2.19 and 2.20 show the distortion of the velocity profile in the presence of waves. In terms of sheared flow discussed in Section 2.3.1, a counter-current wave propagation increases the rate of shear in the velocity profile as is consistent with the increase in apparent bed roughness [72–74] to be substituted to β_{seabed} in Equation 2.52.

The change in the mean tidal velocity profile is due to the mass transport within the water column. Olabarrieta [80] defines three different regions in combined wave and current flow. The first region has a wave-dominated mass transport. The second region is directly below the wave trough where the variation from the steady-state tidal velocity profile is changed by the wave-induced Reynolds stresses. The last corresponds to the near-bottom region. The change in the tidal current velocity in this region, as observed by Kemp and Simons [71, 72] and Klopman [73], is attributed to the compensation of mass flow across the water column [80]. In cases of decreased velocity in the second region, the flow in the third region is accelerated.

Yawed propagation of waves with respect to the current also induces a change in the tidal velocity profile. Visser [81] and Musumeci [82] reported similar findings with counter-current waves without a reduction in near-bed current velocities. Yawed inflow analysis considering yawed propagation will include wave velocity components, can be accommodated using the transformation matrix in Equation 2.3.3. However, it is not discussed in this thesis as it is assumed that the dominant velocity that the designed tidal turbines will operate in a flow parallel with the rotor axis.

2.4.2 Effects of wave-current interactions

Section 2.3.2 showed that a sheared velocity profile may lead to a reduction in performance compared to steady uniform flow. The inclusion of waves does not necessarily change the performance of the turbine even with a distorted velocity profile. However, it is repeatedly observed that waves induce large fluctuations in

loading, leading to fatigue that is not present in steady uniform flow.

Barltrop [83] tested a 400mm-diameter NREL S814 3-bladed turbine in a towing tank with towing speeds of 0.0-1.6 m/s, wave heights of 0.02-0.14m, and wave periods of 1.2s and 1.6s. At fixed rotational speeds, the inclusion of waves increases mean rotor torque in the lower range of speeds. This is an important consideration for less energetic flows as this increase in mean torque is not observed within the faster speeds tested. Additionally, a significant load oscillation for both torque and thrust were observed as waves were included wherein the peak-to-peak oscillation increases proportionally with the wave height.

Gaurier [84] conducted flume testing of a 900mm-diameter 3-bladed turbine under a mean current speed of 0.6m/s, wave heights of 0.08m and 0.14m, and wave periods of 1.42s and 2.0s. The current-only flow induces a 5% standard deviation of the instantaneous power and thrust, from the mean, for each TSR and velocity setting. The inclusion of waves increases this deviation to greater than 15% with larger standard deviations towards higher TSRs. This is also an important consideration for the design of high-TSR blades i.e. high-TSR blades may be subject to higher fatigue loads and must be managed.

Henriques et al [85] tested a 500mm-diameter 3-bladed turbine in a recirculating water channel with a mean current speed of 0.5m/s, wave heights of 0.041m and 0.078m, and wave periods of 0.71s and 0.91s. These results are different from the trend observed by Gaurier [84] as the standard deviation for power decreases at higher TSRs. This was attributed to the difference in control strategy where Henriques [85] used torque-control and Gaurier [84] used speed-control. The difference in the fluctuations between torque and speed control has also been recently studied by Ordonez-Sanchez et al [86] highlighting the low amplitude fluctuations when using torque-control. Control strategies for high-TSR blades may be used to manage the fatigue loads but remain to be outside the scope of this thesis. Nonetheless, the study has shown that increased wave loads are to be expected as wave heights and wave periods are increased.

Effects of waves on less energetic flow. Faudot [87] showed that waves induce a variation in the loads and performance of a tidal turbine. This variation is cyclical following the periodic nature of wave-induced velocities. Faudot used the concept of relative current number defined as the ratio between the current velocity and the amplitude of the horizontal velocity variations computed through the wave and dispersion equations. Figure 2.21 shows the standard deviation of thrust and torque

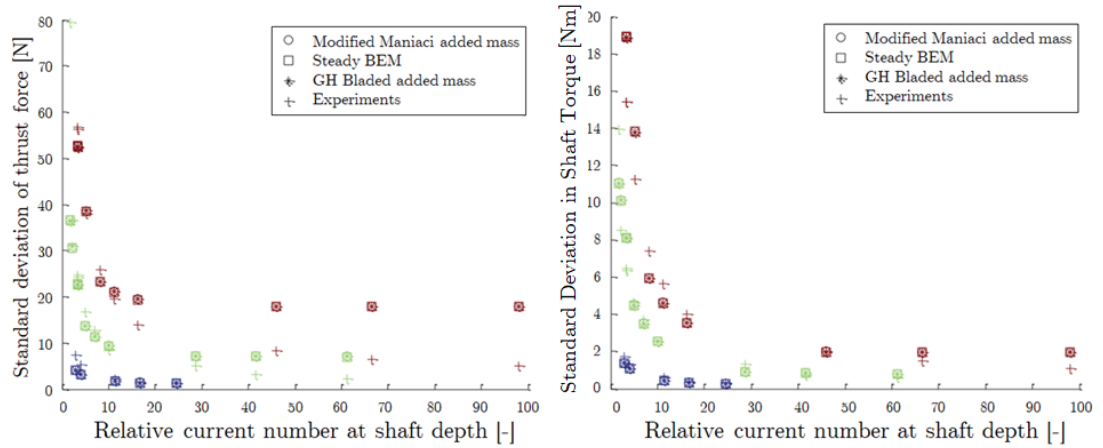


Figure 2.21: Relative Current Number and deviations in Turbine Loads. Adapted from Faudot [87]. CC-BY-ND-3.0

on the shaft of the turbine is exponentially reduced at higher relative current numbers. These are currents that have much higher magnitudes compared to the wave-induced velocities - a characteristic of energetic currents ($U_\infty > 2\text{m/s}$). The same cannot be said for less energetic sites ($U_\infty < 2\text{m/s}$) since these are sites with smaller relative current numbers due to the fact that the wave-induced velocities may remain the same while current velocity magnitude is reduced.

The equation for the relative current number from Faudot [87] is not directly employed in this thesis although the qualitative definition is adopted. Section 2.4.3 discusses how wave-induced velocities are calculated - the same velocities are then used to get the relative current number, and incorporated in the discussion of performance of the turbine in select sites (See Chapter 7).

2.4.3 Incorporating wave-current interactions in BEM

A discussion on the governing differential equations is presented in [59, 88]. The following sections present the adopted solution method to combine wave and current loads to simulate the performance of a tidal turbine.

The solution method presented in this section follows the linear superposition method of Dalrymple with a discussion on the dispersion equation at the latter part of the section.

Superposition method

The superposition method by Dalrymple [89] allows for the simulation of wave-current by addition of current and wave velocities. In this thesis, it is assumed that the vertical velocity of the current is insignificant.

$$U(x, z, t) = U_{\text{wave}}(x, z', t) + U_{\infty}(x, z, t) \quad (2.54)$$

$$W(y, z, t) = W_{\text{wave}}(y, z', t) \quad (2.55)$$

The above equations seem to present a simple addition of the wave velocities typically determined by different wave theories. However, as waves affect the current profile so does the current affects the kinematics of the wave. Waves travelling with a fixed period T experiences a Doppler shift with an apparent period T_{app} as seen from an observer with the depth-averaged current velocity.

$$\frac{L}{T} = \frac{L}{T_{\text{app}}} + \bar{U} \quad (2.56)$$

where L is the wavelength. The depth-averaged current can be approximated by

$$\bar{U} = \frac{2k}{\sinh 2kh} \int_0^h U(z) \frac{z}{h} \cosh 2kz dz \quad (2.57)$$

where k is the wave number, the number of waves present for a unit distance, and is usually solved numerically.

It is seldom the case that the L , T , and T_{app} are all available; these are calculated through the dispersion relation.

$$T_{\text{app}}^2 = \frac{2\pi L}{g \tanh kh} \quad (2.58)$$

The equations above provide a starting point in determining the wave kinematics. The velocity variation along the water column can be solved numerically using CFD or analytically through the Stokes theory.

Linear and Stokes waves

Linear wave theory, or the first-order stokes theory, is the simplest approach to determine wave kinematics - wave height, propagation, and flow variation. Linear waves have infinitely small wave steepness as a consequence of the assumption of an undisturbed mean surface level. This theory has been incorporated to BEM by several researchers and found good agreement with experimental data although it is found to underpredict loading for steeper waves. Stoke wave theories such as those presented by Fenton [88] and Kishida and Sobey [90] are used to resolve wave kinematics for steeper waves. The general solution approach is to use Fourier series expansion according to the stokes order of the wave. Figure 2.22 shows the regions of applicability.

Fenton [88] provided a solution method for a fifth-order Stokes wave. Several cases for starting the solution are presented depending on the known parameters. The wave height, depth, and wave period are generally available upon resource assessment. The mean current speed can be extracted from time-series data as has been the approach from [68–70]. This leads to case 3 of the solution method³ starting with an approximation of k from the linear wave theory for small C_E

$$k_{\text{initial}} \approx \frac{4\pi^2}{T^2 g} \left(1 - \frac{4\pi C_E}{gT} \right) \quad (2.59)$$

where C_E is the Eulerian time-averaged fluid velocity [88], which is equal to the mean

³Fenton describes five different cases according to the availability of wave and current variables.

current measured by a stationary velocity meter.

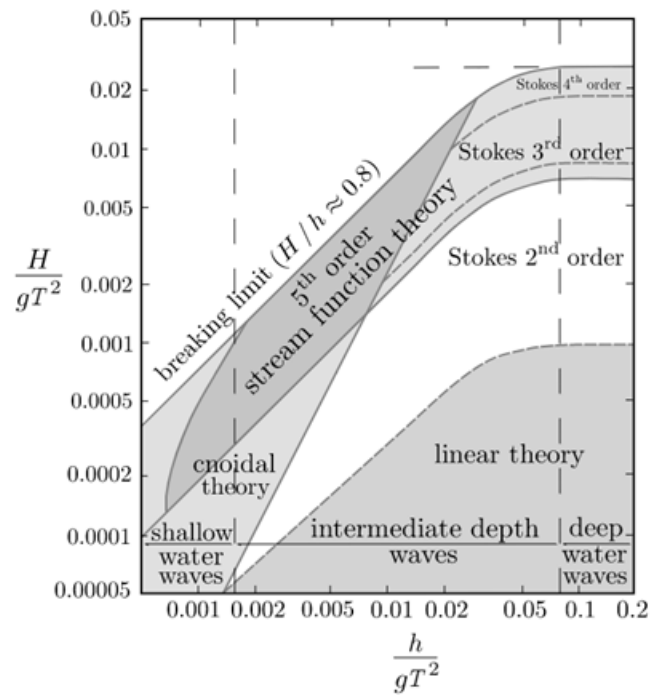


Figure 2.22: Applicability of wave theories. Adapted from WikiMedia Commons under [CC BY-SA 3.0](https://creativecommons.org/licenses/by-sa/3.0/)

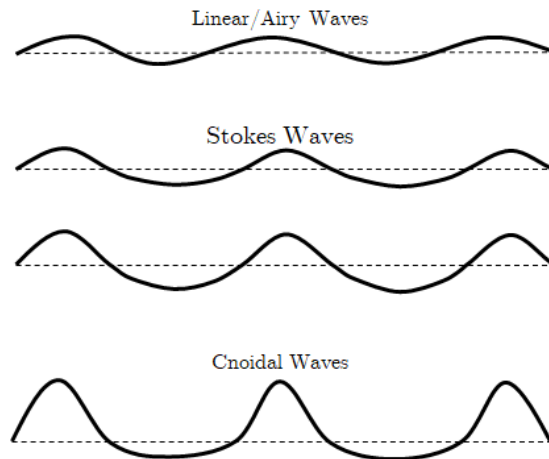


Figure 2.23: Wave types. Linear waves have small amplitudes while Stokes waves and Cnoidal waves have varying wave steepness. Cnoidal waves have long and flat troughs.

The error function used to solve for k is the non-linear dispersion relation

$$C_E \frac{k^{1/2}}{g} - \frac{2\pi}{T\sqrt{gk}} + C_0 + C_2\epsilon^2 + C_4\epsilon^4 = 0 \quad (2.60)$$

$$\epsilon = \frac{kH}{2} \quad (2.61)$$

where C_0 , C_2 , and C_4 are coefficients that are written as functions of kh .

The velocity potential at the free surface within the rotor plane is obtained by differentiating $\psi(x, z, t)$ such that $\frac{\delta\psi}{\delta x} = u_{\text{wave}}$ and $\frac{\delta\psi}{\delta z} = v_{\text{wave}}$

$$\psi(x, z, t) = (C - \bar{u})x + C_0 \left(\frac{g}{k^3}\right)^{1/2} \sum_{i=1}^{N_{\text{stokes}}} \epsilon^i \sum_{j=1}^i A_{ij} \cosh jkz \sin jk(x - Ct) \quad (2.62)$$

$$C = \bar{U} + \left(\frac{g}{k}\right)^{1/2} (C_0 + C_2\epsilon^2 + C_4\epsilon^4) \quad (2.63)$$

Note that the x -coordinate at the rotor plane is set to 0 such that the first term given by Fenton [88] is neglected. The coefficients A_{ij} are given as functions of kh . Raschii Python [91] provides a simple and effective method of extracting these and are adopted into the code.

Swan [92] has shown that Kishida and Sobey [90] provides a more accurate solution for waves propagating with a sheared current. This is due to the inclusion of vorticity terms that are neglected in Fenton's approach; case 3 does specify a mean uniform current. However, using Dalrymple [89] linear superposition method, it is possible to obtain accurate results as was the case when comparing the results (Figure 2.24) from Nevalainen [59] using a 3rd order Stokes from [90] and the foregoing method. This comparison was presented by the author [93] as part of the research.

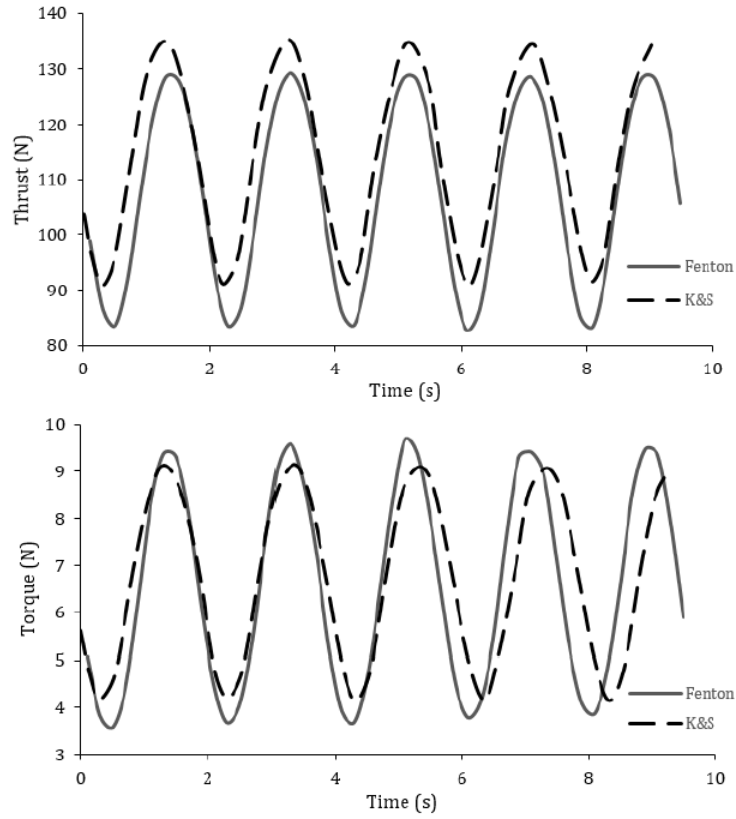


Figure 2.24: Simulated results using Fenton [88] vs simulated results using Kishida and Sobey [90] from Nevailanen [59] of a WCI with 3rd order Stokes wave: Gaurier [84] W&C1 ($U = 0.67\text{m/s}$, $T = 2\text{s}$, $H = 0.16\text{m}$)

Kinematic stretching

Waves cause a vertical displacement within the water column, stretching or compressing the original coordinate system from x - z to x - z' as shown in Figure 2.25. Dalrymple [89] includes this in the superposition method.

$$z' = z + \eta \frac{\sinh kz}{\sinh kh} \quad (2.64)$$

where η is the vertical displacement of the free surface, the effect of which diminishes from the \sinh term. This also reflects the findings of Russel [78] and Norris [79] as previously discussed in this chapter.

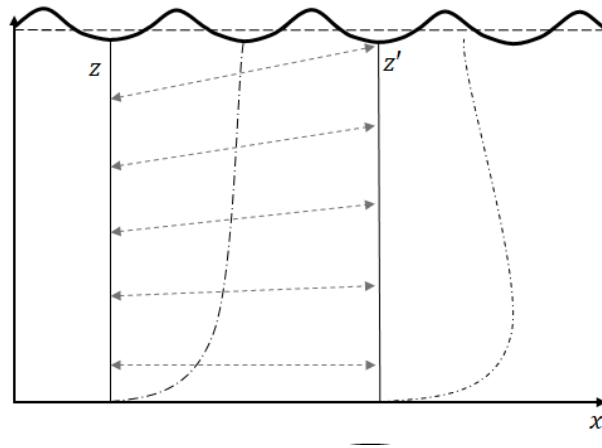


Figure 2.25: Inflow mapping of z -axis as a result of the stretched water column as the free surface is displaced by η

2.5 Summary

The chapter discussed the hydrodynamics of tidal turbines and derived the working equations for the Blade Element Momentum theory and how it is implemented in the thesis, which incorporates wave-current interactions. These wave-current interactions present an important consideration for turbines operating in less energetic currents. That is, higher variability in loading may be expected in less energetic currents due to the lower current magnitudes that are more susceptible to change from wave-induced velocity variations in addition to the changing of the current velocity profile depending on how the wave propagates with respect to the tidal current.

Chapter 3

Tidal turbine blade design

3.1 Methods on blade design

3.1.1 Considerations in Turbine Design Optimisation

The previous chapter discussed the fundamental similarities between wind and tidal turbines. This extends to design techniques and optimisation methods applicable to HATTs. However, there is a need to consider greater loads due to the difference in fluid densities ($\rho_{\text{air}} = 1.225\text{kg/m}^3$, $\rho_{\text{seawater}} = 1020$ to 1029kg/m^3). Additional considerations in the marine environment include biofouling, oxidation, erosion, etc., which affect the life cycle of the device, installation, operation, maintenance, and decommissioning. These additional considerations are not tackled in this thesis but are provided to differentiate the operation of wind turbines from tidal turbines.

From wind turbines to tidal turbines

Chehouri [94] discusses that initial wind turbine optimisation focused on C_P maximisation. This changed to a focus on the maximum energy production over a time period since C_P maximisation may be limited to one or narrow ranges of tip-speed ratios. The change led to the development of blades with smaller root chords and less twist. However optimised for power production, there was still a need to compete with high-yield traditional fossil fuel energy sources. The focus was again shifted towards the improvement in energy economics. This led to slender blades with lower solidity - a trade-off in power production and the cost associated with manufacturing, operation,

and maintenance i.e. slender blades have less mass and experience decreased loads.

There is an agreement within the wind turbine industry that the goal of optimisation is to minimise the cost of energy [94]. This also applies to the tidal turbine industry. Segura [95] notes the importance of assessing the economic viability of tidal technology, which remains to be one of the main challenges faced by stakeholders.

Overview of Optimisation Methods. Much of the work on the optimisation of horizontal axis wind turbine blades generally fall under the three categories [94, 96]:

1. Minimisation of Cost of Energy (COE)
2. Maximisation of the Annual Energy Production (AEP)
3. Minimisation of Blade Mass [94] while managing blade and component stress [96]

Chehourri [94] presented four main categories including multi-objective optimisation. However, minimisation of cost of energy can be considered a multi-objective optimisation problem since striking a balance between cost and production usually leads to a conflict of objectives.

The cost of energy is usually given by

$$COE = \frac{C}{AEP} \quad (3.1)$$

where C is the total cost of an energy technology. It is easy to see how increasing AEP will lead to lower COE. On the other hand, reducing blade mass and reduced loads can lower cost associated with the rotor and other components. However, there also exists a relationship between AEP and loads as aerodynamics dictate both the power produced and the loads developed on the blade i.e. lower loads usually lead to less power production (Equations 2.3 and 2.4). Thus, optimising both at the same time without tackling trade-offs is seldom achieved.

Optimisation of mass while managing stresses. Most wind turbine blades are constructed using composite materials due to the relatively low cost of manufacturing

compared to other materials. However, construction and layup of composite turbine blades still vary. This variation leads to multiple optimisation opportunities and much of the work that deals with mass optimisation deals with the construction, design, and layup of the composites that make up the turbine blade [97–100].

Altering the material for each part of the blade not only optimises mass but may also increase blade stability [97]. The number of composite layers also influence the stresses within a blade i.e. reducing layers effectively reduce overall strength by increasing the stress for each layer. However, for large wind turbines, the increase in blade mass for each additional layer presents a trade-off between stability and cost, as well as power production [98, 99].

For tidal turbines, optimisation by blade mass is more complex as the choice of material is not only dependent on failure by fatigue, creep, or extreme blade loads. The marine environment is highly corrosive, encourages erosion due to abrasive particles, prone to biofouling [101] in addition to turbines sustaining greater loads due to fluid density difference, and the added risk of cavitation. This presents a huge opportunity for optimisation for tidal turbine blades that can survive the ocean environment [102].

However, it is understandable that optimisation of blade mass is not a specific focus in the tidal turbine industry. It is usually the case that blades are constructed with preventive measures against corrosion, erosion, and biofouling without strict cost limitations. This is due to the low cost of the rotor relative to the whole turbine cost (3% of the whole turbine) [95]. There is a priority given to reliability as consequential losses due to failure is a significant element in tidal turbine economics [103].

Optimisation by Annual Energy Production. Chehouri [94] gives the general equation in terms of wind speed distribution, $f(U)$, and the power curve of a given turbine, $P(U)$.

$$AEP = \int_{U_{\min}}^{U_{\max}} P(U)f(U)dU \quad (3.2)$$

The equation presents an additional consideration: site-specific conditions as dictated by the $f(U)$ term. Kenway and Martins [104] demonstrated the need to optimise wind turbines for a specific site i.e. using a one-size-fits-all turbine leads to a

3-4% loss in AEP across sites. There is a difference in modelling wind energy flux and tidal energy flux since tidal currents are predictable¹, but not matching appropriate technologies to sites will still lead to suboptimal operation [22].

AEP maximisation provides an easy but simplistic way to minimise the cost of energy. It is usually employed as it is difficult to optimise by COE without an accurate knowledge of the costs of each component [94, 104]. A few researchers [95, 105] have provided a comprehensive cost breakdown for tidal turbines but it is still difficult to assess economic viability without first having characterised the performance of a device. A change in a component that alters the operational characteristics of the device will require more component changes along the drive train and support structure. This means that high-TSR blades would need generators operating at higher RPMs to accommodate the change in operational speed, among many others.

As mentioned, it is simplistic to optimise AEP while assuming cost constancy to reduce the COE. It is possible to achieve better performance that requires more costly methods of manufacturing, operation, and maintenance. Designers then apply constraints [104, 106–108] on maximum allowable stress, blade mass, material, and even maximum power into the optimisation routines to ensure site and component compatibility while also mitigating increases in costs. Ning and Damiani [106] presented a comprehensive sensitivity analysis on the effects of changing variables, as well as constraints, have on the AEP of turbines.

Kenway and Martins [104] optimised a wind turbine blade by changing the blade shape while applying constraints on blade surface area, fatigue stress, and maximum spar mass. Four control points were identified to dictate the overall chord, twist, and thickness distribution of the whole blade. The geometry of each corresponding blade section at the identified points is then varied. However, the optimisation led to a drastic change in blade shape since the base case turbine used in the study was not a site-specific turbine.

Liu (wind turbine) [107] and Sale (tidal turbine) [108] also identified control points within the blade but used a Bezier curve and employed genetic algorithm (GA) to get

¹The stochastic nature of waves makes the modelling of the energy flux more similar.

an optimised blade geometry. However, both Liu and Sale optimised a site-specific turbine operating within their respective sites. This resulted in a geometry that was not drastically different from the current turbine.

The sites of Kenway and Martins [104] may have different $f(U)$ curves but operating wind speeds remain essentially the same for both sites ranging from 5m/s to 15m/s. Thus, there was no need to drastically change the operational characteristics of the turbine from a C_P –TSR perspective. The resulting blade geometries were similar to each other (and different from the base case). Wang [109] demonstrated the significance of designing turbines for an optimal flow speed even with designs having similar cut-in speeds; turbines producing rated power at higher flow speeds perform worse at lower flow speeds. Wang also demonstrated the importance of design tip-speed ratio for one design flow speed wherein for $U_{\text{wind,design}} = 8.0\text{m/s}$, increasing design TSR results in worse performance in $U_{\text{wind}} < 7.0\text{m/s}$. It may be expected that performance of the turbine may be reduced, which also reduces AEP. However, it is possible that cost may also be reduced leading to better economic feasibility.

These can be extrapolated to the design of tidal turbines for less energetic currents with the following:

- AEP optimisation within the same site leads to minimal changes in blade profile and operational characteristics; optimisation involving different sites leads to larger changes.
- Flow speeds within currently viable sites ($U_\infty > 2\text{m/s}$) and less energetic sites are different.
- Conventional turbines that can operate at low flows speeds in an energetic environment cannot be simply placed into less energetic environments as they would operate suboptimally.
- There is a need to evaluate the efficacy of high-TSR rotors using a measure other than AEP or C_P .

Optimisation by Cost of Energy. Cost minimisation can be achieved through the optimisation of multiple turbine components. This has been the approach of Maki [110] and Giguere [111] where both took into account multiple components for optimisation. Both indicate that a multi-component approach provides more information on how each component reduces the cost of a turbine. This demonstrates the interaction between components wherein a change in one component effectively changes the requirements of another component.

Simpler optimisation routines usually involve changing only one component such as the case of Xudong [112] in the optimisation of a wind turbine blade by varying chord and twist while applying constraints for maximum thrust and torque. Arroyo [113] also studied the benefits of a capacitor bank in enabling better maximum power point tracking during turbine operational times and how it results in reduced cost of energy.

In offshore turbines, methods usually involve changing a component other than the blade. This can either be a single or multi-component approach. The focus is shifted away from the rotor owing to the large contribution of power systems ($> 30\%$) to the total capital cost. Figures 3.1 to 3.4 shows a comparison of the capital cost of onshore, offshore, floating wind and tidal turbines.

Looking closely at the relative turbine cost for each device, it can be inferred why many optimisation methods for onshore wind turbines revolve around rotor design but is not the focus for other technologies. However, even if the rotor only accounts for less than 3% [95] of the whole turbine cost, its indirect cost accounts for more than 30% of the whole turbine since the hydrodynamic performance and operation is dictated by the rotor i.e. high-torque low-RPM generators are much larger and more expensive than low-torque high-RPM generators [114–116].

Even with this information, it is difficult to optimise tidal turbines by minimising the cost of energy due to the lack of an appropriate cost model. Additionally, tidal turbines are usually bespoke and very site-specific. It is seldom the case that a tidal turbine operating at one site is used in another site, which makes the cost modelling approach more complicated.

Operation and maintenance cost modelling is also muddier than what Segura [95]

Tidal turbine blade design

had presented. Reliability and failure management plays a key role as consequential costs and losses from component failure [103]. Scotrenewables² emphasised the importance of intervention and maintenance to ensure continuous operation. A shift towards non-specialist vessels for installation and maintenance is seen as a viable option to drive down the cost of tidal turbines. Naturally, larger and heavier components need larger specialist vessels while smaller components provide the opportunity to use local and smaller vessels.

It is uncertain if changing rotor operation will result in better power capture but it can pave the way for the use of smaller and cheaper components. If proven possible, cost reduction can be achieved not only in the rotor but also generate cost savings along the drive train. Increasing rotor speed may enable the use of smaller and more compact generators in addition to the utilisation of direct-drive power trains.

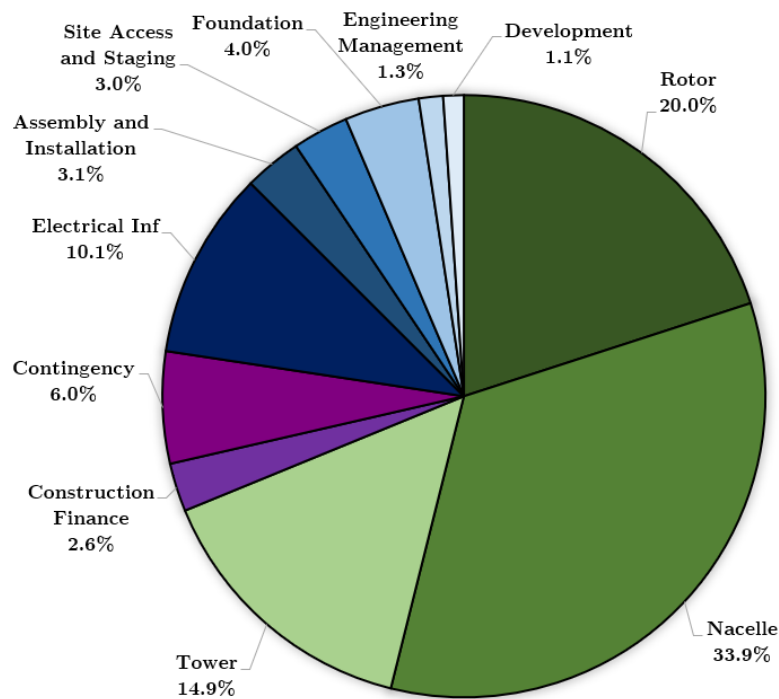


Figure 3.1: Average capital expenditure for onshore wind turbines [117]

²A report from Scotrenewables before the company was renamed Orbital Marine Power

Tidal turbine blade design

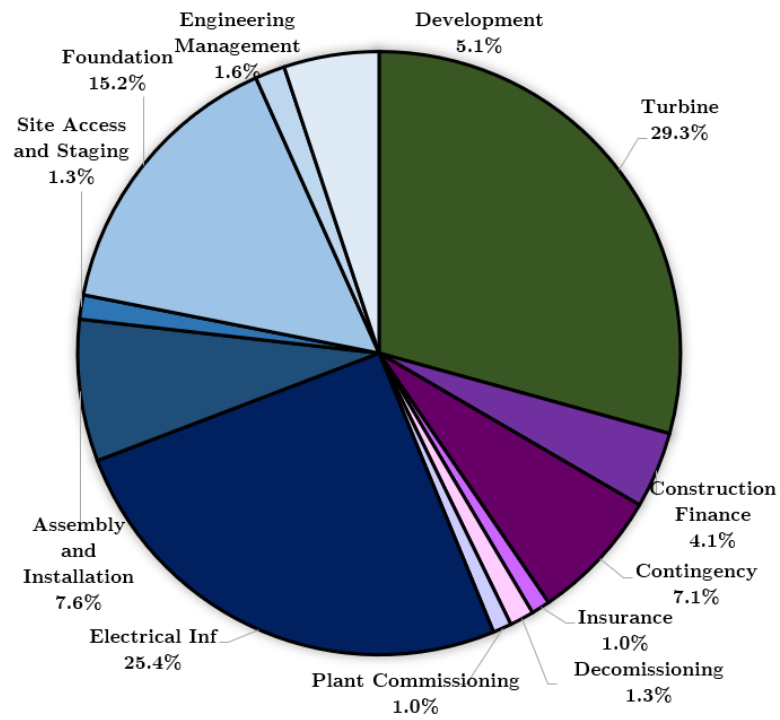


Figure 3.2: Average capital expenditure for offshore wind turbines [117]

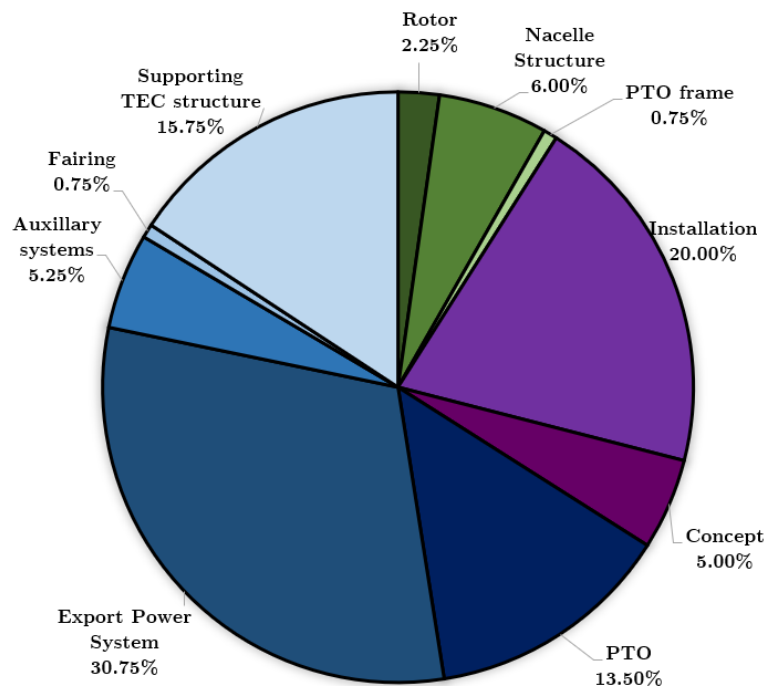


Figure 3.4: Documented capital expenditure for a tidal turbine in Alderney Race [95]

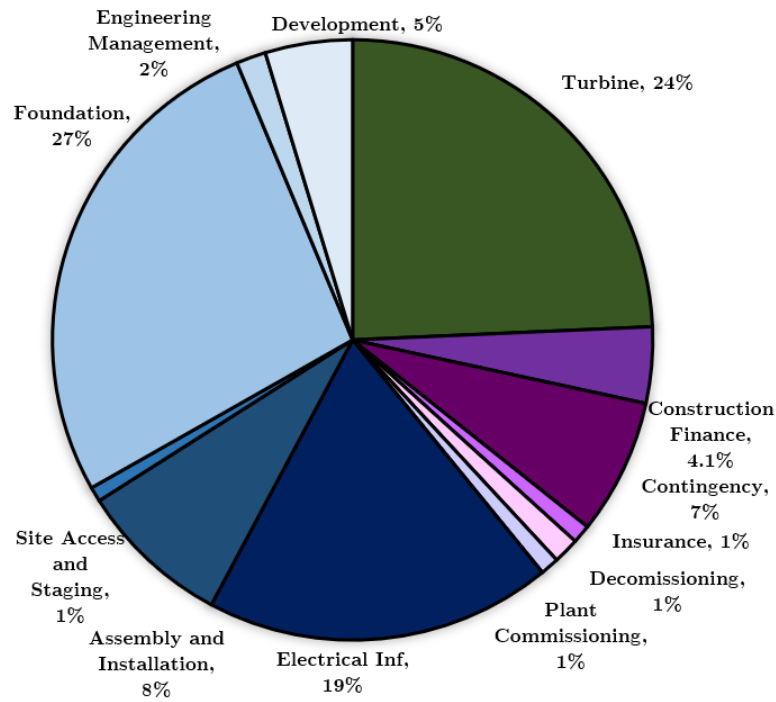


Figure 3.3: Average capital expenditure for floating wind turbines [117]

3.2 The Design Problem

3.2.1 Existing design tools and methods

TidalBladed [118] is a commercial hydro-elastic simulation tool that uses a multi-body formulation to compute turbine loads. TidalBladed is based on BEM and is capable of unsteady simulations including rotor vibration modes and component simulation; it offers a full simulation of a tidal turbine design including components and structure. A turbine designer can use the tool to examine how a design responds by interpreting the output of the simulations. TidalBladed does not output specific blade geometries. This is not used in this thesis due to the commercial nature of the tool.

HarpOpt [119] is a turbine blade design tool, originally intended for wind turbines, that can perform as a multi-objective optimiser for horizontal axis turbines. It calculates the performance of a rotor based on BEM and outputs the optimal shape according to the twist, chord, and hydrofoil distributions. It is mainly used to to

Tidal turbine blade design

maximise AEP of operating under uniform flow where the AEP is calculated using a Rayleigh, Weibull, or user-defined flow vs time distribution. Minimisation of blade mass can be set as a secondary objective leading to a Pareto optimal set of solutions. It is also now used in tidal turbine design due to its functionality, and the similarity of wind and tidal turbines.

Kulkarni [120] explored the possibility of applying biomimicry in the design of tidal turbines. The design method involves the selection of an appropriate fish caudal fin shape to adopt for a NACA 0018 turbine rotor. The result is a set of blades with varying levels of sweep. Turbine variations are then compared to each other and the base case to evaluate the effects of biomimicry and its applicability in tidal turbine design.

Murray [121] developed a blade design method for passively-adaptive blades using a coupled BEM-FEM model. The design tool uses the University of Strathclyde BEM tool [59] to calculate the hydrodynamic loads. The output is then used by FEM as an input for calculations on stress and deflections. The method iterates between the BEM and FEM to account for changes in performance due to the blade deformation. This method also allows the analysis of multiple cases to simulate the effect of different ply-angles to inform about the appropriate method of construction of passively-adaptive blades.

Gracie-Orr [122] developed a blade design method for Overspeed Power Regulation to limit cavitation using the University of Strathclyde BEM tool [59]. The design methodology involves a series of linear function additions to the chord and twist distributions of an NREL S814 turbine blade [51]. Similar to TidalBladed, the design platform does not include an optimisation routine although it informs the designer of relevant performance metrics to evaluate if the blade design fits the requirement - limitation of cavitation inception. The design process in this thesis follows the principle of Gracie-Orr's design and blade alteration method while using a Python-adapted code of the University of Strathclyde's MATLAB code.

The latter design approaches are more exploratory in the sense that rather than having an objective function to minimise or maximise (Section 3.1.1), the blades are first

altered and designs are evaluated to observe how alterations affected the performance of the rotor. In both Murray and Kulkarni, power capture is maximised and loads are minimised while Gracie-Orr reduced risk of cavitation. Novel and *new* concepts ³ in the tidal turbine industry can be explored.

In the case of this thesis, the benefits of moving towards higher TSR operation is not directly apparent. Increasing TSR operation usually employs lower solidity blades [54] that have reduced performance compared to higher solidity blades [123, 124]. The increased blade speed may also lead to cavitation inception. Thus, the hypothesis is vastly different from the aforementioned design approaches. There is a need to quantify the benefits and this can be done only from a cost perspective involving the other components within the turbine. The design approach is then formulated.

3.2.2 Design framework

Reducing the cost of energy is the main goal in design and optimisation but achieving an optimised design for less energetic sites is problematic - there is no commercially verified design for less energetic currents; designs for less energetic currents are practically non-existent. Section 1.2 has listed multiple tidal turbine devices that operate at currents of greater than 2m/s but no successful design for less than 2m/s.

Maximisation of AEP involves better power capture within the same operating conditions. This is an incomplete approach to the design of tidal turbines for less energetic flows since

- Power curves of existing turbines are not optimally matched for less energetic flows as has been the case for the deployment in Portugal [22].
- Current techniques for AEP maximisation involves the improvement of power capture by the rotor, improved rotor stability, improved power regulation and transmission of current designs. These are all achieved within the same flow regime of greater than 2m/s.

³There are many novel concepts in the tidal turbine industry. This includes tidal kites, hydrofoils, etc. 'New' here pertains to innovations within HATT design'

Tidal turbine blade design

- The improvements in the COE after applying AEP optimisation may be minimal compared to the loss in power production in less energetic sites ($P_{\text{lost}} \propto U^3$).
- With respect to the hypothesis that faster rotational speeds are better for operation within less energetic currents, reducing rotor size to allow for faster rotational speeds further decreases the power output ($P_{\text{lost}} \propto R^2$, $\Omega_r \propto R$). This implies a need for a cost of energy verification.

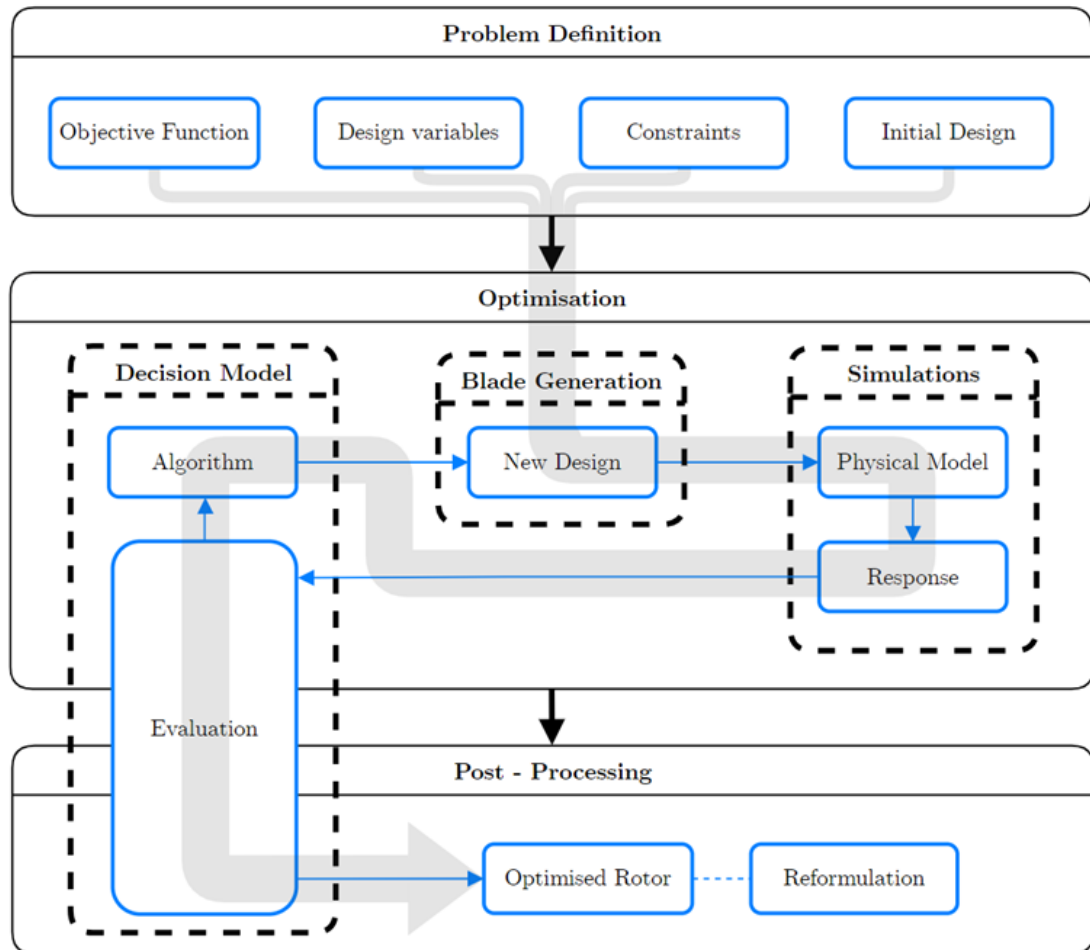


Figure 3.5: Design approach derived from Fuglsang [125, 126]. The blue arrows show Fuglsang’s framework. The thick grey flow line shows the design process employed in the thesis. It is usually the case that designs are generated and evaluated simultaneously. In this process, designs are first generated within a specified design space and are evaluated. The output is a set of optimised blades and data on which to evaluate trends for rotor design for less energetic flow.

The design process in this thesis follows Fuglsang’s design framework [125, 126] and

Tidal turbine blade design

evaluates design from a cost of energy perspective. However, the lack of a proper cost model for high-TSR rotors and environments with currents of less than 2m/s make it difficult for an iterative optimisation process. The outlined design process develops each design block before drawing conclusions on the benefits of choosing to operate at higher TSRs in less energetic currents. The design process is as follows:

1. Development of a methodology for rapid generation of candidate blades with partially constrained blade mass/solidity as a function of chord reduction. This is incorporated to avoid extremely slender blades (Section 3.3 onwards).
2. Evaluation of rotor performance operating under a steady-state and uniform flow with a current speed of less than 2m/s (Chapter 4). This is according to the hypothesis that high-TSR blades are more appropriate for less energetic flows with the following considerations:
 - partially constrained C_P - it is possible to have a large reduction in $C_{P_{\max}}$ and have a better COE in less energetic flow. Rotors with better C_P are still considered superior but a lower limit of acceptable $C_{P_{\max}}$ is set.
 - $TSR_{C_{P_{\max}}}$ capped at $TSR = 12$. It may be possible to further increase the TSR-location of $C_{P_{\max}}$ but this is not usually employed even for wind turbines.
3. Simulation of turbine performance within real-site conditions (Chapter 7).
4. Evaluation and comparison of COE between optimised and conventional blades (Chapter 8).

Chapter 5 provides a check on the output of the simulations in Chapter 4. This is already part of the post-processing (validation studies). In reality, further optimisation is done after validation - this was slightly incorporated in the study because there was a need to recalibrate aerodynamic properties of the aerofoil (Chapter 5).

3.3 Rapid blade generation for evaluation

Testing the hypothesis of high-TSR blades require the generation of high-TSR blades suited for underwater operation. Wind turbines generally operate optimally within higher TSRs but use aerofoils that may not be appropriate to the tidal environment. Ahmed [127] explains that tidal turbines are expected to sustain higher loads leading to a preference for thicker aerofoils. High-TSR blades are then generated by altering existing validated tidal turbine blades. This provides two advantages:

- Aerofoils used for the blade sections are already tested and validated to be appropriate for underwater operation.
- Published data on the performance is available and provides a base case to compare the performance of high-TSR versions operating under less energetic currents.

Similar to the aforementioned studies, the base case blades are altered by changing the distribution of chord and twist. However, a simpler approach patterned from Gracie-Orr [122] is adopted.

3.3.1 Parametric blade modifications

A polynomial function may be fitted over any chord and twist distribution. However, the number of coefficients increase with the degree of a polynomial. This is the same case with the aforementioned design optimisation studies that used Bezier curves and control points i.e. each control point is taken as one design variable. Controlling specific points within the distribution may be advantageous in power maximisation. However, it is reasonable to assume that increasingly complex blades with more inflexions points within their distributions are harder to manufacture and hence, simpler distributions are more practical.

Gracie-Orr [122] built chord and twist distributions from scratch using a three-stage function addition. The approach in this thesis involves a linear chord reduction coupled

Tidal turbine blade design

with a function multiplier applied to an existing blade design. The general 2nd-degree polynomial expression that describes conic sections is used to generate blade geometries.

$$Ax^2 + Bxy + Cy^2 + Dx + Ey + F = 0 \quad (3.3)$$

where A, B, C, D, E , and F are constants. The distributions are derived from the function values within the first quadrant (Q1). Deriving distributions from other quadrants will require additional computational algorithms to handle different scenarios. Thus, limiting distribution within Q1 is optimal.

The general shape of the conic (ellipse, circle, hyperbola) is dictated by the first two constants A and B . D and E are both set to 0 which makes the centre of the conic at $(0,0)$. Setting $F = -1$ results in maximum values of $x = 1$ or $y = 1$ for an ellipse, and a minimum value of $x = 1$ for a hyperbola.

If B is set to 0, the conic section will have the x and y axes as its primary axes. This limits the possible distributions as non-oblique hyperbolic functions within Q1 have no value for $x < 1$ and always result in an increasing value for $y > 0$.

An oblique conic with intercepts at $(0, 1)(1, 0)$ and $A, C = 1, F = -1$, expressed as

$$x^2 + Bxy + y^2 = 1 \quad (3.4)$$

allows for hyperbolic distributions that have function values for $x < 1$ and also limits x and y values to 1. The possible $x - y$ pairs are bound to points within the circle defined by $x^2 + y^2 = 1$ as shown in Figure 3.6. This is not considered to be a disadvantage since turbine blades have more taper and feather than a circular distribution dictates.

This is further simplified to only one design variable (Γ)

$$x^2 + Bxf(x) + f(x)^2 = 1 \quad (3.5)$$

$$r^2 + \Gamma r\lambda(r) + \lambda(r)^2 = 1 \quad (3.6)$$

where $B = \Gamma$ determines the overall distribution of the blade and $\lambda(r)$ are scaling coefficients for the chord and twist values of each control section with radial position

r. Table 3.1 gives a sample base case blade configuration as published by Batten [1].

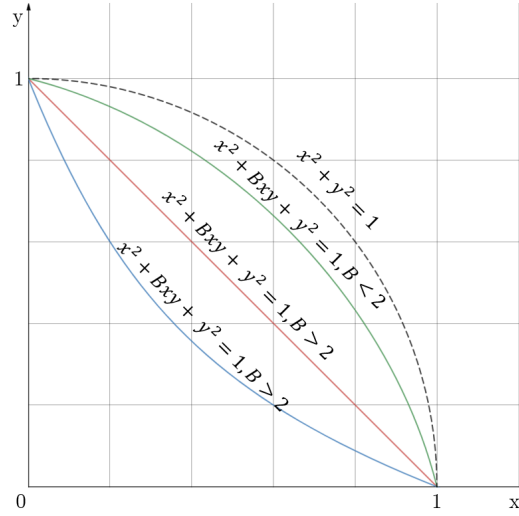


Figure 3.6: Oblique conics within the first quadrant

Table 3.1: NACA 63-8xx Base Case Blade [1]

Normalised Radius (r/R)	Aerofoil	Normalised Chord (c/R)	Total Twist (degrees)
0.2	NACA 63-824	0.1250	20.0
0.3	NACA 63-821	0.1156	14.5
0.4	NACA 63-819	0.1063	11.1
0.5	NACA 63-817	0.0969	8.9
0.6	NACA 63-816	0.0875	7.4
0.7	NACA 63-815	0.0781	6.5
0.8	NACA 63-814	0.0688	5.9
0.9	NACA 63-813	0.0594	5.4
1	NACA 63-812	0.0500	5.0

The value of Γ is user-defined and Equation 3.6 is used to solve for the corresponding scaling coefficients. $\lambda(r)$ is then applied as follows:

$$c^* = c_{\text{root,base}} - c_{\text{tip}} \quad (3.7)$$

$$\lambda^*(r) = \lambda(r)/\lambda_{\text{root}} \quad (3.8)$$

$$c_{\text{new}}(r) = c_{\text{tip}} + c^*\lambda^*(r) \quad (3.9)$$

Tidal turbine blade design

The values of λ are always within $0 \leq \lambda < 1$. However, since $\lambda(r = r_{\text{root}} \neq 0) \neq 1$, using values from $\lambda(r < r_{\text{root}})$, leads to unintended scaling of the chord length at the root section. This is remedied by applying Equation 3.8 such that $\lambda^*(r)$ is always within $0 \leq \lambda^* < 1$.

The normalisation of λ is performed by altering the whole function, $\lambda^*(r)$, but is point-wise for the values of c . Notice that c^* is expressed as a singular value rather than a function. Equation 3.7 sets the reference value, the smallest chord length (c_{tip}), to $c = 0$.

Equation 3.9 only applies λ^* to the adjusted root chord c^* . This prevents the scaling of the relative difference between the chord and twist of each control section. Figures 3.7a to 3.7c show how the difference in chord between each control section is unintentionally altered if the values of λ^* are not applied as presented.

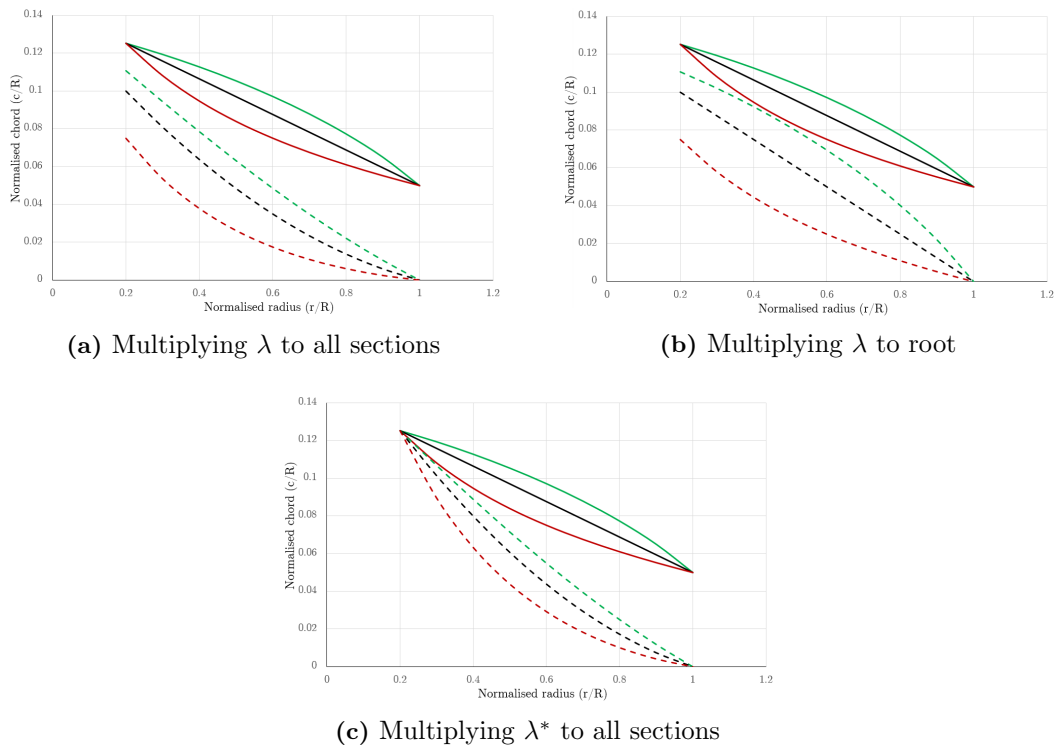


Figure 3.7: Pitfalls in applying scaling coefficients. Solid lines show the correct distributions with λ^* multiplied to the root section only. $\Gamma > 2$ (red), $\Gamma = 2$ (black), $\Gamma < 2$ (green)

This method has been applied by the author in [128] with three values of Γ . Each Γ corresponds to a conic equation where $\Gamma < 2$ is elliptical, $\Gamma = 2$ is linear, $\Gamma > 2$ is

hyperbolic.

An overall chord increase or decrease can also be applied by incorporating a factor to c_{tip} in Equation 3.9. Factors less than 1 result in chord reduction leading to slender blades. For this thesis, only chord reductions are considered as low solidity is a characteristic of high-TSR blades [54]. For twist, altering Equation 3.9 is equivalent to altering the blade pitch.

Physical representations

Using Γ alters chord distributions with an inverse linear relationship with solidity. That is, elliptical distributions ($\downarrow \Gamma$) increase the solidity and hyperbolic distributions ($\uparrow \Gamma$) reduce solidity. Twist distributions are altered such that elliptical distributions move the onset of aggressive feathering further towards the tip and hyperbolic distributions move the onset earlier towards the root.

Table 3.2: Physical Variables

Physical Variable	Altered by	Resulting Blade Modification
Overall Solidity, (c -values)	Equation 3.6, Γ	inversely proportional, changes shape, also linearly proportional to taper
	Equation 3.9, applying a factor to c_{tip}	linearly proportional
Feathering (θ -values)	Equation 3.6, Γ	$\uparrow \Gamma$, earlier onset of aggressive feathering
Blade Pitch (θ -values)	Equation 3.9, applying a factor to θ_{tip}	changing blade pitch (θ_B)

The relationship between Γ and physical design parameters are established in Table 3.2. It is possible to observe general trends in performance using Γ to qualitatively describe solidity (increasing or decreasing), taper, feathering, and pitch. This may not a huge advantage since physical quantities may be calculated post-generation. However, when analysing a huge set of computer-generated blades, it is usually difficult to discern

overall trends and parameter sensitivity (Chapter 6) without additional computational load.

Figure 3.8 show sample comparative outputs with multiple levels of Γ . It is possible to observe the trends by simple graphic post-processing. Calculation of solidities and tapers can also be performed and will give greater resolution although this is seldom done in optimisation studies that use GA and Bezier curve fits.

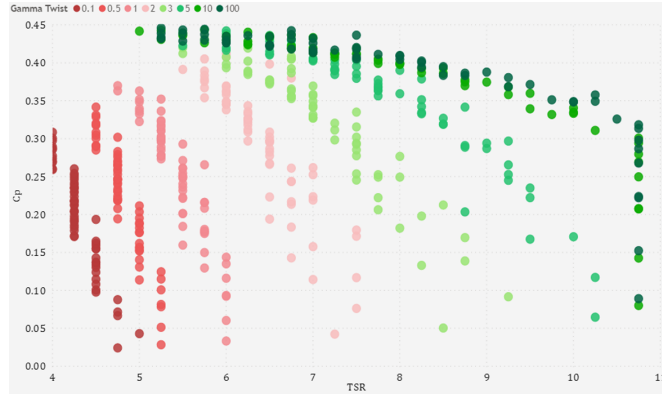


Figure 3.8: Sample post-processed data with different levels (discrete) of Γ for twist alterations. This shows the maximum C_P and corresponding TSR-location of different designs.

3.3.2 Limiting possible values of Γ and defining the design space

Table 3.3: Design Space

Parameter	Values
Γ_{chord}	0.1, 0.5, 1, 2, 3, 5, 10, 100
Γ_{twist}	0.1, 0.5, 1, 2, 3, 5, 10, 100
Chord reduction	10, 20, 30, 40, 50
Blade Pitch	-6, -5, -4, -3, -2, -1, 0, 1, 2, 3, 4, 5, 6
Blade Number	2, 3

At this point, an objective function or evaluation method has not been established. Figure 3.5 illustrated a one-way approach instead of an iterative approach, which requires the generation of a set of candidate blades for evaluation and comparison.

The values considered for Γ are explicitly defined to limit the number of designs to a finite number⁴. To limit the design space, existing blades are analysed (see Chapter

⁴ Γ is a continuous variable that runs from $[0, \infty]$, which leads to an infinite number of blades

4) The resulting values of Γ when a conic is fitted to existing designs serve as a basis for the limits on the design space.

Chord reduction of up to 50% is employed to observe the effects of decreasing solidity to the performance of the turbine. Blade pitch angle setting should also be altered [109] to accommodate changes in distributions even if the root section pitch is controlled.

Lastly, the blade number is altered to observe how much further the optimum TSR could be pushed and to observe the effects, including cost reduction, of using 2-bladed designs compared to 3-bladed designs. The design space is summarised in Table 3.3.

3.3.3 Additional Parameters

Table 3.4: Extended Physical Variables

Physical Variable	Altered by	Resulting Blade Modification
Overall Solidity	Equation 3.6, Γ	inversely proportional, changes shape, also linearly proportional to taper
	Equation 3.9, applying factor to c_{tip}	linearly proportional
Taper	Equation 3.7, applying factor to $c_{root,base}$	linearly proportional, fixed tip values
	Equations 3.7, 3.9, applying factor to c_{tip}	inversely proportional, fixed root values
Feathering	Equation 3.6, Γ	$\uparrow \Gamma$, earlier onset of aggressive feathering
	Equation 3.7, applying factor to $\theta_{root,base}$	linearly proportional, fixed tip values
	Equations 3.7, 3.9, applying factor to θ_{tip}	inversely proportional, fixed root values
Blade Pitch	Equation 3.9, applying factor to θ_{tip}	changing blade pitch (θ_B)

The foregoing method fixes the value of both chord and twist at the root and tip. Many optimised blades result in the reduction of the chord at the root without changing the chord at the tip. This can be captured by incorporating additional parameters to reduce the chord at the root and applied to Equation 3.7. This changes the overall slope/curvature of the distribution. Similarly, the chord at the root can be fixed by applying a factor to c_{tip} in Equation 3.7 although there is a need to set the same factor to c_{tip} in Equation 3.9. Both chord alteration methods change the taper of the blade. For twists, applying the methods changes the overall degree of feathering. The extended design variables are presented here for future work.

3.4 Summary

The chapter discussed relevant considerations in turbine blade design. Similar design methods are employed for wind and tidal turbine industry as much of the knowledge and understanding for tidal turbines has been derived from the former.

The chapter also discussed the focus on recent tidal turbine blade design and how it may not be directly applicable to the design for less energetic tidal environments. Thus, a general design framework involving a rapid blade generation method has been presented. This method involves the use of the general conic equation that is aimed to replace the usual control-point optimisation applied in existing blade design methods.

This lessens the complexity of the design problem through the reduction of design variables. This also allows for parametric design through the use of mathematical variables that are directly related to physical quantities.

Chapter 4

Verification of Blade Design and Analysis Methods with Preliminary Design Evaluation

Methods presented in Chapter 3 use an already established method of using several control points and genetic algorithm (GA). It may be argued that the degree of control on the shape of the blade is limited by using the proposed rapid blade generation methodology. This chapter shows the applicability of the method by applying conic fitting to existing blades designed through conventional design methodologies and the generating preliminary blade designs that promote higher-TSR operation with comparable or better hydrodynamic performance.

4.1 Comparison with GA and control point optimisation

Genetic Algorithm is usually used for optimising blade designs and while it has been mentioned that blade design is an optimisation problem, the hypothesis in this thesis requires more of an exploratory approach. This is especially true at this stage of the design wherein no site-specific design for less energetic currents is available.

Table 3.2 also shows a clear advantage of being able to control multiple aspects of blade geometry using only four variables as opposed to the usual minimum of eight variables (four control points each for chord and twist). This minimises the computational load.

Nonetheless, to demonstrate the capability of the method in capturing an optimised

design, published results of optimised turbines are reproduced using the proposed method.

4.1.1 Conic Fits

Table 4.1 shows the summary of case studies used to test the suitability of using oblique conic sections in generating blade geometries. Appendix A shows the process of how each distribution is fitted with a conic as the equations above are used to generate blade geometries rather than to fit existing geometries.

Table 4.1: GA-generated optimised blade designs and corresponding Γ values for conic fitting

Wind Turbines	Rotor Design	Γ_ϕ	Γ_c
Kenway and Martins [104] Liu [107] Xudong [112]	Wes5 Tulipo - St. Lawrence	9.859	0.517
	Wes5 Tulipo - UTIAS	11.978	0.005
	NACA 63-4xx - Nan'ao	4.994	0.602
	NREL 5MW Virtual Rotor	4.187	0.425
Tidal Turbines			
Sale [108] Zhu [129] Sun [130]	Riso A1-xx	36.475	6.240
	NACA 44xx	5.850	3.331
	NACA 63-815	113.329	3.471
	NREL S825 OptA	1.590	1.078
	NREL S825 OptB	1.775	1.005

In general, twist distributions are hyperbolic with Γ values of greater than 2 except for Sun [130]. Looking closely, the twist generated by Sun has two distinct regions: an elliptical distribution at $r/R < 0.5$ and a hyperbolic distribution at $r/R > 0.5$. Nonetheless, power generation is dominated by the sections nearer the tip [129, 130] and the hyperbolic distribution still follows. The difference in performance between Sun's geometries and the *simplified* twist distribution is discussed in the next section.

For chord distributions, there is a disparity between wind and tidal turbines wherein wind turbines generally have elliptical chord distributions and tidal turbines have hyperbolic except for the geometry of Sun. However, solidities of wind turbines are still lower compared to tidal turbine solidities.

Verification of Blade Design and Analysis Methods with Preliminary Design Evaluation

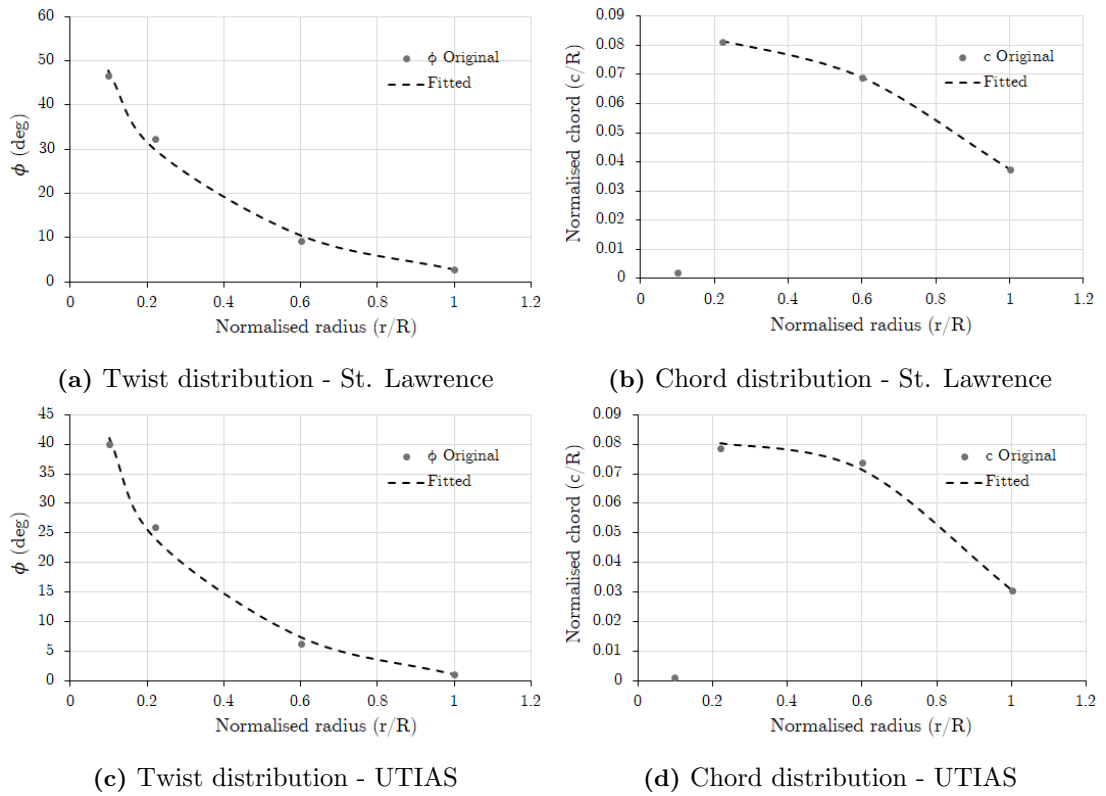


Figure 4.1: Conic Fits for Kenway and Martins [104]

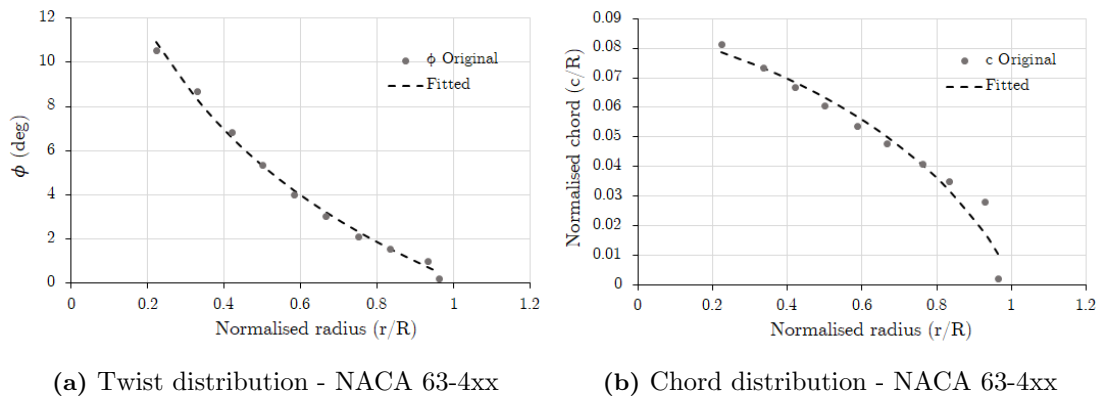
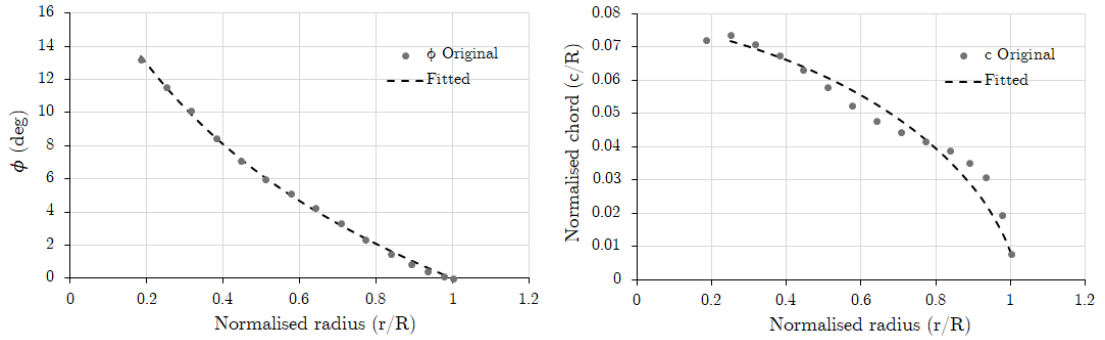


Figure 4.2: Conic Fits for Liu [107]

Tidal turbine chord distributions are accurately captured by the conic fits. However, there is a slight mismatch for conic fits for twist distributions. Figure 4.5 which presents a NACA 63-815 rotor [129] seems to have a base case that could have been accurately captured by a conic. This may be seen as a disadvantage as it presents a limitation

Verification of Blade Design and Analysis Methods with Preliminary Design Evaluation

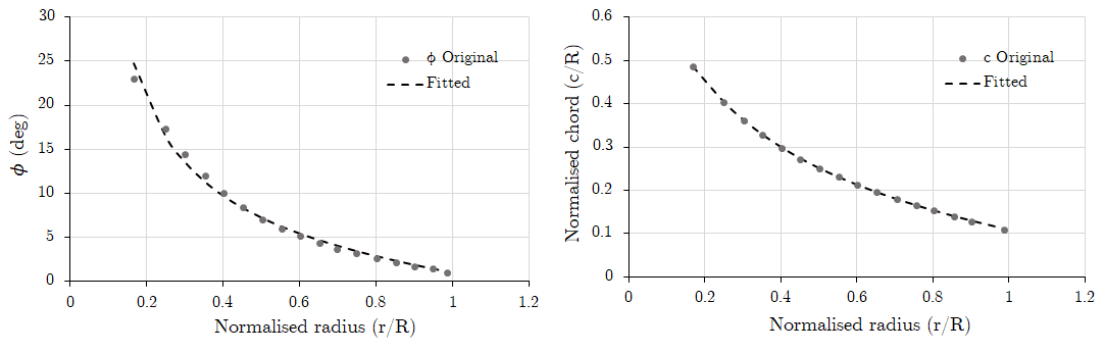
in the kind of distributions that may be generated. However, as previously discussed, additional design variables may be added (Section 3.3.3) to better capture profiles. This is not explored further in this thesis as the initial design variables have been shown to push the maximum C_P point of a rotor towards higher TSRs.



(a) Twist distribution - NREL 5MW

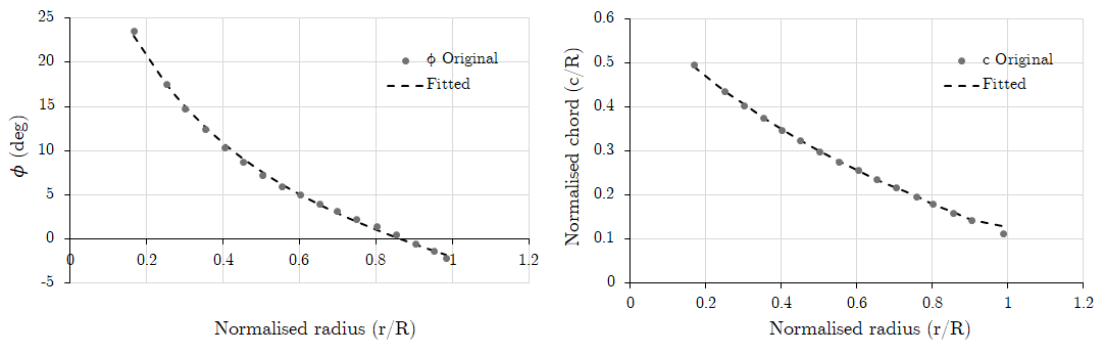
(b) Chord distribution - NREL 5MW

Figure 4.3: Conic Fits for Xudong [112]



(a) Twist distribution - Risa A1-xx

(b) Chord distribution - Risa A1-xx

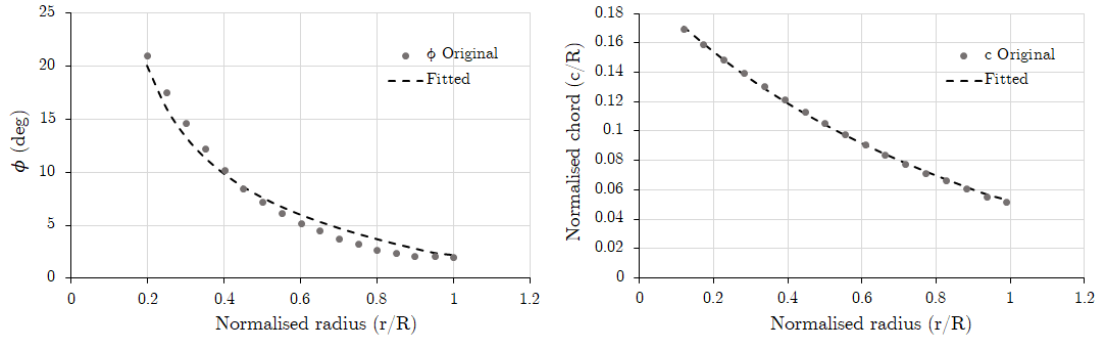


(c) Twist distribution - NACA 44xx

(d) Chord distribution - NACA 44xx

Figure 4.4: Conic Fits for Sale [108]

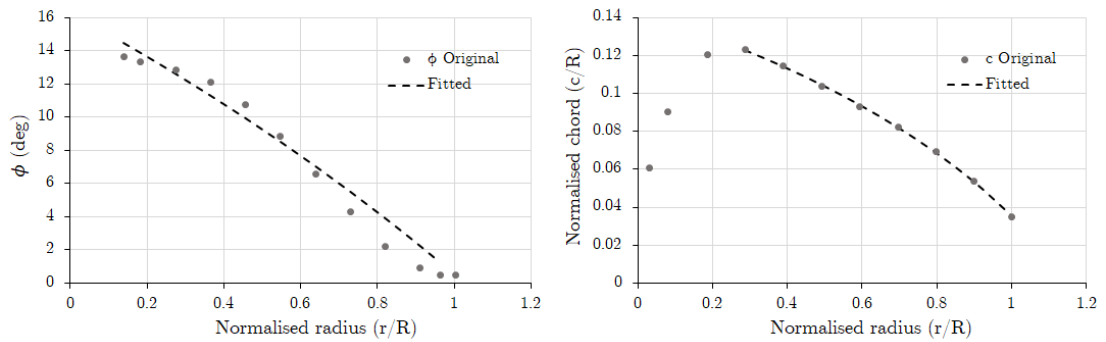
Additionally, the published geometries are just one of the many Pareto-efficient geometries generated using GA optimisation. It is also possible that the conic fitted geometries can perform similarly. Thus, additional verification is done to compare the performance of the conic fitted geometries and the published geometries.



(a) Twist distribution - NACA 63-815

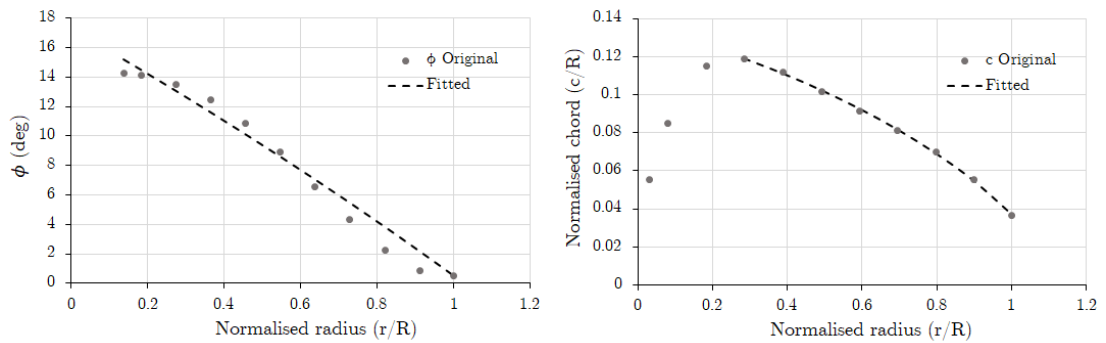
(b) Chord distribution - NACA 63-815

Figure 4.5: Conic Fits for Zhu [129]



(a) Twist distribution - NREL S825 OptA

(b) Chord distribution - NREL S825 OptA



(c) Twist distribution - NREL S825 OptB

(d) Chord distribution - NREL S825 OptB

Figure 4.6: Conic Fits for Sun [130]

Performance Fits

The performance fits are limited by the availability of published data on the sectional make-up of the blade. A priority for verifying tidal turbine performance is employed in this section. However, the wind turbine geometry of Liu [107] is used since information on the sectional make-up of the geometry from Sale [108] is incomplete.

Only the C_P characterisations are used for verification since the GA used AEP as a basis of optimisation; thrust was not included in the objective function.

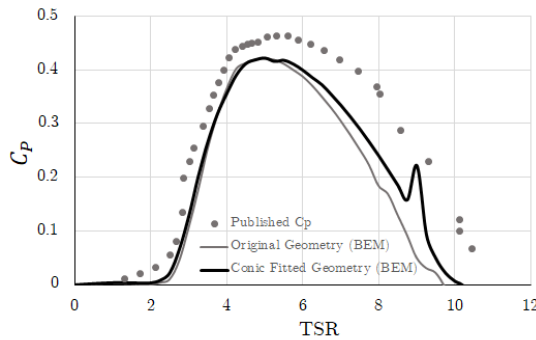


Figure 4.7: C_P -TSR for Zhu [129]

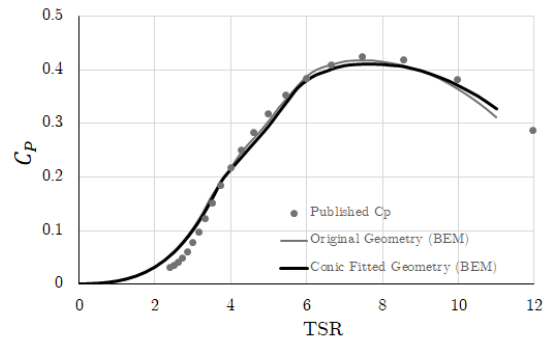


Figure 4.8: C_P -TSR for Liu [107]

For the case of Zhu [129], BEM underpredicts the experimental results. However, the original geometry and the conic fitted geometry have similar performance within their optimal TSR range. There is a slight instability in convergence (one point, $TSR = 9$) with the conic fitted geometry. This simulated result is also better compared to the published CFD simulation of Zhu.

The wind turbine from Liu [107] is accurately simulated using BEM. There is a very slight drop in power when comparing the original geometry and the conic fitted geometry.

Simulations of the geometry from Sun [130] show a difference in performance depending on whether the chord values at $r/R < 0.2$ are included. Figures 4.6b and 4.6d show a chord distribution that extends until near $r/R = 0$. The BEM¹ used in

¹Both Sun and Liu have published simulation results and should not be taken as verification of the BEM tool used in this thesis. Only Zhu provides an experimental validation from the aforementioned studies. The Strathclyde BEM tool has been validated by Nevalainen [59] and a quick validation is also presented in Chapter 5.

Verification of Blade Design and Analysis Methods with Preliminary Design Evaluation

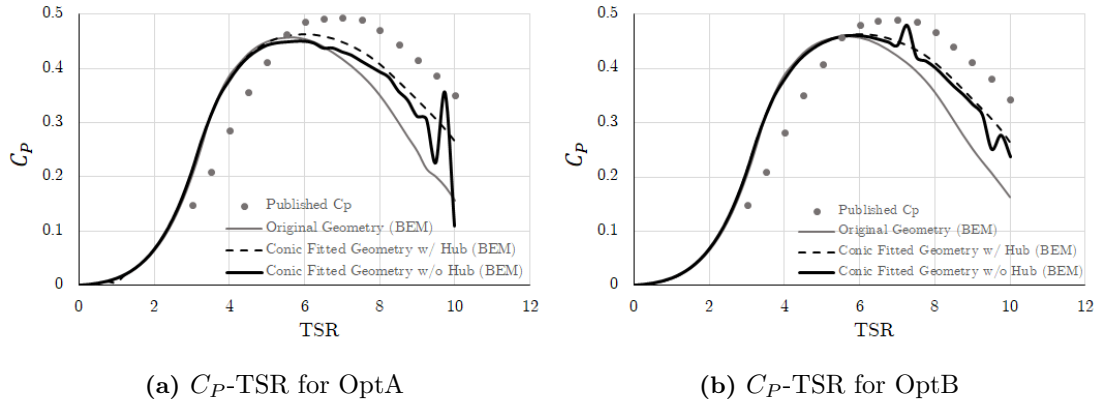


Figure 4.9: C_P -TSR for Sun [130]

the published study may have included this section although manufacturing such a turbine may be physically impossible.

This demonstrates another disadvantage of the foregoing method as the alteration can only consider sections starting from the maximum chord length. However, as mentioned, power production is usually dominated by the sections at $r/R > 0.5$ [129, 130] and should not be a huge problem.

There is a general agreement between the original geometry and the conic fitted geometry within the TSR ranges of maximum C_P despite the mismatch in the conic fitting. A discrepancy is seen within the higher TSRs, which can be attributed to the cavitation control employed in the GA. For this thesis, running at higher TSRs would increase cavitation risk and thus incorporating cavitation at this early stage of designing high-TSR blades would severely limit the design space.

4.2 Establishing a baseline

As discussed in Section 3.3, the methodology alters a base blade geometry as it allows for the comparison of an altered geometry to a validated case that is appropriate for marine operation. The geometries presented below are all experimentally tested and validated. These are used to verify the implementation of BEM in Python.

The rapid blade generation methodology was applied to the first two geometries. These provide a base case for low-TSR blades ($TSR_{C_{P_{\max}}} \leq 5$) and higher TSR blades

Table 4.2: Blade geometries used for alteration and verification

Altered Blades	Aerofoil	Diameter (m)	U_∞ (m/s)	$TSR_{C_{P\max}}$
Ellis et al. [2]	Wortmann FX63137	0.9	1.0	≈ 3.0
Batten et al. [1]	NACA 63-8xx	0.8	1.54	≈ 5.8
Verification Blades				
Gaurier et al. [84]	NACA 63-418	0.9	0.6	≈ 4.5
Doman et al. [51]	NREL S814	0.762	0.8	≈ 4.0
Gracie-Orr [122]	NREL S814	0.762	0.34	≈ 2.0

($TSR_{C_{P\max}} > 5$). The other geometries are only used for verification due to limitations in experimental data such as low Reynolds number values for C_L and C_D .

The Wortmann FX63137 has been studied by the University of Strathclyde and Cardiff University using BEM, CFD, and experimental testing. This provides a good baseline for a conventional low-TSR rotor. The NACA 63-8xx series has been studied by multiple researchers with good agreement between BEM and experimental results for turbine performance. This provides a base case for higher TSR rotors, which may be further pushed towards $TSR > 6$. For both cases, published data derive aerodynamic characteristics from XFOIL [1, 2].

The NREL S814 has been studied extensively by the University of Strathclyde by Barltrop [83], Doman [51], and Gracie-Orr [122]. However, low Reynolds number operation leading to higher drag remains an issue. Further experimental aerodynamic testing is needed to allow for more accurate simulations. This is explained further in the next section.

4.2.1 Steady-State Verification

The experimental data used for verification are obtained from the tow-tank tests of Doman [51], Ellis [2] and Gracie-Orr [122], the cavitation tunnel test of Batten [1] and the flume tank test of Gaurier [84].

The single parameter BEM predicts C_P with good accuracy for $TSR > 3$. However, values for C_T are not accurately predicted with NACA blades having under-predicted thrust and NREL S814 blades being over-predicted. The better fit for

Verification of Blade Design and Analysis Methods with Preliminary Design Evaluation

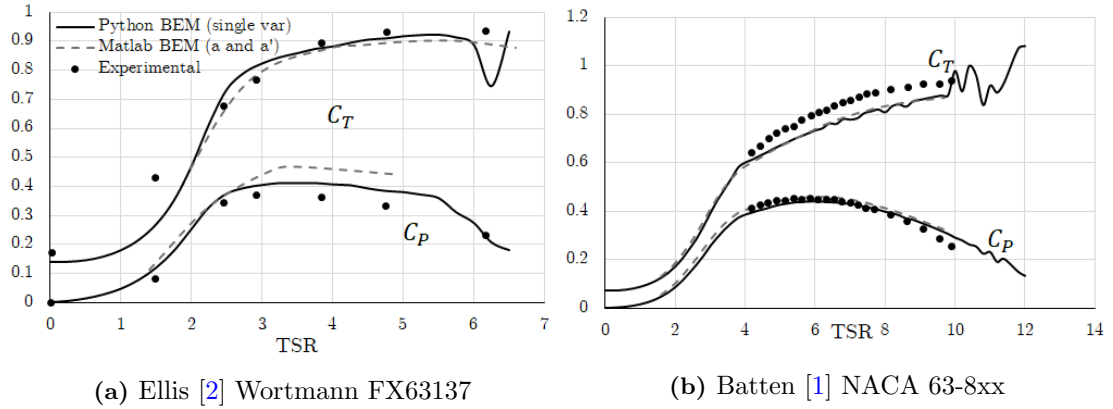


Figure 4.10: C_P and C_T verification for base blade geometries used for alteration

C_P values compared to C_T values was also observed by Nevalainen using the Matlab implementation [59] although C_T prediction is better in Matlab.

The under-predicted thrust in low TSRs (high current speed) of the NREL S814 blades are present for both the 2-variable Matlab and single-variable Python implementation. This has been attributed to the presence of laminar separation bubbles in low Reynolds number flow [131], leading to increased drag. Equation 2.3 shows that majority of the thrust force is dictated by the drag at high inflow angles. This is exactly the reason why the thrust is under-predicted at low TSRs - low TSR operation always has a flow that approaches the aerofoil at a high inflow angle as shown in Figure 4.12a. The increase in drag due to laminar separation bubbles is not captured by the BEM or in the C_L and C_D lookup tables as it is hard to capture such phenomena and have accurate figures, especially when using XFOIL.

Verification of Blade Design and Analysis Methods with Preliminary Design Evaluation

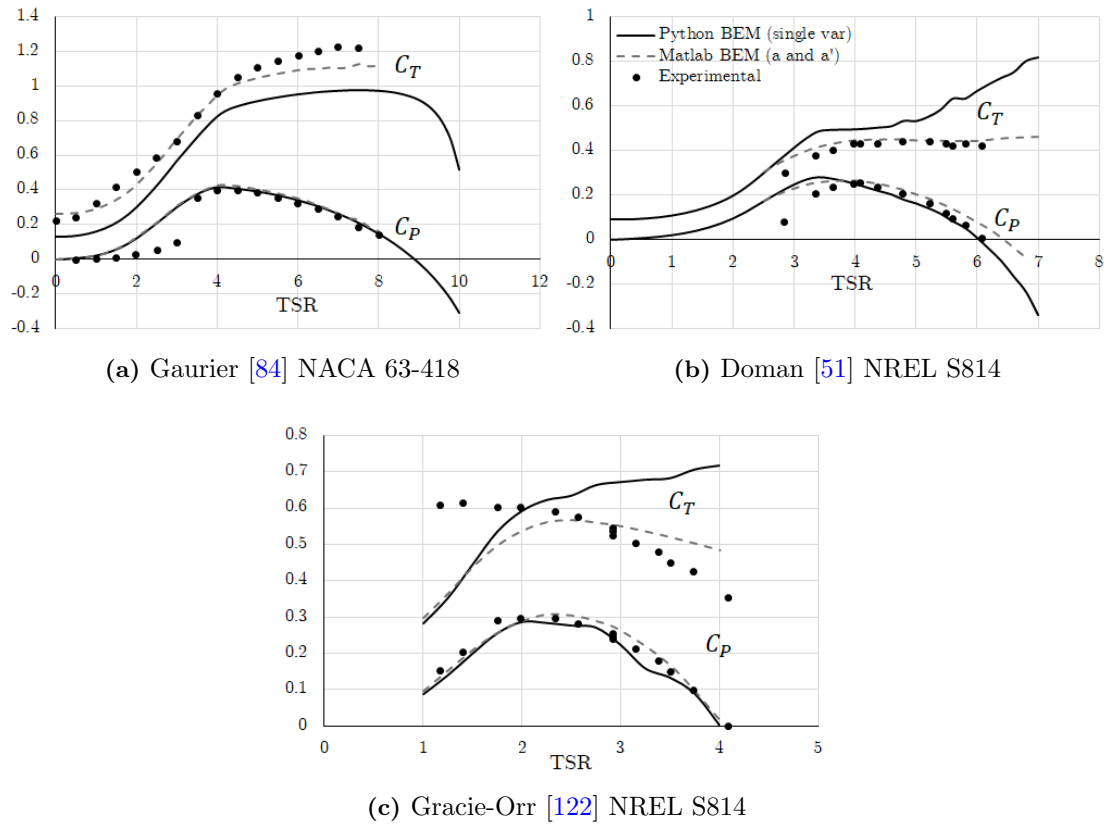


Figure 4.11: C_P and C_T for blade geometries used for verification

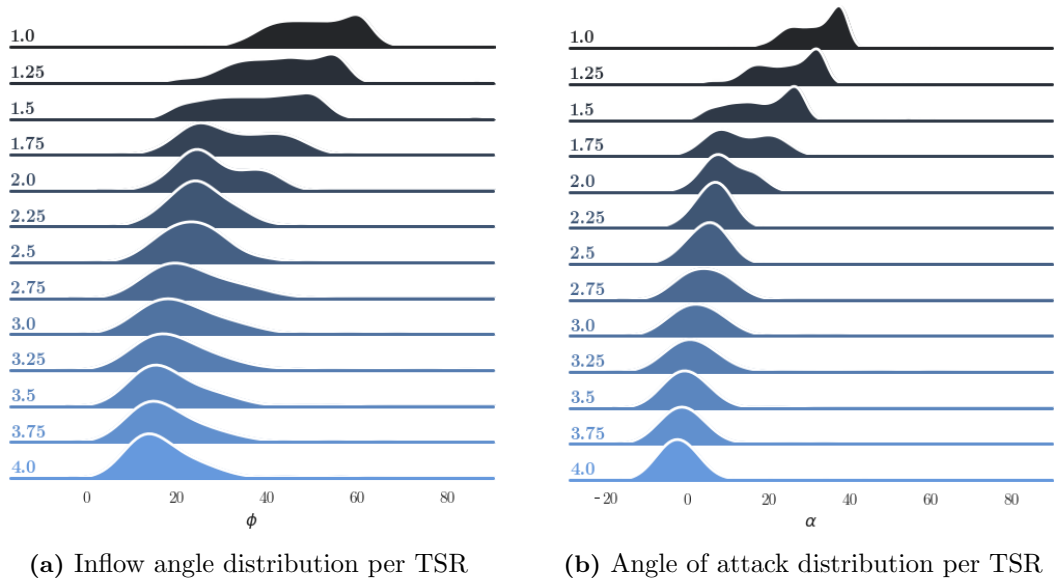


Figure 4.12: Frequency of flow angles per TSR for Gracie-Orr [122] NREL S814. The presented distribution does not correspond to the spatial distribution of angles on the blade. Nonetheless, it can be seen that majority of inflow angles at $TSR < 2$ remains to be high ($> 45^\circ$)

Verification of Blade Design and Analysis Methods with Preliminary Design Evaluation

For over-predicted thrusts, Breton [132] showed the effect of stall delay models in thrust prediction wherein most stall models, including the Viterna-Corrigan post-stall model, leads to an over prediction of thrust. The study was done for NREL aerofoils and may explain the behaviour on NREL aerofoils.

Table 4.3: Wortmann FX63137 Base Case Blade [2]

Normalised Radius (r/R)	Normalised Chord (c/R)	Twist (degrees) $\phi_{\text{root}} = 8$
0.234	0.1688	28.00
0.299	0.1651	13.62
0.391	0.1549	17.62
0.480	0.1470	13.20
0.567	0.1354	10.67
0.659	0.1241	9.09
0.751	0.1118	8.25
0.843	0.1000	7.61
0.932	0.0885	7.13
1.0	0.0654	6.89

Table 4.4: NACA 63-8xx Base Case Blade [1]

Normalised Radius (r/R)	Aerofoil	Normalised Chord (c/R)	Total Twist (degrees)
0.2	NACA 63-824	0.1250	20.0
0.3	NACA 63-821	0.1156	14.5
0.4	NACA 63-819	0.1063	11.1
0.5	NACA 63-817	0.0969	8.9
0.6	NACA 63-816	0.0875	7.4
0.7	NACA 63-815	0.0781	6.5
0.8	NACA 63-814	0.0688	5.9
0.9	NACA 63-813	0.0594	5.4
1	NACA 63-812	0.0500	5.0

Nonetheless, the good fit on C_P for the Wortmann and NACA blades provide good evidence on the quality of the BEM method ² to predict rotor performance. The base Wortmann FX63137 and the NACA 63-8xx blades are shown in Tables 4.3 and 4.4³.

²The single-parameter Python BEM also runs faster with an approximate running time of 2-3 seconds for a complete TSR sweep compared to the 2-variable running at 3 to 4 minutes at a time. This is important for simulations involving the full design space.

³The same table is presented in Table 3.1. The table is repeated for readability.

4.2.2 Implication of C_L/C_D to operational speed

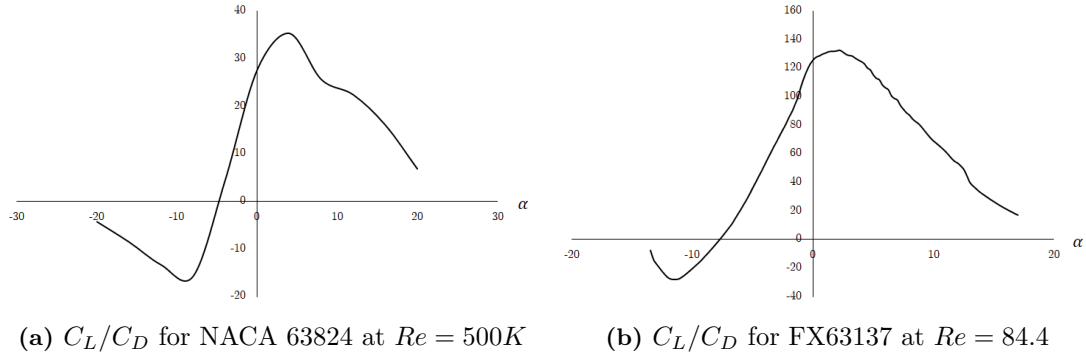


Figure 4.13: C_L/C_D for select aerofoils used in further case studies.

Notice that the $C_L/C_{D_{\max}}$ of the aerofoils in Figure 4.13 differ in peakedness. The absolute scales differ but the relative difference for each is noticeable with the FX63137 having a less pointed peak compared to the NACA 63824. This is expected to lead to large changes in the operational TSR of the NACA 638xx rotor since a small changes in α lead to big changes in the C_L/C_D values i.e. if C_L/C_D is to be maintained, there is a need to always adjust the total flow angle by virtue of the blade pitch and/or the operational speed.

4.3 Decision Modelling

In any real problem, there exist multiple solutions and each has costs and benefits. For simpler problems, the choice of a solution may be easy. The same is true when there is a clear winner that gives the most benefits. However, the nuances of determining a winner are still dependent on the criteria set by the decision-maker/s. Decision modelling formalises the decision-making process to objectively⁴ determine an optimum solution.

⁴It is possible to evaluate a subjective (based on personal preference) decision problem objectively.

4.3.1 Pareto Optimal Solutions

Multi-objective optimisation of turbines using GA usually produce a set of optimised blades that are said to be non-dominated alternatives/solutions. These are solutions that present a trade-off between an n number of objectives. These solutions are called Pareto optimal solutions and lie within the Pareto frontier. Figures 4.14a and 4.14b show examples of Pareto optimal solutions and a Pareto frontier curve for blade optimisation as presented by Zhu [129] and Sun [130].

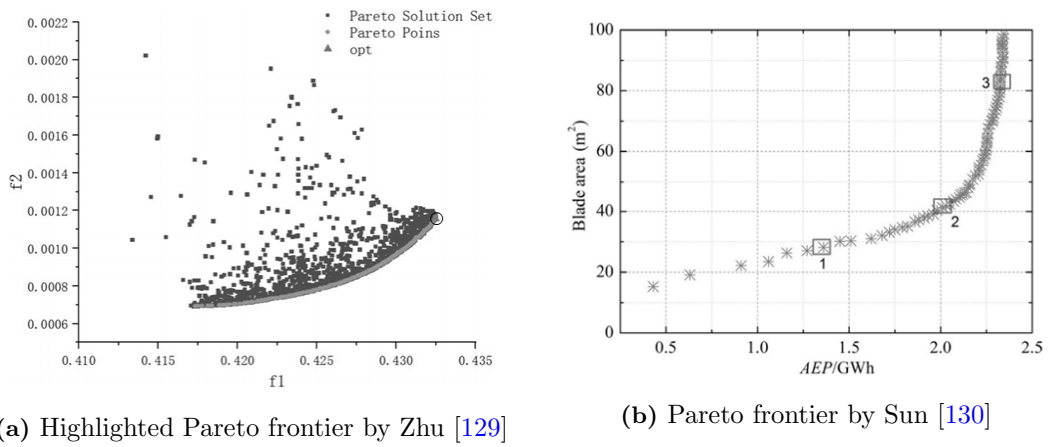


Figure 4.14: Pareto optimal solutions and Pareto frontier. Marked points are selected solutions of Zhu [129] and Sun [130] for further investigation in their respective studies.

Choosing a specific blade geometry within the Pareto optimal set can be done in a number of ways. Zhu [129] opted to select the geometry at the far right end of the Pareto frontier with the justification that the increase in f_2 (minimisation objective) is small compared to the increase in f_1 (maximisation objective). Sun [130] opted to select three geometries that represent a blade with small, medium, and large blade areas. Both methods are non-definitive methods to choose within the Pareto frontier. This is acceptable since these are still optimal solutions. However, it is possible to choose a solution that can be proven to be best considering the set criteria and objectives.

4.3.2 Weighted Decision Matrix

The Analytic Hierarchy Process (AHP) is a method to evaluate alternatives/solutions in a multi-objective decision problem. It is used to select an optimal solution by comparing each solution's attainment of an objective quantitatively and separately.

The method of selecting a solution given a set number of criteria using AHP was originally proposed by Saaty [133]. It is usually used in policy-making where decision-makers need to evaluate multiple scenarios/alternatives and determine the best option or combination of options. The determination of relative importance, or weights, in AHP is calculated by a pair-wise comparison for each criteria using a set scale from 1-10. These are then normalised to determine the overall weight of each criterion. The full method is discussed by Saaty in [133].

The stringent process of AHP is useful when dealing with several objectives but may be tedious when only determining weights for two objectives ($C_{P_{\max}}$ and $TSR_{C_{P_{\max}}}$). AHP is also useful in multi-dimensional problems [134] involving not only technical dimensions i.e. economical, environmental, sociological, psychological, etc.

Thus, a simpler approach of directly assigning weights, in percent, is adopted. This can be loosely defined as the weighted sum method [134] and is applicable for selecting the blade geometry with the best performance (single-dimension, multi-objective). Considering high-TSR blade design, the value of $C_{P_{\max}}$ and $TSR_{C_{P_{\max}}}$ for each blade is normalised before evaluating the total utility given by Equation 4.3.

- Objective Maximisation

$$\bar{X}_{i,j} = \frac{X_{i,j}}{X_{j,\max}} \quad (4.1)$$

- Objective Minimisation

$$\bar{X}_{i,j} = 1 - \frac{X_{i,j}}{X_{j,\max}} \quad (4.2)$$

where $\bar{X}_{i,j}$ is the normalised value for the j^{th} objective and the i^{th} alternative/solution.

Given n number of objectives, the total utility of a solution can be obtained:

$$A_i = \sum_{j=1}^n w_j \bar{X}_{i,j} \quad (4.3)$$

$$\sum_{j=1}^n w_j = 1 \quad (4.4)$$

where A_i is the utility for each solution to be ranked, w_j is the weight (%) of the j^{th} objective. The sum of the weights should always equal to 1. The solution with the highest utility is considered to be the best solution.

AHP and its derivatives, including the simplified approach, has been applied to many renewable energy projects. A full-turbine parametric design is presented by Daim [135] with a full AHP approach considering different turbine components. Relationships between components such as the effect of a 2-bladed design on the drive train of a turbine were also included in the selection process.

The simplified process is applied both in the preliminary investigation and in simulations using the full design space (Chapter 6). However, simulations with the full design space also involve weight sensitivity analysis to provide a basis for robust design.

4.3.3 Simulations in a limited design space

As an initial investigation, the design space was limited to

- $\Gamma_{\text{chord}} = (0.5, 2, 5)$ with $\Gamma = 2$ resulting in similar values with the published chord distribution
- $\Gamma_{\text{twist}} = (0.5, 2)$ and a hyperbolic twist distribution using values from the published twist distribution.
- A chord reduction of 37.5%, which is applied after the first round of the simplified two-round design process discussed in Section 4.3.3. The reduction of 37.5% was chosen semi-arbitrarily⁵ as an initial test case.

⁵37.5% is the average of 25% and 50% where the initial assessment of chord lengths deemed 25% as

Two-round blade design process

A two-round blade design process was implemented to reduce the number of blades needed to be simulated in the initial investigation. Each round is designed to observe or confirm effects of the altering a parameter on rotor performance. Figure 4.15 shows the two-round design process and Table 4.5 shows the expected observations and selection method for each round.

Table 4.5: Alterations and expected observations for each round

	Round 1	Round 2
Alteration	Altered Chord and Twist Distribution by Γ	Chord Reduced by 37.5% of the tip chord
Expected Observation	Observations on the sensitivity of rotor performance to altered parameters	Reduction on $C_{P_{\max}}$ and movement of $TSR_{C_{P_{\max}}}$ to higher TSRs
Candidate Selection	Blades filtered based on more sensitive parameter, Weighted decision matrix in case of non-dominated alternatives	Weighted decisions matrix in case of non-dominated alternatives

The weighted decision matrix discussed in Section 4.3.2 is applied in the candidate selection in case of a non-dominated alternative for the $C_{P_{\max}}$ and $TSR_{C_{P_{\max}}}$ objectives. Each objective is set with equal weights (0.5, 0.5). However, additional conditions are added to the use of the decision matrix. After all, severely reduced performance in terms of C_P is undesirable even if $TSR_{C_{P_{\max}}}$ is 12, which is the maximum TSR set in the simulations. The conditions for the NACA 63-8xx are:

1. $TSR_{C_{P_{\max}}} > 5.75$ (High-TSR criterion)⁶Adjusted for preliminary test. The definition for high-TSR throughout the thesis still remains to be at TSR ≥ 6 . Additionally, the final resulting TSRs still become greater than 6.)

maybe too small and 50% was too aggressive. Nonetheless, a full-sweep is done in the latter parts of the research.

⁶(

Verification of Blade Design and Analysis Methods with Preliminary Design Evaluation

- The difference between $C_{P_{\max}}$ for any alternative is less than 10% (Hydrodynamic efficiency criterion)

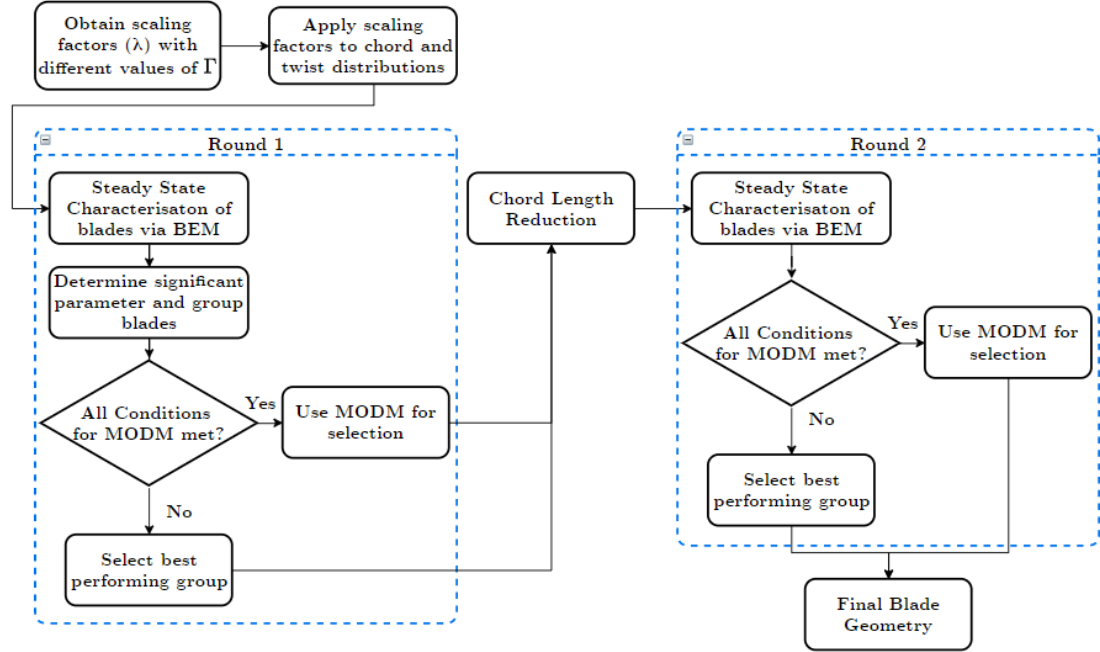


Figure 4.15: Design process for initial investigation.

Thrust is not included in the primary objectives since it is expected to have lower variation compared to torque with $C_P \propto U^3$ and $C_T \propto U^2$. This is a simplification since increased rotational velocity may also increase thrust due to the rotor hydrodynamics (Equation 2.3). However, thrust remains to be a secondary consideration at this initial investigation. Section 6.1.3 discusses the effect of thrust in the final blade selection considering the full design space discussed in Section 3.3.2.

Blade Geometries and Performance

Round 1. Figure 4.16 shows the application of Γ on the NACA 63-8xx. Table 4.6 shows the chord and twist distributions used at this round of simulations. The combination of chord and twist distributions leads to nine (9) blade geometries.

Verification of Blade Design and Analysis Methods with Preliminary Design Evaluation

Table 4.6: Blade geometry specifications for Round 1 NACA blades.

Norm. Radius (r/R)	Norm. Chord (c/R)			Total twist (degrees)		
	$\Gamma = 5$	$\Gamma = 2$	$\Gamma = 0.5$	Base	$\Gamma = 2$	$\Gamma = 0.5$
0.2	0.125	0.125	0.125	20	20	20
0.3	0.107	0.116	0.121	14.5	18.13	19.21
0.4	0.095	0.106	0.116	11.1	16.25	18.24
0.5	0.084	0.097	0.110	8.9	14.38	17.08
0.6	0.075	0.087	0.103	7.4	12.50	15.70
0.7	0.068	0.078	0.095	6.5	10.62	14.03
0.8	0.061	0.069	0.085	5.9	8.75	11.97
0.9	0.055	0.059	0.071	5.4	6.88	9.28
1	0.05	0.05	0.05	5	5	5

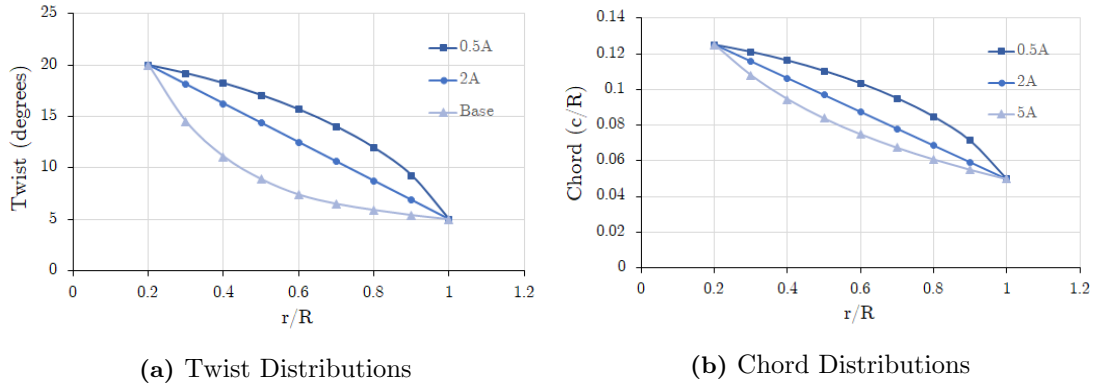


Figure 4.16: Round 1 Blade Geometry Distributions

Figure 4.17 shows the performance of each blade geometry for a rotor with a radius of 1m and $U_\infty = 1\text{m/s}$. Rotor performances are clustered into three groups determined by the twist distribution. This suggests that performance is more sensitive to the twist distribution, considering the same root and tip twist, of the NACA 63-8xx.

Visual inspection of the performance curves would lead to the selection of blades with the base twist distribution. Quantitative confirmation is done by grouping the blade geometries according to twist distribution and calculating the average $C_{P_{\max}}$ and $TSR_{C_{P_{\max}}}$ of the group. Table 4.7 shows the average performance values of each group.

Table 4.7: Round 1: Averaged maximum C_P and $TSR_{C_{P_{\max}}}$ according to twist distribution.

Blade Twist Distribution	Averaged Maximum C_P	Averaged TSR Location
Base	0.436	5.92
$\Gamma = 2$	0.386	6.17
$\Gamma = 0.5$	0.316	5.17

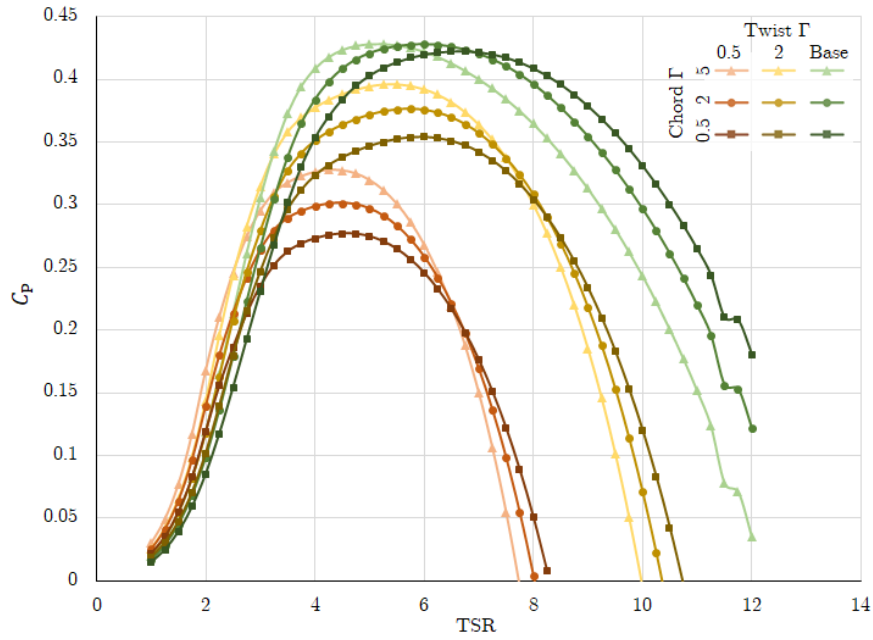


Figure 4.17: Performance of Round 1 blade geometries

The average $C_{P_{\max}}$ for the base twist distribution group has a value that exceeds the average $C_{P_{\max}}$ of the linear ($\Gamma = 2$) distribution (second best) by a factor greater than 10%. This confirms the visual inspection that the base twist distribution should be considered for Round 2.

Round 2. All blade geometries in Table 4.8 uses the base twist distribution (hyperbolic) of the NACA 63-8xx. Rotor performance for Round 2 is also simulated using a rotor radius of 1m and $U_{\infty} = 1\text{m/s}$. Figure 4.19 shows the simulated performance of the three blades.

Verification of Blade Design and Analysis Methods with Preliminary Design Evaluation

Table 4.8: Blade geometry specifications for Round 2 low-solidity NACA blades (37.5% reduced chord length) with base twist distribution.

Norm. Radius (r/R)	Norm. Chord (c/R)		
	$\Gamma = 5$	$\Gamma = 2$	$\Gamma = 0.5$
0.2	0.106	0.106	0.106
0.3	0.089	0.097	0.102
0.4	0.076	0.088	0.097
0.5	0.065	0.078	0.092
0.6	0.056	0.069	0.085
0.7	0.049	0.059	0.076
0.8	0.042	0.050	0.066
0.9	0.036	0.041	0.053
1	0.031	0.031	0.031

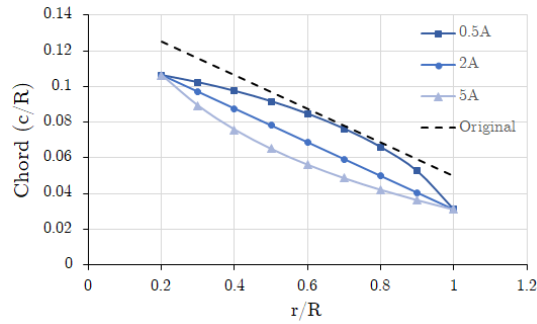


Figure 4.18: Round 2 Chord Distribution. Base twist distribution is applied.

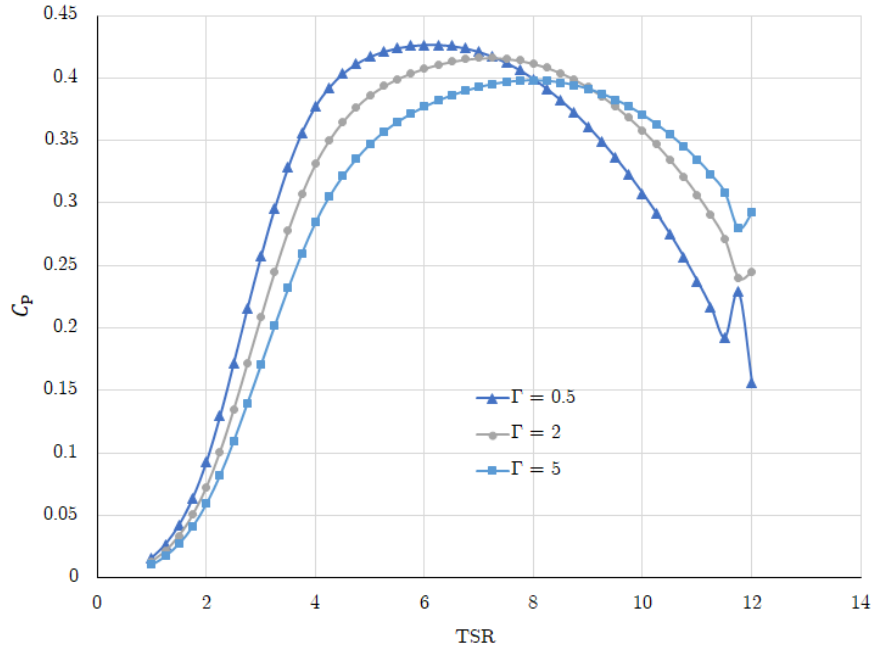


Figure 4.19: Performance of Round 2 blade geometries

Visual inspection shows a trade-off between $C_{P_{\max}}$ and $TSR_{C_{P_{\max}}}$ prompting for the use of a weighted decision matrix. Table 4.9 shows the utility values for each blade geometry. It was found that the chord distribution that produces the best performance according to the weighted objectives is the hyperbolic ($\Gamma = 5$) chord distribution.

The relationship between $TSR_{C_{P_{\max}}}$ and Γ_{chord} (\uparrow TSR \uparrow Γ_{chord} \downarrow solidity) can be seen in Table 4.9. This relationship is consistent with Schubel's [54] discussion that blades having lower solidity tend to operate at higher TSRs. Note that the solidity of the original blade by Bahaj [1] is $\sigma_s = 0.035$.

Table 4.9: Weighted Decision Matrix for the NACA 63-8xx

Objective	Weight	Normalised Values		
		$\Gamma = 5$ $\sigma_s = 0.017$	$\Gamma = 2$ $\sigma_s = 0.019$	$\Gamma = 0.5$ $\sigma_s = 0.022$
Maximum C_P	0.5	0.933	0.976	1
TSR Location	0.5	1	0.906	0.75
Weighted Total	1	0.967	0.941	0.875

The trend for $C_{P_{\max}}$ is reversed wherein higher Γ_{chord} results in lower C_P . This is

also expected since lower solidity decreases hydrodynamic performance for the same twist distribution and pitch setting [123,124]. Figure 4.17 showing the performance for all nine blades also illustrate this relationship wherein higher Γ_{chord} (more hyperbolic) have lower C_P compared to its counterparts with the same twist distribution.

4.4 Summary

The chapter showed capability of the rapid blade generation method in generating candidate blades suitable for high-TSR operation. Chord and twist distributions generated using control-point genetic algorithm optimisation were replicated using the conic equation defined in the proposed design method. Simulated performance of the conic-defined blades and the GA-design blades are comparable even with slight deviations between the two approaches. This shows the applicability of the proposed method in designing blades with an added advantage of generating blades that can be manufactured with more ease compared to blades with a complex distribution.

The implementation of the blade element momentum method has been verified by replicating published results. A preliminary design has been applied with the hydrodynamic performance of candidate high-TSR blades being comparable to the base blade.

Chapter 5

Experimental Validation and Simulation adjustments

Small-scale testing is essential to the development of tidal turbines. These tests give valuable information on the actual performance of a device that may otherwise not be captured in simulations, such as the case for Gracie-Orr [122]. Larger prototypes tested in nursery sites provide a better picture of the challenges and operating conditions associated with real tidal current energy sites. However, testing these large prototypes are too costly especially at the initial design stage. This makes small-scale testing indispensable.

This chapter discusses the small-scale testing to validate the high-TSR blade developed in Chapter 4 with the results prompting adjustments on the simulations through BEM.

5.1 Small-scale testing of high-TSR rotor

Testing is especially important to adjust for factors that affect performance not tackled by the BEM method. These include blade deflections due to reduced solidity and laminar separation due to running in low Reynolds number, and would suggest a need to obtain aerodynamic characteristics.

However, it was discovered that small-scale testing of low-solidity tidal turbine blades may be problematic due to difficulties in fabrication. It is possible to address issues on fabrication by using more precise techniques, although these techniques also

tend to increase cost. The first challenge encountered was during the creation of the SolidWorks model of the selected blade. It was found that the $\Gamma_{\text{chord}} = 5$ blade to be fabricated was very slender in the SolidWorks model. Due to this, the close second was chosen to be fabricated owing to its seemingly more robust structure. This was considered appropriate at this stage because the focus is to experimentally validate the results of the BEM for a high-TSR blade ($TSR_{C_{P_{\text{max}}}} = 7$). The resulting weighted total (0.967 vs 0.941) also shows that the two blades are comparable in terms of overall performance. Nonetheless, a challenge in the minimum fabrication thickness was encountered which then led to adjustments that affected the performance of the rotor.

5.1.1 Rotor Setup

A 0.5mm minimum thickness at the trailing edge was applied due to fabrication limits at the University of Strathclyde. This was accommodated by shifting all the points at the suction side of the aerofoil up by 0.5mm. This resulted in an increased thickness-to-chord (t/C) ratio with some blade sections being severely deformed. Table 5.1 shows the thickness in different sections of the NACA 63-8xx blade before and after alteration.

Table 5.1: Change in thickness for each blade section of the NACA 63-8xx blade

Radius (mm)	Chord (mm)	Thickness		
		Pre-shift	Post-shift	% Change
43.8	23.27	5.58	6.08	8.96%
65.7	19.53	4.04	4.54	12.38%
87.6	16.6	3.10	3.60	16.13%
109.5	14.25	2.51	3.01	19.92%
131.4	12.32	2.04	2.54	24.51%
153.3	10.68	1.67	2.17	29.94%
175.2	9.25	1.35	1.85	37.04%
197.1	7.99	1.09	1.59	45.87%
219.0	6.84	0.86	1.36	58.14%

5.1.2 Experimental Setup

A flume tank test was conducted to validate the performance of the preliminary blade. A 0.545m diameter rotor with 219mm aluminium blades was tested in Inha University's 1.0m x 1.0m flume tank running with $U_\infty = 1.0\text{m/s}$. The tank had a working section of 3.0m. This setup leads to a blockage ratio of greater than 20%, which is also higher than the usual 5-10% blockage. This higher blockage accelerates the flow, which typically leads to higher thrust and torque loads [136]. Thus, it was expected that experimental torque and thrust loads will be higher compared to the simulations. Reynolds number at 70% of the radius is calculated to be $Re = 3.43 \times 10^4$.



Figure 5.1: NACA 63-8xx mounted for testing at Inha University flume tank ($Re = 3.43 \times 10^4$)

The hub was positioned at the middle of the water column at an approximate depth of 0.4m. The hub houses a transmission drive shaft built with a keyway mechanism. A secondary shaft running along the mast is coupled with an encoder and a motor at the top, away from the water level (Figure 5.2). A torque transducer was used to quantify

Experimental Validation and Simulation adjustments

rotor power and the load was regulated using torque control. At most, ten (10) torque settings leading to ten (10) different rotational speeds were tested. Performance for each torque setting was obtained for approximately 2 minutes at a sampling rate of 100Hz.

Flow was characterised at designated points (Figure 5.3) using an Acoustic Doppler Velocimeter that obtains velocity at hub height and 0.25m above the hub. Each measurement was done for 3 minutes with a data capture set to 50Hz.

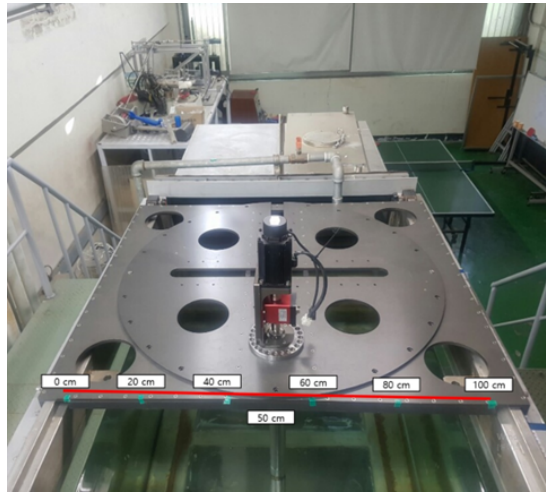


Figure 5.2: Acoustic Doppler Velocimeter measurement points denoted by the green marks at the top panel

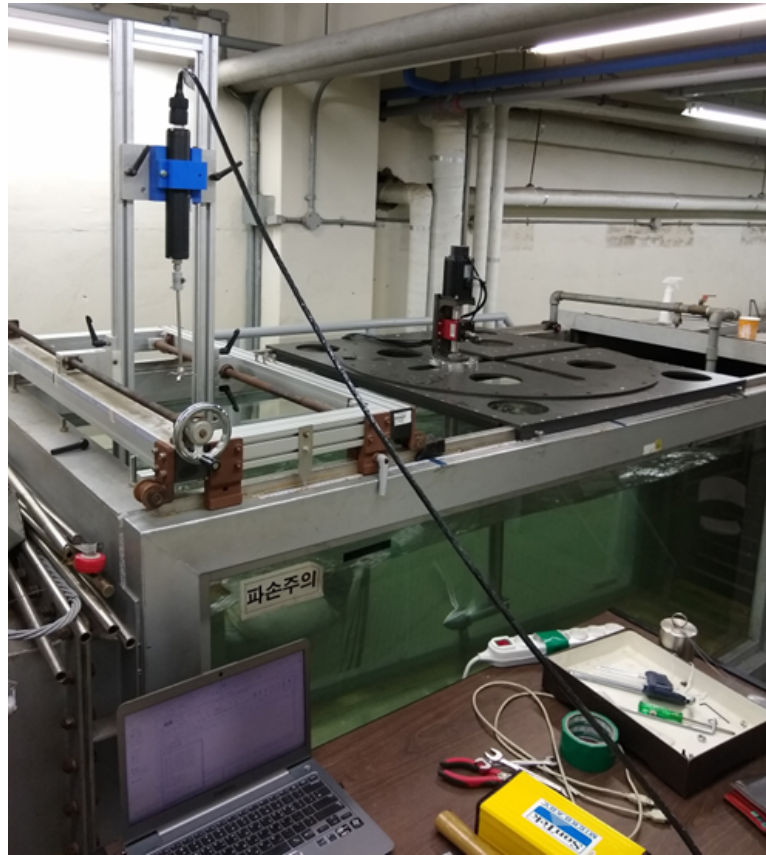


Figure 5.3: Flume tank and mounted experimental setup at Inha University

5.1.3 Experimental Results

Severely reduced performance compared to the simulated performance was observed (Figure 5.4) during the experiment. The huge reduction in performance was attributed to the change in aerodynamic characteristics of sections and significant blade deflections observed during testing.

The 0.5mm minimum thickness fabrication limit applies to all blades that have been fabricated at the University of Strathclyde. However, the same effect was not seen in the Wortmann FX63137 blades [137] tested within the same facility, setup, and aerofoil alteration technique. The main difference between the blades is the base thickness of each blade section - the Wortmann had sections with larger base thickness than the high-TSR NACA.

Figure 5.5 shows the ideal NACA 63-812 aerofoil used in the tip and the resulting

Experimental Validation and Simulation adjustments

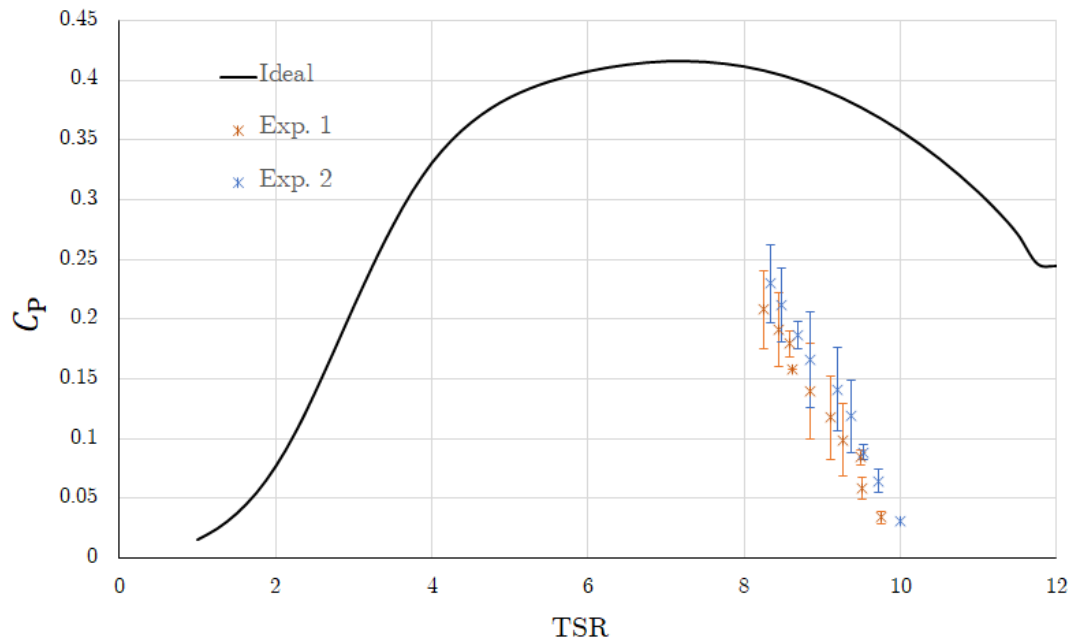


Figure 5.4: Results of Flume Tank Test with $U_\infty = 1.0\text{m/s}$. Error bars calculated using standard deviation (3sd) between similar torque settings.

aerofoil when the tip section of the 219mm blade was altered. The 3D printed foils are zoomed out versions of the tip section of 219mm blade. The tip section presented in Figure 5.5 is for 1m long blades. Here, the deviation from the ideal aerofoil shape is very visible.



Figure 5.5: Ideal and Shifted Case of NACA 63-812 (turbine tip) for a 1m blade (magnified version for a 219mm small-scale blade)

Due to the deformation, it was suspected that performance was severely hampered by a significant increase in drag. Evaluation of the losses is necessary to provide

information on how low-solidity tidal turbine blades should be fabricated when being considered for small-scale testing. Additionally, the source of discrepancy needs to be identified and included in the BEM implementation, if there is any ¹.

It can be argued that low-solidity tidal turbines may have similar solidity values with wind turbine blades. If so, then it might be possible to adopt small-scale wind turbine fabrication techniques to small-scale tidal turbines. However, operational conditions, most especially the use of liquid water instead of air, prevent the application of such techniques to tidal turbine fabrication.

Thus, there are more manufacturing options for fabrication of wind turbine blades that can survive the environment, such as 3D printing [138, 139], which can accommodate a smaller minimum thickness. The degree of deformation using these techniques will reduce the amount of aerofoil deformation, preventing blade sections that look like the one shown in Figure 5.5. Materials used for 3D printing is not usually used in tidal turbine prototypes; aluminium that has good corrosion resistance and high tensile strength is the usual material. It is possible to opt for metal 3D printing but this would increase the cost of testing.

5.2 Adjusting aerofoil trailing edges

5.2.1 Trailing edge alterations

- (a) Ideal - The original aerofoil coordinates are obtained from Javafoil [48]. This provides a benchmark for all the alteration cases.
- (b) Shifted - This alteration was the one adopted for both the NACA 63-8xx and the Wortmann FX63137 blades. This is done by shifting all the points in the suction side up by 0.5mm. This alters the trailing edge as well as the leading edge of the foil as shown in Figure 5.5.

¹The question being addressed is: "Are there any unknown issues in the BEM that needs to be considered?"

- (c) Blunt² - From the trailing edge, a position x/C having a thickness³ of 0.5mm is identified. The aerofoil is then cut perpendicularly to the camber line. This is different from the usual definition of blunt trailing edges that chop off the trailing edge vertically, resulting in a loss in camber [140]. An arc tangent to the upper and lower surface is introduced (Figure 5.6). This trailing edge alteration may be unintentionally introduced in fabrication depending on the machine used. It can be the case that sections with thickness less than 0.5mm are removed from the base working material altogether.
- (d) Extension - The same x/C position as with the blunt trailing edge is selected. The aerofoil is then cut in the same manner before introducing an extension of a 0.5mm constant thickness section towards the original trailing edge (Figure 5.7). An arc tangent to the upper and lower surface, and coincident to the original trailing edge is introduced. This changes the overall camber as the slope of the camber line where the aerofoil is cut is used throughout the extension. Thus, the midpoint of the arc and the original trailing edge is not coincident.

All trailing edge alterations were performed in SolidWorks 2017.

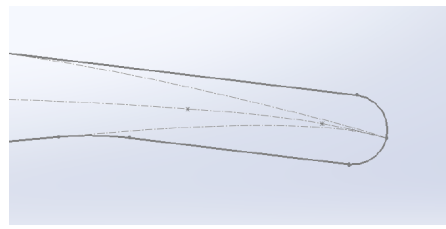
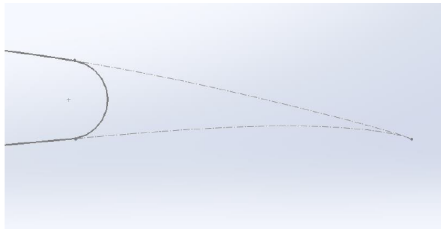


Figure 5.6: Trailing edge for Blunt case.

Figure 5.7: Trailing edge for Extended case

5.2.2 CFD Setup

Aerodynamic characteristics were obtained using 2D CFD simulations on ANSYS Fluent. Two different grid structures were used to accommodate the difference in

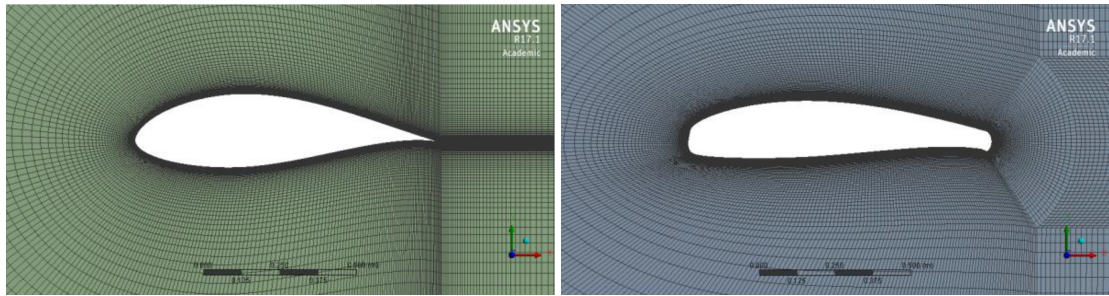
²Blunt trailing edges are usually described in the literature as having vertically flat trailing edge profiles. The term is used here despite having a rounded profile because the method of cutting the trailing edge is similar.

³Thickness perpendicular to the camber line.

trailing edges. A structured C-grid was used for the ideal aerofoil. This structure failed to mesh properly for the altered aerofoils due to the curvature of the trailing edge arc. To accommodate this, an O-grid was used to mesh the inner domain located 0.3m from the aerofoil trailing edge. The remaining outer domain was meshed by the usual C-grid.

Mesh properties. Cells at 30% chord length were set to have a minimum orthogonality of 0.7 and maximum skewness of 0.35. Meshes were refined near the aerofoil surface with 15 cells allocated for the boundary layer. The height of the first cells near the surface was set to $5 \times 10^{-5} \text{m}$.

A grid independence study was then conducted to identify the benefits of increasing cell count. The cell count was set to 50,000, 100,000 and 200,000. It was found that increasing from 50,000 to 100,000 cells changed the result by 1%, and further increasing to 200,000 resulted in a further $<0.5\%$ change. Due to this, it was determined that 50,000 cells can provide enough accuracy for the BEM inputs.



(a) C-grid for NACA 63-824 Ideal Case (b) Hybrid Mesh for NACA 63-812 Shifted Case

Figure 5.8: CFD mesh for ideal and shifted cases.

All domain edges were set to be 20 chord lengths away from the aerofoil surface. The average cell count was set to 52,000 cells although the exact number differed depending on the meshing strategy.

Test parameters. The Reynolds number for the simulations was set at $Re = 5 \times 10^5$. This is considered high for low-TSR operation but reasonably attainable for high-TSRs. This is also a magnitude larger than the Reynolds number for the experiment.

JavaFoil [48] shows that the drag values for the NACA 63-8xx series only become

comparable at Reynolds of $Re > 1 \times 10^5$, with drag increasing for much lower values. Thus, the drag force developed during the experiments may have been higher, further reducing the performance compared to the simulations. Additionally, any new simulation based on the $Re = 5 \times 10^5$ will result in higher C_P compared to performance simulated using $Re = 3.43 \times 10^4$.

However, the simulation Reynolds of $Re = 5 \times 10^5$ was chosen to provide a base case for verification of CFD results since the current literature presents aerodynamic data in this Reynolds number. All simulations, both CFD and further BEM, are then targetted towards further testing rather than recreating the experiment. Section 5.4 also discusses increasing blade length to reduce the deformations on the foil. Lift and drag coefficients were determined for angles of attack from -20° to 20° in 4° increments.

The simulations were run at steady-state and convergence was assumed when the lift and drag coefficients remained constant for up to five significant figures for at least 25 iterations. The $k - \omega$ SST turbulence model was used to resolve RANS equations when flow separation occurred; most positive angles of attack led to flow separation. Nonetheless, the convergence criterion is able to account for this and corresponds to a mass, momentum, and turbulence residual of 1×10^{-7} .

5.3 Resulting Aerofoil characteristics

5.3.1 Comparing CFD and XFOIL ideal aerofoils

A comparison of the CFD and XFOIL values was done to verify the CFD setup. Batten [1] provides the C_{press} values of the NACA 63-813. These were used to compare the NACA 63-812, with an actual t/C of 12.6%, and is shown in Figure 5.9. Additional runs were not performed although it can be seen that the current angles of attack of $\alpha = (-4, 0)$ have comparable C_{press} to the published $\alpha = (-5.18, -0.84)$.

Experimental Validation and Simulation adjustments

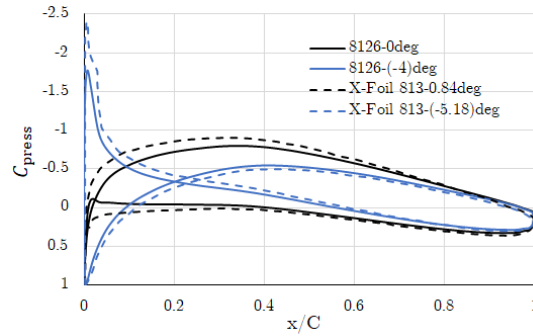


Figure 5.9: XFOIL vs CFD coefficient of pressure for ideal aerofoils ($Re = 5 \times 10^5$)

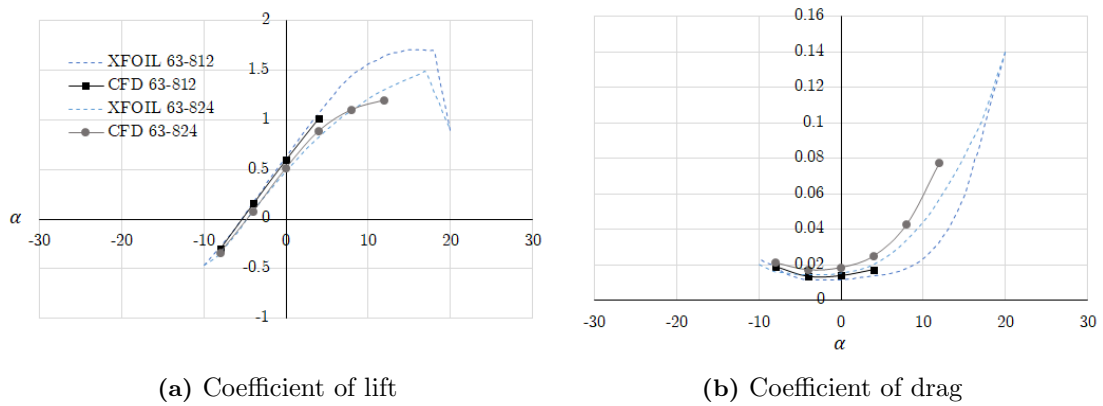
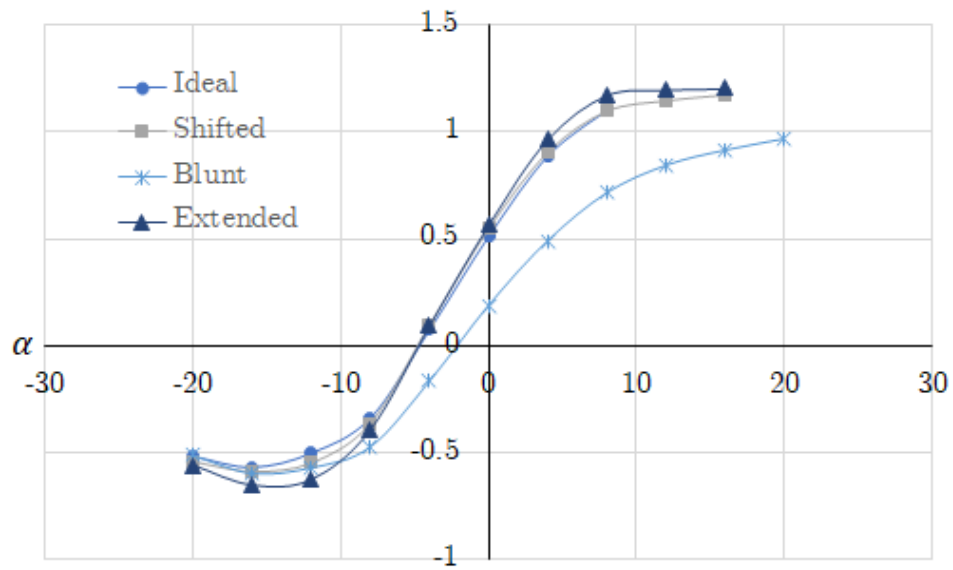


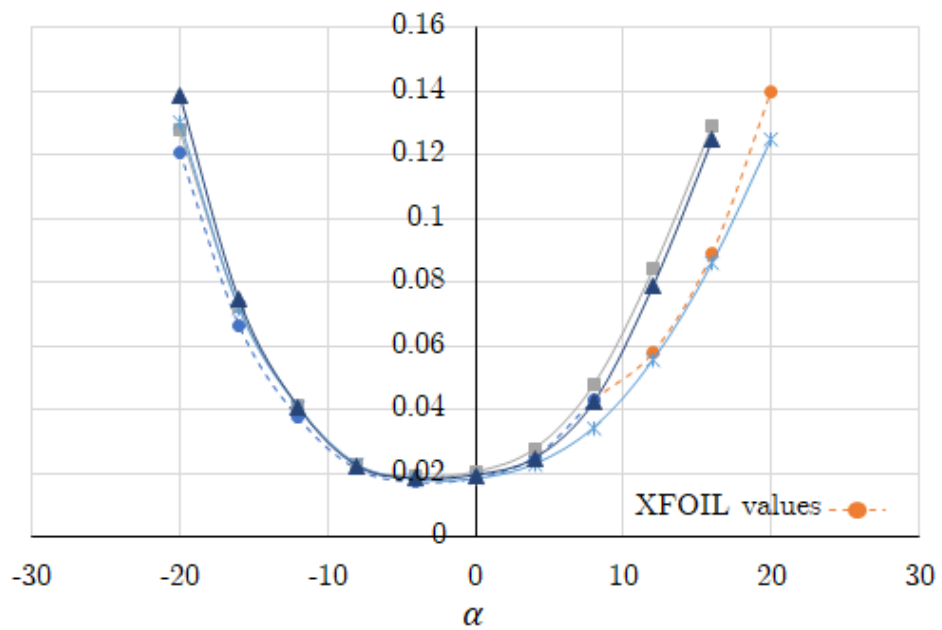
Figure 5.10: XFOIL vs CFD aerodynamic characteristics for ideal aerofoils ($Re = 5 \times 10^5$)

Figure 5.10 shows the comparison of aerodynamic characteristics of the NACA 63-824 and NACA 63-812 from CFD and published XFOIL values. It can be seen that lift values are comparable. However, there is a visible increase in drag for all tested α . Morgado [141] observed this increase and noted a need for correction on the $k - \omega$ SST model for low Reynolds number - the usual $k - \omega$ SST model will predict higher drag at low Reynolds number due to the latter's inability to predict transition and problems on replicating results for sharp corners.

5.3.2 Lift and Drag Results



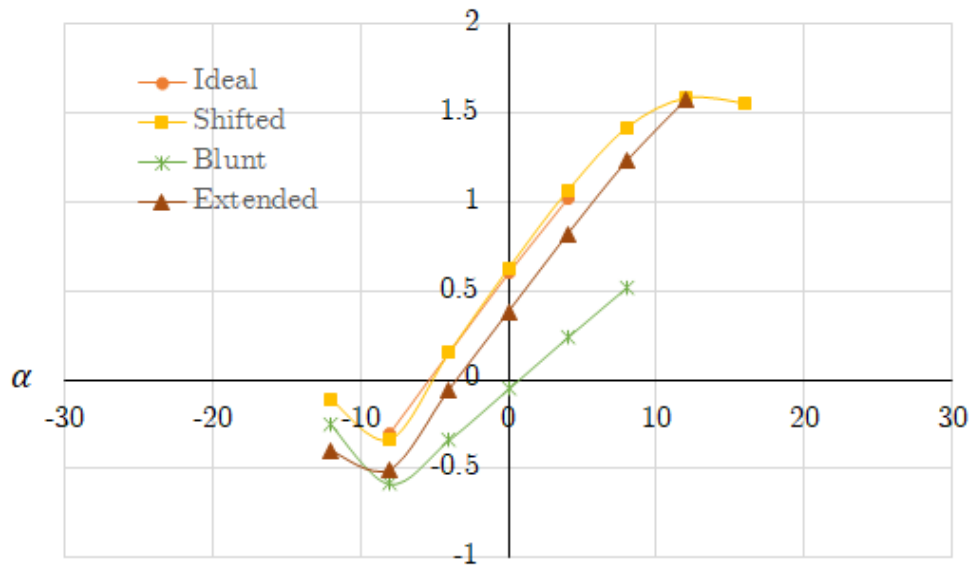
(a) Coefficient of lift



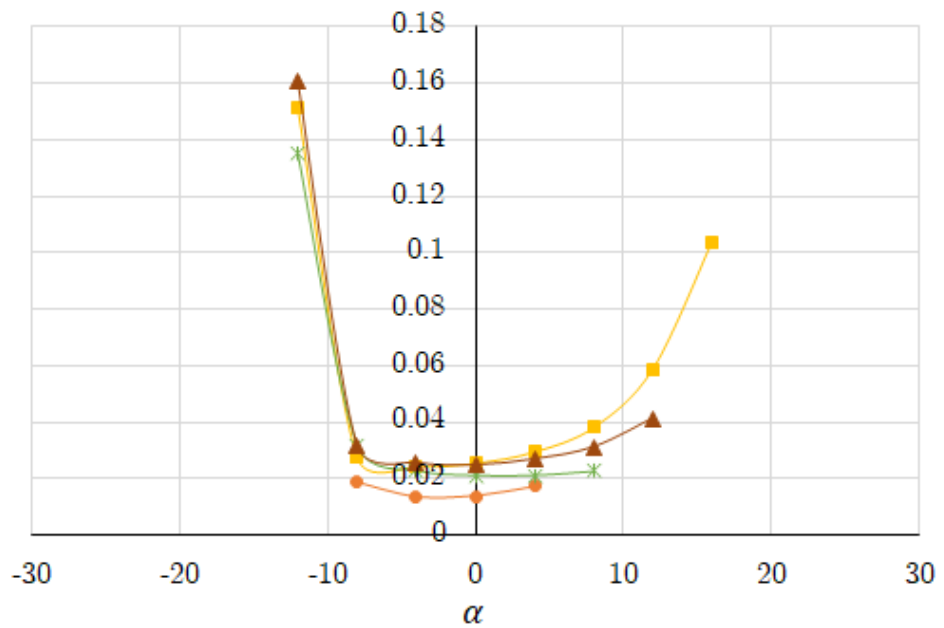
(b) Coefficient of drag

Figure 5.11: Aerodynamic characteristics for NACA 63-824 aerofoils ($Re = 5 \times 10^5$)

Experimental Validation and Simulation adjustments



(a) Coefficient of lift

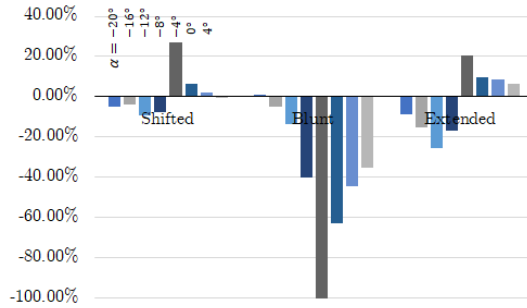


(b) Coefficient of drag

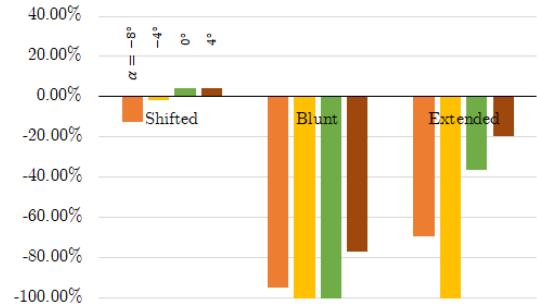
Figure 5.12: Aerodynamic characteristics for NACA 63-812 aerofoils ($Re = 5 \times 10^5$)

5.3.3 Relative Differences

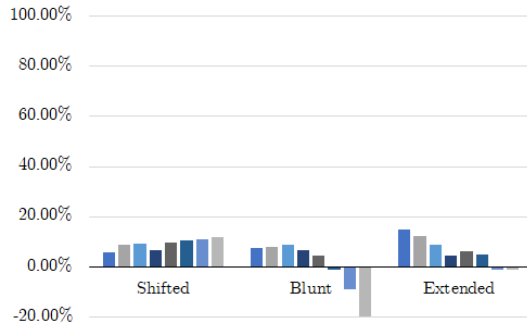
Figures 5.13 and 5.14 show the percentage change in lift and drag values of the altered aerofoils with respect to the baseline ideal aerofoil. Table 5.2 presents the median percentage change for each alteration method. The median is used instead of the average due to the existence of large values of percentage change when dealing with small values of lift and drag especially for $\alpha \approx -4$.



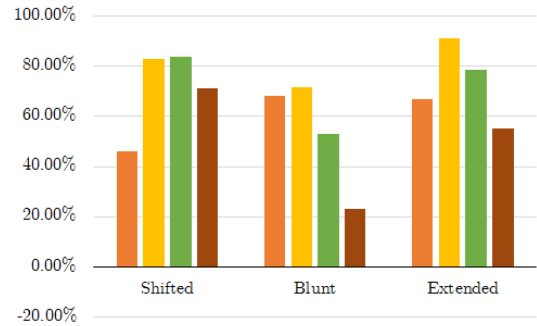
(a) % change for NACA 63-824 C_L



(a) % change for NACA 63-824 C_D



(b) % change for NACA 63-812 C_L



(b) % change for NACA 63-812 C_D

Figure 5.13: % change for Lift

Figure 5.14: % change for Drag

Table 5.2: Median and Average % change for all cases with respect to ideal C_L and C_D

		Shifted	Blunt	Extended
C_L	63-824	-2.0% (1.10%)	-37.60% (-64.34%)	-1.04% (-2.59%)
	63-812	1.07% (-1.52%)	-101.88% (-149.28%)	-53.09% (-65.41%)
C_D	63-824	9.46% (9.17%)	5.52% (0.60%)	5.55% (6.07%)
	63-812	77.03% (71.01%)	60.70% (54.03%)	72.72% (72.92%)

The change in lift and drag of the altered NACA 63-812 is significantly greater than

the altered NACA 63-824 foils. This was expected since the degree of deformation in the NACA 63-812 is greater than the deformation of the NACA 63-824 for all cases. This has been shown in Figure 5.5 for the shifted case. For the blunt and extended alterations, the degree of deformation is still greater as cutting the aerofoil within the section that has 0.5mm thickness either significantly reduces the effective length of the aerofoil (blunt) or changes the contour of the aerofoil (extended).

This could have a significant impact on the performance of the high-TSR blades that would generally have less solidity. Recall from Table 3.2 that low solidity is typically a characteristic of hyperbolic chord distributions. These distributions also have more aggressive tapering near the root. This implies that thickness also decreases rapidly and hence, will approach the performance of the NACA 63-812 even at sections near the root.

NACA 63-824. The lift of the shifted and extended aerofoils are comparable to the ideal aerofoil at $-8 \leq \alpha \leq 8$. High percentage differences are seen at C_L values less than ± 0.01 . This amplifies the perceived difference.

The lift of the blunt aerofoil is severely reduced compared to the ideal aerofoil starting from $\alpha = 12$. The reduction is more pronounced at higher angles of attack where the blunt aerofoil loses a third of the lift that can be generated by an ideal foil. This is contrary to the findings of researchers on the effects of blunt trailing edge profiles which should increase lift [142–144]. This can be explained by the difference in the method of generating and calculating the lift of a blunt aerofoil. The mentioned studies generated a blunt aerofoil by cutting the trailing edge section and subsequently scaling the aerofoil towards $x/c = 1$. For this study, the trailing edges were cut off, not re-scaled, and the lift is calculated using the length of the ideal aerofoil to provide a benchmark.

Cutting essentially removes a portion for the flow to act on and produce a differential pressure as has been found by Thomareis [145]. This leads to a drop in lift and is consistent with the findings of Thomareis [145] and Gomez [146]. However, the degree of reduction of lift is significantly higher than expected and may need further investigation.

It is also apparent that the stall onset is moved towards higher α , which is a direct benefit of blunt trailing edge aerofoils [142–146]. Flow separation is delayed compared to usual sharp trailing edge aerofoils improving structural stability. This was also observed in the CFD simulations and can be seen from Figure 5.11a where the values of C_L successfully converged for all simulated α of the shifted case.

For drag, the blunt trailing edge shows reduced drag compared to the shifted and extended cases. This may seem like a better drag performance compared to the ideal case but a closer look proves otherwise. CFD values for higher angles of attack failed to converge and hence, not included in the figure. Extending the drag data for the ideal aerofoil using XFOIL values (Figure 5.10b), it can be seen that the blunt aerofoil has comparable drag to the ideal aerofoil.

From Figure 5.11b it can be seen that the shifted case already has a significant increase in drag compared to the ideal case. Recalling from Equation 2.4, higher drag values reduces the torque produced by the rotor and will result in lower C_P . The 0.5mm shift introduces an artificial curvature in the leading edge that acts as a wall that leads to significantly higher drag. Additionally, Shen [147] discussed that discontinuities in the gradient-of-curvature distribution affect the pressure differential within the aerofoil.

The 0.5mm shift introduces such a discontinuity making it highly possible that laminar separation bubbles were developed and increased the drag of the foil. This is also true for the extended case as the gradient-of-curvature distribution dramatically changed, especially near the 0.5mm thickness cut and the arc in the trailing edge. The same reasoning can be applied to the blunt aerofoil wherein the gradient-of-curvature is not severely altered leading to comparable drag values.

NACA 63-812. The effects seen in the NACA 63-824 are amplified for the NACA 63-812 due to the significantly smaller base thickness ratio of the latter. Lift of the shifted case remains to be comparable to the ideal case as shown in Figure 5.12a. The blunt case shows worse lift reduction compared to NACA 63-824 as the 0.5mm thickness cut is situated at a much smaller x/C leading to an aerofoil that was almost cut in half as shown in Figure 5.15. The extended case has a flat surface that would resemble a

finite thickness flat plate, and thus would have reduced lift compared to the ideal case.

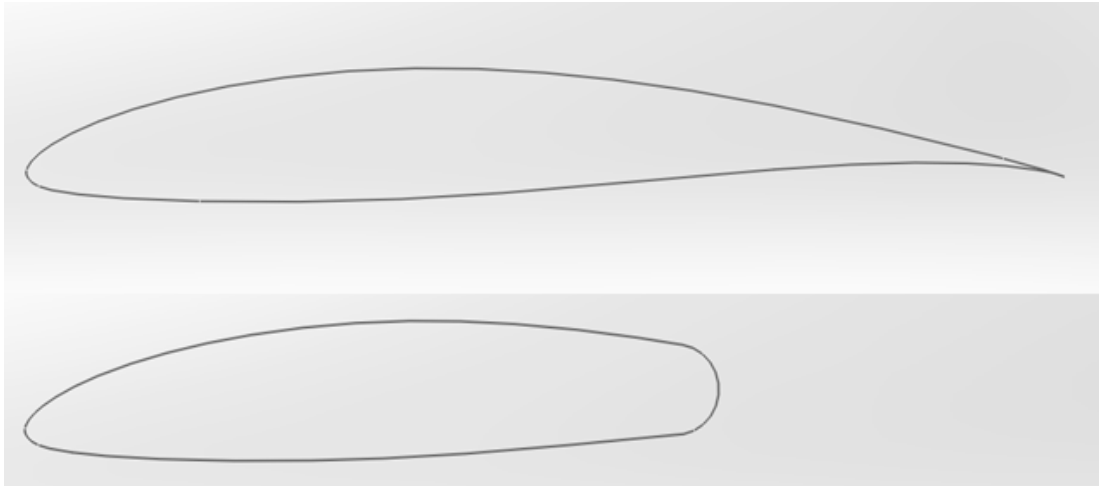


Figure 5.15: NACA 63-812 Ideal (top) and Blunt (bottom) Case

The increase in drag across all cases is at least 54%. As previously discussed, this will lead to adverse effects on rotor performance. Here, the discontinuity on the gradient-of-curvature covers a greater surface area and can lead to larger laminar separation bubbles.

It is to be noted that it is possible to change the sectional makeup of the NACA 63-8xx turbine to incorporate flat back aerofoils such as the one applied by Berg [140] and Standish [144]. These aerofoils have been found to have increased lift and also increase rotor performance. However, this changes the base NACA 63-8xx blade and dwells in the discussion of blade optimisation through aerofoil manipulation instead of altering chord and twist distributions. This essentially changes simulation parameters and the whole rotor instead of just accounting for losses in the small-scale testing of the preliminary design.

5.3.4 Rotor performance of altered aerofoils

Figure 5.16 shows the simulated performance of all rotor cases. All altered trailing edge cases result in a reduction of C_P at all operating conditions with the shifted case having the best performance among the altered cases. The decision to opt for a shifted case on a 400mm blade simulation was based on these results. C_T of the shifted case is

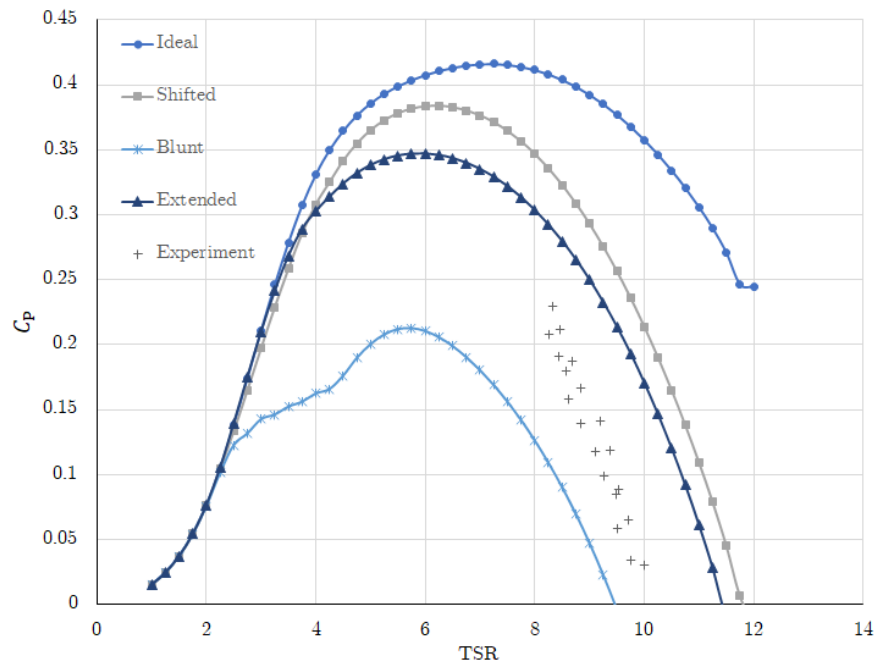
comparable to the ideal case while the remaining two cases result in a huge reduction in C_T . The blunt trailing edge also goes into free-wheeling much earlier than any other case at $TSR = 10$ indicating a severely reduced torque.

The reduction in performance for the shifted case is mainly attributed to the confirmed increase in drag. However, the increase in C_T is small compared to the reduction in C_T . This is due to the small inflow angle at higher TSR. Equations 2.3 and 2.4 dictate that at small inflow angles, thrust is determined by the lift, and reduction to torque force is determined by drag.

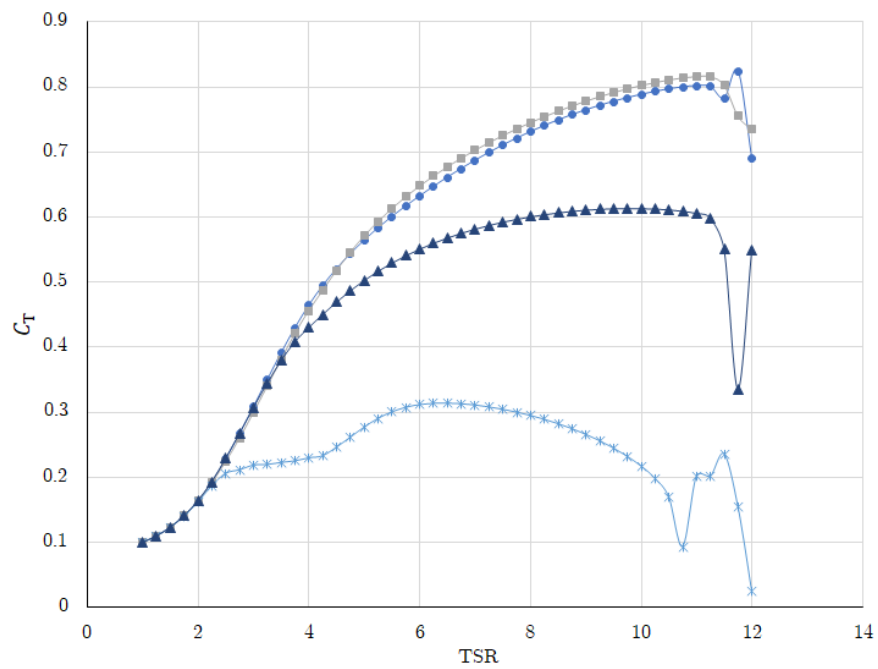
Comparing the simulations to the experimental results, the slope at the latter end of the C_P -TSR graph approaches the slope of the experimental results. However, the difference in simulated and experimental results remain greater than 50%. This may be explained by the rigid blade assumption within BEM. de Arcos [148] developed a BEM-FEM coupled model and showed that C_P can be reduced by 10% if blade deflections are accounted for in a Risøtidal turbine. This is especially true when considering local C_P values near the tip of the blade where most of the deflection occurs. It must be noted that the blade solidity from de Arcos is larger than the designed low-solidity blade.

For a lower solidity blade, Dose [149] noted a reduction of 30-40% reduction in torque for wind turbine rotors. Since loads are expected to be larger in a marine environment, larger deflections leading to severely reduced performance may be expected. At small-scale, the blade deflections of the low-solidity blade was noticeably visible compared to the tested Wortmann FX63137. This implies a need for the use of other materials for small-scale testing, and possibly full-scale implementation.

Experimental Validation and Simulation adjustments



(a) Coefficient of Power



(b) Coefficient of Thrust

Figure 5.16: Turbine Performance for NACA 63-8xx ideal, and 219mm blades with altered trailing edges

Quantifying Blade Deflections

At this time, a static load simulation is performed in SolidWorks to determine the stress and strain developed within the experimental blade. The static load simulation is opted for against heavy CFD simulations, which may come later on as the concept is proven to be technically and economically feasible. The static load shall give an idea of how much deflection is present when the blade is subjected to a steady and static load.

The resulting axial and tangential forces are fitted against r using a 6th order polynomial. This gives an R^2 value of greater than 0.99, implying a good fit. There is no physical explanation in opting for the 6th order polynomial since this is chosen to give the most accurate fit. The polynomial is not used to predict the forces and give an explanation to the trend but rather just to accurately transfer the loads as simulated by BEM to the static simulation in SolidWorks. The 6th order polynomial is also the highest degree polynomial that can be fitted in MS Excel, which is used to post-process data.

All blades were simulated with a rotor diameter of 0.545m (blade length = 219mm) and using a 6061, Plate Aluminium alloy, similar to the aluminium alloy used for testing. The mesh used is the automatically simulated mesh of SolidWorks with default options, with a fixed constraint at the root. This assumes that the connection to the hub is rigid or that the root (smallest r) is directly connected to the hub.

While the deflections are less than 1% of the overall blade length for the given TSRs, the static simulation does lack the fluid effects on the blade and how additional deflection can influence the hydrodynamics of the rotor. During the experiment, the blade was also observed to oscillate between forward and backward oscillation, which may indicate separation of flow and presence of turbulent vortices. Additional simulations may be needed to fully quantify deflections. However, this is placed in future work as the thesis is refocused for the reader, towards developing high-TSR rotors. The next section also shows that these issues may be lessened when the blade is scaled up.

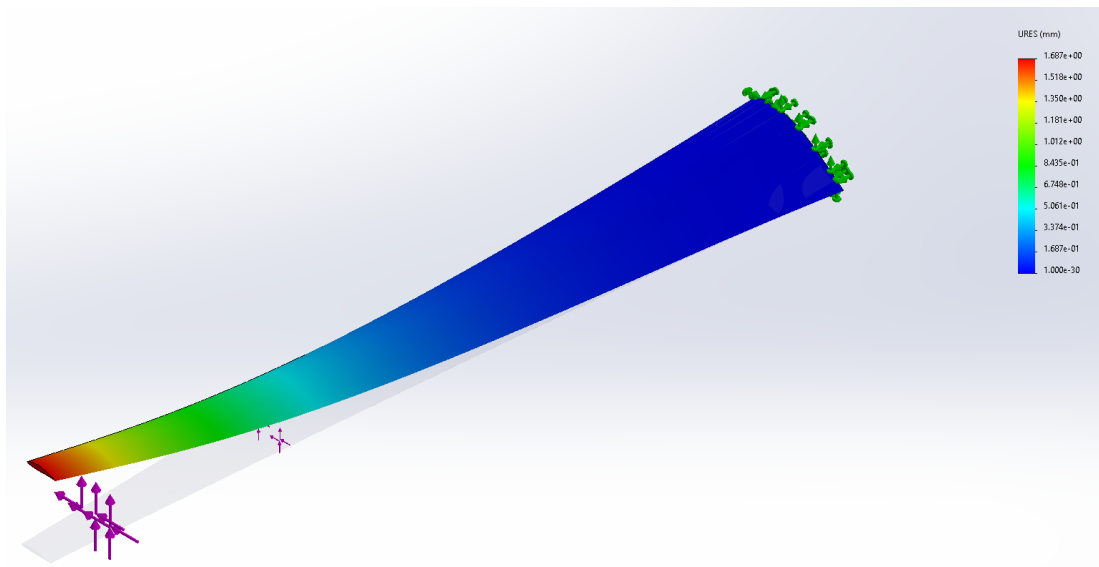


Figure 5.17: Blade deflection at $TSR = 8$

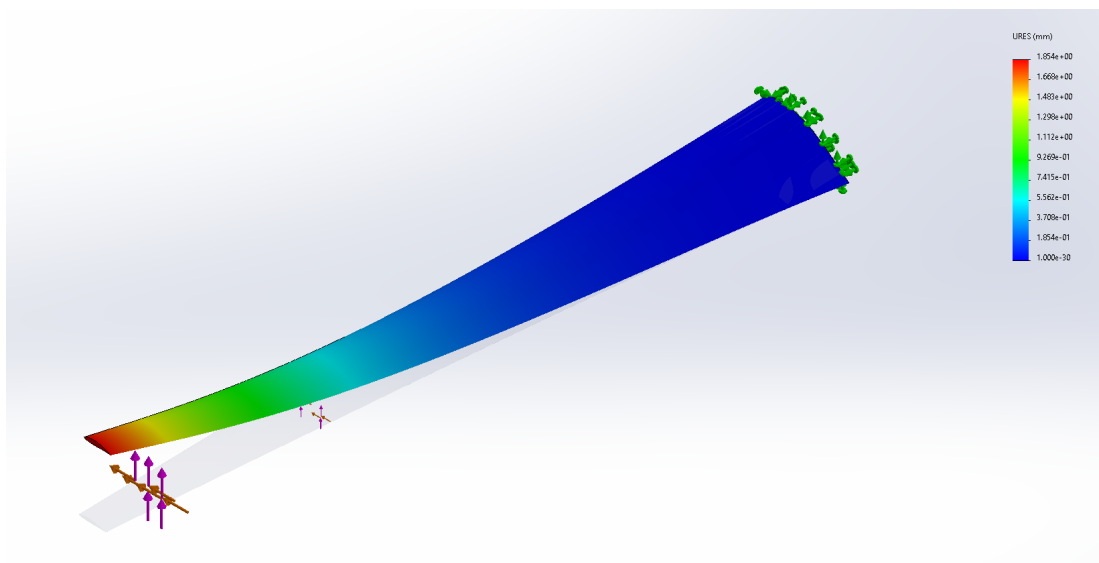


Figure 5.18: Blade deflection at $TSR = 10$. Thrust loads are higher and lead to large deflections.

5.4 Increasing Blade Length

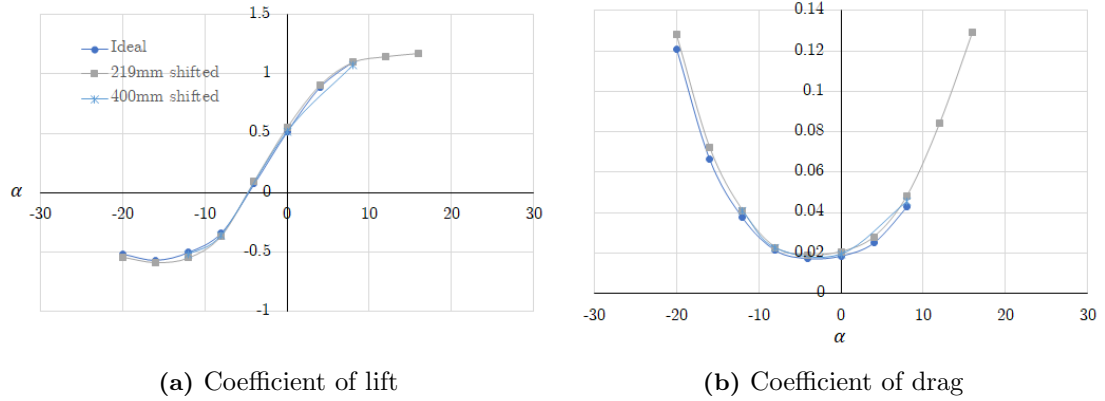


Figure 5.19: Aerodynamic characteristics for NACA 63-824 ideal, 219mm, and 400mm shifted cases ($Re = 5 \times 10^5$)

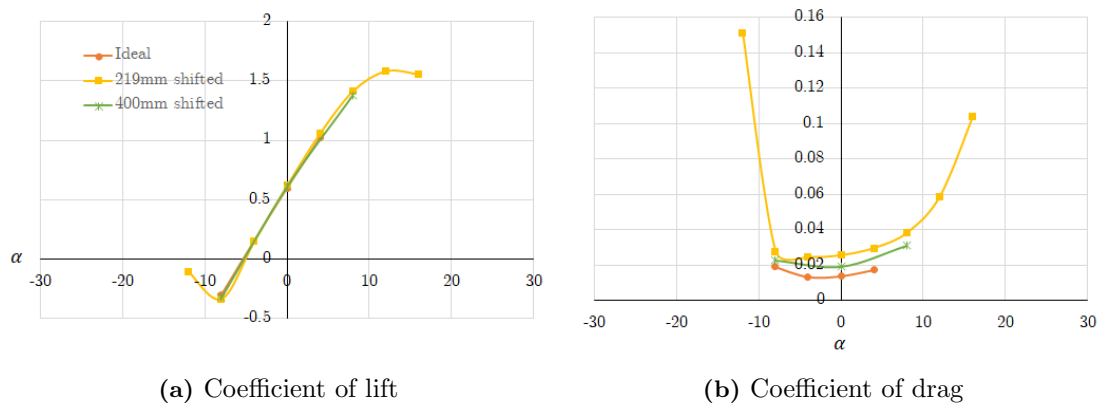


Figure 5.20: Aerodynamic characteristics for NACA 63-812 ideal, 219mm, and 400mm shifted cases ($Re = 5 \times 10^5$)

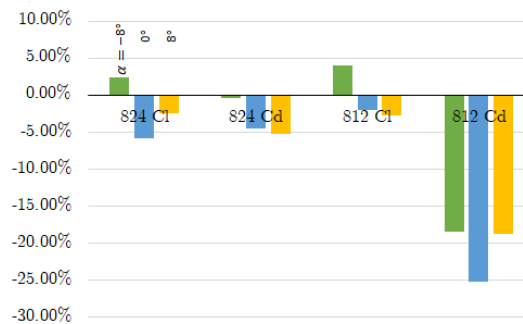
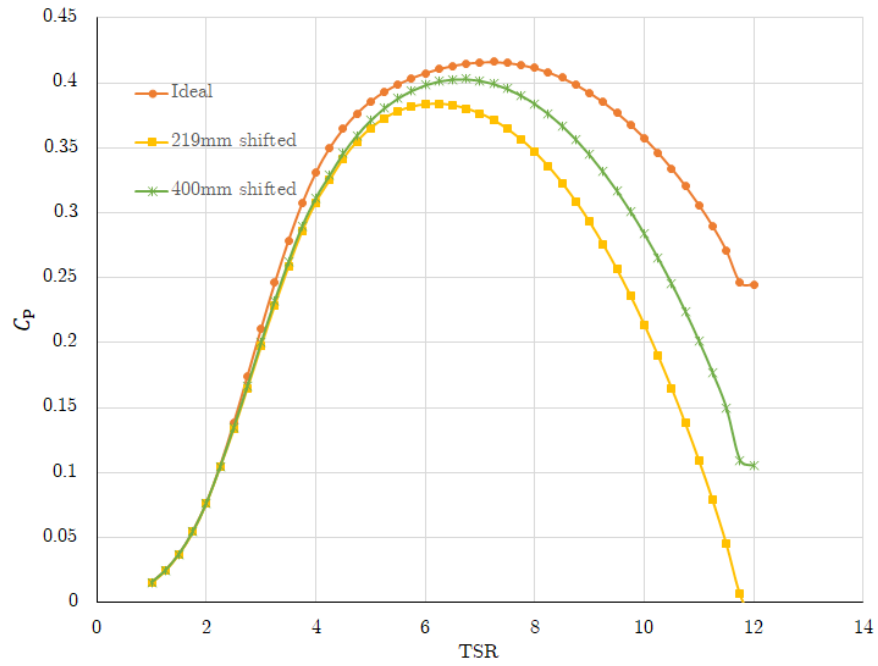
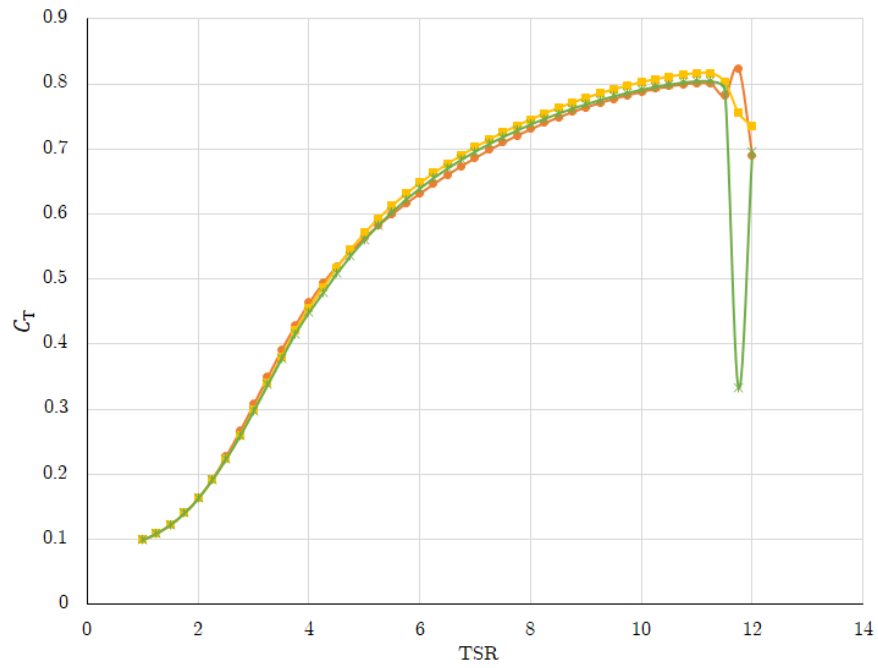


Figure 5.21: XFOIL vs CFD coefficient of pressure for ideal aerofoils

Experimental Validation and Simulation adjustments



(a) Coefficient of Power



(b) Coefficient of Thrust

Figure 5.22: Turbine Performance for NACA 63-8xx ideal, 219mm, and 400mm shifted aerofoil blades

The comparison between the NACA 63-824 and the NACA 63-812 provides a case for increasing blade length. The NACA 63-8xx blade have varying t/C , arranged from root to tip with the root having the largest t/C and decreasing progressively towards the tip. The normalised chord shown in Table 4.4 scale the chord lengths with respect to the radius and thus, increasing blade length also increases the base thickness of each section. This is advantageous since the minimum thickness remains to be 0.5mm no matter the length of the blade. Thus, an additional CFD case was added wherein all points in the suction side were shifted by 0.5mm for a 400mm blade. The decision to opt for a shifted case is discussed in the next section.

Figures 5.19 and 5.20 show the resulting lift and drag compared to the ideal and the previously shifted case at 219mm blade length. Figure 5.21 shows the relative differences between the 219mm scale and the 400mm scale at $\alpha = (-4, 0, 4)$. Drag values are significantly reduced for the NACA 63-812 with minimal difference on lift.

Considering a turbine hub diameter of 200mm, it is possible to have a small-scale 1m diameter rotor and have a better approximation of an ideal turbine. Figure 5.22 also shows that the performance of the ideal blade is approached by the 400mm blade. In real-sites, the performance may be nearer to the ideal aerofoil for the same reason that the 400mm blade length has better performance - the fabrication limit is less of an issue as blade length increases.

5.5 Summary

The chapter presented the results of the small-scale testing of the designed blade. Issues arising from the severely reduced performance of the blades prompted the readjustment of simulation parameters with attempts to explain the deviation in simulated performance. The 0.5mm minimum thickness applied to rotors with larger solidity cannot be directly applied to lower solidity blades since it introduces a large deformation on the aerofoil sections, leading to worse aerodynamic characteristics, and ultimately to reduced hydrodynamic performance.

Further investigation on trailing edge alterations showed that shifting of the points

Experimental Validation and Simulation adjustments

are still the most viable method to accommodate minimum thickness at the trailing edge. With this, it is expected that performance will decrease significantly and thus, it is recommended that small-scale testing be done in a slightly larger scale to limit the possible deviations.

Chapter 6

Parametric investigation using full design space

6.1 Simulations with Full Design Space

Scatter plots provide a simple and direct way to visualise data. In this case, a scatter plot is an effective way to present $C_{P_{\max}}$ and $TSR_{C_{P_{\max}}}$ for each blade configuration.

As mentioned in Section 3.3.1, post-processing the data and formatting the scatterplot is an effective way to see how design variables affect blade performance. Each level of a design variable is coloured and shaped differently to allow for quick and general analysis.

However, graphical formatting of scatterplots may suffer from reduced readability as the number of data points increases. The scatterplots presented in this section show general trends in the effects of each design variable. A thorough discussion is presented in the succeeding sections (Section 6.2).

6.1.1 NACA 63-8xx Rotor

Figures 6.1 to 6.5 show the results of the NACA simulations grouped by each design variable. In general, the Pareto frontier running along the top-right of the scatterplot indicates a trade-off between $C_{P_{\max}}$ and $TSR_{C_{P_{\max}}}$. A weighted decision matrix as discussed in Section 4.3 was used to select a final design among the blade configurations within the Pareto frontier.

Figure 6.6 provides a summary of the effects of each design variable.

Parametric investigation using full design space

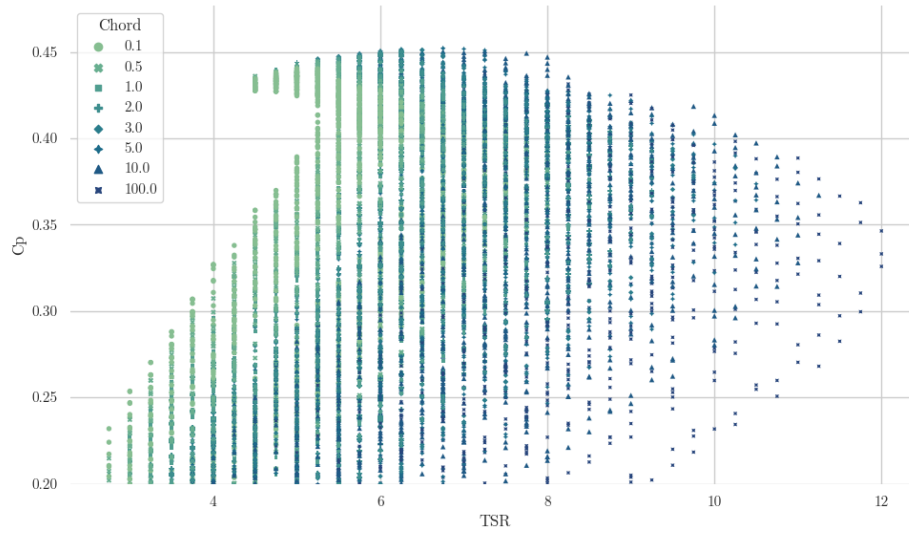


Figure 6.1: NACA simulation results grouped by chord distribution. It can be observed that increasing values of Γ_{chord} push $TSR_{C_{P_{\max}}}$ towards higher values while slightly reducing $C_{P_{\max}}$.

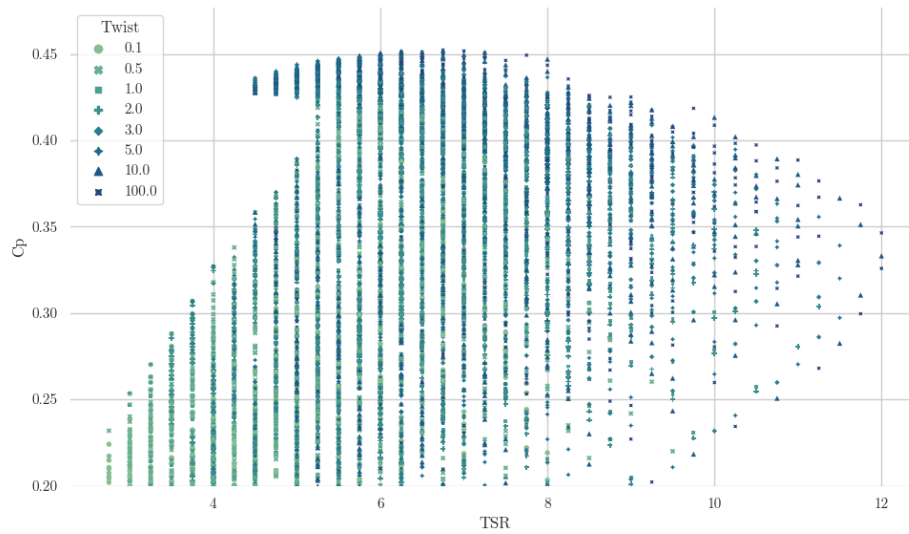


Figure 6.2: NACA simulation results grouped by twist distribution. It can be observed that increasing values of Γ_{twist} push both $C_{P_{\max}}$ and $TSR_{C_{P_{\max}}}$ towards higher values. However, the distinction between different levels is not as apparent compared to the results when grouped by chord distribution.

Parametric investigation using full design space

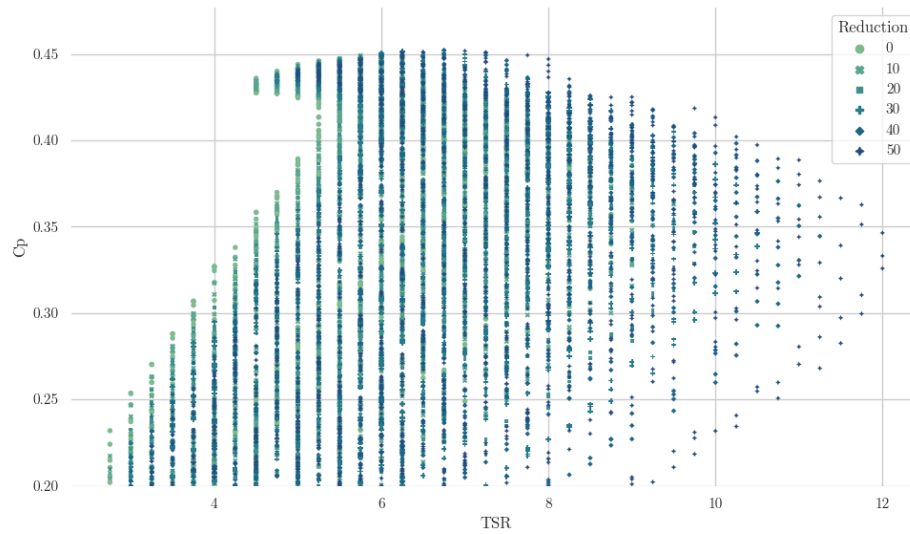


Figure 6.3: NACA simulation results grouped by chord reduction. A general trend cannot be established as values of $C_{P_{max}}$ and $TSR_{C_{P_{max}}}$ are well-spread. It can be noted, however, that only blades with a chord reduction of 30% or higher results in $TSR_{C_{P_{max}}} > 10$.

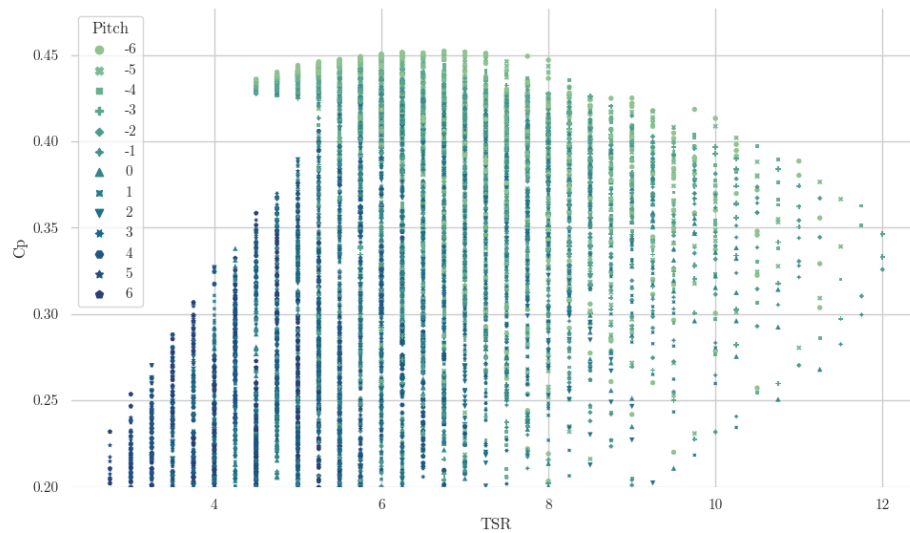


Figure 6.4: NACA simulation results grouped by blade pitch. The same trend from grouping the results by twist distribution can be observed in the plot. Both $C_{P_{max}}$ and $TSR_{C_{P_{max}}}$ increases as the pitch is altered - the values of the objectives increase as the pitch is reduced. Additionally, there seems to be a clearer distinction between results using different values of pitch.

Parametric investigation using full design space

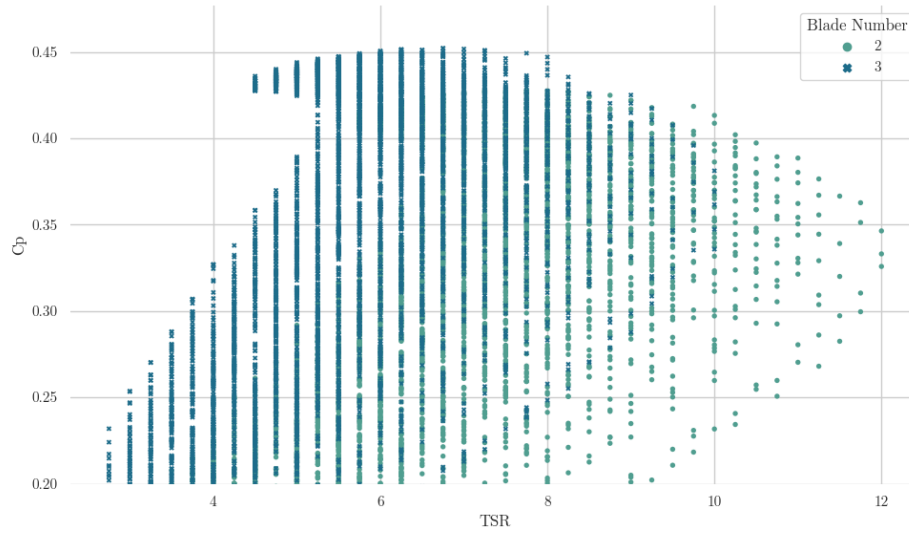


Figure 6.5: NACA simulation results grouped by blade number. There is a clear distinction of performance given a specific blade number with the high- TSR region dominated and almost exclusive to 2-bladed rotors and the low- TSR region for 3-bladed rotors. This can be due to the design variable only having two levels but is still sufficient to inform on suitable blade configurations for the proposed high- TSR blades.

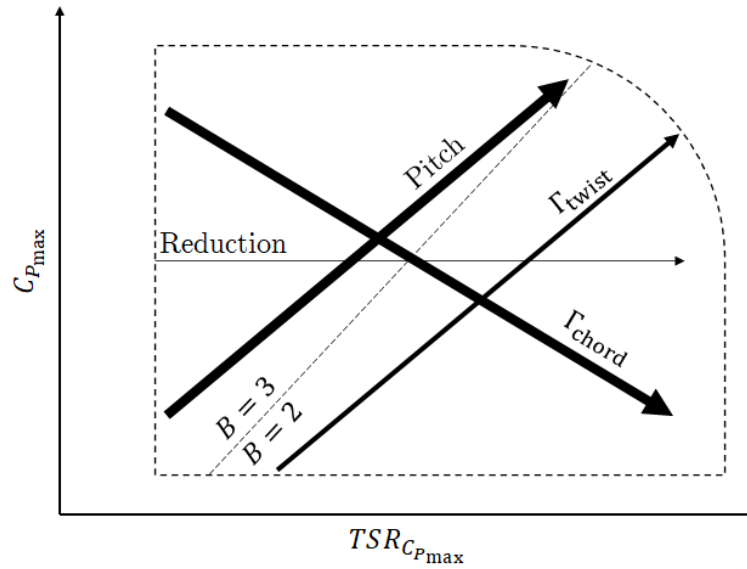


Figure 6.6: Summary effects of design variables on NACA rotor performance. Darker lines indicate more apparent effects. The effect of blade number is shown as two distinct regions.

The increase in the value of $TSR_{C_{P_{max}}}$ as solidity decreases ($\uparrow \Gamma_{chord}, \uparrow chord$)

Parametric investigation using full design space

reduction, ↓ blade number) follows the trend discussed in the literature [54]. Both the twist distribution and pitch setting should be adjusted to align the flow and achieve optimum angle of attack and achieve optimal performance.

As the angular velocity increases, the total inflow angle, ϕ , decreases and moves towards the plane of rotation at $\theta_{\text{root}} = 0$. Thus, reducing the pitch and twist of each section can counteract the reduction in ϕ and maintain optimal α . This is also why blades are feathered towards the tip - the tangential velocity increases as one approaches the blade tip.

6.1.2 Wortmann FX63137 Rotor

Figures 6.7 to 6.11 show the results of the Wortmann simulations grouped by each design variable. The Pareto Frontier for the Wortmann is not well-defined. This may be due to the base Wortmann blade having much greater solidity compared to the base NACA blade. This results in all blade configurations using the rapid blade alteration methodology still having large solidity values and not all possible TSR regions are populated.

Nonetheless, the results show several blade configurations operating optimally at almost double the $TSR_{C_{P_{\max}}}$ of the base blade. A weighted decision matrix was also used to select a final blade since there still exist a small number of non-dominated solutions.

Similar to the discussion in the preceding section for the NACA rotor, Figure 6.12 provides a summary of effects for each design variable on the values of $C_{P_{\max}}$ and $TSR_{C_{P_{\max}}}$.

Parametric investigation using full design space

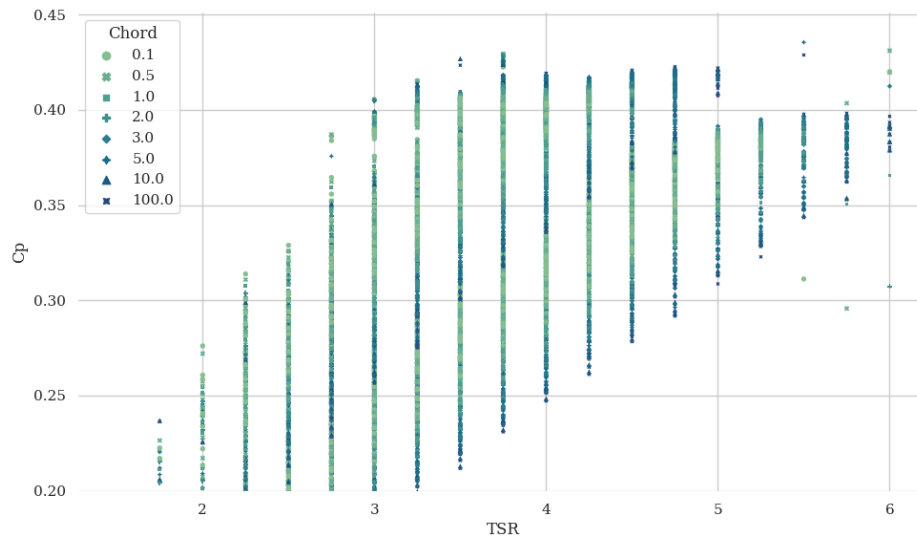


Figure 6.7: Wortmann simulation results grouped by chord distribution. The trend for $C_{P_{\max}}$ and $TSR_{C_{P_{\max}}}$ appears to be bimodal. The trend from Figure 6.1 is carried over for each set.

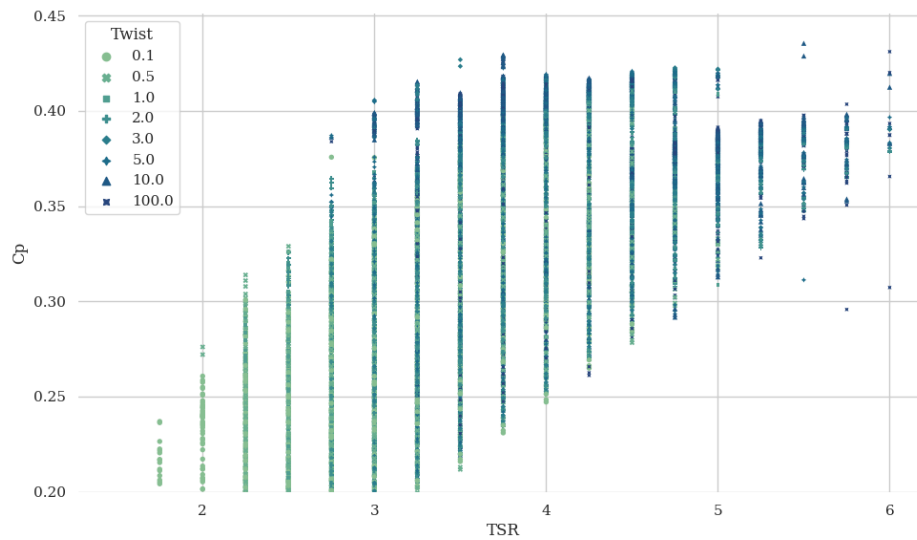


Figure 6.8: Wortmann simulation results grouped by twist distribution. The same trend from Figure 6.2 can be observed. However, a clearer distinction can be seen. This is explained by the narrower TSR range - this makes the result appear to be more densely packed.

Parametric investigation using full design space

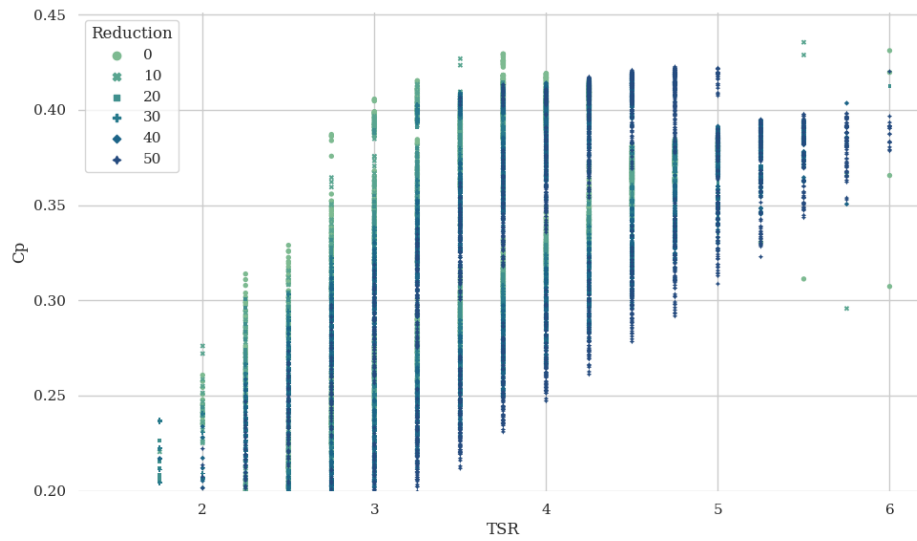


Figure 6.9: Wortmann simulation results grouped by chord reduction. Reducing the chord length still results in pushing $TSR_{C_{P_{max}}}$ towards higher values. However, there seems to have no effect on how $C_{P_{max}}$ is distributed for every TSR .

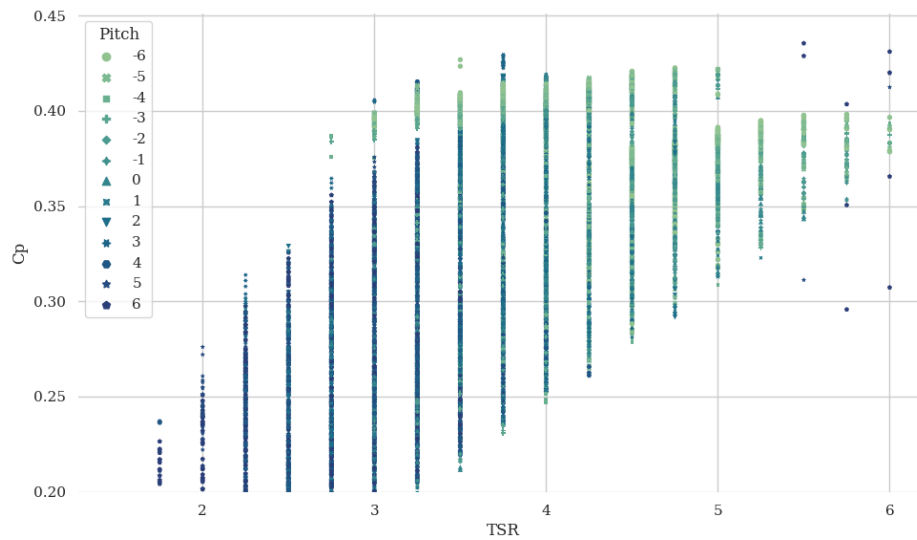


Figure 6.10: Wortmann simulation results grouped by pitch. The trend from Figure 6.4 is also observed.

Parametric investigation using full design space

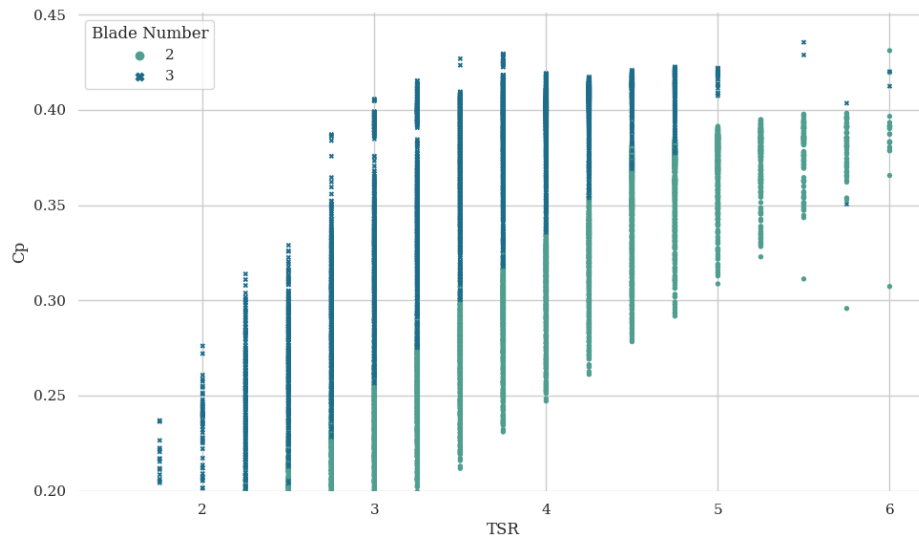


Figure 6.11: Wortmann simulation results grouped by blade number. There seems to be a clear cut between two regions of performance. The same reasoning from Figure 6.5 can be made. Additionally, the narrow range in TSR may explain the strong distinction between 2-bladed and 3-bladed performance.

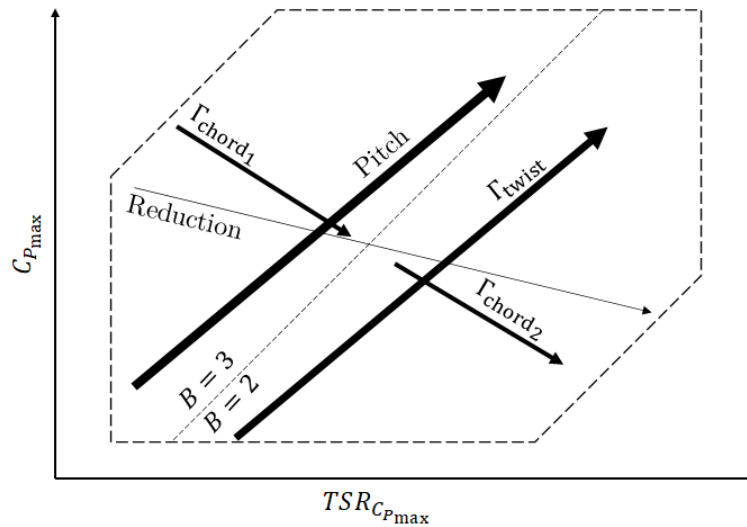


Figure 6.12: Summary effects of design variables on Wortmann rotor performance. Darker lines indicate more apparent effects. The effect of blade number is shown as two distinct regions.

The bimodal behaviour in Figure 6.7 can be explained by the strong distinction between 2-bladed and 3-bladed performance as shown in Figure 6.11. This is supported

Parametric investigation using full design space

by the observation that the line at which the performance goes back to being dominated by Γ_{chord} coincides with the line separating the performance of the 2-bladed and 3-bladed configurations. Additionally, all parameters affecting solidity has the same line although there it may easily be overlooked in Figure 6.9.

The solidity of the base Wortmann blade is larger compared to the NACA blade. As such, reducing the number of blades from 3 to 2 results in a huge drop in solidity compared to altering just the chord distribution or introducing chord reduction.

6.1.3 Finalising candidate blades

Sensitivity to Decision Weights

A weight sensitivity analysis was performed wherein weights are varied to test for possible scenarios wherein one objective should be prioritised more than the other. The same was applied when integrating thrust as an objective ¹.

Weight sensitivity in literature [150–154] is usually employed by changing the weights of a criterion and solving for the weights of other criteria using an objective function. The set of decision weights are called decision vectors and all weights are set to equal to 1 (Equation 4.4). A simplified method was adopted wherein decision weights were defined with distinct and discrete values for each criterion. Figure 6.13 shows the values considered for the decision space totalling 22 decision scenarios.

The candidate blades were filtered down using a base scenario defined with decision weights of 0.5 and 0.5 for C_P and $TSR_{C_{P\max}}$ respectively. The top 10 candidate blades were considered for further analysis via weight sensitivity. Choosing the top 10 blades with the base weighting scenario ensures that all the blades considered for weight sensitivity are within the knee-cap decision point² as used by Gu [155] and Sun [156].

The average rank for each solution was obtained and the lowest value was adopted as the final candidate blade (1 is best).

¹The two-objective problem can be assumed to be a three-objective problem with the third objective (C_T) having a weight of zero.

²The knee-cap decision point here is defined as the alternative that gives a proper trade-off between the two parameters. Using normalised values from Section 4.3.2. This is the maximum utility point for an equal weight scenario.

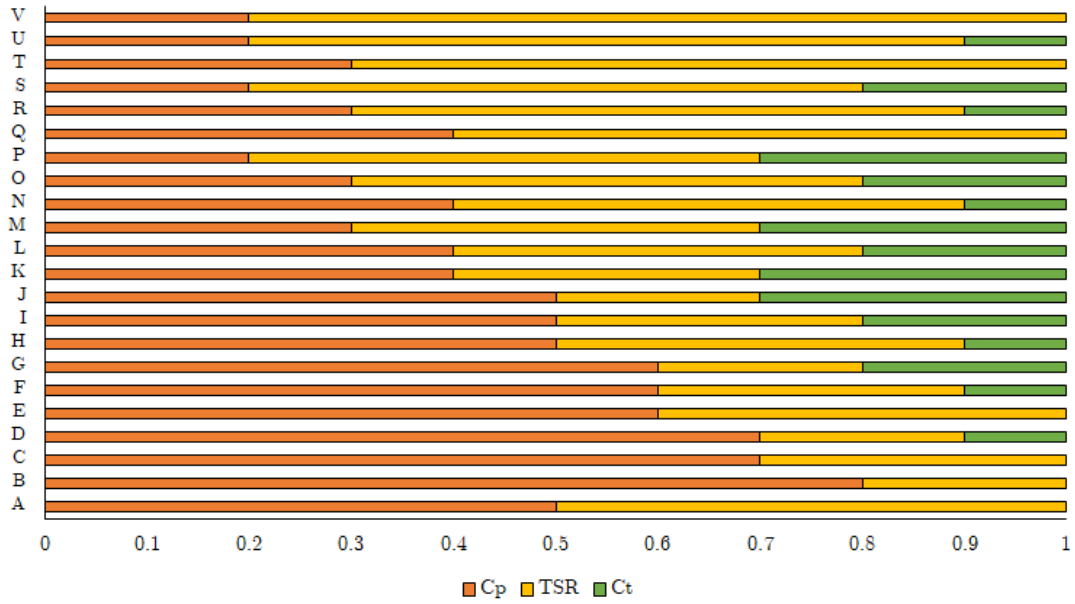


Figure 6.13: Decision Scenarios. The figure above shows the sum of all the weights for each decision scenario. Several scenarios have weights for C_T set to 0.

Issues on Cavitation

As have been discussed, wind turbines operate at higher TSRs compared to tidal turbines. Ning and Dykes [157] further analysed the benefits of pushing the benefits of increasing the tip-speed of wind turbines and found that higher TSR operation can lead to a 5.4% reduction in COE. Chapter 8 shows that this benefit is magnified in the case of tidal turbines due to the exponential³ relationship between cost, weight, and generator rotational speed.

However, pushing the optimal operation point of tidal turbines towards higher TSRs increases the risk of cavitation, which severely limits the operation of tidal turbines in existing sites. Cavitation occurs due to pressure drops beyond the vapourisation pressure of the working fluid e.g. seawater. Large pressure drops can overcome bonding forces of the liquid, leading to a transition from liquid to vapour. This phenomenon causes significant blade erosion and reduces performance as well as maintenance frequency.

³The relationship is dictated by an exponential decay function

The DNV GL guideline (DNV GL-ST-0164) [158] on designing tidal turbines states that cavitation can be avoided by proper blade selection and/or limiting tip-speed ratio. This thesis goes against this guideline by deliberately trying to push operation towards higher TSRs.

As it is, maintenance in existing sites requires large specialised vessels due to heavy components and strong current flows. The foregoing blade designs allow reduced component weight and the weaker currents allow for the use of less specialised vessels. Additionally, the total relative velocity of the blade in less energetic current may be comparable to the relative velocity when the blade is operating in stronger currents - and thus cavitation may still be manageable albeit still an important consideration.

Cavitation is then incorporated in the final selection by selecting multiple blade designs that operate at different TSRs. Chapter 8 then discusses the different benefits and added costs should higher TSR blades be adopted for less energetic environments while keeping in mind the issue on cavitation. Cavitation may not necessarily be avoided but it can be incorporated in COE calculations as well as management schedules.

The tip-speed ratios are selected as: (a) $TSR \leq 12$, (b) $TSR \leq 10$, and (c) $TSR \leq 8$. The first cut of $TSR=8$ for the NACA 63-8xx turbine follows the findings of Murray [159] for an 800mm diameter NACA 63-8xx model turbine where the first onset of cavitation ($\sigma/\sigma_{crit} = 1$) is at $TSR < 8$.

The Wortmann FX63137 turbine does not exceed $TSR \leq 7$ and thus, the method of selecting blades at different TSRs is not necessary.

NACA 63-8xx Rotor. The results for all cases can easily be discernible (darker are better) and are summarised in Tables 6.3 and 6.1. Limiting the TSR towards lower values shortens the Pareto frontier. Using the base scenario (Scenario A: equal weight of 0.5 for $C_{P_{max}}$ and $TSR_{C_{P_{max}}}$) caps the utility value for $TSR_{C_{P_{max}}}$. Thus, compared to the results using the full TSR range, there appears to be a clear best for $TSR \leq 8,10$.

Figure 6.14 shows that limiting the TSR towards lower values also affect the number

Parametric investigation using full design space

of solutions within the localised Pareto frontier. This results in less non-dominated solutions and the selected final blade have $TSR_{C_{Pmax}}$ values equivalent to 10 and 8 (maximum TSR within the reduced TSR range).

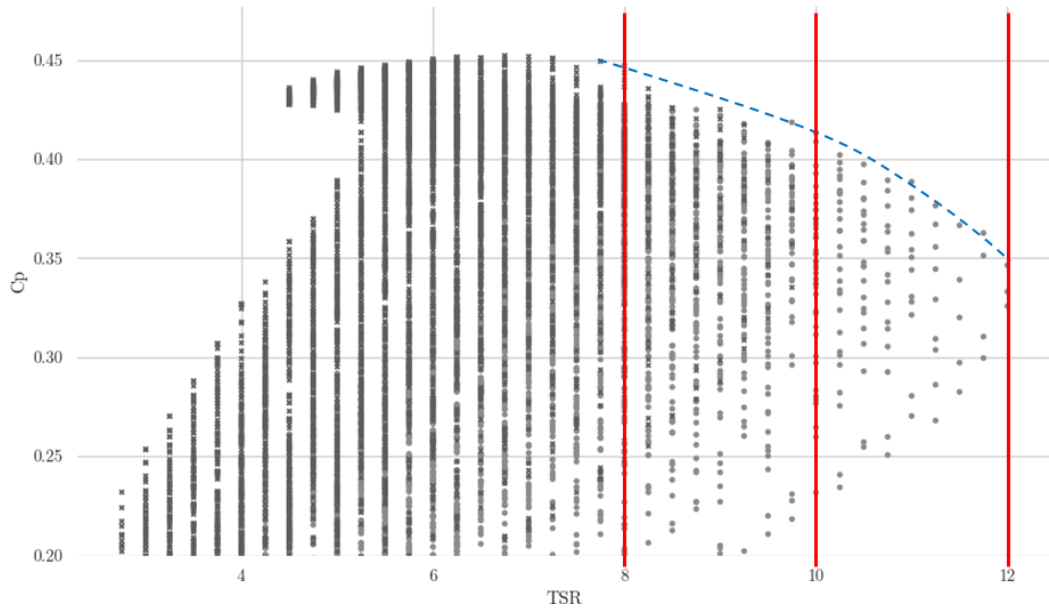


Figure 6.14: TSR cuts for different TSR operating points

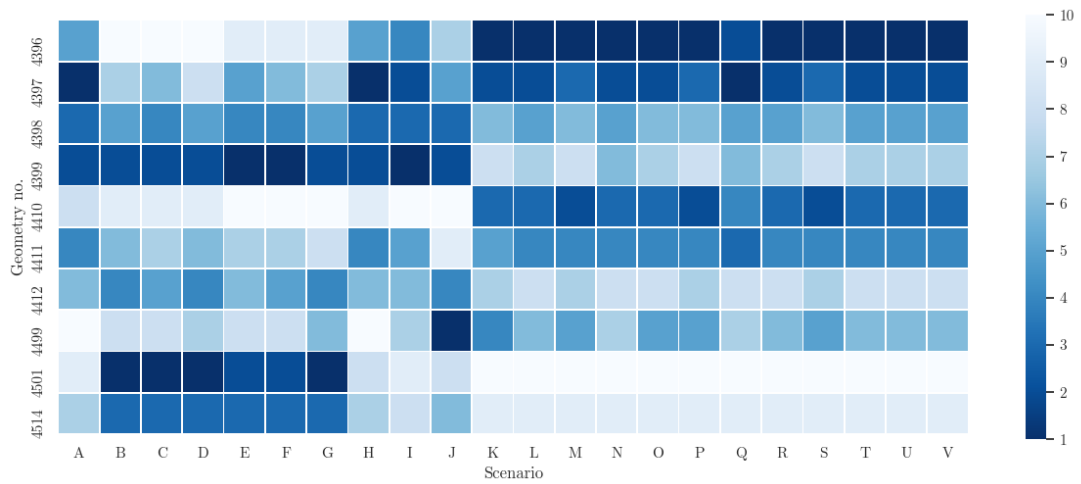


Figure 6.15: Optimal NACA 63-8xx for full the TSR range

Parametric investigation using full design space

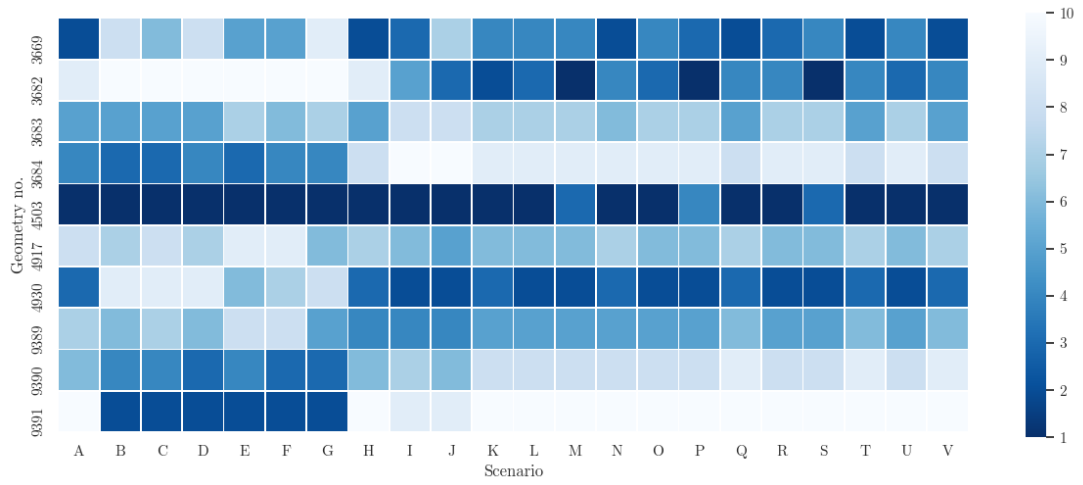


Figure 6.16: Optimal NACA 63-8xx for $TSR \leq 10$

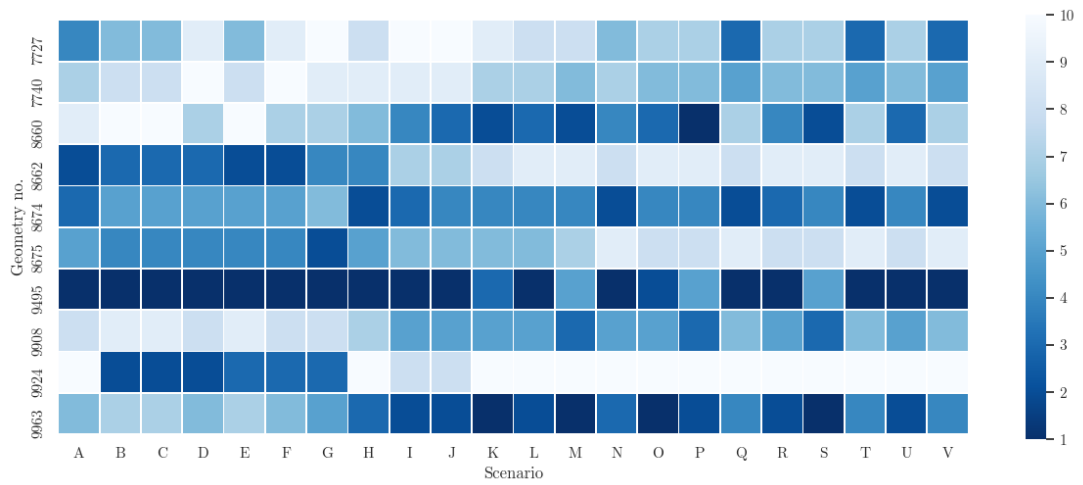


Figure 6.17: Optimal NACA 63-8xx for $TSR \leq 8$

Parametric investigation using full design space

Table 6.1: Summary NACA optimisation (Chord and Twist Distribution)

ID	4396		4503 & 9495	
	$\theta_t(^{\circ})$	c/R	θ_t	c/R
0.20	17	0.1	14	0.1
0.30	8.674	0.0314	5.674	0.067
0.40	5.641	0.0279	2.641	0.0504
0.50	4.267	0.0267	1.267	0.0416
0.60	3.481	0.0261	0.481	0.0359
0.70	2.975	0.0257	-0.025	0.0322
0.80	2.587	0.0254	-0.413	0.0294
0.90	2.27	0.0252	-0.73	0.027
1.00	2	0.025	-1	0.025

θ_t is the total section twist equal to $\theta_t = \theta_s + \theta_p$
r/R and c/R are normalised values using R = 1m

Wortmann FX63137 Rotor. The blade geometry of the final candidate blade for the Wortmann FX63137 is shown in Table 6.2.

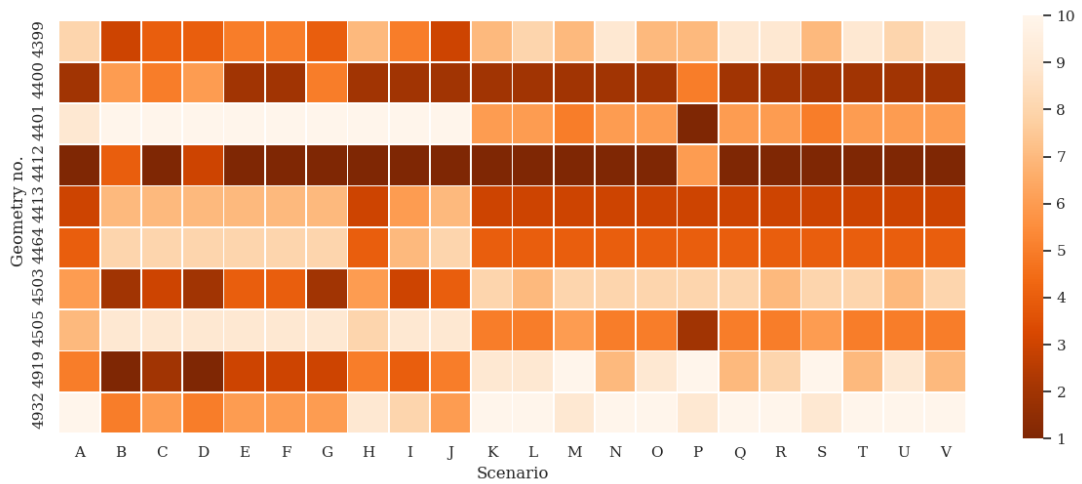


Figure 6.18: Optimal Wortmann FX63137

Table 6.2: Wortmann optimisation (Chord and Twist Distribution)

ID	4412		
	r/R	$\theta_t(^{\circ})$	c/R
0.229		21	0.1296
0.305		16.447	0.1635
0.382		13.219	0.1780
0.459		10.794	0.1521
0.536		8.883	0.1325
0.615		7.277	0.1165
0.692		5.955	0.1035
0.768		4.805	0.0923
0.845		3.783	0.0825
0.922		2.859	0.0736
1		2	0.0655

θ_t is the total section twist equal to $\theta_t = \theta_s + \theta_p$
 r/R and c/R are normalised values using $R = 1\text{m}$

Table 6.3: Summary of optimisation (Design Variables and TSR)

Blade ID	NACA			Wortmann
	4396	4503	9495	4412
Blade number	2	2	3	2
Γ_{chord}	100	10	10	100
Γ_{twist}	100	100	100	10
Root Pitch	-3°	-6°	-6°	2°
Chord Reduction	50%	50%	50%	50%
TSR	12	9.75	7.75	5.75
σ_s	0.0092	0.012	0.012	0.025

σ_s for base NACA [1] = 0.035, σ_s for base Wortmann [2] = 0.045

Recalling from Section 4.2.2, it was discussed that it is expected that the NACA rotor would lead to higher TSR due to the peakedness of the C_L/C_D trend compared to that of the Wortmann rotor. The results confirm this finding as the increase in operational TSR for the Wortmann is only from 3.75 to 5.75 (6 max) while the NACA was able to reach an operational TSR of 12.

6.2 Parameter Sensitivity

Chapter 3 discussed the benefits of parametrising the blade design as opposed to the usual approach used in Genetic Algorithm optimisation routines involving the use of discrete points to define distributions. The use of the parametric design also allows for establishing the relationship between rotor performance and the general blade geometry. Essentially, these relationships have been the subject of studies quantifying the effects of solidity [54, 123, 124], feathering [2, 50], etc.

This section attempts to quantify the effects of each design parameter related to the physical quantities of solidity and feathering as listed in Table 3.2. The sensitivity analysis presented allows for identifying which variables significantly affect the performance of the blade.

6.2.1 Sobol and Morris Methods of Sensitivity Analysis

Sensitivity analysis is usually employed for uncertainty quantification⁴ and model simplification, especially for models that have numerous inputs e.g. > 20 factors. The information provided by sensitivity analysis allows for the elimination of variables that have little to no effect on the outputs.

Sensitivity analysis in the turbine industry is usually employed for cost, and mechanical loading, which is also a main driver of cost. For load quantification, Rinker [160] used the Sobol sensitivity to analyse the response of wind turbines to turbulence parameters. Velarde [161] used regression of Monte Carlo simulations and Morris sensitivity to quantify foundation fatigue loads of an offshore wind turbine. Nevalainen [162] used the Morris sensitivity to identify influential parameters in the loading of a tidal turbine.

The actual operation of turbines in the real world involves dealing with stochastic environmental variables making it difficult to accurately predict how turbines may be affected. Thus, sensitivity analysis helps in determining the variables that must be

⁴Uncertainty quantification is a field of study that aims to determine the likelihood of outcomes given a limited set of information about a system.

Parametric investigation using full design space

considered and studied in-depth as opposed to other variables that have less of an impact.

There are multiple methods of sensitivity analysis with different costs and benefits. Two methods are applied here - the Sobol variance-based method and the Morris randomised one-at-a-time method. These are both global sensitivity analysis methods capable of exploring the whole input space as opposed to local sensitivity that investigates small changes in the input parameters [163]. In this thesis, the input space⁵ is predefined by the author according to the observed values of Γ from Section 4.1 and parameter alterations from literature, most of which are presented in Chapters 3 and 4.

Both methods are available in Python using the open-source SALib [164] package. The package is being used to develop projects in the field of chemistry, physiology, building energy analysis, exploratory modelling, and decision making. A list of projects that use the package is listed on the SALib project website. The implementation of the package in Python is deemed adequate for the identification of influential variables subject to additional post-processing of the results presented in Section 6.1.

Elementary Effects by Morris

Sensitivity by the Morris method [165] is determined by calculating the *elementary effect* (EE) of a parameter. For k number of parameters with a change in the i^{th} parameter, the EE is given by:

$$EE_i(x) = \frac{y(x_1, x_2, \dots, x_{i-1}, x_i + \Delta, x_{i+1}, \dots, x_k) - y(x)}{\Delta} \quad (6.1)$$

The above equation is similar to the limit definition of the derivative of a function $f(x)$ for a specific x . The two are essentially the same as the EE calculates the changes in the output for every change in the input.⁶

The Morris method is a randomised one-at-a-time (OAT) method. Traditional OAT

⁵It is to be noted that all the possible values for each parameter e.g. $\Gamma = 3.5674$ was not used. However, the parametrisation allows for the exploration of multiple areas of the input space.

⁶The derivative calculates the amount of change in $f(x)$ for every change in x .

Parametric investigation using full design space

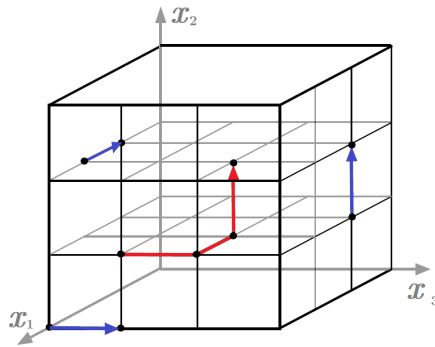


Figure 6.19: Morris Method input space for 3 variables, $k = 3$. If traditional one-at-a-time is adopted, the model needs to be evaluated 6 times to get one elementary effect (blue lines, black dots represent model evaluations). The Morris method reduces the number of model evaluations to 4 or $2(k - 1)$ (red line). Adapted from Nevalainen [59].

involves changing the value of one variable while holding all other variables constant.

This leads to two problems:

- The minimum model evaluations needed to evaluate an EE is $2k$ as shown in Figure 6.19.
- Accounting for interaction effects as to how each additional level in parameter x_1 affects the EE of parameter x_2 increases the number of evaluations needed. Letting all other parameters except the one being examined stay at base value decreases accuracy exponentially [163].

The Morris method overcomes these by creating a random trajectory that goes through the whole input space. An N number of trajectories are evaluated to get sensitivities within different regions of the input space.

The sensitivity indices in the Morris method are:

- μ^* - the absolute mean value wherein higher values of μ^* indicate that the model output changes significantly according to changes of x_i .
- σ - the standard deviation of μ^* wherein high values of σ indicate non-linearities and interaction effects.

Parametric investigation using full design space

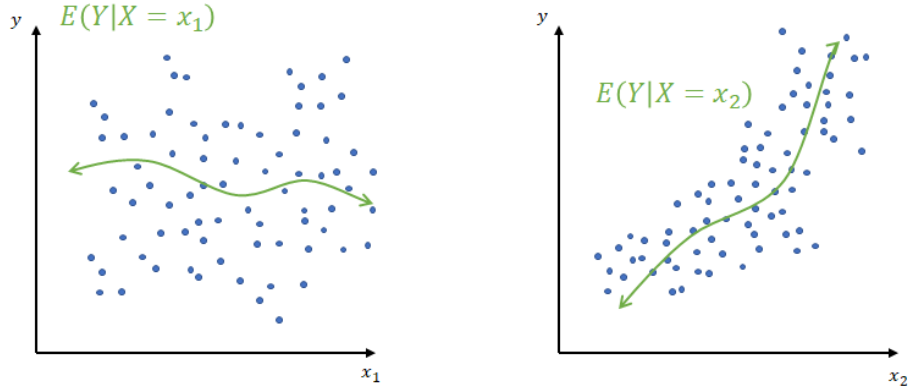


Figure 6.20: Comparison between significant (right) and less significant (left) variable according to Sobol sensitivity. The more significant variable has data points that are less spread out within the line of $E(Y|X = x_2)$. This means that most of the variance of the expected output $Var[E(Y)]$ can be greatly attributed to the change in $X = x_2$.

Variance-based Sobol

Variance-based methods in sensitivity analysis quantify the contribution of an input parameter to the total variance of the output. Figure 6.20 shows a representation of how a more influential parameter x_2 affects the model output.

The variation in the expected value E of output Y given the variation in the i^{th} parameter x_i from K number of parameters is divided by the total variation of Y :

$$\frac{Var[E(Y|x_i)]}{Var(Y)} \quad (6.2)$$

This gives the contribution of x_k to the total variation. Further illustrating this, any model output can be expressed as a sum of effects, including interaction, dictated by all the parameters X :

$$Y = f(X) = f_0 + \sum_{i=1}^K f_i(x_i) + \sum_{1 \leq i < i' \leq K} f_{i,i'}(x_i, x_{i'}) + \dots + f_{1,2,\dots,K}(x_1, x_2, \dots, x_K) \quad (6.3)$$

where i' is an additional parameter considered to quantify interaction effects between the i^{th} and i'^{th} parameters. The final part of the expression quantifies higher-order interaction involving more parameters from x_1 to x_K .

Parametric investigation using full design space

Getting the variances of each term

$$D_i = \text{Var}[E(Y|x_i)] \quad (6.4)$$

$$\text{Var}(Y) = \sum_{i=1}^K D_i + \sum_{1 \leq i \leq i' \leq K} D_{i,i'} + \dots + D_{1,2,\dots,K} \quad (6.5)$$

where the variance of f_0 is zero and the terms in Equation 6.5 can be written as partial variances as in Equation 6.2

$$S_i = \frac{D_i}{\text{Var}(Y)} \quad (6.6)$$

$$S_{i,i'} = \frac{D_{i,i'}}{\text{Var}(Y)} \quad (6.7)$$

⋮

$$S_{1,2,\dots,K} = \frac{D_{1,2,\dots,K}}{\text{Var}(Y)} \quad (6.8)$$

The above expressions are the Sobol Indices used to quantify the most influential parameter.

In theory, the sum of all the Sobol Indices should equal 1. However, Equation 6.5 is an approximation and is usual to get summation values that are not equal to 1. Such cases indicate high interaction effects and result from the non-linearity of the model. The BEM model is one such non-linear model and thus, one can expect the sum of variations to be more than one [166].

The sensitivity indices in this method are:

- S^1 - First order Sobol Index. This describes the sole contribution of the i^{th} parameter to the output variance without interaction effects from other parameters.
- S^T - Total order Sobol Index. This describes the total contribution of the i^{th} parameter to the output variance including interaction effects from other variables.
- S^n - n^{th} order Sobol Index. This describes the variance contribution of $n(n > 1)$

Parametric investigation using full design space

number of parameters considered. The number of samples needed for increasing n is determined by $N(nk + 2)$ [164].

6.2.2 Setup and Results of Sensitivity Analysis

The number of samples needed for both Sobol and Morris sensitivity analyses varies depending on the complexity of the model. For Sobol, the samples needed may range from a few thousand to a couple million. There is no set rule of thumb on the value of N that is sufficient for an accurate estimate of sensitivity indices. Considering this, a sample-independence study was undertaken wherein the number of samples (Sobol) or trajectories (Morris) was altered. This shows how each sensitivity index moves when the number of samples/trajectories is varied. This has been the approach of Gan [167] to determine the number of samples. The same has been discussed in Waterprogramming, the community website made by SALib makers [168].

The full sample space considering both the NACA 63-8xx and the Wortmann FX63137 is sufficient for a Sobol analysis with $N = 1000$ and a subset of this data considering only one aerofoil is sufficient for $N = 800$. The method of sampling is specific for each method with the Morris method having a random sampling of trajectories, each generated without replication. The Sobol sequence is implemented in SALib to identify samples. The Sobol sequence ensures that the sample space is adequately and uniformly sampled as compared to truly random brute force sampling (Figure 6.21). In the case of the design space, the Sobol sequence ensures that each parametric combination is sure to be sampled at least once.

As discussed, the Sobol method is computationally expensive due to the number of sample points needed to get the indices. Considering the parameters and $N = 800$, the total samples needed is equal to 9600. This means that the BEM model needs to run 9600 times.⁷ Running a sample independence Sobol study with increasing values of N will further increase the computational load when running with BEM. The same is true for the Morris method considering the pre-defined input space.

⁷It is possible to use parallel computing to reduce the required computational time.

Parametric investigation using full design space

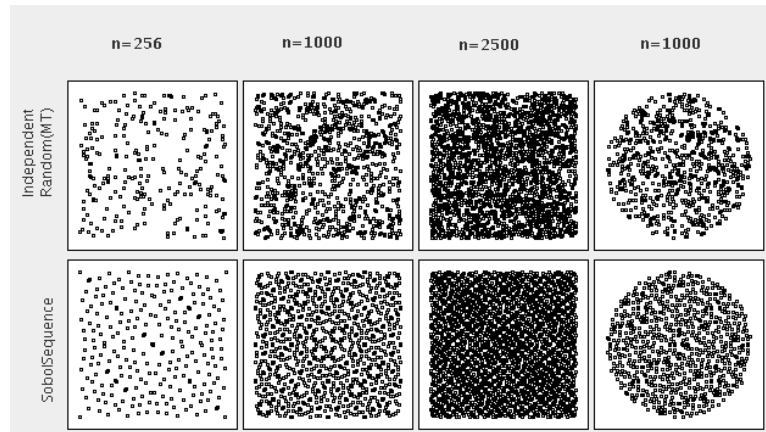


Figure 6.21: Comparison of Independent Random Sampling and Sobol Sequence Sampling. Sobol Sampling results in better coverage within the input space at all values of n . The samples are more equally spaced. Adapted from Apache Commons [Math].

Thus, as presented here, the BEM simulations were run first and stored in a lookup table to be analysed using both Sobol and Morris methods. This posed two challenges:

- Sobol sampling results in a uniform distribution within the sampling space. This is the main advantage of the sampling method but poses a challenge in dealing with discrete variables such as the ones used in the blade design methodology. This has been remedied by setting up proxy variables that have ranges of $(0, L - 1)$ where L is the number of levels each design parameter was defined with (Table 3.3). The samples are then rounded off and the design parameters are coded as categorical variables with values of $(0, L - 1) \in \mathbb{Z}$. This has been the method proposed by Baroni and Tarantola [169] and discussed in SALib (Waterprogramming notes) [168].
- The Morris sampling is usually employed using even and symmetric levels for each variable. The design parameters have unequal levels and while Morris [165] mentions the possibility of analysing an asymmetrical sample space, it is deemed appropriate to cut the input space into a size where the Morris sensitivity analysis can be applied directly. This gives as much valuable information regarding the input parameters with $L = 6$. Additionally, the blade number variable is dropped and a case study for 3-bladed and 2-bladed designs was run. The other design

Parametric investigation using full design space

parameters are coded as categorical variables with values of $(0, 5) \in \mathbb{Z}$.

The inclusion of the blade number variable is driven by the objective to push operation towards higher TSR. The non-inclusion of the variable in the Morris sensitivity, although still included in the Sobol sensitivity, does not affect the objectives of the thesis since comparison can still be performed using only one blade number. The discussion in Section 6.1 is independent and delivers the optimum blade based on the decision model.

Sensitivity analysis was done for all performance parameters $C_{P_{\max}}$, $TSR_{C_{P_{\max}}}$, and corresponding C_T at $TSR_{C_{P_{\max}}}$.

Sobol Results

The Sobol indices for the NACA blades retain the same ranking or order of significance in both S^1 and S^T . This indicates that 1st order effects dictate which design variable would have the most effect on the performance objectives. Altering one significant design variable will most likely change the performance of the blade irrespective of the other design variables.

In all objectives, the most significant design variable is the pitch setting of the blade followed by the twist distribution of the blade. These are design parameters that directly alter flow angles and consequently, the forces developed on the blade as per Equations 2.3 and 2.4. This is also the concept behind feathering, which aims to maintain the optimum angle of attack for each section along the blade.

Surprisingly, chord reduction seems to be the least significant design variable in influencing the $TSR_{C_{P_{\max}}}$. This is contrary to the literature [54] and the hypothesis. Section 6.2.2 discusses this and shows that the chord reduction, or reduced solidity, is still required for pushing $TSR_{C_{P_{\max}}}$ to higher values. As it stands, Sobol indices measure the significance in terms of how much the mean or expected value shifts. It does not indicate whether the shift is towards the left (decreasing) or right (increasing). It does not indicate whether distribution becomes flattened. Finally, it does not indicate whether new regions for objective values are unlocked e.g $TSR > 10$.

A possible explanation for the low significance of the design variables that alter the

Parametric investigation using full design space

solidity of the blade is the fact that there is also a need to alter the pitch and twist of the blades to obtain optimum performance. This implies that only reducing solidity will not lead to better blades for less energetic flow.

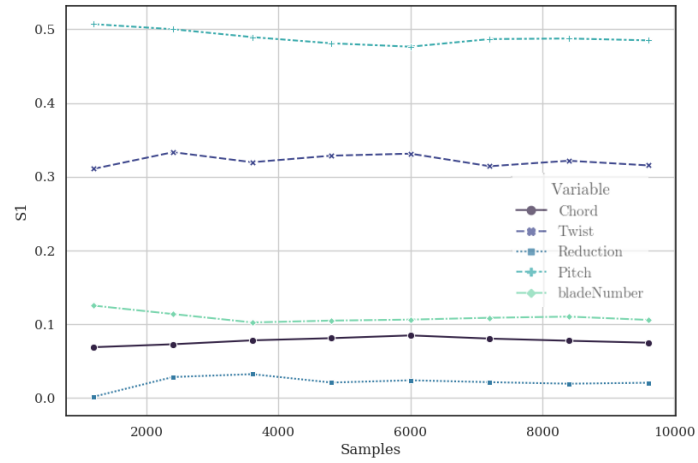
Higher-order Sobol indices can better explain the interaction between the design variables and the issue seen in S^T values for $TSR_{C_{P_{\max}}}$. However, these are not included in the body of the thesis since the sample independence study for higher-order Sobol shows that there is a need for a greater number of samples. These are presented in Appendix B. Section 6.2.2 presents an alternative discussion to explain these effects.

At the current number of samples, both S^1 and S^T behave similarly for all samples greater than 3600. This shows that there are enough samples to evaluate at least 1st order effects. However, it can be seen that the sum of S^T values for $TSR_{C_{P_{\max}}}$ are greater than 1. This also indicates high interaction effects between variables.

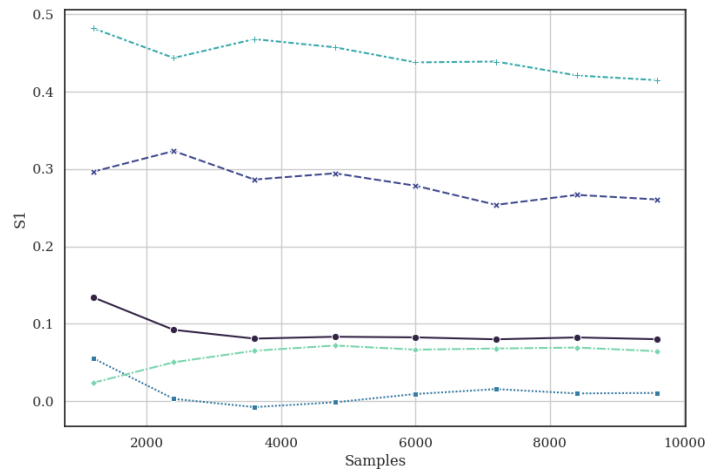
Similar to the NACA Sobol results, the Wortmann Sobol indices have the same order of significance for both S^1 and S^T . However, blade number seem to have an increased level of significance for $C_{P_{\max}}$. This is understandable since reducing the blade number for the Wortmann blade results in a large drop in solidity due to the base Wortmann blade having at least double the maximum chord length of the base NACA blade. Thus, removing a blade has a greater impact on the overall solidity. This may also be interpreted as a benefit for low solidity blades such that the $C_{P_{\max}}$ may be less dependent on blade-number-derived-solidity. However, such blades are still dependent on the aerodynamic properties of the aerofoil used along the blade. The NACA 63-8xx is an excellent example of this.

Further comparing from the NACA results that have a relatively stable behaviour in the sample independence study, the corresponding C_T for $TSR_{C_{P_{\max}}}$ for the Wortmann displays erratic behaviour. While the significance ranking is maintained at $n > 4800$, the S^T values for C_T still move about compared to the more behaved S^1 values. This again indicates higher-order interaction effects.

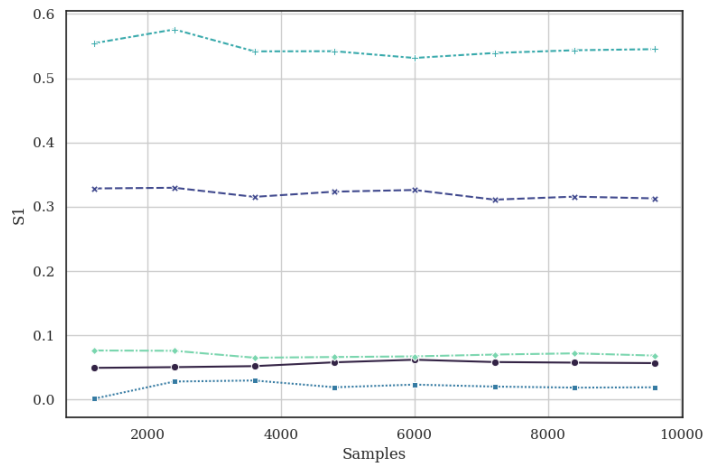
Parametric investigation using full design space



(a) S1 Indices for $C_{P_{\max}}$



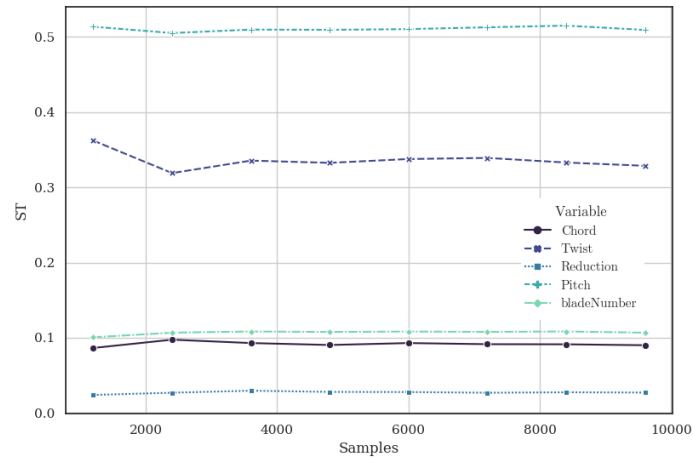
(b) S1 Indices for $TSR_{C_{P_{\max}}}$



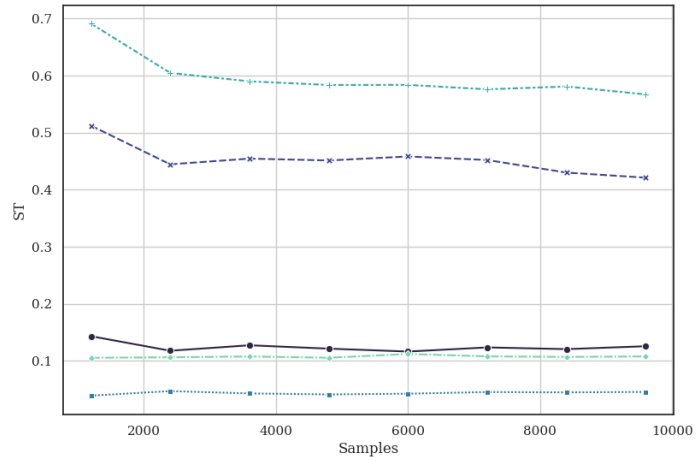
(c) S1 Indices for corresponding C_T

Figure 6.22: 1st order Sobol Indices for NACA

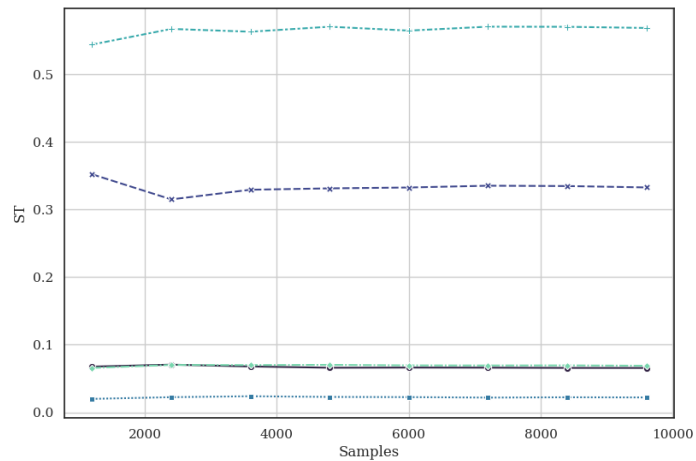
Parametric investigation using full design space



(a) ST Indices for $C_{P_{\max}}$



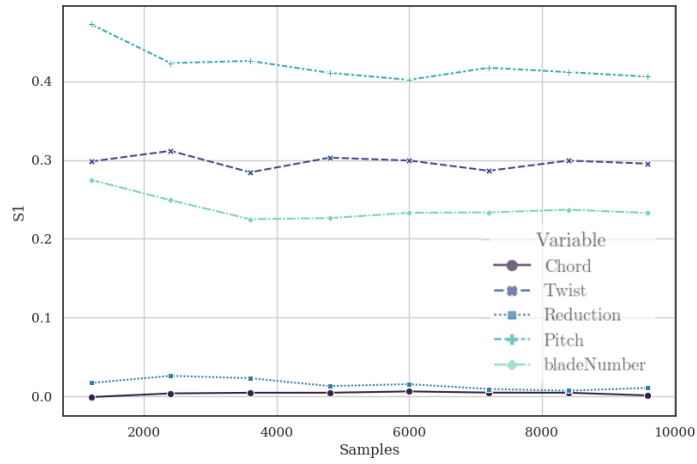
(b) ST Indices for $TSR_{C_{P_{\max}}}$



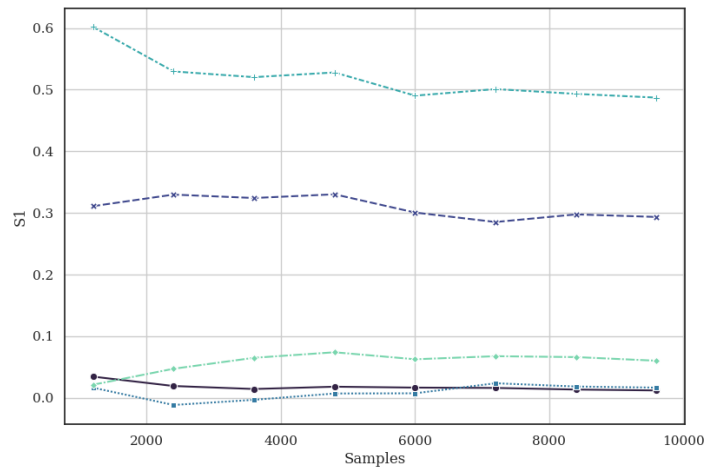
(c) ST Indices for corresponding C_T

Figure 6.23: Total Sobol Indices for NACA

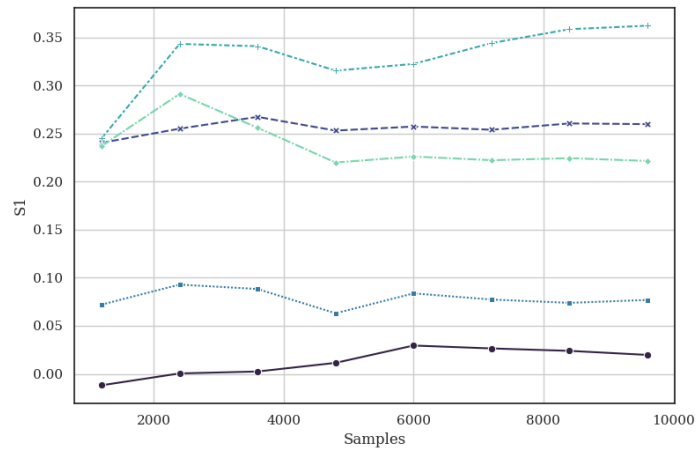
Parametric investigation using full design space



(a) S1 Indices for $C_{P_{\max}}$



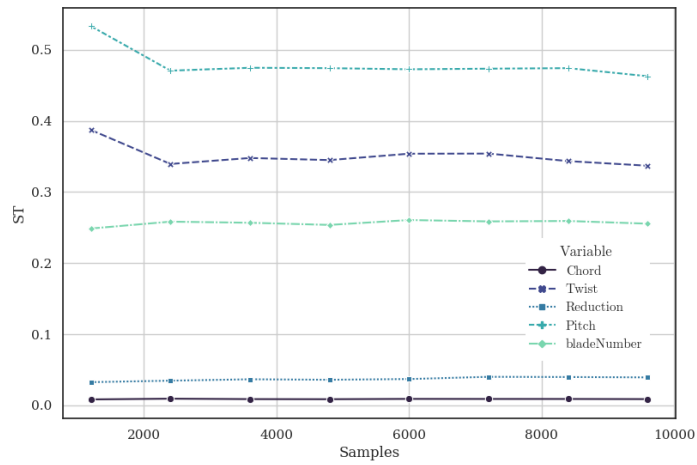
(b) S1 Indices for $TSR_{C_{P_{\max}}}$



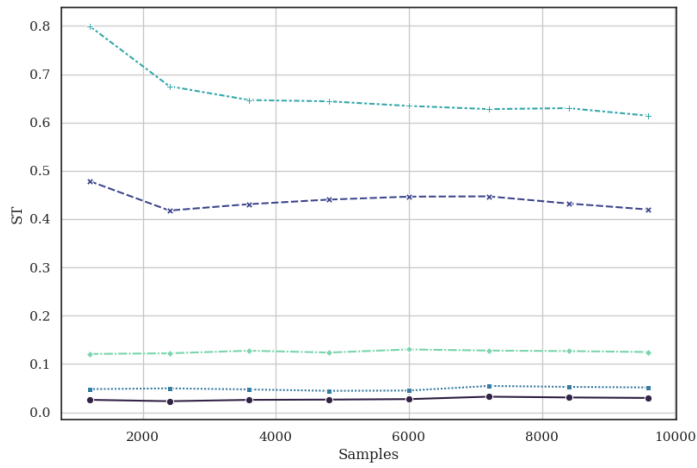
(c) S1 Indices for corresponding C_T

Figure 6.24: 1st order Sobol Indices for Wortmann

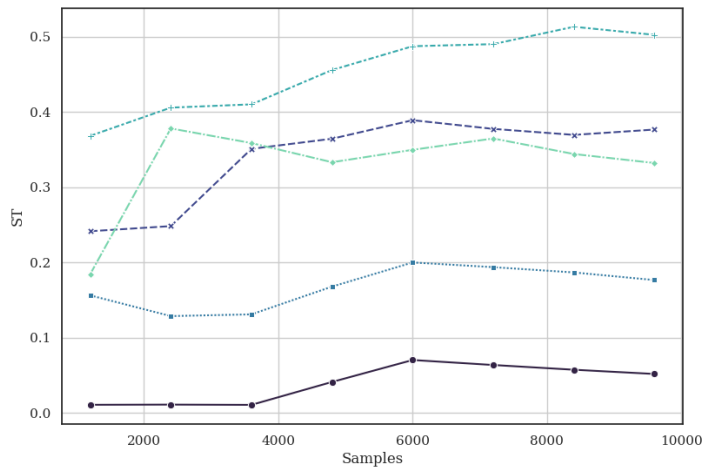
Parametric investigation using full design space



(a) ST Indices for $C_{P_{max}}$



(b) ST Indices for $TSR_{C_{P_{max}}}$



(c) ST Indices for corresponding C_T

Figure 6.25: Total Sobol Indices for Wortmann

Morris Results

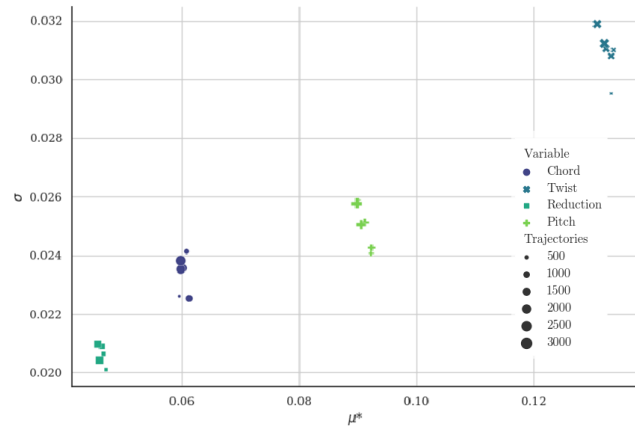
The Morris results also show that the most significant design variables are twist and pitch. However, the twist distribution is the most significant of the parameters compared to the Sobol results indicating that pitch is the most significant. This is due to Sobol taking into account the variance contribution which includes the total data spread while Morris only takes into account the absolute mean change.

The presence of higher-order or interaction effects are confirmed through the σ indices for all performance objectives. The results, similar to the Sobol results, does not add evidence to the relationship between solidity and $TSR_{C_{P_{\max}}}$.

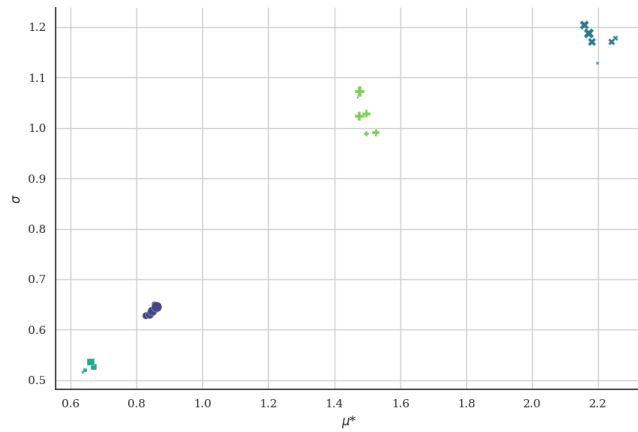
Additional information regarding the magnitude of variation, or elementary effects, can be extracted from the values of μ^* and σ when comparing the NACA and Wortmann blades. For μ^* , the elementary effects are roughly similar for $C_{P_{\max}}$ and the corresponding C_T . The main difference is seen when comparing $TSR_{C_{P_{\max}}}$ as the elementary effects of the NACA are more than double of those seen from the Wortmann. This reflects the range of TSRs seen in the figures of Section 6.1. $TSR_{C_{P_{\max}}}$ for the NACA varies from 2 to 12 while $TSR_{C_{P_{\max}}}$ for the Wortmann is only from 2 to 7.

The values of σ for $C_{P_{\max}}$ are comparable for both blades. For $C_{P_{\max}}$, the NACA has greater interaction effects indicating a greater need to match the solidity-related variables to the twist distribution and pitch. This is expected as the NACA blades are operating at nearly double the TSR compared to the Wortmann blades and thus, have greater variation in terms of flow angles. For the corresponding C_T , the Wortmann is the one experiencing greater interaction effects. This may be due to blade number, which is not included in the Morris sensitivity analysis, inducing a large variation in the performance of the blades. The large drop in solidity when one blade is not included, however, does not induce the same effect on $C_{P_{\max}}$.

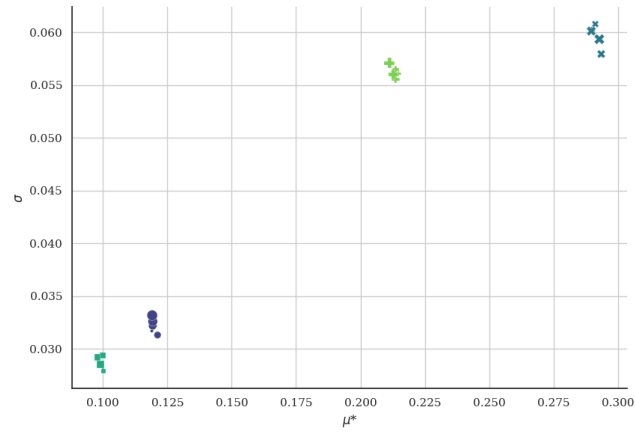
Parametric investigation using full design space



(a) Indices for $C_{P_{max}}$



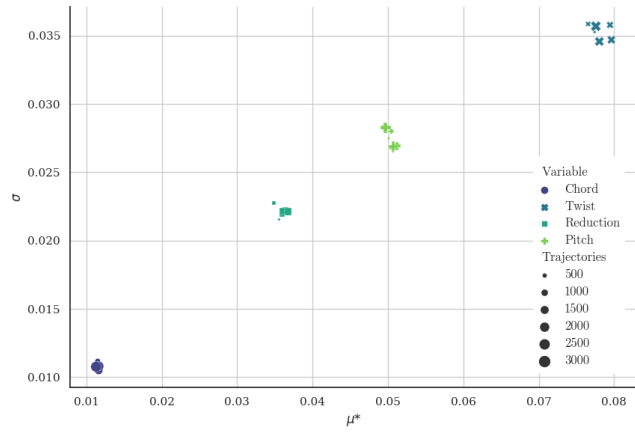
(b) Indices for $TSR_{C_{P_{max}}}$



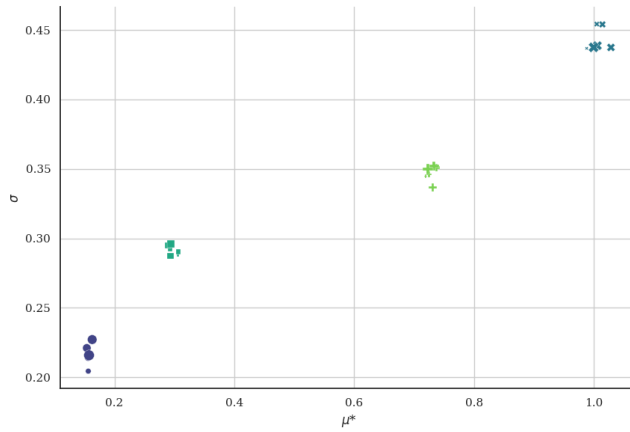
(c) Indices for corresponding C_T

Figure 6.26: Morris Indices for NACA blades

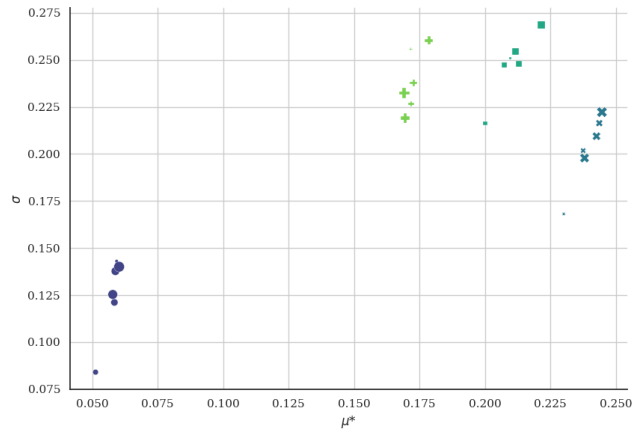
Parametric investigation using full design space



(a) Indices for $C_{P_{max}}$



(b) Indices for $TSR_{C_{P_{max}}}$



(c) Indices for corresponding C_T

Figure 6.27: Morris Indices for Wortmann blades

Parametric investigation using full design space

Trajectory independence for Morris sensitivity shows consistent results except for C_T at the corresponding $TSR_{C_{P_{\max}}}$ for the Wortmann. The value of μ^* stays relatively the same but there is a noticeable spread for σ . This also confirms the need for a greater number of samples, or a larger design space for the Morris method, to evaluate higher-order effects.

Additional studies for the variation in C_T are needed to investigate the discrepancies. However, for both Sobol and Morris methods, the first order results are sufficient for further analysis of the main performance objectives $C_{P_{\max}}$ and $TSR_{C_{P_{\max}}}$.

Thresholds for high TSR

Saltelli [163] criticises the usage of traditional one-at-a-time analysis wherein one factor is altered while all others remain constant, possibly ignoring interaction effects and how the probability distribution function (*pdf*) changes as other design variables are altered.

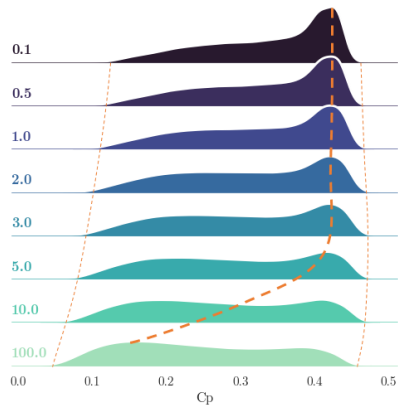
In this section, we analyse the effect of a design variable on the *pdf*, which does not necessarily quantify how other design variables alter the effects of the specific design variable on the performance objectives. This approach, however, can quantify the effects of one variable while taking other design variables as system states. The resulting *pdf* shows how the expected value of the performance objectives changes for a specific design variable. The Sobol and Morris indices give a rough idea of how much the effects will be but they provide an incomplete picture for this study because there is a goal of pushing towards higher TSRs i.e. the magnitude and direction of the shift is an important consideration.

This approach also explains the results of the Sobol and Morris methods that seemingly counter the hypothesis of reducing solidity to allow for high-TSR operation. The approach explores the idea of thresholds wherein a particular performance objective would have a *pdf* value of nearly 0 if a design variable is not altered. This is in line with Saltelli's discussion that there is a need to sample the whole design space to see the effects of each design variable 'globally' (Section 6.2.1) i.e. the effects of different system states derived from different levels of other design variables are taken into account.

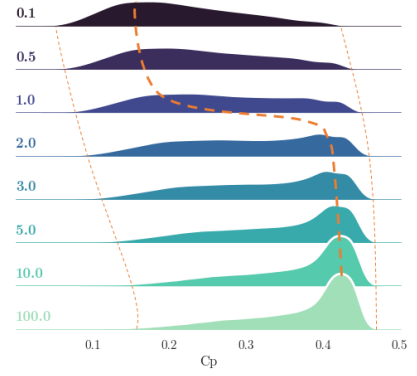
Parametric investigation using full design space

Finally, this section answers the question of 'How do we design the blade to push for an optimal high-TSR operating point?'

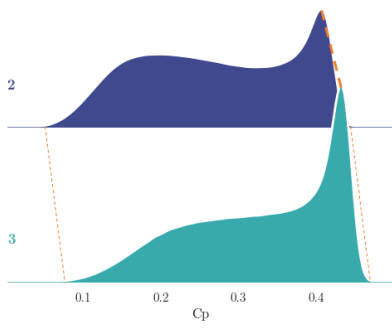
Parametric investigation using full design space



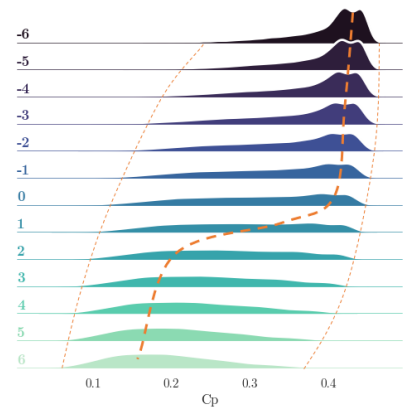
(a) $C_{P_{\max}}$ vs Γ_{chord}



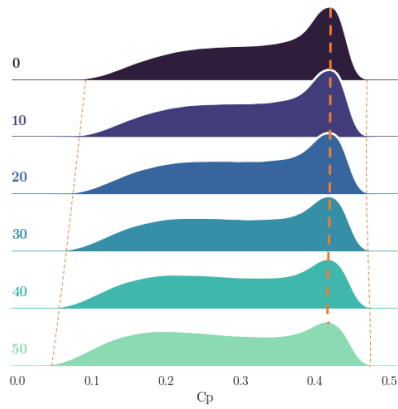
(b) $C_{P_{\max}}$ vs Γ_{twist}



(c) $C_{P_{\max}}$ vs Blade number



(d) $C_{P_{\max}}$ vs Pitch



(e) $C_{P_{\max}}$ vs Chord Reduction

Figure 6.28: Probability Distribution for NACA $C_{P_{\max}}$ according to different design variables

Parametric investigation using full design space

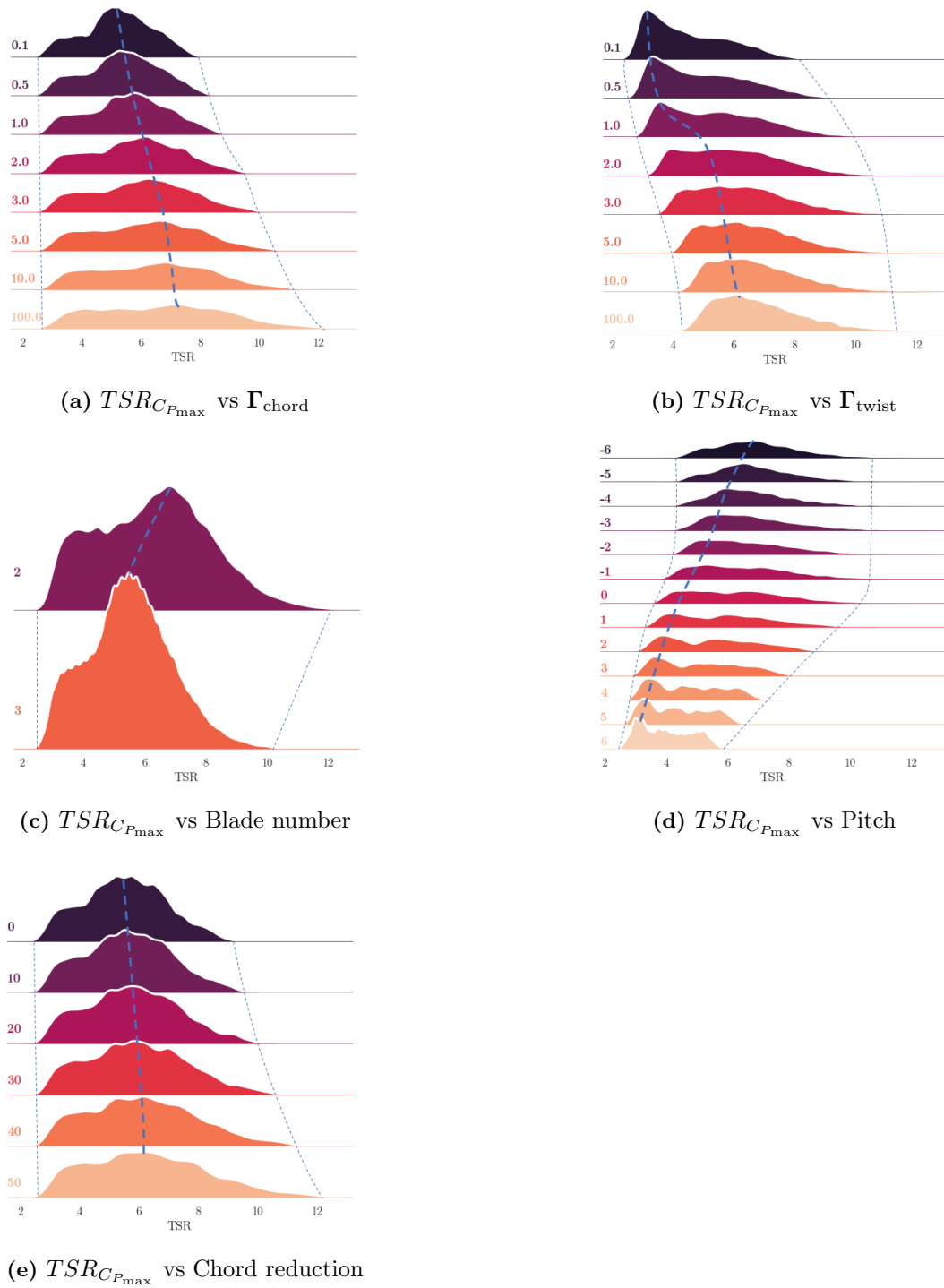


Figure 6.29: Probability Distribution for NACA $TSR_{C_{P_{max}}}$ according to different design variables

Variable effects on $C_{P_{\max}}$. The movement of the peaks which correspond to the expected value of the $C_{P_{\max}}$ given a specific design variable, $E(Y|x_i)$ is shown in Figure 6.28. A line is drawn in each plot to show the position of the expected value and how much each change. The range of change confirms the Sobol and Morris results and the apparent effects discussed in Section 6.1.

For design variables altering solidity, the expected value for $C_{P_{\max}}$ increases by a small amount as solidity increases. The same is true for minimum and maximum $C_{P_{\max}}$ values as shown by the broken lines.⁸

Changes in the *pdf* are more apparent when looking at the twist distribution and pitch. These are highly influential variables as shown from both Sobol and Morris for all objectives. For the twist distribution, the expected value of $C_{P_{\max}}$ changes rapidly after a critical value of $\Gamma_{\text{twist}} > 2$. The *pdf* significantly changes as $E(Y|x_{\Gamma_{\text{twist}}})$ shifts from the left (low values of $C_{P_{\max}}$) to the right.

The same is observed for the effect of pitch on the *pdf* of $C_{P_{\max}}$. The identified critical value is within $1 < \theta_p < 0$ although the shift is more gradual. This effect on the performance has been discussed in Section 6.1.

Recall from Section 4.1 that all twist distributions, or at least portions along the blade length (Figure 4.6), follow a hyperbolic ($\Gamma_{\text{twist}} > 2$) distribution. Even Sun [130], who has the most complex twist distribution, adopted a hyperbolic twist distribution for $r/R > 0.5$, which dictate much of the blade performance.

Minimum $C_{P_{\max}}$ increase as Γ_{twist} increase and pitch decreases. The range of change is greater for pitch than it is for Γ_{twist} , which may explain the difference in the significance ranks of twist and pitch for Sobol and Morris. The *pdf* for each level of pitch has a smaller spread compared to the *pdf* for each level of Γ_{twist} . This is not taken into account in the Morris results.

It is still possible to design optimal blades with less feathering compared to best cases as the probability of $C_{P_{\max}} > 0.4$ is still greater than zero⁹ although there will be

⁸The broken lines do not indicate the true minimum or maximum as there may be outliers. The broken lines indicate the minimum or maximum values within the estimated lower and upper fences of a boxplot with the same data (1.5 times the interquartile range from the first and third quartile respectively.)

⁹Please refer to the previous footnote.

very few blades that will have such design and performance.¹⁰

The *pdfs* for the Wortmann are shown in Appendix C. The results and discussion for the Wortmann are similar to the NACA except for the case of blade number. The *pdf* of $C_{P_{\max}}$ considering blade number shows a huge peak when the blade number is set to 3, which also reduces the spread of the data. This results in a high Sobol index.

Variable effects on $TSR_{C_{P_{\max}}}$. In Figure 6.29, there is a visible shift in $TSR_{C_{P_{\max}}}$ when looking at the effect of the blade number on the *pdf*. However, Sobol still reports this as having low significance. Even the chord distribution that seems to result in a lesser variation in the expected value of $TSR_{C_{P_{\max}}}$ has a higher significance in the Sobol results. This is due to Equation 6.2 which takes into account how much of the variance can be explained using the variance of the design variable. Visually, the change is large but two levels cannot fully explain the spread of data as well as the levels provided by the chord distribution and reduction.

Looking at chord reduction, there is little to no variation in the expected value of $TSR_{C_{P_{\max}}}$ so it remains to be ranked the lowest in both Sobol and Morris sensitivity indices. The variation in the expected value is a bit more apparent when looking at the chord distribution but also remains to be minimal.

Similar to the trend when looking at $C_{P_{\max}}$, the change in the expected value is more apparent when looking at the twist distribution and pitch. However, there is no sudden shift in the expected value of $TSR_{C_{P_{\max}}}$, and hence, there is no critical value. There is, however, a tendency for the *pdf* to be skewed to the left, or the expected value to be nearer to the minimum as Γ_{twist} decreases and pitch increases.

This thesis is interested in pushing the value of $TSR_{C_{P_{\max}}}$ towards higher values and the *pdfs* show the requirements to achieve this.

- Γ_{chord} should be increased to achieve high TSR operation. Setting a value of $\Gamma_{\text{chord}} = 2$ has an apparent maximum $TSR_{C_{P_{\max}}}$ less than 10. While this is still considered to be high, pushing higher require less solidity i.e. the probability of

¹⁰This is not without merit since it can be easier to manufacture less feathered blades due to a simpler profile.

Parametric investigation using full design space

generating an optimal blade design that has high solidity and high TSR is very low.

- Reducing the blade number from 3 to 2 significantly increases the probability to generate optimal blade designs that operate in higher TSR.
- Reducing the chord length has huge potential to push optimal TSR operation towards higher values. The same discussion with Γ_{chord} can be used to explain this requirement since the probability of obtaining optimal blade designs that have higher $TSR_{C_{P_{\max}}}$ is significantly greater compared to unreduced chord lengths (probability near zero).

It is important to note that Figure 6.29 only shows the *pdf* for the $TSR_{C_{P_{\max}}}$. Thus, the term "probability of generating an optimal blade design" is not limited to the *pdfs* shown. Not all blade designs that have high $TSR_{C_{P_{\max}}}$ have good $C_{P_{\max}}$, which implies that going for higher solidity blades with less aggressive feathering and high values of pitch may result in high TSR blades but low $C_{P_{\max}}$.

In a real world sense, finding the optimal blade can be much more important than dealing with the probability of generating an optimal blade. However, knowing where to find a good number of optimal blades gives value as the design space is narrowed down.

6.3 Summary

The chapter presented the output of the rapid blade generation method applied to the full design space. The performance of all blade designs were evaluated and a generalised decision model with different weight scenarios allowed for the selection of multiple candidate blades, with different TSR-operating points. The general shift in performance ($C_{P_{\max}}$ and $TSR_{C_{P_{\max}}}$) is shown to follow a pattern according to the variation of the parameters defined in Chapter 3. This pattern is consistent for both the NACA and the Wortmann aerofoils used in this thesis.

The chapter also presented a sensitivity analysis using Sobol and Morris sensitivity

Parametric investigation using full design space

methods to determine influential design variables. It was shown that hydrodynamic performance ($C_{P_{\max}}$, and C_T) generally depend on pitch and twist, as has been expected from literature. Sobol and Morris sensitivity showed that the expected value (mean for all samples) for $TSR_{C_{P_{\max}}}$ given all the values within a possible design space is not significantly affected by the solidity. However, an analysis on probability distributions showed that it is only possible to push the $TSR_{C_{P_{\max}}}$ towards higher values if solidity is reduced - either by a lower blade number or chord length reduction.

Chapter 7

Technical Performance of Designed Blades in Characteristic Sites

7.1 Characteristic sites: Country Profiles

7.1.1 Mexico

Power in Mexico is mainly provided by thermal power plants and has steadily increased since 1980; thermal power also has the biggest growth rate, more than any other form of power generation. Of this, oil remains to be the top choice although it has seen a significant decrease from a peak utilisation of 102027ktoe in 2005 to 90347ktoe in 2015. Its share in the power generation mix has also seen a significant drop from a peak of 69.29% in 1990 to 51.60% in 2015 in favor of cleaner alternatives such as natural gas [170].

In recent years, Mexico has pushed for cleaner technologies with an aim of 40% of power generation from zero/low-emission sources by 2035, and 50% by 2050 compared to the baseline energy share in 2000 [171]. Since then, additional capacity for renewable energy has been added although its total share to the power generation mix remains stagnant over the recent years. It is apparent that most of the target is met by using natural gas and IRENA cautions with the steady increase in the country's use of cleaner but still non-renewable natural gas [172].

Technical Performance of Designed Blades in Characteristic Sites

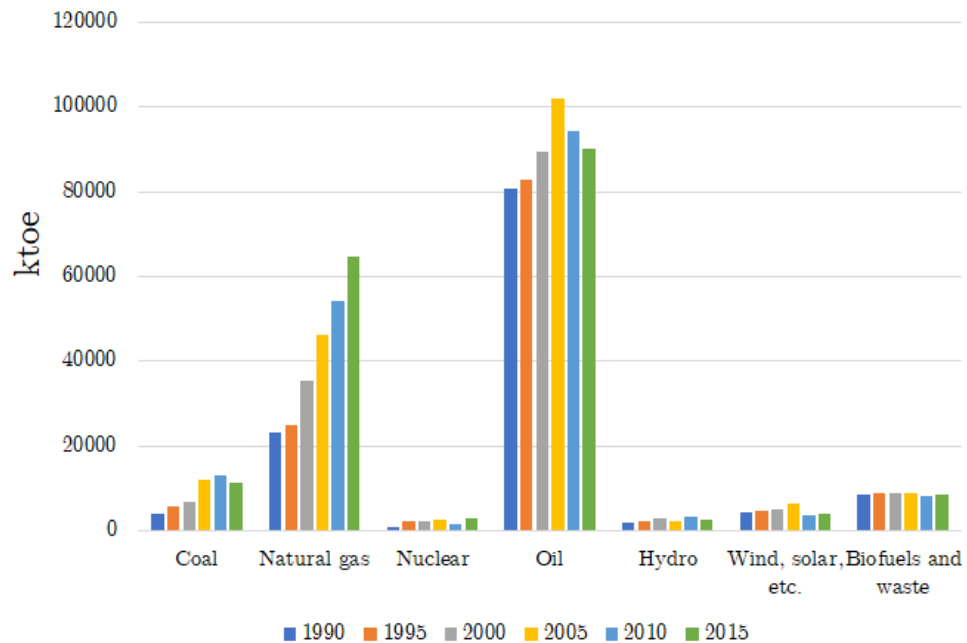


Figure 7.1: Power mix of Mexico in terms of kilotonne of oil equivalent (2017).

The renewable energy plan (REmap 2030) [172] recommends more growth for renewables as the current plan only aims to achieve 10% share by 2030. Encouraging more growth will diversify the supply and reduce demand of coal by 62%, natural gas by 21%, and oil by 6% with almost half of electricity demand being provided by renewables (2015 values). Currently, conventional hydroelectric power generation leads the renewable energy sector but is also aimed to be complemented by additional wind, solar, and geothermal to fully diversify the energy mix.

Tidal stream energy is not highlighted in REmap 2030 but recent assessments show that it can augment power generation especially in localised grids. Hernandez-Fontes [173] studied the potential marine energy resources in Mexico and found sites with a potential of greater than $32\text{W}/\text{m}^2$ with one site exceeding a potential of $512\text{W}/\text{m}^2$, with an availability of at least 50%.

Hernandez-Fontes [173] mapped the ocean energy potential in Mexico and the Yucatan peninsula is marked in 7.2 as a particular site of interest. Within the channel flows the Yucatan current, an ocean-driven current, that can be a possible provider of a continuous unidirectional flow driving a TST. The area has since been studied by

Technical Performance of Designed Blades in Characteristic Sites

Alcerreca-Huerta et al. [174] for its tidal stream potential and it is estimated that at least 3.2MW of tidal stream power can be extracted.

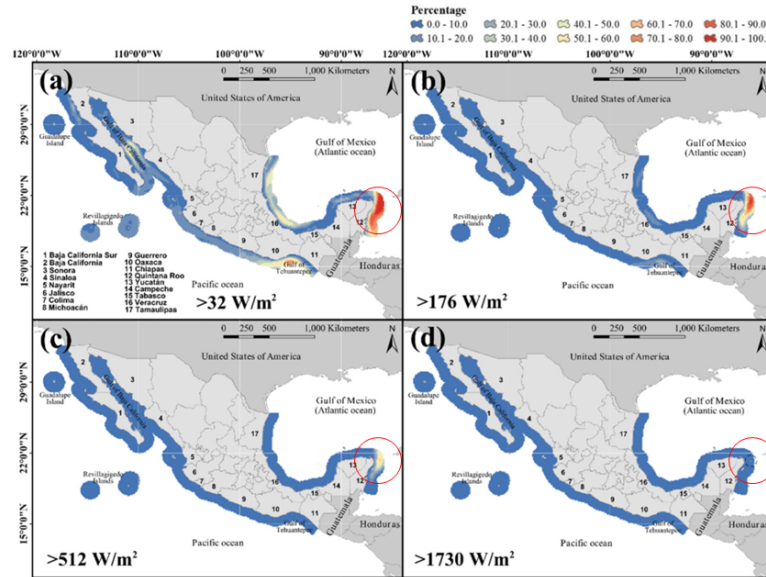


Figure 7.2: Location and potential of the Yucatan Peninsula. Adapted from Hernandez-Fontes [173]. CC-BY 4.0

Within the area is the island of Cozumel that primarily gets its supply of through a submarine cable connection to Playa del Carmen in the main island and small diesel power plants. The addition of tidal stream energy in this area can contribute to 10% of the power consumption within the island which is projected to increase in the future due to growth from tourism [175]. While far from being a dominant, it can provide a starting point for tidal stream energy development in the country and tackle areas with greater energy potential.

7.1.2 Philippines

The Philippines have pushed to increase the share of renewable energy sources into the power mix since 2008 through the National Renewable Energy program. However, the country's dependence on fossil fuels continues to grow over the past years with a majority of the power supplied by coal-fired sources. Figure 7.3 shows that energy from coal-fired sources continue to rise over the past 5 years while much of the renewable

Technical Performance of Designed Blades in Characteristic Sites

energy utilisation has stagnated. Additionally, over 80% of the renewable energy (RE) share is from geothermal and hydroelectric power. This shows a heavy dependence on conventional sources of energy [176].

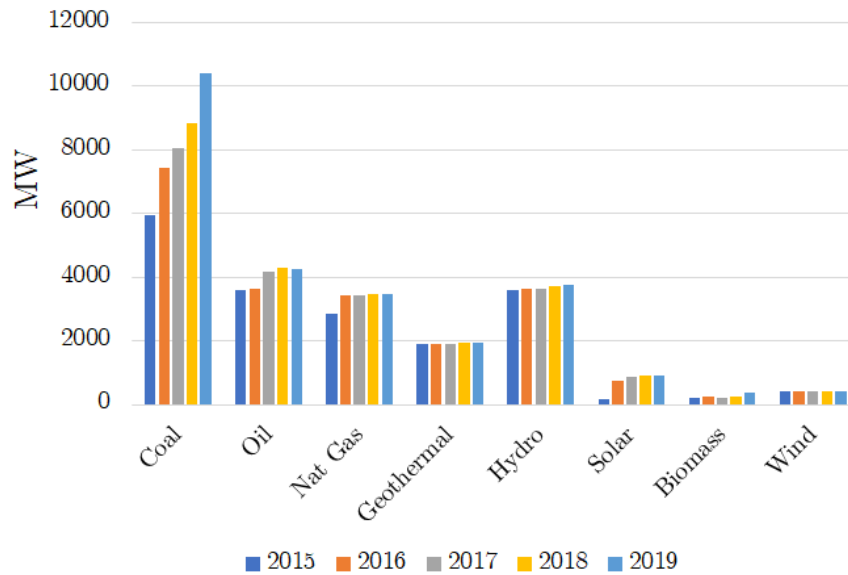


Figure 7.3: Power mix of the Philippines in MW (2017).

The slow growth in the renewable energy sector is hindered by socio-political-economic situation within the country although additional energy capacity is envisioned with newly awarded projects [177]. Table 7.1 shows a summary of awarded projects and the projected additional capacity when all power plants are operational [178].

Table 7.1: Potential and Installed Capacity of renewable energy power plants in the Philippines according to resource (2017)

Resources	Potential Capacity (MW)		Installed Capacity (MW)	
	Commercial	Own-use	Commercial	Own-use
Hydroelectric	11284.95	1.56	1105.02	
Ocean Energy	24			
Geothermal	814.2		1928.07	
Wind	5760.28		442.9	0.01
Solar	11892.31	8.35	1187.91	6.43
Biomass	182.03	3.1	619.3	179.27
Subtotal	2958.07	13.01	5283.2	185.71
Total	29971.08		5468.91	

Technical Performance of Designed Blades in Characteristic Sites

The ocean energy sector is yet to produce useable power as much of the awarded projects are still in the assessment or device development phase. Of the awarded projects, TSTs are of particular interest for ocean energy with all 6 projects being tidal stream energy technologies (Table 7.2) [179]. These sites have relatively energetic flow with current magnitudes of greater than 2m/s [23, 35].

Table 7.2: Awarded Ocean Energy Projects in the Philippines (2019)

Province	City/Municipality	Stage of Contract	Capacity
Zambales	Cabangan	Pre-Development	5
Sorsogon	Matnog	Pre-Development	5
Northern Samar	Capul	Development	3
Northern Samar	San Antonio	Pre-Development	5
Northern Samar	San Bernardino Strait	Pre-Development	0
Surigao del Norte		Pre-Development	6
Total			24

However, other sites in the country are characterised by less energetic flow ($U_\infty < 2\text{m/s}$) [35]. While it is estimated that the country has a tidal-stream potential of 80GW, most of these sites have less energetic flow [23, 23, 180], presenting a problem on extraction of energy in these sites. This includes parts of the San Bernardino Strait, which has parts that peak at greater than 4.5m/s but the whole area have an annual average current of only 1.2-1.6m/s [35].

Assessment of the ocean energy potential in the country makes up most of the research and development in the country with the development in San Bernadino Strait [33] being the only project that is within the development phase that designs a device that would work well within the flow regime in the country. However, this may still fall within the current conventional low-TSR tidal turbines due to a relatively high current magnitude. This leaves much of the potential from less energetic currents far from being tapped as further research on these sites only include simulations wherein tidal devices developed in the UK are matched to the current using the respective cut-in speeds [181–183].

7.2 Velocity Profile Modelling

7.2.1 Data Processing

Mexico

Data on the Cozumel channel was obtained from a concurrent study published by Alcerreca-Huerta *et al.* [174] wherein field measurements were conducted during 21-29 September 2019. The variation of the current velocity, for both depth and distance to shore, were obtained in seven transects within the channel. A vessel-mounted ADCP with an integrated GPS was used to record the current velocity and position along the transect.

This method of data gathering gives one unique measurement for each combination of depth and distance to shore. Figure 7.4 shows the location of each transect in the channel while Figure 7.5 shows the velocity variations for transects 1-4 (T1-T4).

Four of the seven transects are selected as case studies, all of which are within the northern region of the island. For each transect, three 10m windows were selected to be modelled. Each window is set to have a maximum depth variation of 1m within the whole 10m window. This is done to limit the effects of irregular bathymetry on the velocity field.

Table 7.3: Location and mean depth of 10m windows within each transect

Transect	Window	Distance	Mean Depth
A	1	105-115	22.13
	2	150-160	21.70
	3	210-220	21.91
B	1	130-140	17.96
	2	160-170	18.47
	3	230-240	18.00
C	1	105-115	19.42
	2	160-170	18.47
	3	240-250	17.19
D	1	100-110	19.04
	2	150-160	15.98
	3	200-210	12.86

Technical Performance of Designed Blades in Characteristic Sites

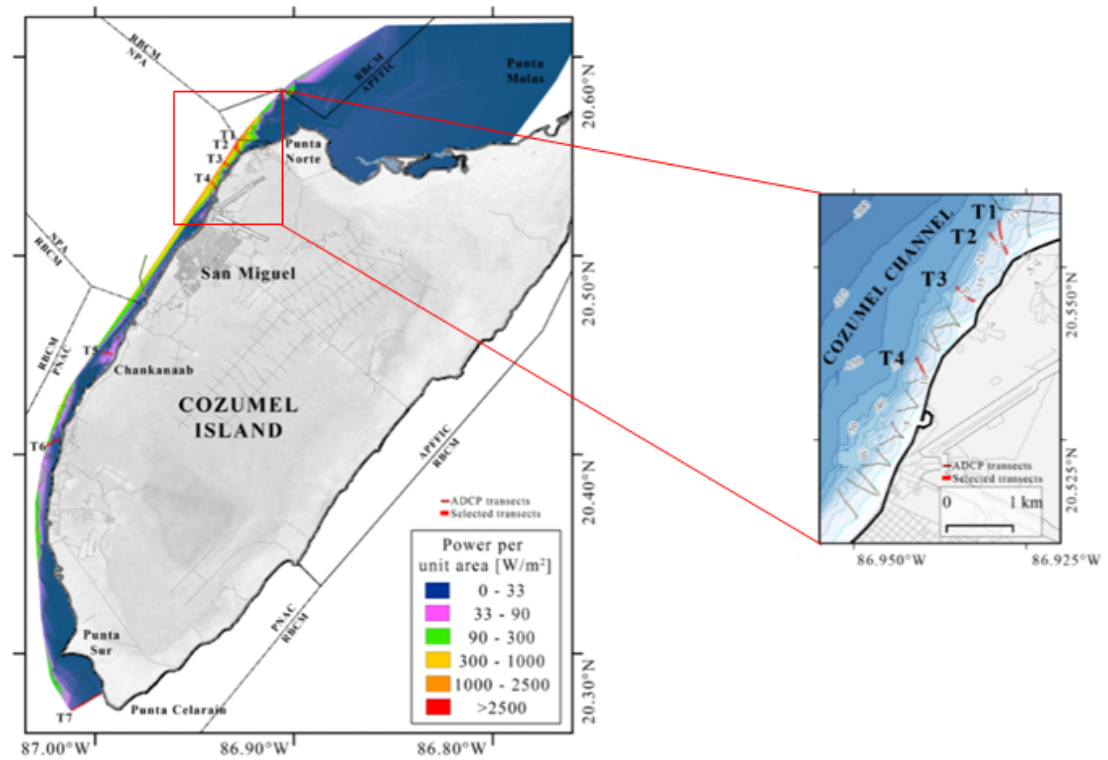


Figure 7.4: Location of each transect in the Cozumel Channel. Adapted from Alcerreca-Huerta *et al.* [174]. CC-BY 4.0

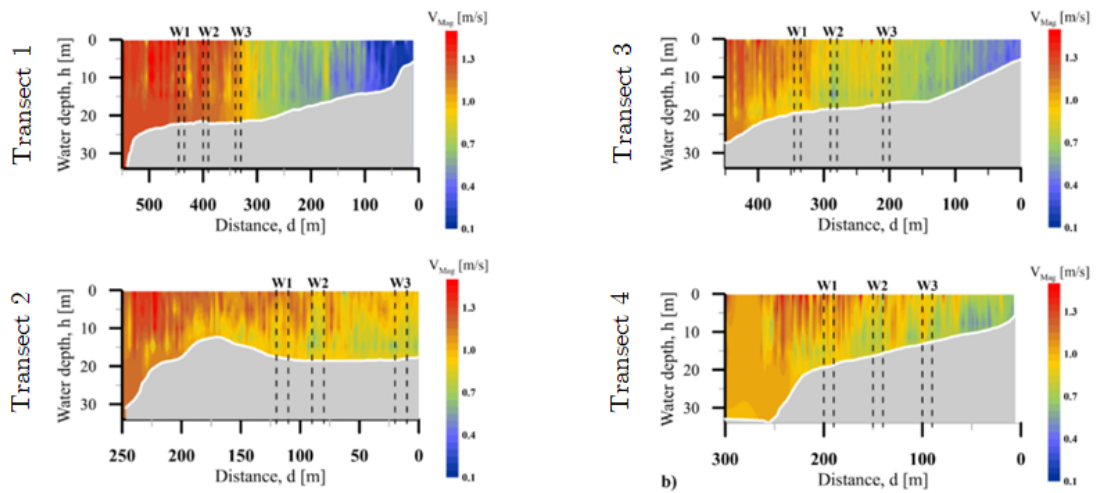


Figure 7.5: Velocity variation in each transect and location of each 10m window. The reported values in Table 7.3 are taken as the distance from maximum distance to shore as presented in the dataset. Adapted from Alcerreca-Huerta *et al.* [174]. CC-BY 4.0

Philippines

ADCP measurements in an anonymous site in the Philippines¹ were provided by a Filipino developer². A single current magnitude flowing along an identified azimuthal direction is given at 1m depth intervals for a depth of 1.5m to 21.5m. The data gives the current velocity from 25 May 2015 to 07 July 2015 with 5-minute intervals between each reading.

The ADCP measurements already include both wave and current velocities making it difficult to do the superposition of wave and current (Section 2.3.3) as the orbital velocities that can help characterise the effect of waves on the water column can be hard to determine. Thus, a power law fit is done for each row of data³ and the mean and median values for each variable is obtained for further analysis.

Wave data was generated by the same developer using the NOAA WW3 model. The wave data includes significant wave height, wave period, and mean wave direction for the months of May to September at 3-hr intervals. The location is also anonymised although it was disclosed the location used for the model is not directly on top of the location of the ADCP; the location is within the vicinity with an undisclosed distance.

The difference in time intervals presents a problem and thus, the mean tidal velocity for each 3hr-time interval while wave parameters are taken as constant for the whole three hours. The resulting power law fit is considered as the current-only velocity profile and the wave data is categorised according to its orthogonality with the mean current direction. Wave directionality and wave parameters are used to discuss deviations from 1/7th power law as consistent with the findings of [71–74, 80]. However, the analysis is limited to concurrent wave and current - the downstream condition with ebb flow is not fully evaluated although it is expected that such turbine orientation will lead to reduced performance [184].

¹Data provided was anonymised and exact location cannot be pinpointed with full certainty

²Name redacted

³one row of data is the set of data for a given time interval

Table 7.4: Direction of wave propagation with respect to dominant tidal direction (both flood and ebb)

Direciton	Angle	N		Mean H_s (m)	Mean T_p (s)
		Unfiltered	Filtered		
FF	≤ 30	93	81	0.4909	5.993
CC	> 150	67	57	0.3507	6.577
PERP	$60 < \theta_{dir} \leq 120$	734	540	0.4801	6.537
DIAG+	$30 < \theta_{dir} \leq 60$	83	69	0.6989	5.821
DIAG-	$120 < \theta_{dir} \leq 150$	70	66	0.3199	6.974

7.2.2 Power Law Fit

Mexico. The following tables give the power law coefficients for each transect. The modelled bed roughness is consistent within each transect as well across all transects. However, the $1/\alpha_{prof}$ power law varies with some negative values.

The median values are more consistent in coefficient values within each transect. For this reason, the median values are used for further analysis since the huge discrepancy between the mean and median values indicate the presence of outliers that may have been caused by random effects outside the scope of the study.

Table 7.5: Mean Power Law Coefficients for each transect

Transect	Window	U_o	α_{prof}	β
A	1	0.97	-11.90	0.33
	2	0.96	-17.98	0.33
	3	0.95	8.90	0.32
B	1	0.79	3.38	0.33
	2	0.72	2.63	0.35
	3	0.82	3.41	0.32
C	1	0.80	153.00	0.33
	2	0.70	8.41	0.35
	3	0.79	-12.80	0.33
D	1	0.76	8.09	0.33
	2	0.68	12.20	0.35
	3	0.69	6.91	0.35

Table 7.6: Median Power Law Coefficients for each transect

Transect	Window	U_o	α_{prof}	β
A	1	0.97	-11.85	0.33
	2	0.97	-12.32	0.33
	3	0.97	-12.20	0.33
B	1	0.85	3.97	0.31
	2	0.74	2.59	0.35
	3	0.84	3.76	0.31
C	1	0.83	4.00	0.32
	2	0.67	3.67	0.35
	3	0.82	-16.50	0.32
D	1	0.77	8.60	0.33
	2	0.77	7.48	0.33
	3	0.71	5.44	0.35

Philippines. Table 7.4 shows that wave-current interaction is predominantly orthogonal. While the numerical method discussed in Section 2.4.3 presents a way to incorporate wave-current interaction, it is limited to following waves only. However, Section 2.3.3 can still be used to analyse the effect of the inflow profile, already affected by the waves, on the hydrodynamic performance of the designed turbines.

Table 7.4 also shows that more than 10% of the data for the specific time period has been filtered out due to extreme values of α_{prof} . Table 7.7 also confirms the presence of extremes in both negative and positive coefficients. Filtering within the reasonable values of $-10 < \alpha_{\text{prof}} < 10$ results in a power law coefficient of ≤ 1 .

Table 7.7: Mean Power Law Coefficients for each wave-tidal direction

Direction	U_o		α_{prof}		β	
	Unfiltered	Filtered	Unfiltered	Filtered	Unfiltered	Filtered
FF	0.11	0.11	20.20	1.00	0.78	0.78
CC	0.05	0.04	1.05	0.28	0.81	0.80
PERP	0.31	0.27	30.20	-3.43	0.44	0.42
DIAG+	0.22	0.19	-9.05	0.50	0.65	0.66
DIAG-	0.05	0.05	-3.30	-0.89	0.68	0.67

For consistency, the median values for the coefficients were used for further analysis although only the Perpendicular case is used to determine hydrodynamic performance

within a sheared velocity profile.

Table 7.8: Median Power Law Coefficients for each wave-tidal direction

Direction	U_o		α_{prof}		β	
	Unfiltered	Filtered	Unfiltered	Filtered	Unfiltered	Filtered
FF	0.11	0.10	1.00	1.00	0.83	0.82
CC	0.03	0.03	1.00	1.00	0.91	0.92
PERP	0.27	0.23	-4.00	-3.57	0.39	0.39
DIAG+	0.20	0.18	1.00	1.00	0.68	0.69
DIAG-	0.03	0.01	-1.00	0.00	0.88	0.84

Presence of highly sheared flow. In the case of Mexico, highly sheared flow can be observed in Transects B and C while a mix of both highly sheared and a similar 1/7th power law can be observed in Transect D. Transect A is near to Transect B and it is expected the direction of waves and current are of different angles due to the orientation of Transect A.

However, it should also be noted that Transect A has the highest mean depth out of all the transects studied. The discrepancy between Transect A and B despite their proximity may be due to the interaction between the presence of boundary layer effects and the difference in orientation of the two transects.

In the case of the Philippines, the median values for β from Table 7.8 is the same for the mean but α_{prof} becomes the same for all cases. This does not conform to the literature except for the presence of a negative α_{prof} . Investigating further using the third quartile (Appendix D), the presence of a highly sheared flow is confirmed. The value obtained for Q3 can be interpreted as majority of the flow being highly sheared compared to the usual flow dictated by the 1/7th power law.

7.3 Performance under a less energetic current profile

All rotors from Chapter 6 are simulated. Simulations are performed using 5m diameter rotors positioned at the middle of the water column with average coefficients from each transect in Table 7.6 and coefficients of the filtered perpendicular case from Table 7.8.

7.3.1 Hydrodynamic performance in characteristic sites

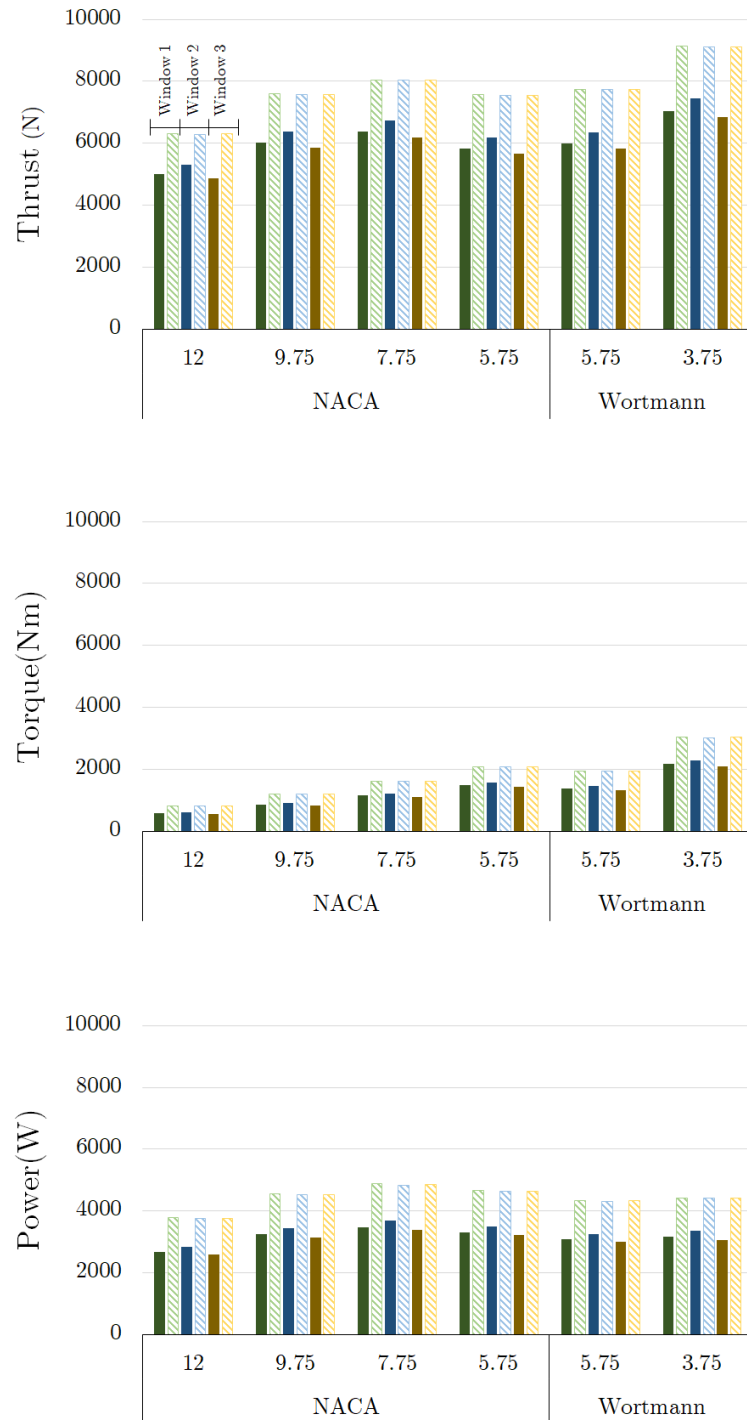


Figure 7.6: Turbine performance for Mexico Transect A

Technical Performance of Designed Blades in Characteristic Sites

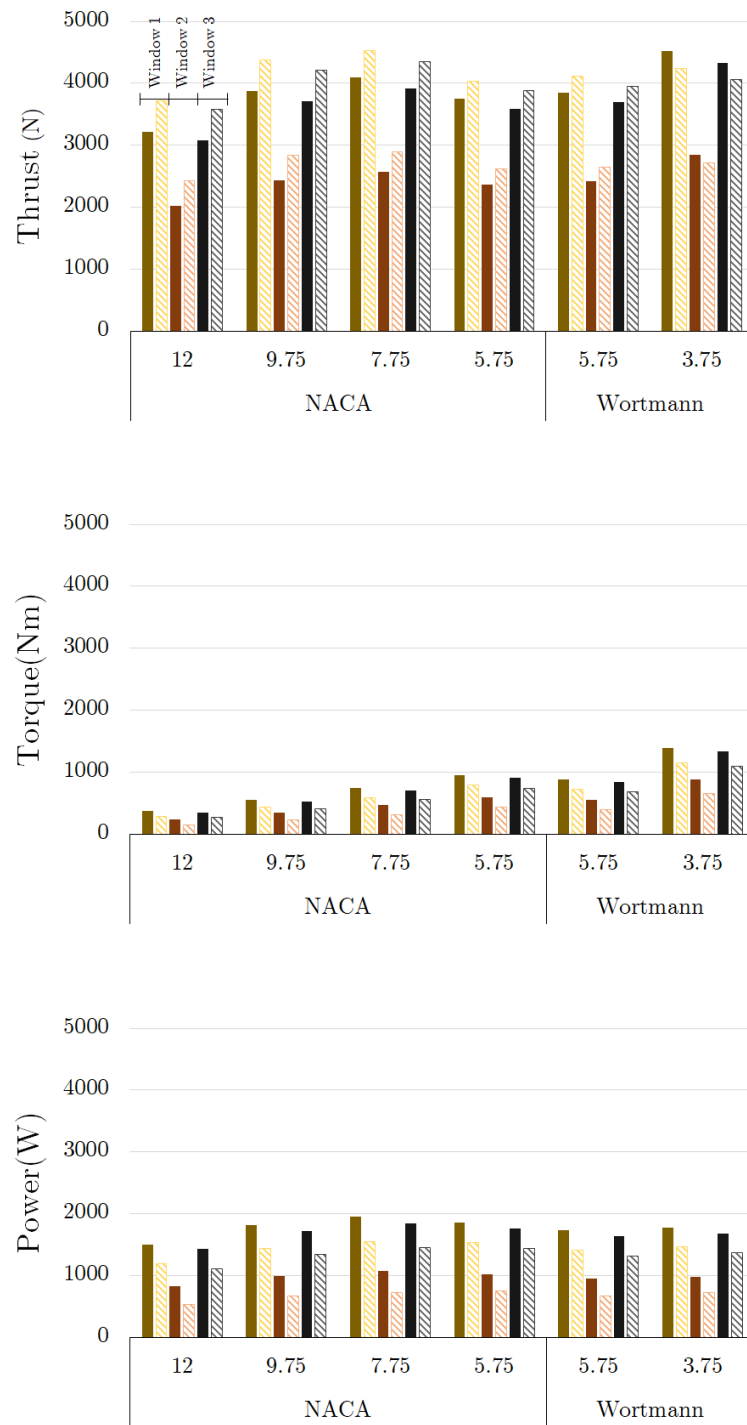


Figure 7.7: Turbine performance for Mexico Transect B

Technical Performance of Designed Blades in Characteristic Sites

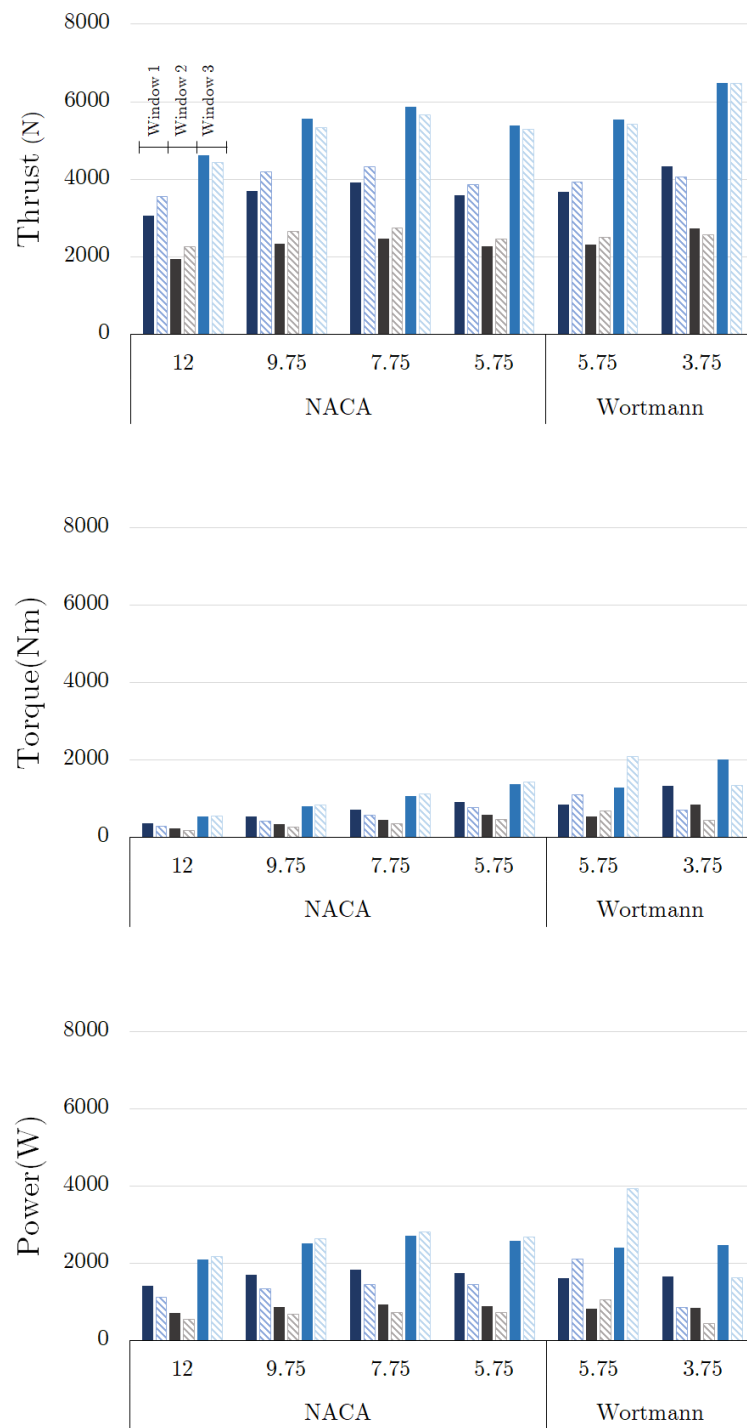


Figure 7.8: Turbine performance for Mexico Transect C

Technical Performance of Designed Blades in Characteristic Sites

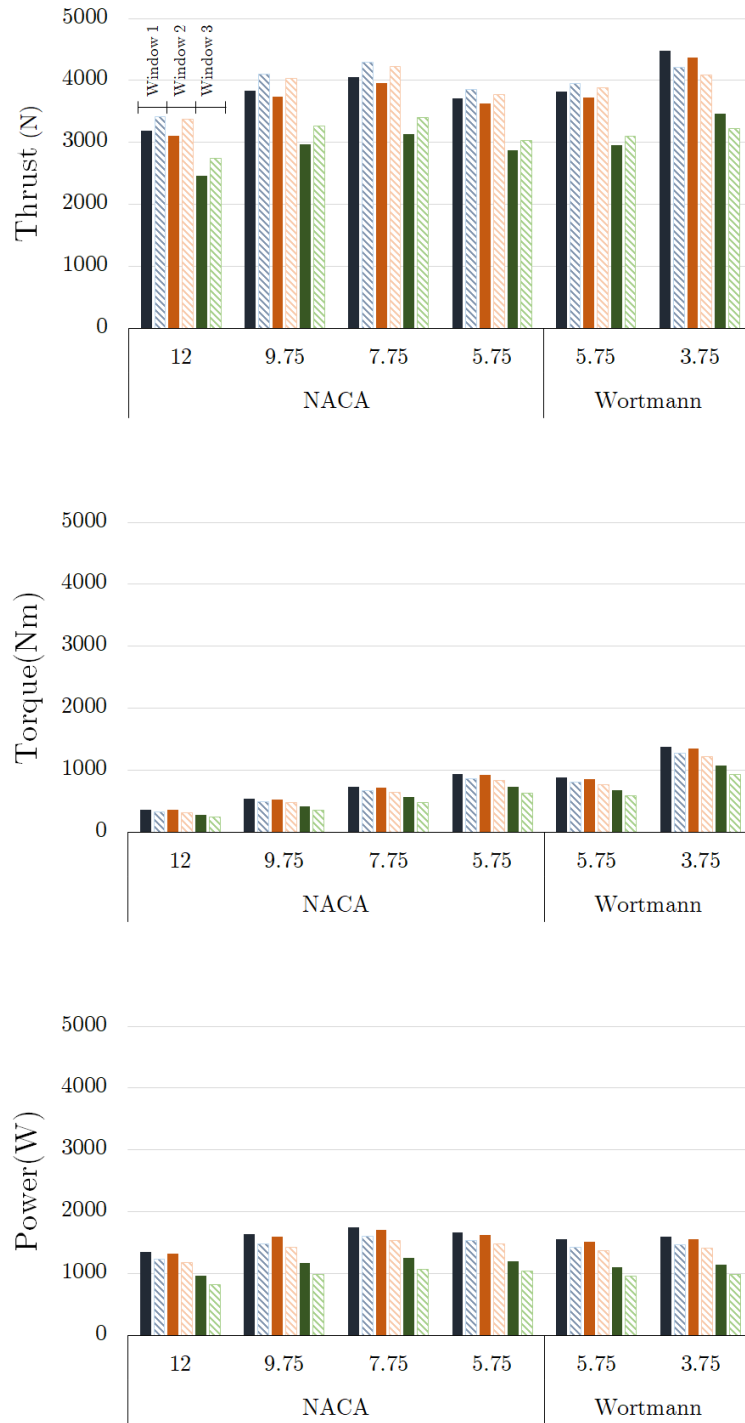


Figure 7.9: Turbine performance for Mexico Transect D

Technical Performance of Designed Blades in Characteristic Sites

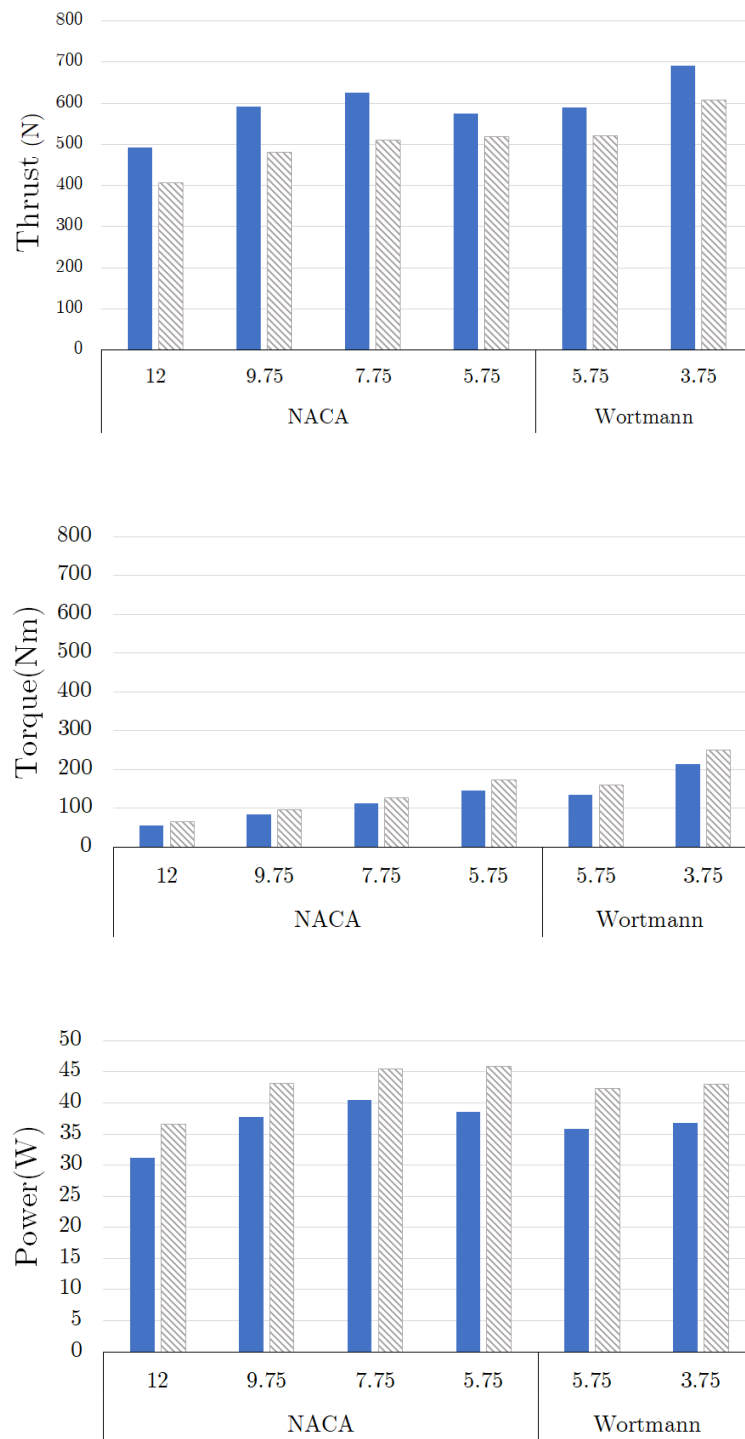


Figure 7.10: Turbine performance for Philippines Median Case

Technical Performance of Designed Blades in Characteristic Sites

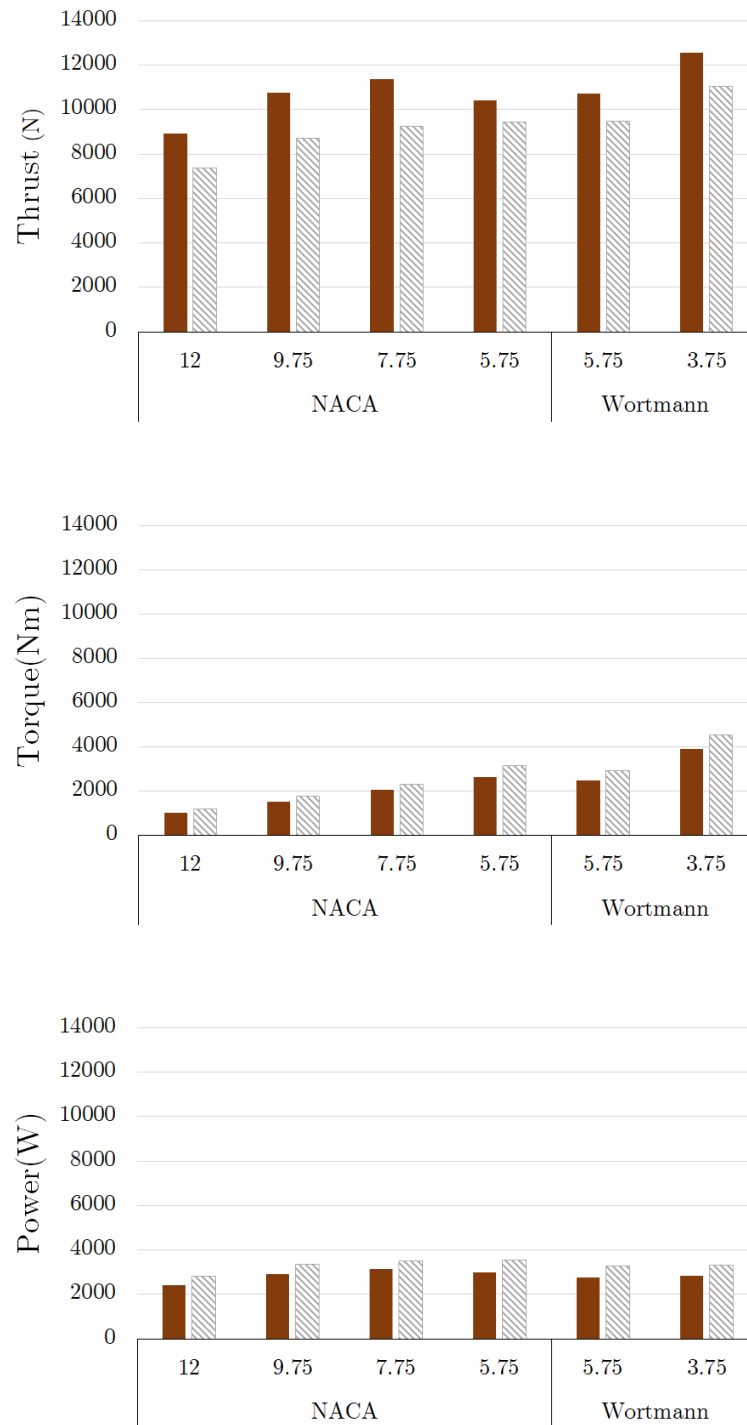


Figure 7.11: Turbine performance for Philippines Max Case

Mexico. For Transect A, the incorporation of the velocity profile led to an increase in thrust, torque, and power. This is expected since a negative value for α_{prof} increases the total average velocity across the rotor, and the reverse is true for a positive value of α_{prof} .

The apparent increase in thrust for almost all cases can be explained by how the uniform flow is modelled vis-a-vis the profiled flow. The steady flow is based on the velocity dictated by the profiled flow at the centre of the hub. This is different from Encarnacion [93] and Mason-Jones [76] who both used the surface velocity for the uniform velocity case.

The power values in Transect D show that the relative power drop when going from a steady flow to a profiled flow is larger as α_{prof} becomes smaller or as the flow becomes more sheared. This is an additional consideration when operating tidal turbines as a decrease in power can largely affect the economics of the technology.

Philippines. An additional case for the Philippines⁴ is added to include the maximum velocity $U_{o,\text{max}} = 0.98\text{m/s}$ modelled when applying the power law fit. This is due to the expected low power output when using $U_o < 0.5\text{m/s}$. No significant difference in trend is observed - the same conclusions from the Mexico case. For the Philippines case, the value of α_{prof} is also negative leading to an increase in power output.

Benefits to Power. In all cases, the torque developed in the rotor is reduced to as much as 50% from the base case. This poses both a benefit and drawback since lower torque means that the torque requirement for the generator can be reduced but may require a starting motor to overcome the inertia of the system when operating from rest.

Nonetheless, the reduction in torque reduces the loading while power output remains comparable for all rotors except for the TSR12 NACA rotor that sees at least 10% reduction in power. Thrust loads are also generally greater for rotors with lower optimal

⁴For all bar graphs, solid bars correspond to uniform velocity within the water column while diagonally-shaded bars correspond to profiled flow.

TSR with the base Wortmann FX63136 TSR3.75 rotor developing the largest thrust across all cases.

7.3.2 Wave Loading

The Philippines data include the results of simulations with 3-hr intervals. This data is processed and categorised as in Table 7.4. However, since the current BEM code can only handle waves that are concurrent with the tidal flow, only following waves are considered. Table 7.4 gives the significant wave height H_s as 0.4909m and wave period T_p as 5.993s. Simulations were done at $U_o = U_{o,max} = 0.98\text{m/s}$, with the hub at the middle of the water column ($h = 10\text{m}$).

Figure 7.12 shows the relative current numbers that a turbine (NACA TSR12) is subjected to, considering wave-current interactions. The relative current numbers seem to be within the reasonable region wherein Faudot [87] has found little to no variation in torque and thrust load. However, it is apparent that relative current numbers with current wave setup remain higher for energetic sites than that of less energetic sites. Though the calculated numbers suggest that it can be expected that there will be little variation in loads, other wave setups may do produce different results and push the relative current numbers for less energetic sites towards smaller values.

Technical Performance of Designed Blades in Characteristic Sites

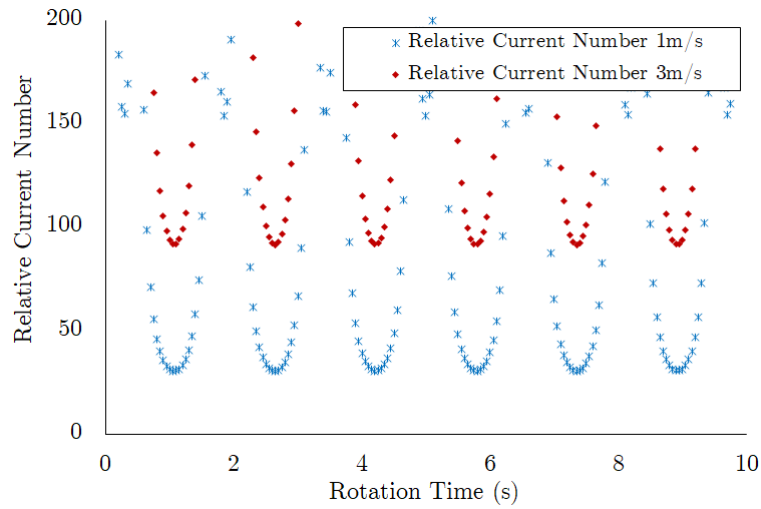


Figure 7.12: Relative Current Numbers for different current magnitudes at blade root. The relative current number is calculated using the unsteady BEM code where the blade root rotates over rotor plane. This leads to an oscillation of the relative current number. However, most of the values fall within values of 30 for $U_\infty = 1\text{m/s}$ and 90 for $U_\infty = 3\text{m/s}$.

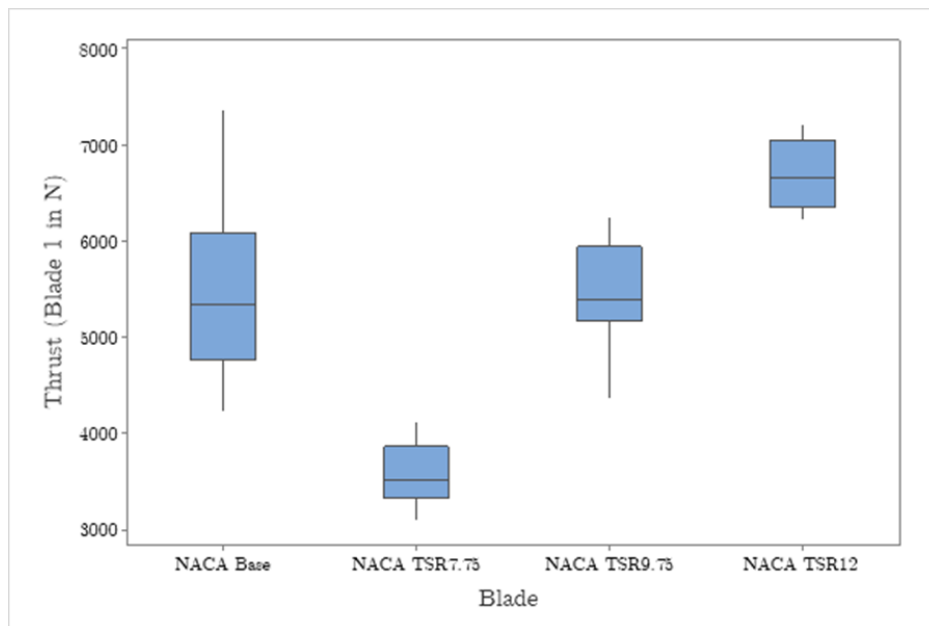


Figure 7.13: Variation in Thrust for NACA Blades given under wave loading ($H_s = 0.4909\text{m}$, $T_p = 5.993\text{s}$, $h = 10\text{m}$, $U = 0.98\text{m/s}$)

Technical Performance of Designed Blades in Characteristic Sites

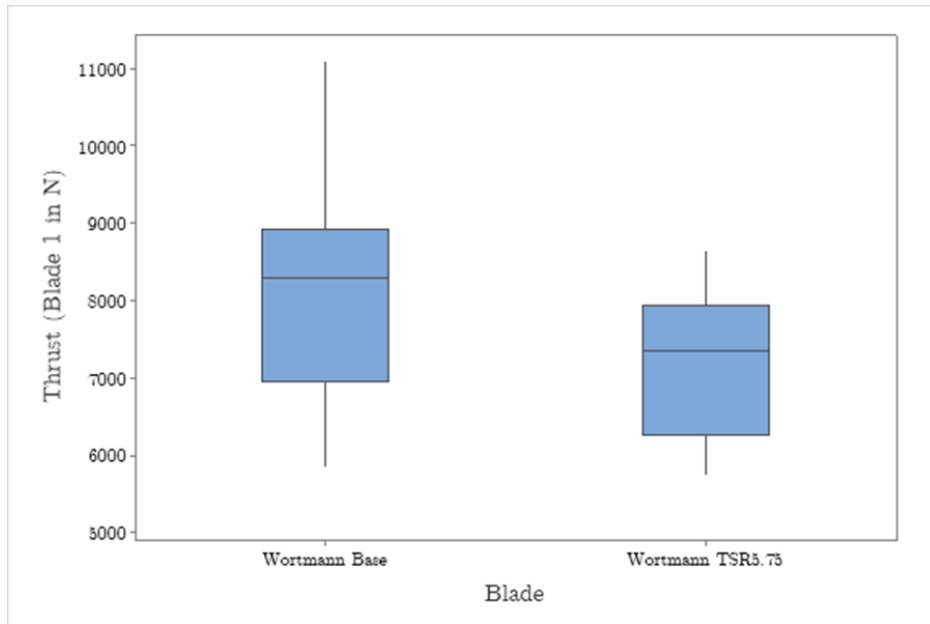


Figure 7.14: Variation in Torque for NACA Blades under wave loading ($H_s = 0.4909m$, $T_p = 5.993s$, $h = 10m$, $U = 0.98m/s$)

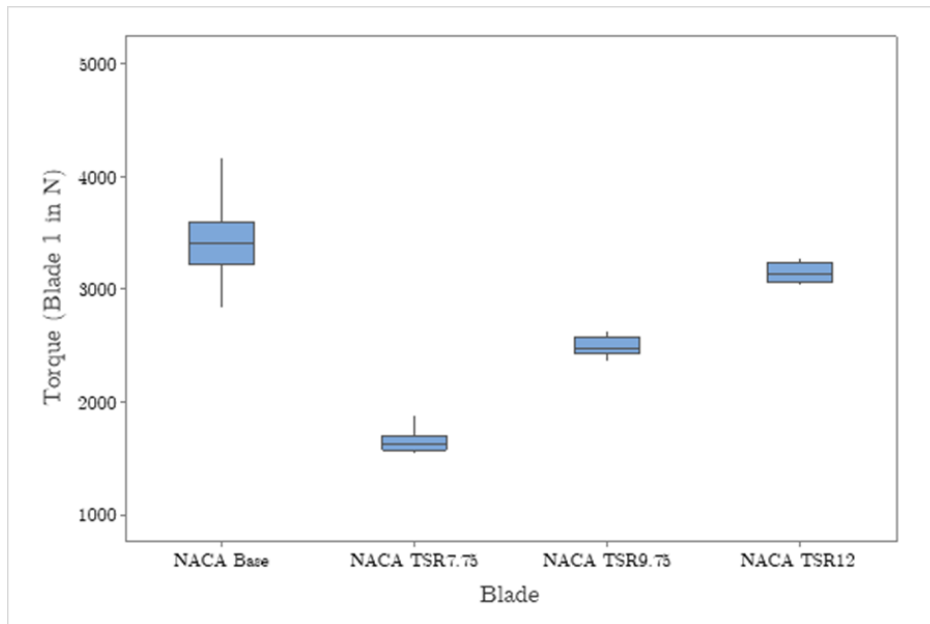


Figure 7.15: Variation in Thrust for Wortmann Blades given under wave loading ($H_s = 0.4909m$, $T_p = 5.993s$, $h = 10m$, $U = 0.98m/s$)

Technical Performance of Designed Blades in Characteristic Sites

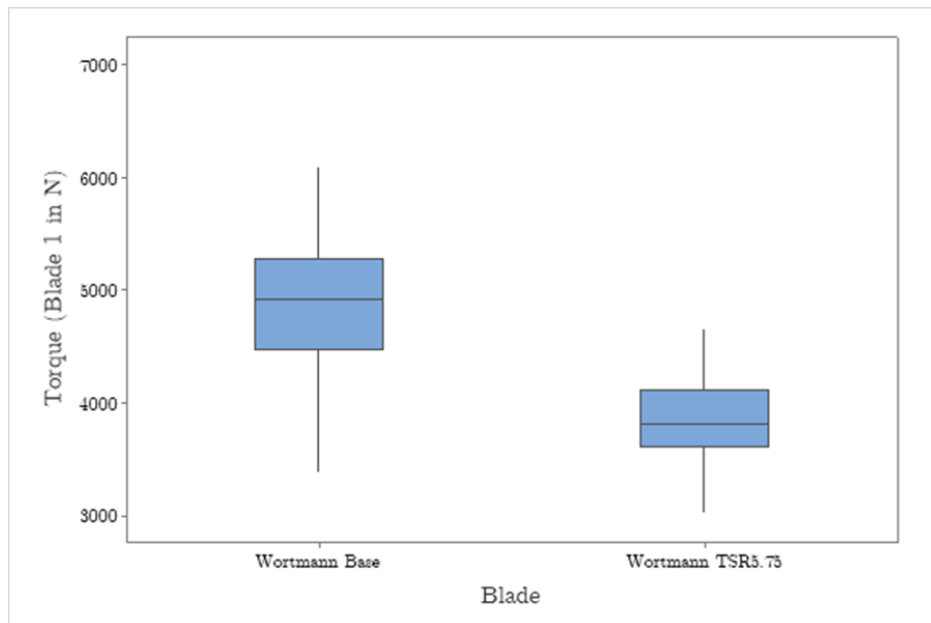


Figure 7.16: Variation in Torque for Wortmann Blades given under wave loading ($H_s = 0.4909m$, $T_p = 5.993s$, $h = 10m$, $U = 0.98m/s$)

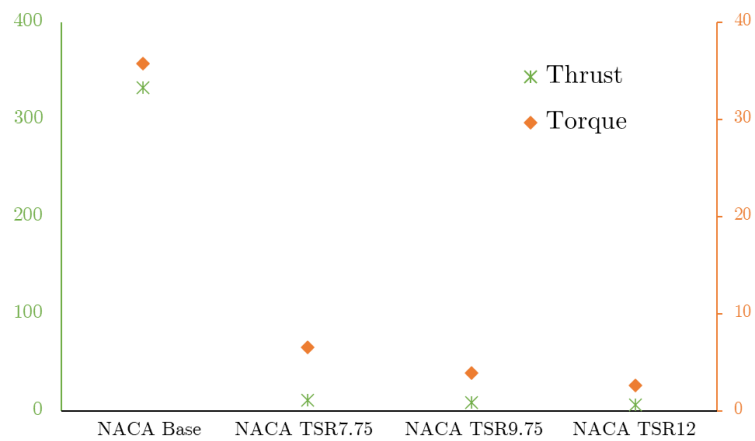


Figure 7.17: Trend in Coefficient of Determination for NACA Blades (left axis, *: thrust; right axis, \diamond : torque)

Technical Performance of Designed Blades in Characteristic Sites

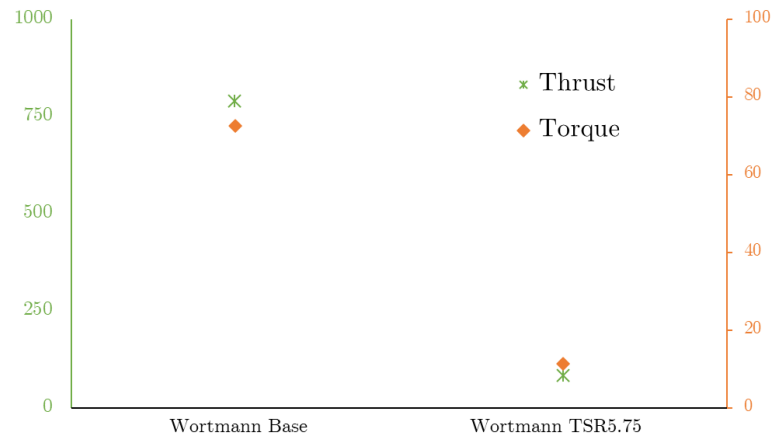


Figure 7.18: Trend in Coefficient of Determination for Wortmann Blades(left axis, *: thrust; right axis. \diamond : torque)

The thrust and torque experienced by a single blade when waves are included are shown in Appendix H. There are two points of discussion when waves are included: the number of cycles per unit time, and the effect of waves on the sinusoidal loading which is an effect of the profiled flow. As expected, the number of cycles per unit time increases as the operational TSR is increased. The increase in loads in one blade combined with the higher number of cycles indicates higher fatigue loading and may decrease lifetime. It can be implied that adopting the TSR7.75 blade is most beneficial since the power output is not drastically reduced due to the higher rotational speed of the TSR7.75 compared to the base blade, and loading is reduced.

However, there is benefit to increasing the operational TSR of turbine blades as shown in Figures 7.13 to 7.16. Here, the variation in the torque and thrust loads are significantly reduced for higher TSR rotors compared to the low-TSR base blades.

7.3.3 Annual Energy Production with Theoretical Power Curve

At this point, all of the calculations on the power output only takes the velocity profile without taking into account variability in flow. That is, it assumes that there is steady flow, using the velocity profile, over the rotor. This does not typically happen in reality.

The IEC TS 62600-200 standard [185] calculates the power output, or more appropriately, the annual energy production (AEP) using the method of bins. This

has been applied to get the AEP for the Mexico⁵ site with the following assumptions:

1. An ideal control method is applied. There is perfect adherence to maximum power point tracking (MPPT) [122] until the point of rated power.
2. The turbines are always operating at maximum C_P but the corresponding RPMs change to match the value of $TSR_{C_{P_{max}}}$ at different values of U_∞ .
3. Turbines are rated at 1m/s, 1.5m/s, and 2m/s with a corresponding cut-in speed of 0.3m/s, 0.45m/s, and 0.6m/s. This follows the standardised power curve for tidal turbines proposed by Lewis et al. [186] wherein the cut-in speed is set at 30% of the rated speed. The reported velocity in Figure 7.20 are the rated speeds of each turbine.
4. It is recognised that the Mexico site features an oceanic current. The values are for AEP are used for comparison since the cost model is more applicable to tidal turbines operating under tidal currents. Additional discussion for comparison against diesel values in Chapter 8 do not take into account differences in needed material and turbine structural support between tidal current turbines and oceanic current turbines even if their hydrodynamic design may remain the same.

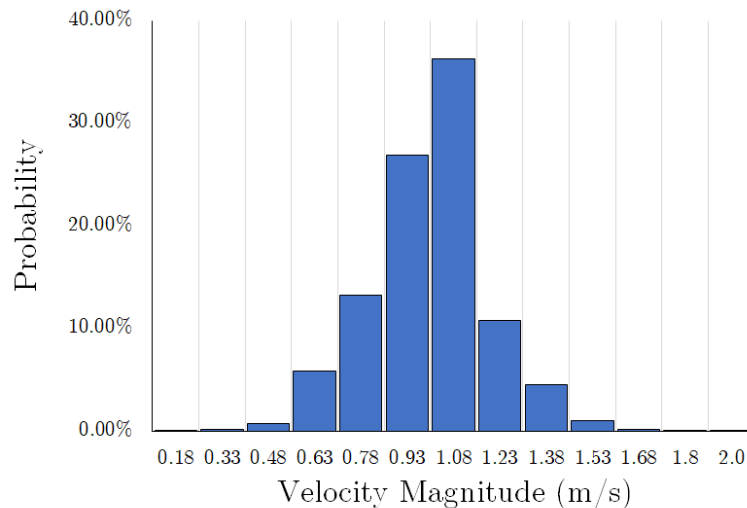


Figure 7.19: Histogram of Velocities

⁵Lack of geographical identifiers and other data on the Philippines site prevent its inclusion on calculation of AEP according to the standard.

Technical Performance of Designed Blades in Characteristic Sites

All AEP calculations in this Chapter considers an 80% power efficiency. This should not be confused with the calculated power loss in Chapter 8 wherein additional calculations on power loss according to the RPM and size of the generator is considered. Appendix G shows a sample calculation of the AEP.

The presentation of bins is different from the presentation in the standard but follows the same concept (number of data points vs frequency distribution). Additionally, all values are taken at hub height.

AEP trends follow the trends of C_P due to the assumptions of ideal operation and perfect adherence to maximum power point tracking. It can be observed that there is no apparent difference at the 2m scale from MWh perspective. Additionally, high-TSR rotors outperform its low-TSR counterparts the smaller the scale, in both rated power and diameter, of the turbine. This is true up to $TSR = 9.75$ where a drop in AEP is consistent across all configurations thereafter. There is also no significant improvement in the the AEP when opting for 2m/s rated turbine and this is mainly due to the limitation in the resource.

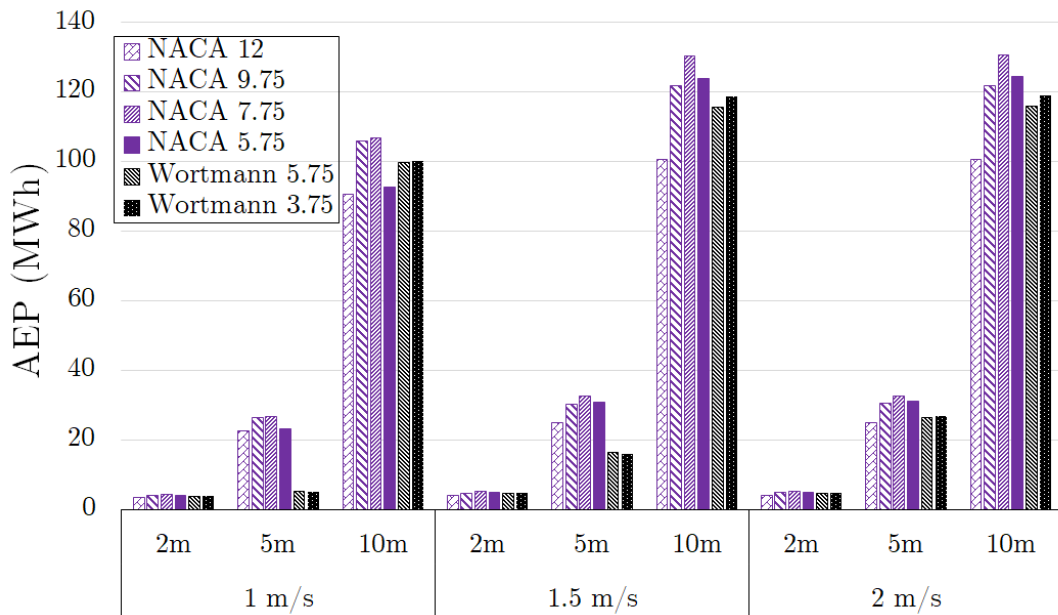


Figure 7.20: Annual Energy Production for turbines with different rated flowspeeds (1, 1.5, 2m/s)

These AEP values are used in the levelised cost of energy (LCOE) calculations in

7.4 Summary

The chapter presented the profile fit for representative sites. The resulting profile fit leads to power laws that are characteristic of highly sheared flows, different from what is dictated by the $1/7^{th}$ power law. This implies the unsuitability of the $1/7^{th}$ power law, typically used for modelling within energetic currents, on modelling currents with less energetic flow.

The analysis on the performance using the different velocity profiles show that less power output is expected for high-TSR rotors owing to the lower $C_{P_{max}}$. However, both torque loads and thrust loads are also reduced for high-TSR rotors which may have implications in the design of support structures and auxiliary systems. Additionally, high-TSR rotors are less susceptible to load variation induced by the waves that have increased effect in less energetic currents as evidenced by lower relative current numbers.

High-TSR rotors, though having relatively lower rated power output are more appropriate for less energetic currents as evident with AEP estimates using the IEC TS 114 62600-200 standard. This is true up to a TSR of 9.75 with AEP dropping significantly thereafter. Higher rated turbines or generators are also not recommended for less energetic sites since available power is concentrated at lower current magnitudes.

Chapter 8

Economic Evaluation of Designed Blades

Section 3.2.2 discussed the general flow of the design process. Up to now, evaluation was made using the hydrodynamic performance of the rotor. Section 7.3.3 showed a calculation of the AEP but the trends followed the C_P trend due to the assumptions made at this point in the conceptualisation and design of high-TSR rotor.

This Chapter develops the economic evaluation of the rotors to determine whether the hypothesis of increasing the optimal TSR operation for a rotor improves the cost for tidal turbines in less energetic currents.

8.1 Cost Modelling

Section 3.1.1 discussed the cost breakdown for a typical turbine array. It was shown that a big part of the cost (20%) is driven by installation, which includes local fees for vessels, transport, labour, and other specialists. A change in the design of the rotor has the capacity to affect 51.5% (rotor, PTO, support, commissioning) of all costs associated with a tidal turbine. However, cost can vary from region to region and the design shift towards higher TSRs adds another layer of uncertainty from on the cost estimate for tidal turbines.

Exact values cannot be determined without further analysis of relevant factors/effects. It is at least possible to estimate costs starting from the generator, and cascading using the different percentages shown in Section 3.1.1.

The discussion on this section is limited to the costs due to the generator and Appendix E presents a sample LCOE calculation with values presented in Section 8.3.

8.1.1 Generator Configuration

Hart *et al.* [116] developed a cost model that compares different drive train configurations used in a 6MW wind turbine. Four different configurations on gear ratios and rotational speed are analysed from a cost per weight of material perspective.

The cost model separates the gearbox and generator costs making it convenient to isolate the cost associated with the generator. Thus, the cost model is adopted but all configurations are reduced to direct-drive generators and the relationship between cost, and generator rotational speed is made to be proportional to the rotor TSR.

Figure 8.1 shows the modification of the model [116] to fit the purpose of this study. Table 8.1 shows the material weight related to the generator only tabulated from the original model [116].

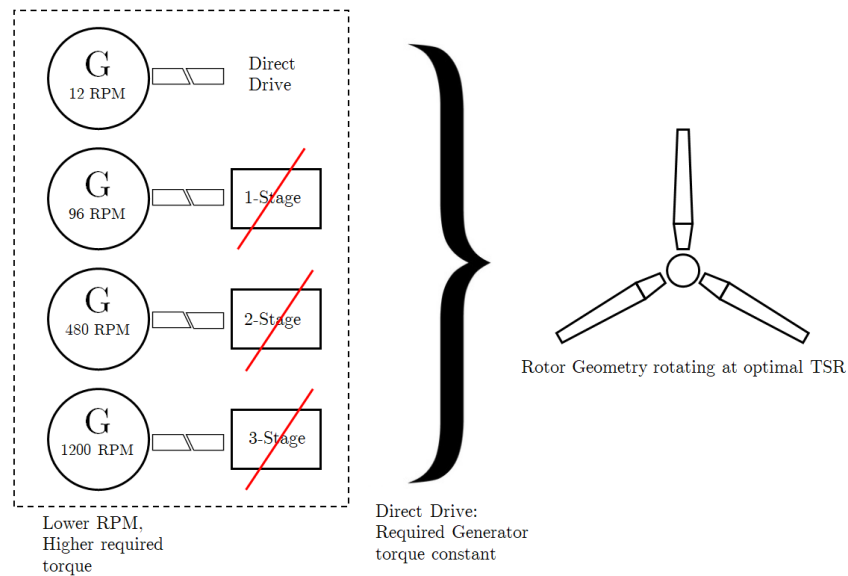


Figure 8.1: Direct-drive configuration for cost modelling

Table 8.1: Drive train configurations and material weight

Drive Train	Gear Reduction	RPM	Material weight (tonne)		
			Iron	Copper	Magnet
Direct Drive	1:1	12	30.6	6.6	2.9
1-Stage Gearbox	1:8	96	6.4	2	0.6
2-Stage Gearbox	1:40	480	3.3	1	0.3
3-Stage Gearbox	1:100	1200	2.8	1.1	0.3

The original direct drive configuration uses the most material since it is the generator that has the highest rated torque and lowest RPM. Since all gearboxes are eliminated for all configurations, higher RPM generators are able to accommodate low torque rotors such as the ones selected in Chapter 6. Figure 8.2 then plots the material weight against generator RPM.

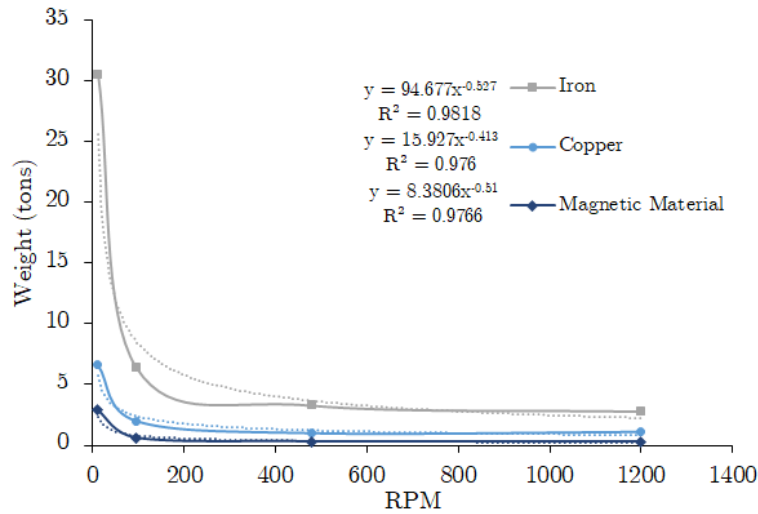


Figure 8.2: Fit for Material Weight (tons) vs RPM

A fitted line is used to predict values outside the defined material weights in Table 8.1. The general equation is

$$Y = aX^n \tag{8.1}$$

where X is the generator RPM and the equation establishes an exponential relationship between the RPM and the weight. This form is adopted since this gives the highest R^2

value without overfitting.

The associated cost for the construction of the generator is then calculated using the following prices: (a) Copper: €15.00/kg [116], (b) Magnets: €48.00/kg [116], and (c) Iron: €0.80/kg [115].

8.1.2 Energy Loss

The model identifies three main sources of losses [116, 187]:

1. Iron Loss - the combined loss due to hysteresis and eddy currents. Both losses have units in J/kg.
2. Copper Loss - the armature loss, which is an important consideration for permanent magnet generators. The generators considered in this cost model are all permanent magnet generators.
3. Converter Loss - the energy loss associated with back-to-back power converters. The amount varies with respect to the modules used to build the generator, the resulting frequency, and temperature [188]

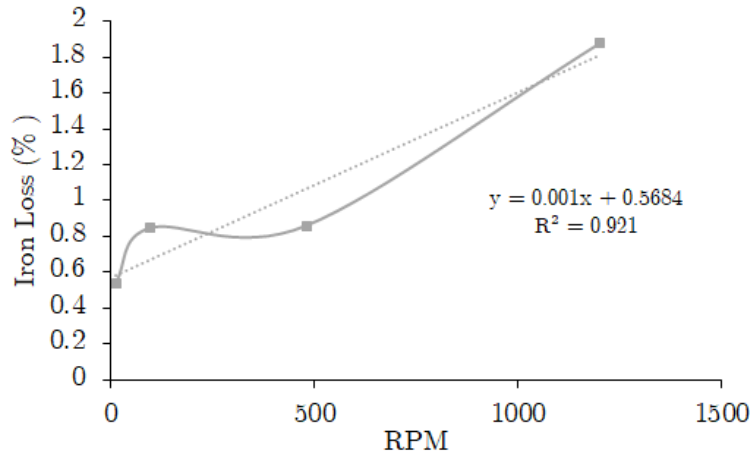


Figure 8.3: Fit for Iron Losses (%) vs RPM

Figure 8.3 plots the iron loss against the RPM after getting the mass from Figure 8.2 and converting it to energy values according to the data provided by Hart *et al.* [116].

Economic Evaluation of Designed Blades

A linear line is used to avoid overfitting; the general trend is that there is an increase in energy loss from iron loss as the RPM increases.

Copper Loss is plotted against torque in Figure 8.4 as the general relationship of $\tau = I\alpha$, where I is the current, dictates. This implies that copper loss decreases as RPM increases since $\tau \propto \omega^{-1}$.

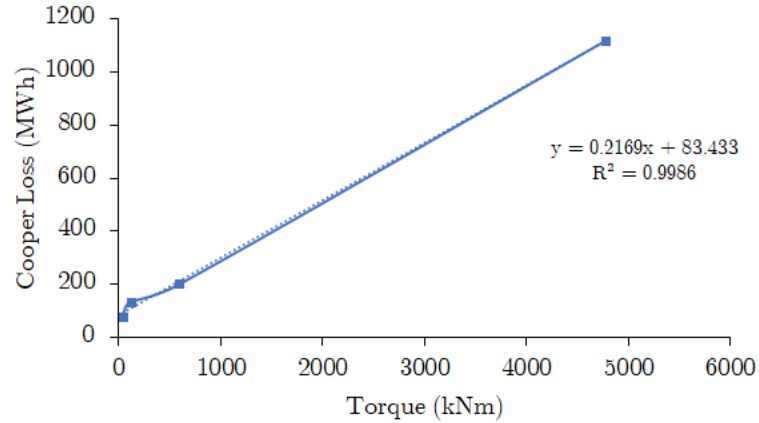


Figure 8.4: Fit for Copper Loss (MWh) vs Torque (kNm)

Converter loss is modelled by Hart *et al.* [116] and Mrcela *et al.* [188] to have a constant value. However, the values from [116] are for a 6MW wind turbine and this cannot be directly adopted for the study of < 1MW tidal turbines. Thus, the maximum efficiency (percentage) for the converter from [188] at 98.52% is adopted.

8.1.3 Availability and Capacity Factor

Turbine availability is a ratio used to measure the amount of time a turbine is able to operate in a given time period [189]:

$$\text{Availability} = \frac{\text{Time available to operate}}{\text{Total time within the period in question}} \quad (8.2)$$

although this ratio does not consider the inflow conditions wherein no power is produced due to the current being too weak. The availability defined here is only concerned on the maintenance and overall state of the turbine - is it capable to produce power if

energy is available?

The costs due to less than 100% availability cannot be easily extracted from [116]. To account for availability, this study adopts the model of Carroll *et al.* [189], which discusses the availability of permanent magnet generators against the distance from shore. The average availability is then set to 92.7%, which is the availability of turbines that are within 20km from shore.

The capacity factor then relates to the time that the inflow conditions will result in power production. This is multiplied by the availability to get the total time that a turbine can produce power, taking into account both the turbine state and the inflow state. The adopted capacity factor in this study is 35% which is not far off from the assumed capacity factor of Lamy and Azevedo [190] at 37%, and is only a percent higher than the capacity factor assumed by Clark *et al.* [191].

8.1.4 Power Scaling

All the values in the foregoing discussion were used to model for a 6MW wind turbine. While generator technology between wind and tidal turbines are shared, the mismatch between the 6MW wind turbine model and the < 1MW tidal turbine designed in this study still needs to be fixed. The values are then scaled accordingly using the scaling law by Shrestha *et al.* [114], which is used to estimate the cost associated with the generator.

The scaling relates the mass of each generator component to the rated power of the generator, and is given by:

$$\frac{m_{\text{genA}}}{P_{\text{genA}}^n} = \frac{m_{\text{genB}}}{P_{\text{genB}}^n} \quad (8.3)$$

Figure 8.5 plots the total generator weight against the total power output as obtained from the data of [114]. The scaling is applied directly to all discussed components as all prices are given as a function of weight with availability and converter loss accounted for in the power production (rated power).

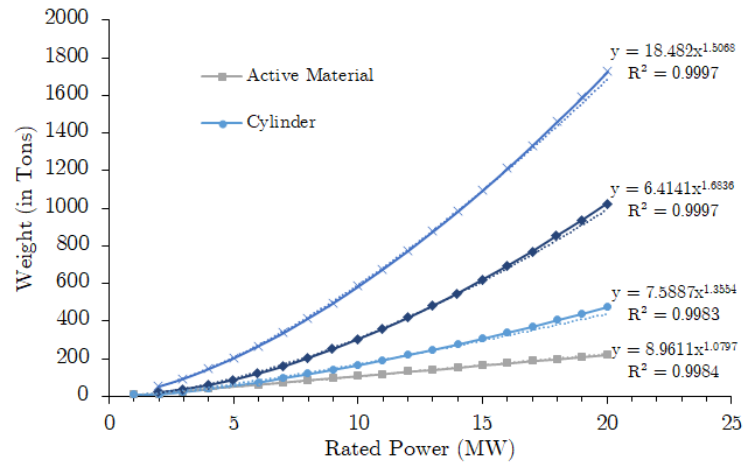


Figure 8.5: Scaling of Weight (tons) with respect to Power (MW)

8.2 Costs considering different inflow and diameter

The cost model is applied to all rotors studied in the previous sections. The power output and resulting costs are calculated for three different inflow speeds and three different diameters at 2m, 5m, and 10m.

8.2.1 Costs due to the generator

The costs due to the generator generally decrease as the operating RPM is increased. This implies that rotors operating optimally at higher TSRs may employ cheaper generators although the cost of cabling and converter units may stay the same.

The cost drops rapidly up until 50RPM wherein cost savings at even higher RPMs are marginal compared to the initial drop. The same trend can be observed in Figures 8.2 from Section 8.1. Figures 8.6 and 8.7 also show that there is a drop in power output (disadvantage) and weight (advantage). There are three different groups of data points for each inflow speeds with each of the groups corresponding to different rotor diameters i.e. a 10m diameter turbine produces the highest power output and weights the heaviest.

Economic Evaluation of Designed Blades

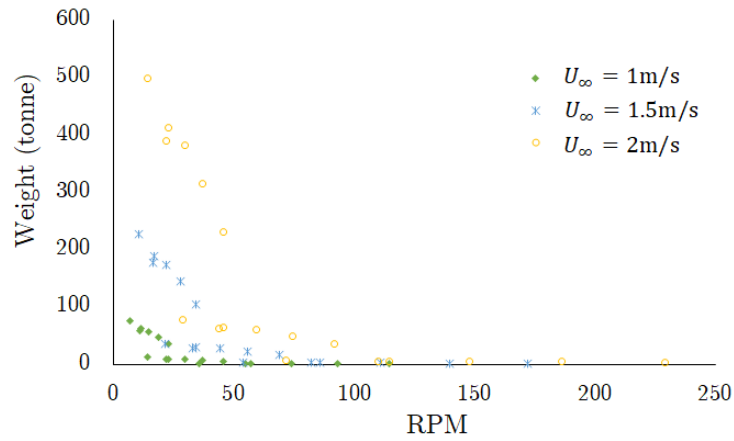


Figure 8.6: Scatter plot of total generator weight (tonne) vs RPM

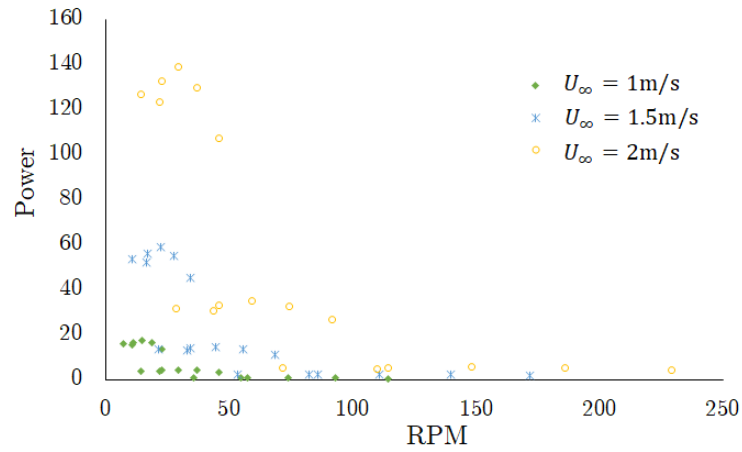


Figure 8.7: Scatter plot of generator power (kW) vs RPM

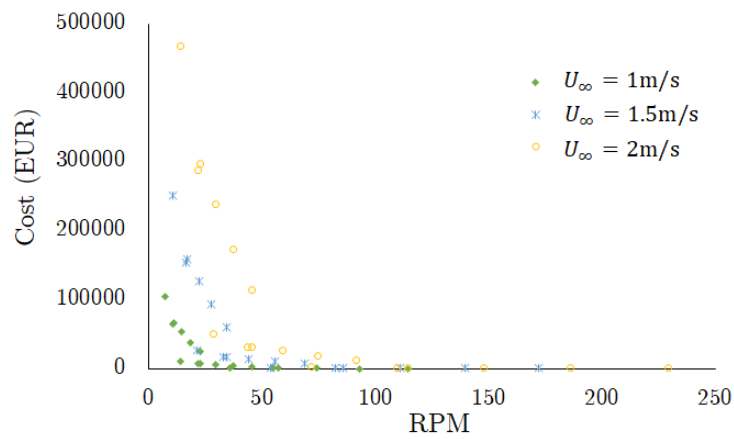


Figure 8.8: Scatter plot of total generator cost (EUR) vs RPM

Combining the cost and power output graph, Figure 8.9 shows the cost/kW for all

Economic Evaluation of Designed Blades

turbine cases. Here, a clear trend is shown with the threshold of about 50RPM still present. This supports the hypothesis that increasing the operational TSR for turbines are beneficial although there exists a threshold before cost savings become marginal. Table 8.2 shows the different design TSRs, which serve as an upper limit considering rotor diameter and inflow speed. Certain design TSRs are not feasible e.g. 26.25, while others do not present a high-TSR rotor case e.g. all 2m diameter rotors. A design TSR of 6.56 and 8.75 is seen to be feasible in addition to the fact that these are 5m diameter rotors that may produce a reasonable amount of power (Figure 8.10).

Table 8.2: Maximum Design TSR points considering Rotor Diameter and Inflow Velocity

Rotor Diameter (m)	2			5			10		
U_∞ (m/s)	1	1.5	2	1	1.5	2	1	1.5	2
Max Design TSR	5.25	3.5	2.63	13.13	8.75	6.56	26.25	17.5	13.13

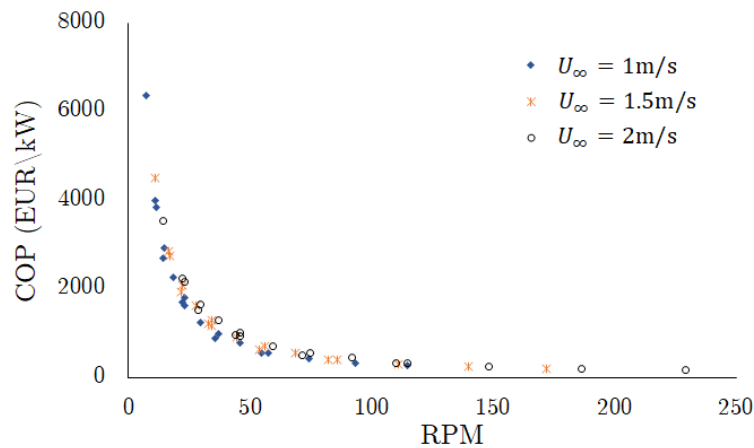


Figure 8.9: Scatter plot of cost of power (EUR/kW, generator only) vs RPM

8.2.2 Turbine Sizing

Power Output

From the perspective of power output, increasing scale is attractive especially since it has been shown in industry that increasing diameter improves economic viability and base load capability.

Economic Evaluation of Designed Blades

Isolating for the effects of turbine sizing by setting a fixed velocity magnitude of $U_\infty = 1.5\text{m/s}$, it can be seen that the relative difference in power output between each rotor geometry remains relatively constant for a given rotor diameter.

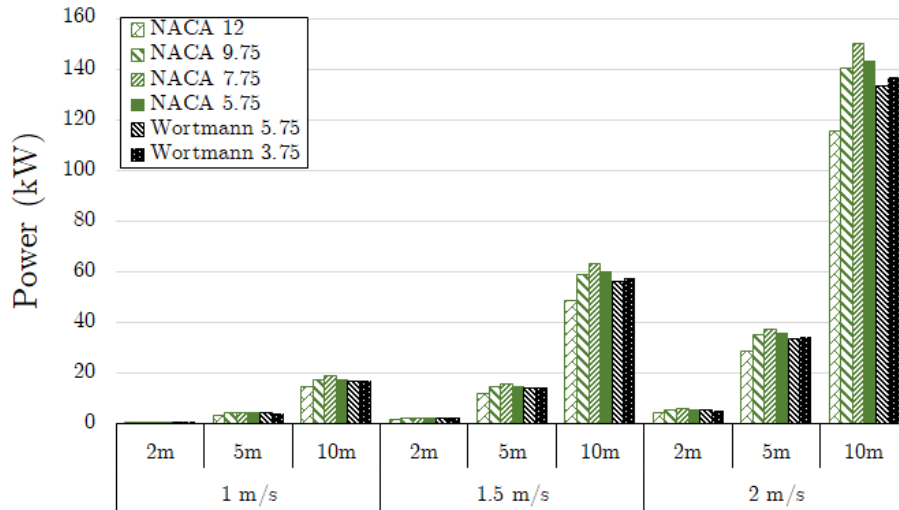


Figure 8.10: Comparison of Power considering multiple diameter rotors

Energy Cost associated with generator only

The cost per kW of power output remains to be best for the rotor with the highest TSR operation. However, the reduction in cost, as per the previous discussion on the threshold at 50RPM, is reduced since $\omega > 90\text{RPM}$ for a 10m TSR12 NACA rotor. Nonetheless, there is great benefit when a 5m TSR12 NACA rotor is adopted since it operates at $\approx 55\text{RPM}$. This minimises the disadvantage of the high TSR rotor seen when upscaled to 10m.

Figure 8.11 also shows that costs shoot up exponentially when upscaling the rotor. This is contrary to the general consensus although, additional costs such as turbine foundation and underwater cabling, which are considered less flexible, need to be accounted for since these are included in quantifying the economic viability of renewable energy technology.

Comparing within the same geometry i.e. Wortmann vs Wortmann, there is an observed improvement in cost/kW when the operational TSR is increased. The average drop in cost/kW in the Wortmann rotors is at 36.4% across all diameters, and 23.1%,

51.3%, 85.6% (TSR7.75, TSR9.75, TSR12) for the NACA rotors with the base NACA as reference.

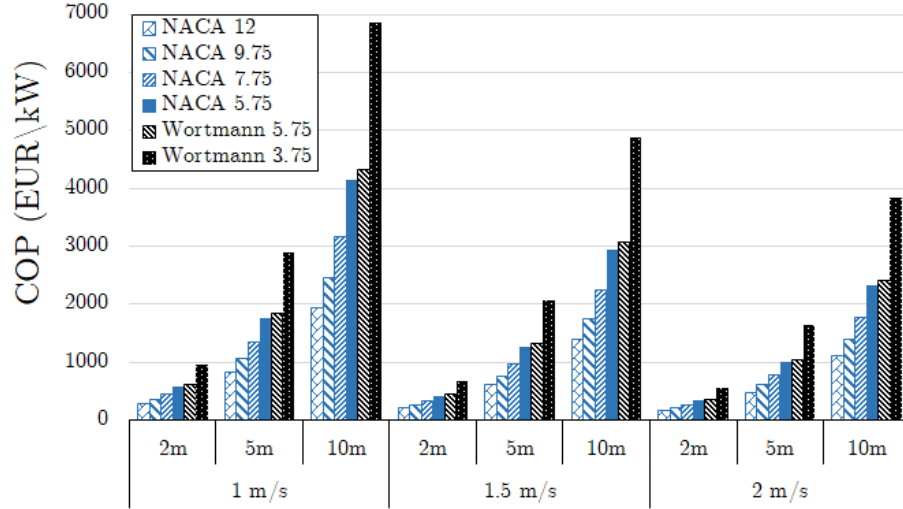


Figure 8.11: Comparison of cost of power (COP EUR/kW, generator only) considering multiple diameter rotors. Note that the figure does not take into account project lifetime.

8.3 Levelised Cost of Energy

The levelised cost of energy is a useful measure to evaluate the economic viability of different energy technologies. It is a measure of the total cost of electricity produced over the lifetime of the energy technology/project.

Equation 3.1 can further be expanded to include elements of cost as identified by Johnstone et al. [105].

$$LCOE = \frac{ICC + COM + OM_{\text{fixed}}}{AEP \times n} + OM_{\text{variable}} \quad (8.4)$$

where

1. *ICC* or CAPEX: Initial Capital Cost which is the cost associated with the device, equipment, and installation
2. *COM*: Cost of Money over the capital calculated over the term of the project such that it is fully paid by the end of its useful life at an annual interest rate of

Economic Evaluation of Designed Blades

10% per year.

3. OM_{fixed} or $OPEX_{\text{fixed}}$: Cost of Operation and Maintenance over the lifetime of the project
4. OM_{variable} or $OPEX_{\text{variable}}$: Cost of consumables for power generation i.e. fuel costs, calculated in cost/kWh.

However, since OPEX is usually presented as an annual average¹ and taken as a percentage of CAPEX, Equation 8.4 can be simplified to:

$$LCOE = \frac{ICC + COM}{AEP \times n} + OM_{\text{fixed, annual}} + OM_{\text{variable}} \quad (8.5)$$

The annual energy production (AEP) is multiplied by the total number of operational years (n). This takes into account the projected energy production over the lifetime of the project. Thus, the LCOE have the units of cost/kWh produced on a yearly basis.

Equation 8.4 may also be expressed using

$$LCOE = \frac{(FCR \times ICC) + OM}{AEP} \quad (8.6)$$

where FCR is the fixed charge rate on the capital per year. Note that the AEP is not multiplied to n as both numerator and denominator gives cost and production on a yearly basis.

8.3.1 CAPEX Estimates

Section 8.1 focused on the calculation of cost derived from a direct drive generator. This essentially removed the cost related to the gearbox and other auxiliaries needed to ensure proper operation of the gearbox. Of course, there are other sources of cost within the device and the generator is but a single component.

While it is difficult to accurately calculate the total cost associated with the total system design using high-TSR blades, it is possible to estimate the capital cost using the

¹The maintenance of turbines can be scheduled every 1, 2, 5, etc. years

values in Section 3.1.1 (Figure 3.4) where 13.5% of the total capital cost is attributed to the PTO. There are, however, other adjustments needed to incorporate other changes in design due to the change in the overall operating regime induced by the high-TSR blades.

Changes in CAPEX

Three other components of capital cost is hypothesised to change. The discussion here revolves around the base case using low-RPM high torque rotors/generators installed in less energetic currents. The total system design of the alternative revolves around the high-RPM low torque direct-drive generators coupled to the designed high-TSR rotors.

All other drivers for cost (export power system, nacelle and subsystems, rotor) are based on equations by Segura *et al.* [95] with updated values to match the scale (1.2MW for Segura [95] down to <160kW for case study) using Bertheau *et al.* [192] for submarine and ground exportation power cables. Appendix E shows a sample calculation for the LCOE values presented in this section and Section 8.3.4.

Cost due to Vessels and Labour. The cost due to vessels account for about 63% of the total installation cost. Reducing the installation cost provides a great benefit for tidal turbine technology. Wind Power Monthly [193] notes that smaller vessels can be about 65% cheaper than the usual large vessels used for installation of tidal turbines. This may be the main driver at this point since larger and heavier turbines will require larger and more specialised vessels.

The number of blades can also play a huge part with two-bladed turbines enabling the possibility of working on the ground, while three-bladed turbines require hoists to assemble within the same work area. These two-bladed rotors are included in the results presented in Chapter 6 - the TSR9.75 and TSR12 blades. However, the discussion in Section 7.3.2 presents both an advantage for high TSR blades - reduced variation but a possible increase in fatigue loads.

While the TSR7.75 blade is a three-bladed rotor, it is wholly possible to design a

two-bladed variant that can perform similarly. The analysis will need to be expanded to include the developed cost model in the decision model. This can be done with greater accuracy in the cost model as more study in high TSR blades are undertaken.

Cost for foundation. The cost for foundation is also reduced since less energetic currents lead to less loads for the turbine. This is incorporated into the calculation by taking the lowest TSR blade (Wortmann TSR3.75) as the reference cost accounting for 15.75% of the total cost. All others are scaled according to the fraction of the average thrust force acting on the Wortmann TSR3.75.

Below is a summary of predicted changes. The percentages (%) in the parentheses are all derived from Segura [95] as shown in Section 3.1.1 (Figure 3.4).

1. Cost due Vessels (< 20% of total capital cost) ↓↓ - Smaller and less specialised vessels can be used for deployment, as well as maintenance. There can be a huge reduction in cost due to the lower weight of the rotor and the generator i.e. easier to handle.
2. Labour Costs (< 20% of total capital cost) ↓ - There is not enough information on specialists and locally available workforce. However, the number of onboard crew can be reduced if the rotors are downsized. Conservative estimates place labour costs as constant but it is predicted to go down.
3. Foundation (15.75% of total capital cost) ↓ - Less load is expected although the blade structure needs to be optimised for structural integrity.

Meanwhile, there are also components where no change in cost is expected.

1. Rotor (2.25% of total capital cost) - There is no change expected for the cost of associated with the rotor since any decrease in material may be offset by the need for stronger and more durable blades. This is evidenced by the large deflections observed during small-scale testing (Section 5.1) that led to reduced performance.²

²The velocity during small-scale testing was 1 m/s and it is estimated that the deflections will be reduced if full-scale turbines are deployed in a site with the same velocity. Nonetheless, the increase in cost is allowed/predicted to ensure structural integrity given the reduced cross-section of the blades.

Economic Evaluation of Designed Blades

2. Cabling (30% of total capital cost) - There is no change expected for the cost of export power cabling since this is unaffected by the components in the nacelle and the rotor. However, cabling costs may vary when considering array sizing.

CAPEX trends

Figure 8.11 showed that the cost of power is directly proportional to the scale of the rotor. Figure 8.13 follows this closely although a levelling off is seen for many of the rotors. This levelling off is due to the high cost associated to the export power system (submarine cables, transformers, etc.) as shown in Figure 8.12, which remains to be relatively fixed no matter how small the generator. This is evident in Figure 8.13 with the 2m diameter rotors having almost the same CAPEX as the 5m turbine.

Nonetheless, solely from a CAPEX perspective, higher TSR rotors become more cost effective at larger diameters with the TSR12 rotor eventually being the most cost effective at the largest scale of 10m.

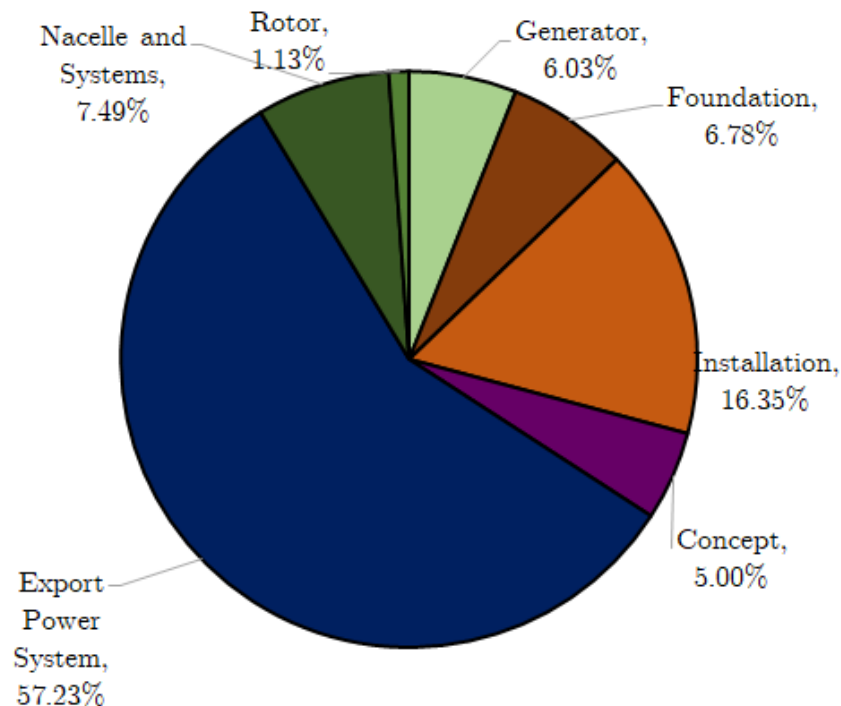


Figure 8.12: Average CAPEX share of components and activities for tidal turbine installation

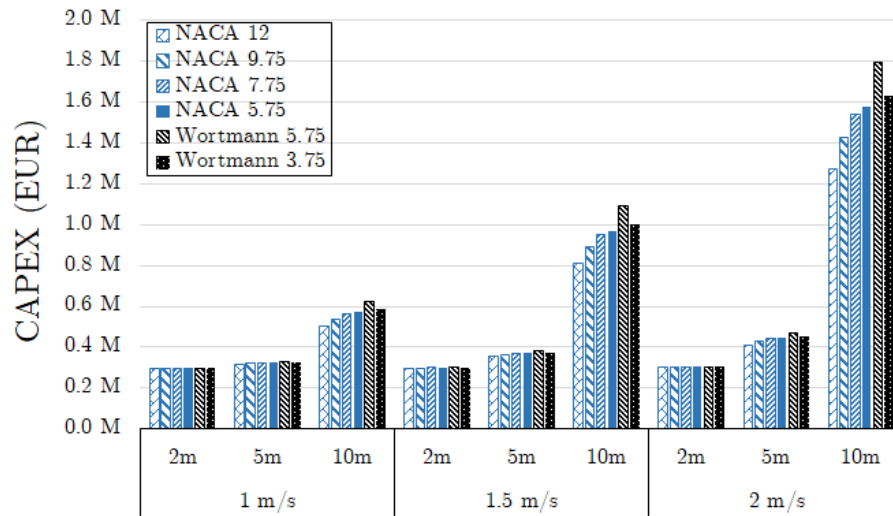


Figure 8.13: Estimated CAPEX (EUR) considering multiple diameter rotors

Note that the above calculation only takes into account the CAPEX for one turbine. Section 8.3 further investigates the levelised cost with a preliminary investigation on array sizing since.

8.3.2 OPEX Estimates

The operating and maintenance cost may vary according to the site. However, a general assumption may be made such that OPEX is about 4% of the CAPEX [194]. This is also supported by other authors [95,195–197] with actual cost values calculated to have OPEX-to-CAPEX ratio of 2.5-6%.

Increased cost due to perceived cavitation. Issues on cavitation, as discussed in Section 6.1.3, will have impacts on both technical and economic performance. A TSR3-4 blade deployed in energetic currents of 3-4m/s results in about 9-16m/s linear speed at the tip while a TSR7-10 blade deployed in less energetic currents of 1-2m/s results in 7-20m/s linear speed at the tip. It is wholly possible to limit the size of the blade and select lower TSR blades (NACA TSR7.75) but this limits the exploration of possible alternatives in both design and maintenance.

Replacement or rehabilitation of the turbine rotor can be included in routine

maintenance to mitigate the effects of degrading performance. This means that the 2.25% of CAPEX associated with the rotor should be added to the OPEX calculation. A conservative estimate of 1/3 of the usual vessel and labour cost during installation is also added to the OPEX to account for any other vessel requirements during the replacement.

It is indeed possible to manage cavitation using necessary coatings and other methods as detailed by Gracie-Orr [122] such as over-speed regulation (limiting speed), these methods would entail additional cost or move away from the proposed design.

8.3.3 Calculated LCOE of tidal turbine with designed blades

Trends for LCOE are seemingly reversed compared to the trend for CAPEX. This is expected since power is exponentially greater at larger scales and the fixed cost from the export power system is more distributed.

OPEX at 4% CAPEX

Two separate observations are seen: the NACA high-TSR blades are more cost effective than its base blade operating at a lower TSR. The same is not seen for the Wortmann blade although the operation of the higher-TSR Wortmann may still be considered at the lower end at $TSR < 6$. The observation for the NACA holds except for the NACA TSR12 blade that was seen to have least power output. At 5m, the NACA TSR9.75 is comparable in terms of economics (less than 0.01% difference, $LCOE_{9.75} < LCOE_{5.75}$) and the Wortmann TSR5.75 is outperformed by its lower TSR counterpart by at least 8%.

In general, it is not recommended to go for small scale 2m diameter rotors not only because of the high LCOE but also because of the low power output ($P < 1kW$). The calculated LCOE is also considered very high compared to the reported LCOE of 0.08-0.3MW TRL 5 tidal technologies of LCOE (EUR/kWh) = 2.57 [197] and the CFD AR4 projects [11].

Economic Evaluation of Designed Blades

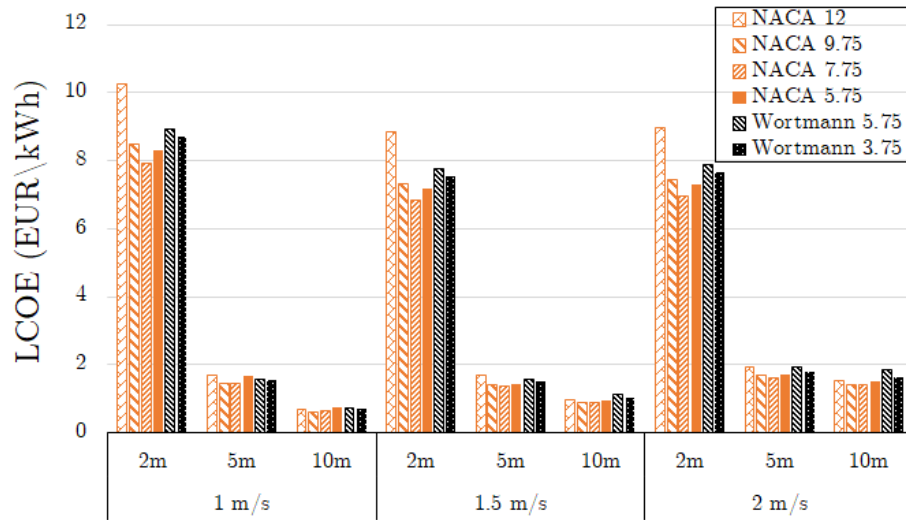


Figure 8.14: Estimated LCOE (EUR/kWh) considering multiple diameter rotors with OPEX at 4% of CAPEX

OPEX at 6.25%+ of CAPEX

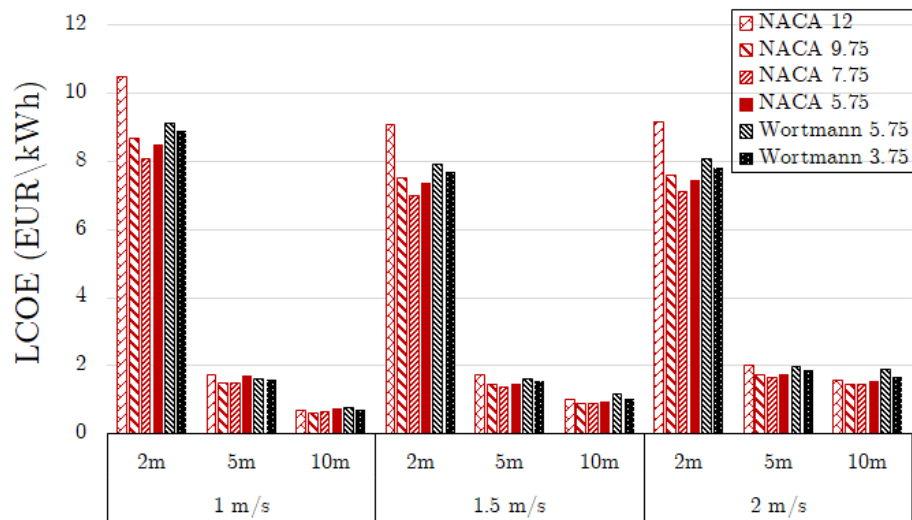


Figure 8.15: Estimated LCOE (EUR/kWh) considering multiple diameter rotors with OPEX at 6.25% of CAPEX

Adding 2.25% of the CAPEX and 1/3 of the installation cost to allow for changing of blades does not change the general trend with respect to LCOE. The estimated

additional OPEX also allows for other methods in lieu of the proposed mitigation mechanism. Cavitation analysis can also aid in further refinement of design and appropriate maintenance schedules.

8.3.4 LCOE Sensitivity with respect to array size

The sensitivity analysis³ in this Section is used to quantify the effect of upscaling by adding more turbines in an array. In all cases, turbine-only costs are fixed at cost/kW values since each additional turbine increase both cost and power output proportionally. Export power system costs are then varied according to the length of the cable used with the rating being changed according to the pricing schedule set by Bertheau [192].

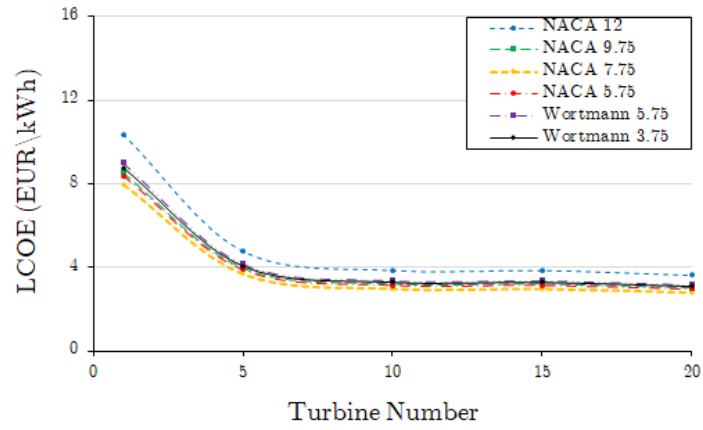
Calculated LCOE values are continuously reduced as array size is increased. This is mainly due to the export power system, and consequently the cost, being shared by many devices even if cost per unit km increases as total capacity increases. This means that the total cost for the export power system increases a bit slower compared to the total power produced.

The biggest drop in LCOE is observed when moving from single device to a 5-device array with LCOE with as much as 54% reduction for the 2m diameter rotors. This reduction effects is reduced at larger diameter rotors since the cable length also increases more substantially when considering an array spacing of 5D. However, LCOE from the 2m diameter case still remains to be high and it is more economically feasible to deploy turbines that are least 5m in diameter.

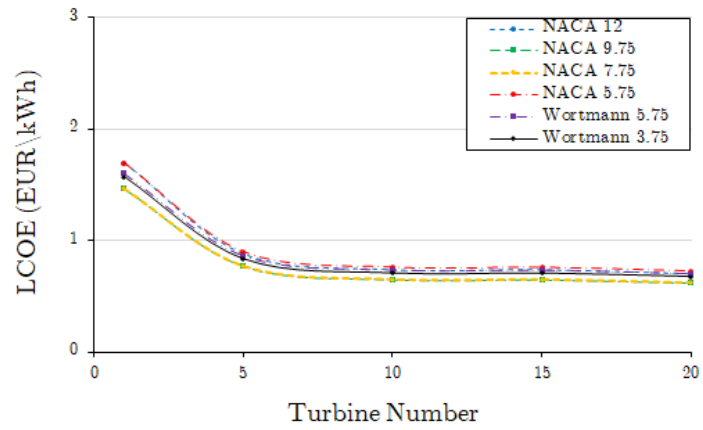
There is no apparent change among rankings of cost effectiveness. The most cost effective rotors across all cases are the NACA9.75 and NACA7.75, which are both high-TSR rotors although the performance of these rotors are more appropriately compared to the base NACA blade with a design TSR of 5.75.

³This is more of a one-at-a-time sensitivity and is more similar to comparisons in diameter as previously presented in this same chapter. This is different from the Global Sensitivity Analysis in Chapter 6 that was done to identify the factor that contributes the most to pushing operation towards higher TSR.

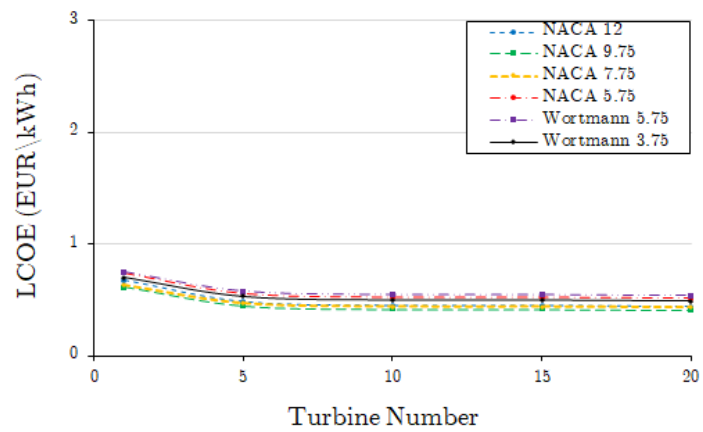
Economic Evaluation of Designed Blades



(a) D=2m



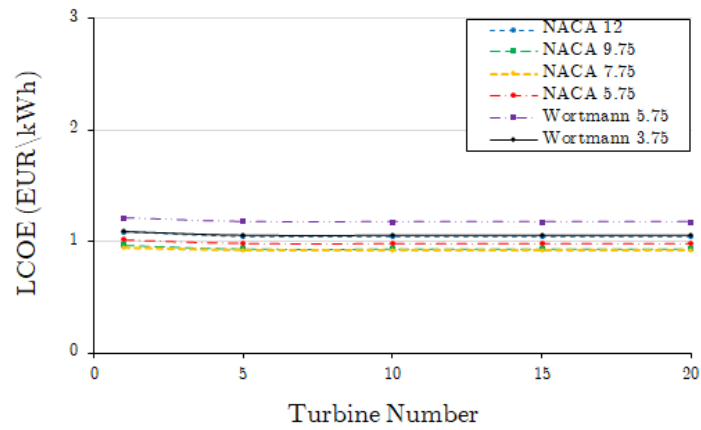
(b) D=5m



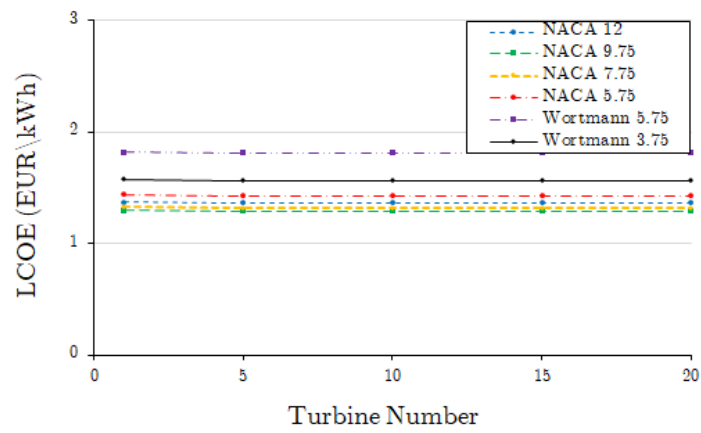
(c) D=10m

Figure 8.16: Sensitivity of LCOE for varying turbine number for arrays operating at 1.0m/s

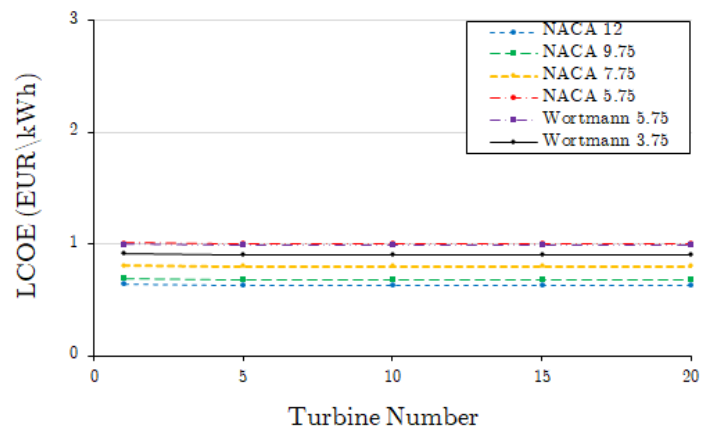
Economic Evaluation of Designed Blades



(a) D=2m



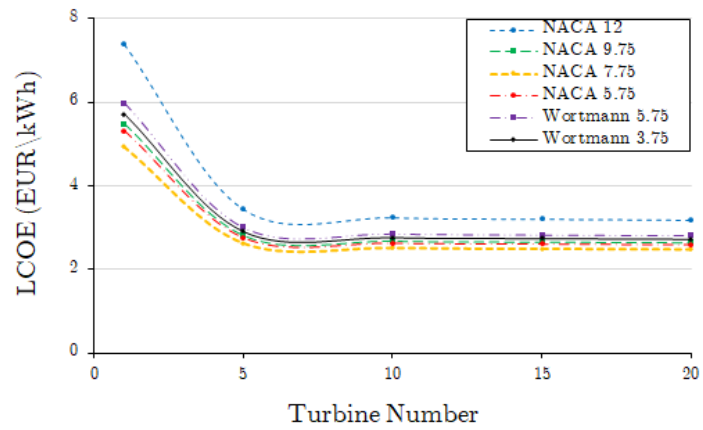
(b) D=5m



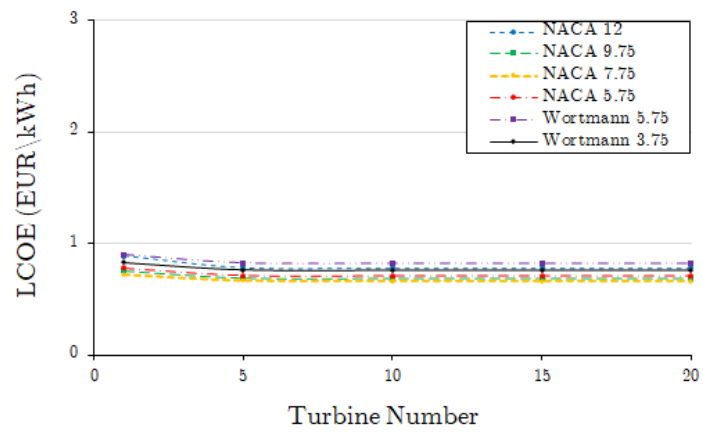
(c) D=10m

Figure 8.17: Sensitivity of LCOE for varying turbine number for arrays operating at 1.5m/s

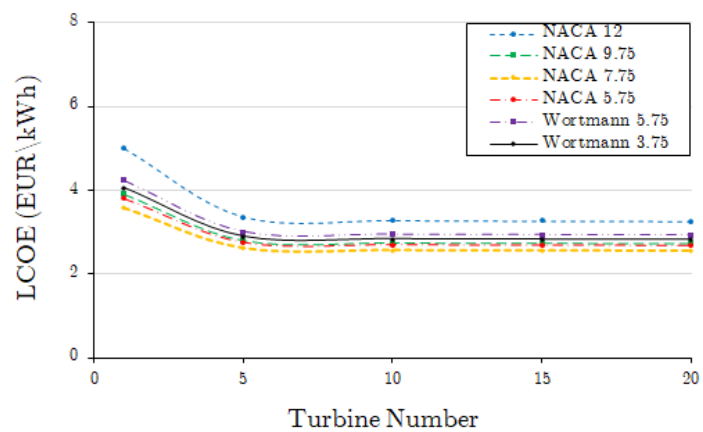
Economic Evaluation of Designed Blades



(a) D=2m



(b) D=5m



(c) D=10m

Figure 8.18: Sensitivity of LCOE for varying turbine number for arrays operating at 2.0m/s

Economic Evaluation of Designed Blades

Table 8.3: Power production in kW for 1, 10, and 20 devices given different current magnitudes and diameter

D	N	NACA Blade TSR			
		12	9.75	7.75	5.75
$U = 1.0\text{m/s}$					
2	1	0.46	0.57	0.62	0.58
	10	4.56	5.69	6.16	5.83
	20	9.12	11.38	12.32	11.67
5	1	3.27	3.98	4.27	4.07
	10	32.75	39.83	42.74	40.71
	20	65.50	79.66	85.49	81.42
10	1	13.34	16.18	17.34	16.53
	10	133.44	161.77	173.41	165.26
	20	266.88	323.53	346.82	330.52
$U = 1.5\text{m/s}$					
2	1	1.73	2.11	2.27	2.16
	10	17.29	21.12	22.69	21.60
	20	34.58	42.23	45.38	43.20
5	1	11.24	13.63	14.62	13.93
	10	112.42	136.32	146.16	139.30
	20	224.84	272.65	292.31	278.59
10	1	45.22	54.78	58.72	55.97
	10	452.24	547.85	587.16	559.67
	20	904.47	1095.70	1174.31	1119.34
$U = 2.0\text{m/s}$					
2	1	4.21	5.11	5.49	5.23
	10	42.07	51.13	54.87	52.29
	20	84.13	102.27	109.75	104.57
5	1	26.75	32.42	34.75	33.13
	10	267.52	324.19	347.51	331.26
	20	535.04	648.37	695.01	662.51
10	1	107.30	129.96	139.28	132.77
	10	1072.97	1299.62	1392.81	1327.69
	20	2145.94	2599.23	2785.62	2655.39

Better LCOE for High TSR at larger diameters. Increasing array size does not really change the findings from the comparison of single turbine cases. The high-TSR rotors are the most cost effective at all sizes. However, it can be observed that the LCOE

Economic Evaluation of Designed Blades

for the NACA TSR12 rotor continuously approaches the LCOE of the other high-TSR at larger diameters. This seem to counter the hypothesis that cost drops because high TSR rotors enable the use of high RPM generators. However, as discussed in Section 8.2, the perceived reduction in cost is exponentially related to RPM and the threshold for substantial cost reduction is at 50RPM.

That is, smaller diameter rotors at a fixed TSR typically rotate faster than there larger diameter counterparts. This means that all rotors all operate with an RPM greater than the discussed threshold of substantial cost reduction at approximately 50RPM. Meanwhile, larger diameter rotors are spread out through the highly sloped region of cost reduction ($<50\text{RPM}$) - higher TSR, higher RPM rotors at this region lead to a substantial reduction in cost. The NACA TSR12 operates at $\text{RPM}>50$ at smaller diameters while having reduced power production compared to its counterparts.

In terms of generator sizing and rating, it is better to go for lower rated generators (1m/s). This can be seen in LCOE when comparing the 1.5m/s and 2m/s rated turbines. In addition to the marginal increase in AEP (Section 7.3.3), the increase in cost (Figure 8.13) actually leads to a slight increase in LCOE.

Considering all cases, average LCOE is best for the NACA TSR7.75 with an average of 4.36% in LCOE reduction from the base NACA. However, the configuration that yields the most reduction in LCOE is the 10m NACA TSR9.75, which yield at least a 9% reduction in LCOE compared to the base NACA; the RPM of such rotor is still less than 50RPM.

A case is made to go for larger turbines provided that the CAPEX and OPEX can be supported as there is large cost of power (Figure 8.11) and it might not be easy to finance such a project. Thus, while the previous figures seem to support going for larger turbines in less energetic sites, it is not recommended to upscale and stick within the 5m to 10m range since no substantial cost reduction is foreseen and power output remains small.

In addition, the findings show that 2m turbines will lead to substantially greater LCOE since an array of 20 turbines at 2m each could only produce upto 84kW ($<0.1\text{MW}$) of power while and 20-turbine array of 5m turbines can produce upto

750kW (0.75MW), which can be enough to power small islands directly connected to a tidal farm project. Table 8.3 show the total power output for the 1.5m/s case where it can be seen that 2m diameter rotors produce too small an amount to be considered.

Comparison of calculated LCOE values to published values. The calculated LCOE values are greater than the calculated LCOE of Klaus [198] of 0.274USD/kWh using a hybrid tidal, solar and battery installation on a 10% interest rate with a 10-year lifetime for the battery and 20-year lifetime for the project. The values are also magnitude greater than the strike price of 178 GBP/MWh from the CFD AR4 results [11]. This shows that the technology for less energetic currents using HATTs are not yet ready for utility scale.

However, these values are comparable to resulting LCOE values using CAPEX and OPEX estimates of European Commission on Maritime Affairs and Fisheries [197] ranging from 0.41-4.11EUR/kWh depending on project capacity. Larger values of LCOE are set for lower TRLs (TRL<4), which is the case for the design in this thesis.

Figure 8.19 compares the calculated LCOE values to the local diesel LCOE of Mexico [199], which is not far from the value LCOE in the Philippines [192]. It can be seen that the the LCOE of the designed rotors are comparable to diesel LCOE.

Economic Evaluation of Designed Blades

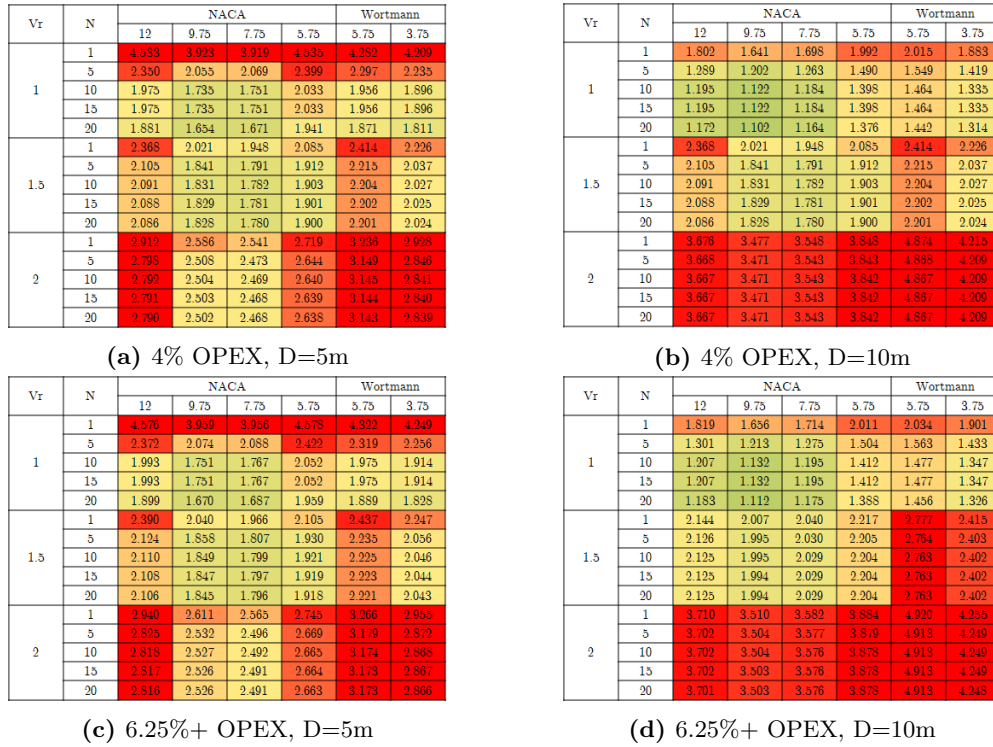


Figure 8.19: Normalised LCOE values against diesel LCOE of 0.37EUR/kWh (2019 value) [192]. Green values are comparable to diesel LCOE; Red highlighted values indicate an LCOE value greater than 2.5x the diesel LCOE.

As previously discussed, the NACA TSR12 blade is more economical at larger diameters. At 5m, the NACA TSR7.75 remains the best among the options. It can also be seen that the rotor with the slowest rotation - the 10m Wortmann TSR3.75 - becomes unfeasible at a current magnitude of 1.5m/s. It is possible that a larger array can make the LCOE lower but at that point, the LCOE values of the faster rotating rotors will also be better. This supports the hypothesis of going for higher RPMs for less energetic currents.

The viability of the designed turbines, especially the NACA TSR7.75 and TSR9.75 is evident. Recent trends in diesel price also support the case for tidal turbines. As discussed in Chapter 7, Cozumel is supported by a single submarine cable and multiple small diesel-fired plants [39]. Adding marine energy to the mix can augment sustainability efforts for the island. The same can be said for the Philippines that has many small island with off-grid connection [176].

8.4 Summary

The chapter developed a cost model to estimate cost reduction when adopting higher TSR rotors connected to the generator via direct-drive coupling. The resulting costs were used to estimate the overall turbine cost using the cost percentage of different components in both CAPEX and OPEX.

A region of substantial cost reduction at about $\text{RPM} < 50$ was observed wherein the cost reduction flat lines afterwards. This results in minimal changes in LCOE at smaller diameter rotors of 5m below. At 10m, the cost reductions are more evident since all rotors are within the 50RPM cost reduction range; high TSR rotors become the most viable in this region.

LCOE values were derived using the CAPEX, OPEX, calculated COM, and AEP (Chapter 7). Larger diameter rotors do see more cost saving due to the aforementioned threshold. However, increasing the rated power of the turbine has negative effects to the LCOE across all turbine sizes.

LCOE reduction is greatest for the 10m NACA TSR9.75 ($\text{RPM} < 50$), yielding at least 9% reduction in LCOE compared to the base NACA. However, the NACA TSR7.75 rotors give an overall improvement in LCOE, yielding an average of 4.36% reduction in LCOE. LCOE values for all cases are slightly greater than diesel LCOE and may be viable if sustainability goals are considered.

Chapter 9

Conclusions and Future Work

The thesis aimed to design a technically and economically feasible horizontal axis tidal turbine rotor for application in less energetic tidal environments. The objectives stated in Section 1.3.3 were formulated towards this aim. This chapter summarises the findings of the thesis and recommends future research pathways stemming from the design presented in this thesis.

9.1 Development of rapid blade design methodology

Usual blade design methodologies used to generate multiple blade designs involve genetic algorithms that vary control points along the blade. This leads to a large number of design parameters with an n -number of control points each for the chord and twist distribution. Additionally, these design methodologies may lead to overly complicated distributions even though similar performance may be achieved by simpler chord distributions.

The developed blade design methodology reduces the number of variables while maintaining control on the number of physical variables. The methodology includes fitting a conic with a single variable Γ each for the chord and twist distribution. Additional parameters such as pitch and chord reduction (or addition) are included using basic equations. This enables for the parametric study of blades, while also reducing the total number of variables. It has been shown that most blade design generated from GA optimisation also lead to distributions that can be simply fitted with a conic.

The reduction in variables reduces the overall computational overhead with the confidence that each blade generated follows a smooth and simple curve. Additional complexities in the simplified parametric conic-derived design methodology can be added but the current output of the methodology is still able to capture the performance of blades generated using the conventional multiple control point method.

9.2 Performance in representative sites

While most energetic sites seem to be conforming to the usual $1/7^{th}$ power law, the same is not the case for less energetic sites. The Cozumel channel in Mexico provided ample data for characterisation and the presence of highly sheared flow $\alpha < 7$ is present in most transects. It was discussed that this may be due to the large influence of the seabed boundary layer as the depth in the channel is less than 20m. The same is true for the site in the Philippines although the wave and current is mostly orthogonal to each other which results in a negative power law.

High-TSR rotors are subjected to reduced deviations from expected sinusoidal loading when considering wave-current interactions. This is especially important for less energetic sites considering a lower magnitude of relative current number, which indicates higher susceptibility to wave-induced variations in flow.

Resulting AEP values showed that there was no sufficient merit in using larger generators with higher rated power and speed considering that the resource is mostly concentrated over current speeds around 1.0m/s. It was shown that the designed high-TSR rotors perform better than its lower TSR counterparts up to a certain point - this is evidenced by the drop in performance of the NACA TSR12 rotor.

9.3 Economics of high-TSR rotors

A cost model used in estimating offshore wind turbine generator costs was adopted and scaled to fit the power output of the small tidal turbines studied in this thesis. Cost associated to other components of a tidal turbine are calculated using the relative share of the components in existing projects while AEP was calculated using the IEC TS 114

6260-200 standard.

Calculations in cost leading to cost of power showed an exponential reduction in cost as operational RPM is increased. However, this significant reduction in cost is only present until a threshold operational speed of 50RPM. Anything beyond this threshold leads to more loss in power than reduction in cost. Thus, design of high-TSR rotors should be carefully manage to ensure that the design TSR results in a rotational speed not more than 50RPM, with consideration on the rotor diameter and the inflow speed. It was then found that 5m diameter rotors lead to a maximum design TSR within reasonable values and also produce reasonable power output for its scale.

Calculated LCOE values show promise at this point in the conceptualisation and design of high-TSR rotors. No LCOE value for any array size nor turbine size leads to a better LCOE value than that of diesel set at 0.33-0.37 EUR/kWh. This means that less energetic currents is still out of reach for utility scale deployment especially considering new target prices of 178 GBP/MWh from CFD AR4. However, LCOE values of 0.6-0.8 EUR/kWh is within allowable range considering the stage and scale of the technology and also if sustainability goals of a site is considered.

9.4 Design considerations for high-TSR rotors operating in less energetic currents

The rapid blade design methodology (Chapter 3 and Chapter 4), performance evaluation (Chapter 7), economic evaluation (Chapter 8), global sensitivity analysis and probability distribution inspection (Chapter 6), and validation attempts leading to adjustment in simulations (Chapter 5) inform on the considerations and expectations when design high-TSR rotors for operation in less energetic currents.

In general, the following recommendations are given for the design of high-TSR rotors operating in less energetic currents:

1. Similar to usual blade design, there is a need to tune the twist and pitch of the blade. These remain to be the most significant variables when designing a

Conclusions and Future Works

high-TSR blade. However, twist distribution always tend towards higher values of Γ , which is characterised by an aggressive taper nearer the root section. This is because total blade velocities are dominated by the tangential velocity due to the fast rotational speed.

2. Blade number and chord length are less significant parameters in determining the hydrodynamic performance of a rotor. However, it is impossible to push the design TSR of rotor towards higher values if the solidity is not reduced. This means that the blade number and the chord length need to be reduced to promote high-TSR operation.
3. Reduction in solidity must be carefully managed to ensure that blade deflections and stresses are within allowable ranges.
4. Chord and Twist distributions generally follow general conic equation driven distributions. While GA optimisation allows for flexibility in different control points, limiting the distribution to simple conics lead to designs that have similar performance to intricate GA-designed blades.

The following benefits of high TSR rotors are identified:

1. Reduced cost of generator due to increase in operational RPM and decrease of required torque
2. Possible reduction in turbine foundation cost due to less weight
3. Reduced cost of vessels and installation
4. Reduced overall turbine loading
5. Reduced deviations from expected sinusoidal loading when considering wave-current interactions.

The following drawbacks of high TSR rotors are identified:

Conclusions and Future Works

1. Increased blade stress and deflection due to reduction in cross-sectional area
2. Increased fatigue loading due to increased individual blade loading and cycles per unit time
3. Small-scale testing for validation still needs work due to drawback (1)
4. Increased risk of cavitation
5. Difficulty in small-scale testing due to lower solidity and probable deflections

9.5 Future Work

The following are identified sources of uncertainties:

1. Discretised design space for use in exhaustive search versus genetic algorithm
2. Presence of other less energetic sites
3. Anonymity and non-availability of data for both technical and economic evaluation
4. Orthogonality in wave-current interaction
5. Use of static simulations to get stresses and deflection
6. Cost can largely vary from region to region and made more complex due to the study in high TSR tidal turbine rotors being in infancy
7. Possible materials and construction for slender tidal turbine blades

9.5.1 Improvements in blade design methodology

The utilisation of genetic algorithm allows for greater precision with respect to the parametric design methodology. The current methodology assigns possible values for the parameters and does an exhaustive search to find an optimal solution. Genetic algorithm can lead to better solutions while also expanding the design space. The inclusion of sensitivity analysis in this thesis gives more information on how to do the

genetic algorithm as the GA can be made to focus on certain parameters at the start of generation.

9.5.2 Data from representative sites

The anonymity in the data reduces the freedom to take more accurate models i.e. the anonymised location and usage of NOAA to obtain wave data reduced the precision which can be offset by superimposing with other sets of data.

Additional datasets are generally welcome in order to improve the estimates and generalisations obtained from modelling. This is an essential part in developing a design for less energetic currents as a generalised characterisation, if it exists, can greatly accelerate the development of designs. If there is no generalised characterisation, the increase in datasets can provide more scenarios for evaluation and comparison.

9.5.3 Improvements in load simulation

A fully irregular sea-state can be simulated with an expanded BEM code that incorporates a full unsteady simulation. An irregular sea-state will always be nearer to the actual conditions that remain to be stochastic in nature and thus simulations incorporating unsteady simulation will be more accurate.

The current BEM model is only able to handle following current and wave cases. Additional modules are needed to accurately compute the x -, y -, and z - velocities as a result of wave-current interaction. This has since been done by other researchers but additional work needs to be done in order to incorporate it in BEM. At this point, it is also important to determine whether such incorporation is beneficial compared to BEM-CFD coupled models.

The thesis also used static simulation in line with the overarching theme of simple and low computational overhead simulations. Failure in the static simulations was not encountered even with a factor of safety of 5 but simulations in CFD can provide greater fidelity and accuracy.

9.5.4 Improvement on the cost model

Since costs can vary from region to region, expanded research on actual prices (estimates within an area/country) is needed to accurately model costs. This is especially important since the current cost model has a large prospective cost reduction derived from installation costs. These costs are dependent on local rates and can greatly vary across the globe.

The design of high TSR tidal turbine rotors area also in infancy. This can make way to different construction methods to compensate for the high stresses. This is a three-step improvement wherein (1) better characterisation of blade loads is needed, (2) research on possible materials and construction, and (3) modelling of costs for these materials/construction.

9.5.5 Small-scale testing

Small-scale testing is needed to validate simulation results. This has since been done and presented in Chapter 4. The preliminary results showed that there is more work to be done in developing high TSR rotors as well as the testing methodology for these blades.

Since high TSR rotors are very slender, additional work on varying of aerofoils to accurately capture small-scale performance is needed. Additionally, materials used for conventional testing of low TSR rotors may or may not be applicable to small-scale testing of high TSR rotors.

Bibliography

- [1] A. Bahaj, A. Molland, J. Chaplin, and W. Batten, “Power and thrust measurements of marine current turbines under various hydrodynamic flow conditions in a cavitation tunnel and a towing tank,” *Renewable Energy*, vol. 32, no. 3, pp. 407–426, mar 2007. [Online]. Available: <https://linkinghub.elsevier.com/retrieve/pii/S0960148106000516>
- [2] R. Ellis, M. Allmark, T. O’Doherty, A. Mason-Jones, S. Ordoñez-Sánchez, K. Johannesen, and C. Johnstone, “Design Process for a Scale Horizontal Axis Tidal Turbine Blade,” in *4th Asian Wave and Tidal Energy Conference*, Taipei, Taiwan, 2018.
- [3] G. Li and W. Zhu, “Tidal current energy harvesting technologies: A review of current status and life cycle assessment,” *Renewable and Sustainable Energy Reviews*, vol. 179, p. 113269, jun 2023. [Online]. Available: <https://linkinghub.elsevier.com/retrieve/pii/S1364032123001259>
- [4] “European Marine Energy Centre LTD.” [Online]. Available: <http://www.emec.org.uk/marine-energy/tidal-developers/>
- [5] S. Astariz, A. Vazquez, and G. Iglesias, “Evaluation and comparison of the levelized cost of tidal, wave, and offshore wind energy,” *Journal of Renewable and Sustainable Energy*, vol. 7, no. 5, p. 053112, sep 2015. [Online]. Available: <http://aip.scitation.org/doi/10.1063/1.4932154>
- [6] “Scotrenewables SR2000.” [Online]. Available: <https://orbitalmarine.com/technology-development/sr2000>

Bibliography

- [7] “Atlantis AR2000.” [Online]. Available: <https://simecatlantis.com/2018/09/13/simec-atlantis-energy-unveils-worlds-largest-single-rotor-tidal-turbine-the-ar2000/>
- [8] “Atlantis SSIMEC MeyGen.” [Online]. Available: <https://simecatlantis.com/projects/meygen/>
- [9] “Nova M100.” [Online]. Available: <https://www.novainnovation.com/nova-m100>
- [10] D. Magagna and A. Uihlein, “Ocean energy development in Europe: Current status and future perspectives,” *International Journal of Marine Energy*, vol. 11, pp. 84–104, sep 2015. [Online]. Available: <https://linkinghub.elsevier.com/retrieve/pii/S2214166915000181>
- [11] “Contracts for Difference (CfD) Allocation Round 4: results,” The Department for Business, Energy and Industrial Strategy, Tech. Rep. [Online]. Available: https://assets.publishing.service.gov.uk/government/uploads/system/uploads/attachment_data/file/1103022/contracts-for-difference-allocation-round-4-results.pdf
- [12] V. Buenfil Román, G. Espadas Baños, C. Quej Solís, M. Flota-Bañuelos, M. Rivero, and M. Escalante Soberanis, “Comparative study on the cost of hybrid energy and energy storage systems in remote rural communities near Yucatan, Mexico,” *Applied Energy*, vol. 308, p. 118334, feb 2022. [Online]. Available: <https://linkinghub.elsevier.com/retrieve/pii/S0306261921015841>
- [13] S. Pennock, A. Garcia-Teruel, D. Noble, O. Roberts, A. de Andres, C. Cochrane, and H. Jeffrey, “Deriving Current Cost Requirements from Future Targets: Case Studies for Emerging Offshore Renewable Energy Technologies,” *Energies*, vol. 15, no. 5, p. 1732, feb 2022. [Online]. Available: <https://www.mdpi.com/1996-1073/15/5/1732>
- [14] Z. Zhou, M. Benbouzid, J.-F. Charpentier, F. Sculler, and T. Tang, “Developments in large marine current turbine technologies – A review,” *Renewable and Sustainable Energy Reviews*, vol. 71, pp. 852–858,

Bibliography

- may 2017. [Online]. Available: <https://linkinghub.elsevier.com/retrieve/pii/S1364032116311698>
- [15] A. Roberts, B. Thomas, P. Sewell, Z. Khan, S. Balmain, and J. Gillman, “Current tidal power technologies and their suitability for applications in coastal and marine areas,” *Journal of Ocean Engineering and Marine Energy*, vol. 2, no. 2, pp. 227–245, may 2016. [Online]. Available: <http://link.springer.com/10.1007/s40722-016-0044-8>
- [16] D. Haverson, J. Bacon, H. C. Smith, V. Venugopal, and Q. Xiao, “Cumulative impact assessment of tidal stream energy extraction in the Irish Sea,” *Ocean Engineering*, vol. 137, pp. 417–428, jun 2017. [Online]. Available: <https://linkinghub.elsevier.com/retrieve/pii/S0029801817301798>
- [17] R. Roche, K. Walker-Springett, P. Robins, J. Jones, G. Veneruso, T. Whitton, M. Piano, S. Ward, C. Duce, J. Waggitt, G. Walker-Springett, S. Neill, M. Lewis, and J. King, “Research priorities for assessing potential impacts of emerging marine renewable energy technologies: Insights from developments in Wales (UK),” *Renewable Energy*, vol. 99, pp. 1327–1341, dec 2016. [Online]. Available: <https://linkinghub.elsevier.com/retrieve/pii/S0960148116307364>
- [18] I. G. Bryden, S. J. Couch, A. Owen, and G. Melville, “Tidal current resource assessment,” *Proceedings of the Institution of Mechanical Engineers, Part A: Journal of Power and Energy*, vol. 221, no. 2, pp. 125–135, mar 2007. [Online]. Available: <http://journals.sagepub.com/doi/10.1243/09576509JPE238>
- [19] P. E. Robins, S. P. Neill, M. J. Lewis, and S. L. Ward, “Characterising the spatial and temporal variability of the tidal-stream energy resource over the northwest European shelf seas,” *Applied Energy*, vol. 147, pp. 510–522, jun 2015. [Online]. Available: <https://linkinghub.elsevier.com/retrieve/pii/S0306261915003293>
- [20] R. Carballo, G. Iglesias, and A. Castro, “Numerical model evaluation of tidal stream energy resources in the Ría de Muros (NW Spain),” *Renewable*

Bibliography

- Energy*, vol. 34, no. 6, pp. 1517–1524, jun 2009. [Online]. Available: <https://linkinghub.elsevier.com/retrieve/pii/S0960148108004011>
- [21] M. Atcheson, P. MacKinnon, and B. Elsaesser, “A large scale model experimental study of a tidal turbine in uniform steady flow,” *Ocean Engineering*, vol. 110, pp. 51–61, dec 2015. [Online]. Available: <https://linkinghub.elsevier.com/retrieve/pii/S0029801815005326>
- [22] A. Pacheco, E. Gorbeña, T. Plomaritis, E. Garel, J. Gonçalves, L. Bentes, P. Monteiro, C. Afonso, F. Oliveira, C. Soares, F. Zabel, and C. Sequeira, “Deployment characterization of a floatable tidal energy converter on a tidal channel, Ria Formosa, Portugal,” *Energy*, vol. 158, pp. 89–104, sep 2018. [Online]. Available: <https://linkinghub.elsevier.com/retrieve/pii/S0360544218310934>
- [23] M. A. J. R. Quirapas, H. Lin, M. L. S. Abundo, S. Brahim, and D. Santos, “Ocean renewable energy in Southeast Asia: A review,” *Renewable and Sustainable Energy Reviews*, vol. 41, pp. 799–817, jan 2015. [Online]. Available: <https://linkinghub.elsevier.com/retrieve/pii/S1364032114006923>
- [24] M. Quirapas and A. Taeihagh, “Ocean renewable energy development in Southeast Asia: Opportunities, risks and unintended consequences,” *Renewable and Sustainable Energy Reviews*, vol. 137, p. 110403, mar 2021. [Online]. Available: <https://linkinghub.elsevier.com/retrieve/pii/S1364032120306912>
- [25] P. A. J. Bonar, A. M. Schnabl, W.-K. Lee, and T. A. A. Adcock, “Assessment of the Malaysian tidal stream energy resource using an upper bound approach,” *Journal of Ocean Engineering and Marine Energy*, vol. 4, no. 2, pp. 99–109, may 2018. [Online]. Available: <http://link.springer.com/10.1007/s40722-018-0110-5>
- [26] Y. S. Lim and S. L. Koh, “Analytical assessments on the potential of harnessing tidal currents for electricity generation in Malaysia,” *Renewable Energy*, vol. 35, no. 5, pp. 1024–1032, may 2010. [Online]. Available: <https://linkinghub.elsevier.com/retrieve/pii/S096014810900442X>

Bibliography

- [27] H. Faez Hassan, A. El-Shafie, and O. A. Karim, “Tidal current turbines glance at the past and look into future prospects in Malaysia,” *Renewable and Sustainable Energy Reviews*, vol. 16, no. 8, pp. 5707–5717, oct 2012. [Online]. Available: <https://linkinghub.elsevier.com/retrieve/pii/S1364032112004030>
- [28] A. M. Firdaus, G. T. Houlsby, and T. A. Adcock, “Opportunities for Tidal Stream Energy in Indonesian Waters,” in *Proceedings of 12th European Wave and Tidal Energy Conference, Cork, Ireland, Cork, 2017*.
- [29] L. Blunden, A. Bahaj, and N. Aziz, “Tidal current power for Indonesia? An initial resource estimation for the Alas Strait,” *Renewable Energy*, vol. 49, pp. 137–142, jan 2013. [Online]. Available: <https://linkinghub.elsevier.com/retrieve/pii/S0960148112000572>
- [30] K. Orhan, R. Mayerle, and W. W. Pandoe, “Assesment of Energy Production Potential from Tidal Stream Currents in Indonesia,” *Energy Procedia*, vol. 76, pp. 7–16, aug 2015. [Online]. Available: <https://linkinghub.elsevier.com/retrieve/pii/S1876610215016100>
- [31] M. R. Behera and P. Tkalich, “Assessment of Kinetic Tidal Energy Resources Using SELFÉ,” *The International Journal of Ocean and Climate Systems*, vol. 5, no. 3, pp. 141–149, sep 2014. [Online]. Available: <http://journals.sagepub.com/doi/10.1260/1759-3131.5.3.141>
- [32] B. Jones, C. Lee, G. Toro-Farmer, E. Boss, M. Gregg, and C. Villanoy, “Tidally Driven Exchange in an Archipelago Strait: Biological and Optical Responses,” *Oceanography*, vol. 24, no. 01, pp. 142–155, mar 2011. [Online]. Available: <https://tos.org/oceanography/article/tidally-driven-exchange-in-an-archipelago-strait-biological-and-optical-res>
- [33] J.-C. Allo, “From France to the Philippines: Pioneering tidal stream energy,” Manila, Philippines, 2019. [Online]. Available: http://asiacleanenergyforum.pi.bypronto.com/2/wp-content/uploads/sites/2/2019/06/2-Jean-Allo_Ocean-Energy.pdf

Bibliography

- [34] M. Bausas, O. D. G. de Luna, and M. R. C. O. Ang, “Tidal In-stream Energy Resource and Conversion Device Suitability Analysis in the Northern Philippines,” in *37th Asian Conference on Remote Sensing*, Colombo, Sri Lanka, 2016.
- [35] R. Ibañez, E. J. G. Mañalac, and N. Chua, “Tidal Current Resource Power quantification using NAMRIA data sets of the Philippines,” in *11th AUN/SEED-Net Regional Conference on Energy Engineering*, Manila, Philippines, 2018.
- [36] R. Bosch, “Hybrid energy systems for remote island electrification in the Philippines,” Master’s Thesis, TU Delft, 2019. [Online]. Available: <https://repository.tudelft.nl/islandora/object/uuid:b02cb64a-5ac3-49ef-848e-9f88bb135cc9?collection=education>
- [37] G. Chávez, J. Candela, and J. Ochoa, “Subinertial flows and transports in Cozumel Channel,” *Journal of Geophysical Research: Oceans*, vol. 108, no. C2, pp. n/a–n/a, feb 2003. [Online]. Available: <http://doi.wiley.com/10.1029/2002JC001456>
- [38] J. Ochoa, J. Candela, A. Badan, and J. Sheinbaum, “Ageostrophic fluctuations in Cozumel Channel,” *Journal of Geophysical Research*, vol. 110, no. C2, p. C02004, 2005. [Online]. Available: <http://doi.wiley.com/10.1029/2004JC002408>
- [39] J. C. Alcérreca-Huerta, J. I. Encarnacion, S. Ordoñez-Sánchez, M. Callejas-Jiménez, G. Gallegos Diez Barroso, M. Allmark, I. Mariño-Tapia, R. Silva Casarín, T. O’Doherty, C. Johnstone, and L. Carrillo, “Energy Yield Assessment from Ocean Currents in the Insular Shelf of Cozumel Island,” *Journal of Marine Science and Engineering*, vol. 7, no. 5, p. 147, may 2019. [Online]. Available: <https://www.mdpi.com/2077-1312/7/5/147>
- [40] F. Chen, *The Kuroshio Power Plant*, ser. Lecture Notes in Energy. Cham: Springer International Publishing, 2013, vol. 15. [Online]. Available: <http://link.springer.com/10.1007/978-3-319-00822-6>

Bibliography

- [41] F.-C. Chiu, C.-Y. Hsin, H.-Y. Lin, and Y.-H. Lin, “Development of a floating Kuroshio turbine equipped with a foil float: Deployment and recovery simulation,” in *OCEANS 2016 - Shanghai*. IEEE, apr 2016, pp. 1–5. [Online]. Available: <http://ieeexplore.ieee.org/document/7485647/>
- [42] K. Shirasawa, K. Tokunaga, H. Iwashita, and T. Shintake, “Experimental verification of a floating ocean-current turbine with a single rotor for use in Kuroshio currents,” *Renewable Energy*, vol. 91, pp. 189–195, jun 2016. [Online]. Available: <https://linkinghub.elsevier.com/retrieve/pii/S0960148116300350>
- [43] T. Liu, B. Wang, N. Hirose, T. Yamashiro, and H. Yamada, “High-resolution modeling of the Kuroshio current power south of Japan,” *Journal of Ocean Engineering and Marine Energy*, vol. 4, no. 1, pp. 37–55, feb 2018. [Online]. Available: <http://link.springer.com/10.1007/s40722-017-0103-9>
- [44] “European Marine Energy Centre.” [Online]. Available: <http://www.emec.org.uk/>
- [45] R. Whittlesey, “Vertical Axis Wind Turbines,” in *Wind Energy Engineering*, T. Letcher, Ed. Elsevier, 2017, ch. Vertical A.
- [46] M. Shives and C. Crawford, “Overall Efficiency of Ducted tidal current turbines,” in *OCEANS 2010 MTS/IEEE SEATTLE*. IEEE, sep 2010, pp. 1–6. [Online]. Available: <http://ieeexplore.ieee.org/document/5664426/>
- [47] “UK Marine Energy Database.” [Online]. Available: <https://www.renewableuk.com/>
- [48] M. Hepperle, “Javafoil.” [Online]. Available: <https://www.mh-aerotoools.de/airfoils/javafoil.htm>
- [49] G. S. Bir, M. J. Lawson, and Y. Li, “Structural Design of a Horizontal-Axis Tidal Current Turbine Composite Blade,” in *Volume 5: Ocean Space Utilization; Ocean Renewable Energy*. ASMEDC, jan 2011, pp. 797–808.

Bibliography

- [Online]. Available: <https://asmedigitalcollection.asme.org/OMAE/proceedings/OMAE2011/44373/797/351028>
- [50] T. O'Doherty, A. Mason-Jones, D. M. O'Doherty, C. B. Byrne, I. Owen, and Y. X. Wang, "Experimental and Computational Analysis of a Model Horizontal Axis Tidal Turbine," in *Proceedings of the 8th European Wave and Tidal Energy Conference*, 2009.
- [51] D. A. Doman, R. E. Murray, M. J. Pegg, K. Gracie, C. M. Johnstone, and T. Nevalainen, "Tow-tank testing of a 1/20th scale horizontal axis tidal turbine with uncertainty analysis," *International Journal of Marine Energy*, vol. 11, pp. 105–119, sep 2015. [Online]. Available: <https://linkinghub.elsevier.com/retrieve/pii/S2214166915000259>
- [52] H. Glauert, "Aerodynamic Theory," *The Journal of the Royal Aeronautical Society*, vol. 34, no. 233, pp. 409–414, may 1930. [Online]. Available: https://www.cambridge.org/core/product/identifier/S0368393100114397/type/journal_article
- [53] —, "Airplane Propellers," in *Aerodynamic Theory*. Berlin, Heidelberg: Springer Berlin Heidelberg, 1935, pp. 169–360. [Online]. Available: http://link.springer.com/10.1007/978-3-642-91487-4_3
- [54] P. J. Schubel and R. J. Crossley, "Wind Turbine Blade Design," *Energies*, vol. 5, no. 9, pp. 3425–3449, sep 2012. [Online]. Available: <http://www.mdpi.com/1996-1073/5/9/3425>
- [55] R. Froude, "On the part played in propulsion by differences of fluid pressure," *Transactions of the Institute of Naval Architects*, vol. 30, 1889.
- [56] A. Betz, "Das Maximum der theoretisch möglichen Ausnützung des Windes durch Windmotoren," *Zeitschrift für das gesamte Turbinenwesen*, vol. 26, pp. 307–309, 1920.

Bibliography

- [57] T. Burton, D. Sharpe, N. Jenkins, and E. Bossanyi, *Wind Energy Handbook*. John Wiley & Sons, Ltd, 2011.
- [58] J. Meyers and C. Meneveau, “Optimal turbine spacing in fully developed wind farm boundary layers,” *Wind Energy*, vol. 15, no. 2, pp. 305–317, mar 2012. [Online]. Available: <http://doi.wiley.com/10.1002/we.469>
- [59] T. Nevalainen, “The Effect of Unsteady Sea Conditions on Tidal Stream Turbine Loads and Durability,” PhD Thesis, University of Strathclyde, 2016.
- [60] I. Masters, J. C. Chapman, M. R. Willis, and J. A. C. Orme, “A robust blade element momentum theory model for tidal stream turbines including tip and hub loss corrections,” *Journal of Marine Engineering & Technology*, vol. 10, no. 1, pp. 25–35, jan 2011. [Online]. Available: <https://www.tandfonline.com/doi/full/10.1080/20464177.2011.11020241>
- [61] A. Ning, “A simple solution method for the blade element momentum equations with guaranteed convergence,” *Wind Energy*, pp. n/a–n/a, jul 2013. [Online]. Available: <http://doi.wiley.com/10.1002/we.1636>
- [62] H. Glauert, *The analysis of experimental results in the windmill brake and vortex ring states of an airscrew*. London, UK: HM Stationery Office, 1926.
- [63] W. Z. Shen, R. Mikkelsen, J. N. Sørensen, and C. Bak, “Tip loss corrections for wind turbine computations,” *Wind Energy*, vol. 8, no. 4, pp. 457–475, oct 2005. [Online]. Available: <http://doi.wiley.com/10.1002/we.153>
- [64] M. L. Buhl, “A New Empirical Relationship between Thrust Coefficient and Induction Factor for the Turbulent Windmill State,” National Renewable Energy Laboratory, Golden, Colorado, Tech. Rep., 2005.
- [65] D. Spera, *Wind Turbine Technology: Fundamental Concepts in Wind Turbine Engineering, Second Edition*, D. A. Spera, Ed. Three Park Avenue New York, NY 10016-5990: ASME, jan 2009. [Online]. Available: <http://ebooks.asmedigitalcollection.asme.org/book.aspx?bookid=271>

Bibliography

- [66] R. Soulsby, *Dynamics of Marine Sands: A Manual for Practical Applications*. London, UK: Thomas Telford, 1997.
- [67] “Environmental conditions and environmental loads (DNV-RP-C205),” 2007.
- [68] L. Furgerot, P. B. Du Bois, Y. Méar, M. Morillon, E. Poizot, and A.-C. Bennis, “Velocity profile variability at a tidal-stream energy site (Alderney Race, France): From short (second) to yearly time scales,” in *OCEANS 2018 and MTS/IEEE Kobe Techno-Oceans*, Kobe, Japan, 2018, pp. 2779–2789.
- [69] M. Lewis, S. Neill, P. Robins, M. Hashemi, and S. Ward, “Characteristics of the velocity profile at tidal-stream energy sites,” *Renewable Energy*, vol. 114, pp. 258–272, dec 2017. [Online]. Available: <https://linkinghub.elsevier.com/retrieve/pii/S0960148117302884>
- [70] B. Sellar and G. Wakelam, “Characterisation of Tidal Flows at the European Marine Energy Centre in the Absence of Ocean Waves,” *Energies*, vol. 11, no. 1, p. 176, jan 2018. [Online]. Available: <http://www.mdpi.com/1996-1073/11/1/176>
- [71] P. H. Kemp and R. R. Simons, “The interaction between waves and a turbulent current: waves propagating with the current,” *Journal of Fluid Mechanics*, vol. 116, no. -1, p. 227, mar 1982. [Online]. Available: http://www.journals.cambridge.org/abstract_S0022112082000445
- [72] —, “The interaction of waves and a turbulent current: waves propagating against the current,” *Journal of Fluid Mechanics*, vol. 130, p. 73, may 1983. [Online]. Available: http://www.journals.cambridge.org/abstract_S0022112083000981
- [73] G. Klopman, “Vertical structure of the flow due to waves and currents,” Delf Hydraulics, Tech. Rep., 1994.
- [74] M. Umeyama, “Reynolds Stresses and Velocity Distributions in a Wave-Current Coexisting Environment,” *Journal of Waterway, Port, Coastal, and Ocean Engineering*, vol. 131, no. 5, pp. 203–212, sep

Bibliography

2005. [Online]. Available: <http://ascelibrary.org/doi/10.1061/%28ASCE%290733-950X%282005%29131%3A5%28203%29>
- [75] R. Wagner, M. Courtney, T. Larsen, and U. S. Paulsen, "Simulation of shear and turbulence impact on wind turbine performance," Danmarks Tekniske Universitet, Risø Nationallaboratoriet for Bæredygtig Energi, Roskilde, Denmark, Tech. Rep., 2010.
- [76] A. Mason-Jones, D. O'Doherty, C. Morris, and T. O'Doherty, "Influence of a velocity profile & support structure on tidal stream turbine performance," *Renewable Energy*, vol. 52, pp. 23–30, apr 2013. [Online]. Available: <https://linkinghub.elsevier.com/retrieve/pii/S0960148112006672>
- [77] N. Hafeez, S. Badshah, M. Badshah, and S. J. Khalil, "Effect of velocity shear on the performance and structural response of a small-scale horizontal axis tidal turbine," *Marine Systems & Ocean Technology*, vol. 14, no. 2-3, pp. 51–58, sep 2019. [Online]. Available: <http://link.springer.com/10.1007/s40868-019-00057-0>
- [78] D. Russel, "Longitudinal and Transverse Wave Motion," 2016. [Online]. Available: <https://www.acs.psu.edu/drussell/Demos.html>
- [79] J. V. Norris and E. Droniou, "Update on EMEC activities, resource description, and characterisation of wave-induced velocities in a tidal flow," in *Proceedings of the 7th European Wave and Tidal Energy Conference*, Porto, Portugal, 2007.
- [80] M. Olabarrieta, R. Medina, and S. Castanedo, "Effects of wave-current interaction on the current profile," *Coastal Engineering*, vol. 57, no. 7, pp. 643–655, jul 2010. [Online]. Available: <https://linkinghub.elsevier.com/retrieve/pii/S0378383910000165>
- [81] P. J. Visser, "Wave basin experiments on bottom friction due to current and waves," *Coastal Engineering Proceedings*, vol. 1, no. 20, p. 61, jan 1986. [Online]. Available: <https://journals.tdl.org/icce/index.php/icce/article/view/4062>

Bibliography

- [82] R. E. Musumeci, L. Cavallaro, E. Foti, P. Scandura, and P. Blondeaux, “Waves plus currents crossing at a right angle: Experimental investigation,” *Journal of Geophysical Research*, vol. 111, no. C7, p. C07019, 2006. [Online]. Available: <http://doi.wiley.com/10.1029/2005JC002933>
- [83] N. Barltrop, K. S. Varyani, A. Grant, D. Clelland, and X. P. Pham, “Investigation into wave—current interactions in marine current turbines,” *Proceedings of the Institution of Mechanical Engineers, Part A: Journal of Power and Energy*, vol. 221, no. 2, pp. 233–242, mar 2007. [Online]. Available: <http://journals.sagepub.com/doi/10.1243/09576509JPE315>
- [84] B. Gaurier, P. Davies, A. Deuff, and G. Germain, “Flume tank characterization of marine current turbine blade behaviour under current and wave loading,” *Renewable Energy*, vol. 59, pp. 1–12, nov 2013. [Online]. Available: <https://linkinghub.elsevier.com/retrieve/pii/S0960148113001353>
- [85] T. de Jesus Henriques, S. Tedds, A. Botsari, G. Najafian, T. Hedges, C. Sutcliffe, I. Owen, and R. Poole, “The effects of wave—current interaction on the performance of a model horizontal axis tidal turbine,” *International Journal of Marine Energy*, vol. 8, pp. 17–35, dec 2014. [Online]. Available: <https://linkinghub.elsevier.com/retrieve/pii/S221416691400023X>
- [86] S. Ordonez-Sanchez, M. Allmark, K. Porter, R. Ellis, C. Lloyd, I. Santic, T. O’Doherty, and C. Johnstone, “Analysis of a Horizontal-Axis Tidal Turbine Performance in the Presence of Regular and Irregular Waves Using Two Control Strategies,” *Energies*, vol. 12, no. 3, p. 367, jan 2019. [Online]. Available: <http://www.mdpi.com/1996-1073/12/3/367>
- [87] C. Faudot and O. G. Dahlhaug, “Prediction of Wave Loads on Tidal Turbine Blades,” *Energy Procedia*, vol. 20, pp. 116–133, 2012. [Online]. Available: <https://linkinghub.elsevier.com/retrieve/pii/S1876610212007448>
- [88] J. Fenton, “A fifth-order Stokes theory for steady waves,” *Journal of Waterway Port Coastal and Ocean Engineering*, vol. 111, no. 2, pp. 216–234, 1985.

Bibliography

- [89] R. Dalrymple and J. Heideman, “Nonlinear Water Waves on a Vertically-Sheared Current,” in *The Oil Industry Int. Exploration & Production Forum*, Rueil-Malmaison, France, 1989.
- [90] N. Kishida and R. J. Sobey, “Stokes Theory for Waves on Linear Shear Current,” *Journal of Engineering Mechanics*, vol. 114, no. 8, pp. 1317–1334, aug 1988. [Online]. Available: <https://ascelibrary.org/doi/10.1061/%28ASCE%290733-9399%281988%29114%3A8%281317%29>
- [91] T. Landet, “Raschii,” 2018. [Online]. Available: <https://raschii.readthedocs.io/>
- [92] C. Swan, “An Experimental Study of Waves on a Strongly Sheared Current Profile,” in *Coastal Engineering 1990*. Delft, The Netherlands: American Society of Civil Engineers, may 1991, pp. 489–502. [Online]. Available: <http://ascelibrary.org/doi/10.1061/9780872627765.040>
- [93] J. I. Encarnacion and C. M. Johnstone, “Investigation on the sea-state performance of a horizontal axis tidal turbine designed for less energetic flows,” in *Proceedings of the 13th European Wave and Tidal Energy Conference*, Naples, Italy, 2019.
- [94] A. Chehouri, R. Younes, A. Ilinca, and J. Perron, “Review of performance optimization techniques applied to wind turbines,” *Applied Energy*, vol. 142, pp. 361–388, mar 2015. [Online]. Available: <https://linkinghub.elsevier.com/retrieve/pii/S0306261914013002>
- [95] E. Segura, R. Morales, and J. Somolinos, “Cost Assessment Methodology and Economic Viability of Tidal Energy Projects,” *Energies*, vol. 10, no. 11, p. 1806, nov 2017. [Online]. Available: <http://www.mdpi.com/1996-1073/10/11/1806>
- [96] P. K. Nigam, N. Tenguria, and M. Pradhan, “Review on Design of Horizontal Axis Wind Turbine Blades,” *International Journal of Research and Analytical Reviews*, vol. 5, no. 4, pp. 871–878, 2018.

Bibliography

- [97] M. Jureczko, M. Pawlak, and A. Meżyk, “Optimisation of wind turbine blades,” *Journal of Materials Processing Technology*, vol. 167, no. 2-3, pp. 463–471, aug 2005. [Online]. Available: <https://linkinghub.elsevier.com/retrieve/pii/S0924013605005856>
- [98] J. Zhu, X. Cai, P. Pan, and R. Gu, “Optimization design of spar cap layup for wind turbine blade,” *Frontiers of Structural and Civil Engineering*, vol. 6, no. 1, pp. 53–56, mar 2012. [Online]. Available: <http://link.springer.com/10.1007/s11709-012-0147-9>
- [99] J. Chen, Q. Wang, W. Z. Shen, X. Pang, S. Li, and X. Guo, “Structural optimization study of composite wind turbine blade,” *Materials & Design*, vol. 46, pp. 247–255, apr 2013. [Online]. Available: <https://linkinghub.elsevier.com/retrieve/pii/S0261306912007340>
- [100] L. Mishnaevsky, K. Branner, H. Petersen, J. Beauson, M. McGugan, and B. Sørensen, “Materials for Wind Turbine Blades: An Overview,” *Materials*, vol. 10, no. 11, p. 1285, nov 2017. [Online]. Available: <http://www.mdpi.com/1996-1944/10/11/1285>
- [101] S. R. Turnock, R. F. Nicholls-Lee, R. Wood, and J. Wharton, “Tidal Turbines That Survive?” 2009.
- [102] P. Davies, G. Germain, B. Gaurier, A. Boisseau, and D. Perreux, “Evaluation of the durability of composite tidal turbine blades,” *Philosophical Transactions of the Royal Society A: Mathematical, Physical and Engineering Sciences*, vol. 371, no. 1985, p. 20120187, feb 2013. [Online]. Available: <https://royalsocietypublishing.org/doi/10.1098/rsta.2012.0187>
- [103] A. Scott, “Enabling low cost tidal energy,” 2017.
- [104] G. Kenway and J. Martins, “Aerostructural Shape Optimization of Wind Turbine Blades Considering Site-Specific Winds,” in *12th AIAA/ISSMO Multidisciplinary Analysis and Optimization Conference*. Reston, Virginia:

Bibliography

- American Institute of Aeronautics and Astronautics, sep 2008. [Online]. Available: <http://arc.aiaa.org/doi/10.2514/6.2008-6025>
- [105] C. Johnstone, D. Pratt, J. Clarke, and A. Grant, “A techno-economic analysis of tidal energy technology,” *Renewable Energy*, vol. 49, pp. 101–106, jan 2013. [Online]. Available: <https://linkinghub.elsevier.com/retrieve/pii/S0960148112000651>
- [106] A. Ning, R. Damiani, and P. Moriarty, “Objectives and Constraints for Wind Turbine Optimization,” in *51st AIAA Aerospace Sciences Meeting including the New Horizons Forum and Aerospace Exposition*. Reston, Virginia: American Institute of Aeronautics and Astronautics, jan 2013. [Online]. Available: <http://arc.aiaa.org/doi/10.2514/6.2013-201>
- [107] X. Liu, Y. Chen, and Z. Ye, “Optimization model for rotor blades of horizontal axis wind turbines,” *Frontiers of Mechanical Engineering in China*, vol. 2, no. 4, pp. 483–488, oct 2007. [Online]. Available: <http://link.springer.com/10.1007/s11465-007-0084-9>
- [108] D. Sale, J. Jonkman, and W. Musial, “Development of a Hydrodynamic Optimization Tool for Stall-Regulated Hydrokinetic Turbine Rotors,” in *Volume 4: Ocean Engineering; Ocean Renewable Energy; Ocean Space Utilization, Parts A and B*. ASMEDC, jan 2009, pp. 901–906. [Online]. Available: <https://asmedigitalcollection.asme.org/OMAE/proceedings/OMAE2009/43444/901/337026>
- [109] L. Wang, X. Tang, and X. Liu, “Blade Design Optimisation for Fixed-Pitch Fixed-Speed Wind Turbines,” *ISRN Renewable Energy*, vol. 2012, pp. 1–8, 2012. [Online]. Available: <https://www.hindawi.com/archive/2012/682859/>
- [110] K. Maki, R. Sbragio, and N. Vlahopoulos, “System design of a wind turbine using a multi-level optimization approach,” *Renewable Energy*, vol. 43, pp. 101–110, jul 2012. [Online]. Available: <https://linkinghub.elsevier.com/retrieve/pii/S096014811100629X>

Bibliography

- [111] P. Giguere and M. Selig, “Blade geometry optimization for the design of wind turbine rotors,” in *2000 ASME Wind Energy Symposium*. Reston, Virginia: American Institute of Aeronautics and Astronautics, jan 2000. [Online]. Available: <http://arc.aiaa.org/doi/10.2514/6.2000-45>
- [112] W. Xudong, W. Z. Shen, W. J. Zhu, J. N. Sørensen, and C. Jin, “Shape optimization of wind turbine blades,” *Wind Energy*, vol. 12, no. 8, pp. 781–803, nov 2009. [Online]. Available: <http://doi.wiley.com/10.1002/we.335>
- [113] A. Arroyo, M. Manana, C. Gomez, I. Fernandez, F. Delgado, and A. F. Zobaa, “A methodology for the low-cost optimisation of small wind turbine performance,” *Applied Energy*, vol. 104, pp. 1–9, apr 2013. [Online]. Available: <https://linkinghub.elsevier.com/retrieve/pii/S0306261912008008>
- [114] G. Shrestha, H. Polinder, and J. Ferreira, “Scaling laws for direct drive generators in wind turbines,” in *2009 IEEE International Electric Machines and Drives Conference*. IEEE, may 2009, pp. 797–803. [Online]. Available: <http://ieeexplore.ieee.org/document/5075295/>
- [115] Y. Guan, Z. Q. Zhu, G.-J. Li, Z. Azar, A. S. Thomas, F. Vedreno-Santos, and M. Odavic, “Influence of Pole Number and Stator Outer Diameter on Volume, Weight, and Cost of Superconducting Generators With Iron-Cored Rotor Topology for Wind Turbines,” *IEEE Transactions on Applied Superconductivity*, vol. 27, no. 6, pp. 1–9, sep 2017. [Online]. Available: <http://ieeexplore.ieee.org/document/7951015/>
- [116] K. Hart, A. McDonald, H. Polinder, E. J. Corr, and J. Carroll, “Improved cost energy comparison of permanent magnet generators for large offshore wind turbines,” in *Proceedings of the European Wind Energy Association Annual Conference*, Barcelona, Spain, 2014.
- [117] T. Stehly and P. Beiter, “2018 Cost of Wind Energy Review,” National Renewable Energy Laboratory, Golden, Colorado, Tech. Rep., 2020.
- [118] E. Bossanyi, “GH Bladed Theory Manual,” Garrad Hassan, Tech. Rep., 2003.

Bibliography

- [119] D. Sale, M. Lawson, J. Jonkman, D. Maniaci, and M. Buhl, “HarpOpt.” [Online]. Available: http://nrel.github.io/HARP_Opt/
- [120] S. S. Kulkarni, “Design study of a horizontal axis tidal turbine blade,” PhD Thesis, Birmingham City University, 2016.
- [121] R. E. Murray, “Passively Adaptive Tidal Turbine Blades: Design Methodology and Experimental Testing,” Ph.D. dissertation, Dalhousie University, 2016.
- [122] K. Gracie-orr, “A blade design methodology for overspeed power regulation of horizontal axis tidal turbines,” PhD Thesis, University of Strathclyde, 2017.
- [123] M. M. Duquette and K. D. Visser, “Numerical Implications of Solidity and Blade Number on Rotor Performance of Horizontal-Axis Wind Turbines,” *Journal of Solar Energy Engineering*, vol. 125, no. 4, pp. 425–432, nov 2003. [Online]. Available: <https://asmedigitalcollection.asme.org/solarenergyengineering/article/125/4/425/464739/Numerical-Implications-of-Solidity-and-Blade>
- [124] T. Hernández Madrigal, A. Mason-Jones, T. O’Doherty, and D. O’Doherty, “The Effect of Solidity on a Tidal Turbine in Low Speed Flow,” in *Proceedings of the 7th European Wave and Tidal Energy Conference*, Cork, Ireland, 2017.
- [125] P. Fuglsang, C. Bak, J. G. Schepers, B. Bulder, T. T. Cockerill, P. Claiden, A. Olesen, and R. van Rossen, “Site-specific Design Optimization of Wind Turbines,” *Wind Energy*, vol. 5, no. 4, pp. 261–279, oct 2002. [Online]. Available: <http://doi.wiley.com/10.1002/we.61>
- [126] P. Fuglsang and H. Madsen, “Optimization method for wind turbine rotors,” *Journal of Wind Engineering and Industrial Aerodynamics*, vol. 80, no. 1-2, pp. 191–206, mar 1999. [Online]. Available: <https://linkinghub.elsevier.com/retrieve/pii/S0167610598001913>
- [127] M. R. Ahmed, “Blade sections for wind turbine and tidal current turbine applications-current status and future challenges,” *International Journal of*

Bibliography

- Energy Research*, vol. 36, no. 7, pp. 829–844, jun 2012. [Online]. Available: <http://doi.wiley.com/10.1002/er.2912>
- [128] J. I. Encarnacion, C. Johnstone, and S. Ordonez-Sanchez, “Design of a Horizontal Axis Tidal Turbine for Less Energetic Current Velocity Profiles,” *Journal of Marine Science and Engineering*, vol. 7, no. 7, p. 197, jun 2019. [Online]. Available: <https://www.mdpi.com/2077-1312/7/7/197>
- [129] F.-w. Zhu, L. Ding, B. Huang, M. Bao, and J.-T. Liu, “Blade design and optimization of a horizontal axis tidal turbine,” *Ocean Engineering*, vol. 195, p. 106652, jan 2020. [Online]. Available: <https://linkinghub.elsevier.com/retrieve/pii/S0029801819307723>
- [130] Z. Sun, Z. Li, M. Fan, M. Wang, and L. Zhang, “Prediction and multi-objective optimization of tidal current turbines considering cavitation based on GA-ANN methods,” *Energy Science & Engineering*, vol. 7, no. 5, pp. 1896–1912, oct 2019. [Online]. Available: <https://onlinelibrary.wiley.com/doi/abs/10.1002/ese3.399>
- [131] I. Milne, “An experimental investigation of turbulence and unsteady loading on tidal turbines,” PhD thesis, University of Auckland, 2014.
- [132] S.-P. Breton, F. N. Coton, and G. Moe, “A study on rotational effects and different stall delay models using a prescribed wake vortex scheme and NREL phase VI experiment data,” *Wind Energy*, vol. 11, no. 5, pp. 459–482, sep 2008. [Online]. Available: <http://doi.wiley.com/10.1002/we.269>
- [133] R. Saaty, “The analytic hierarchy process—what it is and how it is used,” *Mathematical Modelling*, vol. 9, no. 3-5, pp. 161–176, 1987. [Online]. Available: <https://linkinghub.elsevier.com/retrieve/pii/0270025587904738>
- [134] S. Pohekar and M. Ramachandran, “Application of multi-criteria decision making to sustainable energy planning—A review,” *Renewable and Sustainable Energy Reviews*, vol. 8, no. 4, pp. 365–381, aug 2004. [Online]. Available: <https://linkinghub.elsevier.com/retrieve/pii/S1364032104000073>

Bibliography

- [135] T. U. Daim, E. Bayraktaroglu, J. Estep, D. J. Lim, J. Upadhyay, and J. Yang, “Optimizing the NW off-shore wind turbine design,” *Mathematical and Computer Modelling*, vol. 55, no. 3-4, pp. 396–404, feb 2012. [Online]. Available: <https://linkinghub.elsevier.com/retrieve/pii/S0895717711004985>
- [136] B. Gaurier, G. Germain, J. Facq, C. Johnstone, A. Grant, A. Day, E. Nixon, F. Di Felice, and M. Costanzo, “Tidal energy “Round Robin” tests comparisons between towing tank and circulating tank results,” *International Journal of Marine Energy*, vol. 12, pp. 87–109, dec 2015. [Online]. Available: <https://linkinghub.elsevier.com/retrieve/pii/S2214166915000223>
- [137] M. Allmark, S. Ordonez-Sanchez, S. Wang, Y. S. Kang, C.-H. Jo, T. O’Doherty, and C. Johnstone, “An investigation into Reynolds scaling and solidity for a HATT tidal turbine,” in *13th European Wave and Tidal Energy Conference*, Naples, Italy, 2019.
- [138] T. A. Burdett and K. W. Van Treuren, “Scaling Small-Scale Wind Turbines for Wind Tunnel Testing,” in *Volume 6: Oil and Gas Applications; Concentrating Solar Power Plants; Steam Turbines; Wind Energy*. American Society of Mechanical Engineers, jun 2012, pp. 811–820. [Online]. Available: <https://asmedigitalcollection.asme.org/GT/proceedings/GT2012/44724/811/241180>
- [139] A. Tummala, R. K. Velamati, D. K. Sinha, V. Indraja, and V. H. Krishna, “A review on small scale wind turbines,” *Renewable and Sustainable Energy Reviews*, vol. 56, pp. 1351–1371, apr 2016. [Online]. Available: <https://linkinghub.elsevier.com/retrieve/pii/S1364032115014100>
- [140] D. Berg and J. Zayas, “Aerodynamic and Aeroacoustic Properties of Flatback Airfoils,” in *46th AIAA Aerospace Sciences Meeting and Exhibit*. Reston, Virginia: American Institute of Aeronautics and Astronautics, jan 2008. [Online]. Available: <http://arc.aiaa.org/doi/10.2514/6.2009-271><http://arc.aiaa.org/doi/10.2514/6.2008-1455>

Bibliography

- [141] J. Morgado, R. Vizinho, M. Silvestre, and J. Páscoa, “XFOIL vs CFD performance predictions for high lift low Reynolds number airfoils,” *Aerospace Science and Technology*, vol. 52, pp. 207–214, may 2016. [Online]. Available: <https://linkinghub.elsevier.com/retrieve/pii/S1270963816300839>
- [142] V. Ramjee, E. G. Tulapurkara, and V. Balabaskaran, “Experimental and theoretical study of wings with blunt trailing edges,” *Journal of Aircraft*, vol. 23, no. 4, pp. 349–352, apr 1986. [Online]. Available: <https://arc.aiaa.org/doi/10.2514/3.45311>
- [143] J. Sato and Y. Sunada, “Experimental research on blunt trailing-edge airfoil sections at low Reynolds numbers,” *AIAA Journal*, vol. 33, no. 11, pp. 2001–2005, nov 1995. [Online]. Available: <https://arc.aiaa.org/doi/10.2514/3.12905>
- [144] K. J. Standish and C. P. van Dam, “Aerodynamic Analysis of Blunt Trailing Edge Airfoils,” *Journal of Solar Energy Engineering*, vol. 125, no. 4, pp. 479–487, nov 2003. [Online]. Available: <https://asmedigitalcollection.asme.org/solarenergyengineering/article/125/4/479/464738/Aerodynamic-Analysis-of-Blunt-Trailing-Edge>
- [145] N. Thomareis and G. Papadakis, “Effect of trailing edge shape on the separated flow characteristics around an airfoil at low Reynolds number: A numerical study,” *Physics of Fluids*, vol. 29, no. 1, p. 014101, jan 2017. [Online]. Available: <http://aip.scitation.org/doi/10.1063/1.4973811>
- [146] A. Gomez and A. Pinilla, “Aerodynamic Characteristics of Airfoils with Blunt Trailing Edge,” *Revista de Ingenieria*, vol. 24, pp. 23–33, 2006.
- [147] X. Shen, E. Avital, G. Paul, M. A. Rezaenia, P. Wen, and T. Korakianitis, “Experimental study of surface curvature effects on aerodynamic performance of a low Reynolds number airfoil for use in small wind turbines,” *Journal of Renewable and Sustainable Energy*, vol. 8, no. 5, p. 053303, sep 2016. [Online]. Available: <http://aip.scitation.org/doi/10.1063/1.4963236>

Bibliography

- [148] F. Zilic De Arcos, C. Vogel, and R. H. Willden, “Hydrodynamic modelling of flexible tidal turbine blades,” in *13th European Wave and Tidal Energy Conference*, Naples, Italy, 2019.
- [149] B. Dose, H. Rahimi, I. Herráez, B. Stoevesandt, and J. Peinke, “Fluid-structure coupled computations of the NREL 5 MW wind turbine by means of CFD,” *Renewable Energy*, vol. 129, pp. 591–605, dec 2018. [Online]. Available: <https://linkinghub.elsevier.com/retrieve/pii/S0960148118305858>
- [150] M. Jiří, “The Robustness of TOPSIS Results Using Sensitivity Analysis Based on Weight Tuning,” in *World Congress on Medical Physics and Biomedical Engineering IFMBE Proceedings*, 2019, pp. 83–86. [Online]. Available: http://link.springer.com/10.1007/978-981-10-9038-7_15
- [151] G. Kumar and N. Parimala, “A Sensitivity Analysis on Weight Sum Method MCDM Approach for Product Recommendation,” 2019, pp. 185–193. [Online]. Available: http://link.springer.com/10.1007/978-3-030-05366-6_15
- [152] N. Zhao, C. Wei, and Z. Xu, “Sensitivity Analysis of Multiple Criteria Decision Making Method Based on the OWA Operator,” *International Journal of Intelligent Systems*, vol. 28, no. 11, pp. 1124–1139, nov 2013. [Online]. Available: <http://doi.wiley.com/10.1002/int.21620>
- [153] C. Wang, J. Shi, X. Niu, S. Jia, S. Liu, and L. Mu, “Sensitivity analysis on the weights in power system restoration decision-making,” in *2011 4th International Conference on Electric Utility Deregulation and Restructuring and Power Technologies (DRPT)*. IEEE, jul 2011, pp. 653–656. [Online]. Available: <http://ieeexplore.ieee.org/document/5993974/>
- [154] A. Memariani, A. Amini, and A. Alinezhad, “Sensitivity Analysis of Simple Additive Weighting Method (SAW): The Results of Change in the Weight of One Attribute on the Final Ranking of Alternatives,” *Journal of Optimization in Industrial Engineering*, vol. 2, no. 4, pp. 13–18, 2009.

Bibliography

- [155] X. Gu, G. Sun, G. Li, L. Mao, and Q. Li, “A Comparative study on multiobjective reliable and robust optimization for crashworthiness design of vehicle structure,” *Structural and Multidisciplinary Optimization*, vol. 48, no. 3, pp. 669–684, sep 2013. [Online]. Available: <http://link.springer.com/10.1007/s00158-013-0921-x>
- [156] G. Sun, G. Li, Z. Gong, X. Cui, X. Yang, and Q. Li, “Multiobjective robust optimization method for drawbead design in sheet metal forming,” *Materials & Design*, vol. 31, no. 4, pp. 1917–1929, apr 2010. [Online]. Available: <https://linkinghub.elsevier.com/retrieve/pii/S0261306909006049>
- [157] A. Ning and K. Dykes, “Understanding the Benefits and Limitations of Increasing Maximum Rotor Tip Speed for Utility-Scale Wind Turbines,” *Journal of Physics: Conference Series*, vol. 524, p. 012087, jun 2014. [Online]. Available: <https://iopscience.iop.org/article/10.1088/1742-6596/524/1/012087>
- [158] “DNVGL-ST-0164 Tidal Turbines,” DNV GL AS, Tech. Rep., 2015.
- [159] R. E. Murray, “Predicting Cavitation on Marine and Hydrokinetic Turbine Blades with AeroDyn V15.04,” National Renewable Laboratory, Golden, Colorado, Tech. Rep., 2017.
- [160] J. M. Rinker, “Calculating the sensitivity of wind turbine loads to wind inputs using response surfaces,” *Journal of Physics: Conference Series*, vol. 753, p. 032057, sep 2016. [Online]. Available: <https://iopscience.iop.org/article/10.1088/1742-6596/753/3/032057>
- [161] J. Velarde, C. Kramhøft, and J. D. Sørensen, “Global sensitivity analysis of offshore wind turbine foundation fatigue loads,” *Renewable Energy*, vol. 140, pp. 177–189, sep 2019. [Online]. Available: <https://linkinghub.elsevier.com/retrieve/pii/S096014811930360X>
- [162] T. Nevalainen, C. Johnstone, and A. Grant, “A sensitivity analysis on tidal stream turbine loads caused by operational, geometric design and inflow parameters,” *International Journal of Marine Energy*, vol. 16, pp. 51–64, dec 2016. [Online]. Available: <https://linkinghub.elsevier.com/retrieve/pii/S2214166916300364>

Bibliography

- [163] A. Saltelli, K. Aleksankina, W. Becker, P. Fennell, F. Ferretti, N. Holst, S. Li, and Q. Wu, “Why so many published sensitivity analyses are false: A systematic review of sensitivity analysis practices,” *Environmental Modelling & Software*, vol. 114, pp. 29–39, apr 2019. [Online]. Available: <https://linkinghub.elsevier.com/retrieve/pii/S1364815218302822>
- [164] J. Herman and W. Usher, “SALib: An open-source Python library for Sensitivity Analysis,” *The Journal of Open Source Software*, vol. 2, no. 9, p. 97, jan 2017. [Online]. Available: <http://joss.theoj.org/papers/10.21105/joss.00097>
- [165] M. D. Morris, “Factorial Sampling Plans for Preliminary Computational Experiments,” *Technometrics*, vol. 33, no. 2, pp. 161–174, may 1991. [Online]. Available: <http://www.tandfonline.com/doi/abs/10.1080/00401706.1991.10484804>
- [166] H. Rabitz, “Global Sensitivity Analysis for Systems with Independent and/or Correlated Inputs,” *Procedia - Social and Behavioral Sciences*, vol. 2, no. 6, pp. 7587–7589, 2010. [Online]. Available: <https://linkinghub.elsevier.com/retrieve/pii/S1877042810012723>
- [167] Y. Gan, Q. Duan, W. Gong, C. Tong, Y. Sun, W. Chu, A. Ye, C. Miao, and Z. Di, “A comprehensive evaluation of various sensitivity analysis methods: A case study with a hydrological model,” *Environmental Modelling & Software*, vol. 51, pp. 269–285, jan 2014. [Online]. Available: <https://linkinghub.elsevier.com/retrieve/pii/S1364815213002338>
- [168] “Water Programming: A Collaborative Research Blog,” 2014.
- [169] G. Baroni and S. Tarantola, “A General Probabilistic Framework for uncertainty and global sensitivity analysis of deterministic models: A hydrological case study,” *Environmental Modelling & Software*, vol. 51, pp. 26–34, jan 2014. [Online]. Available: <https://linkinghub.elsevier.com/retrieve/pii/S1364815213002211>

Bibliography

- [170] “IEA World Energy Balances,” 2020. [Online]. Available: <https://www.iea.org/subscribe-to-data-services/world-energy-balances-and-statistics>
- [171] “Diario oficial de la Federacion.” [Online]. Available: http://www.dof.gob.mx/nota_detalle.php?codigo=5463923&fecha=02/12/2016
- [172] D. Gielen, D. Saygin, N. Wagner, L. I. Gutierrez, and E. R. Narvaez-Torres, “Renewable Energy Prospects: Mexico,” IRENA, Abu Dhabi, UAE, Tech. Rep., 2015.
- [173] J. V. Hernández-Fontes, A. Felix, E. Mendoza, Y. R. Cueto, and R. Silva, “On the Marine Energy Resources of Mexico,” *Journal of Marine Science and Engineering*, vol. 7, no. 6, p. 191, jun 2019. [Online]. Available: <https://www.mdpi.com/2077-1312/7/6/191>
- [174] J. C. Alcérreca-Huerta, J. I. Encarnacion, S. Ordoñez-Sánchez, M. Callejas-Jiménez, G. Gallegos Diez Barroso, M. Allmark, I. Mariño-Tapia, R. Silva Casarín, T. O’Doherty, C. Johnstone, and L. Carrillo, “Energy Yield Assessment from Ocean Currents in the Insular Shelf of Cozumel Island,” *Journal of Marine Science and Engineering*, vol. 7, no. 5, p. 147, may 2019. [Online]. Available: <https://www.mdpi.com/2077-1312/7/5/147>
- [175] A. P. Muñoz and L. Z. Villareal, “Distribucion territorial y turismo en Cozumel, Estado de Quintana Roo, Mexico,” in *Gestion Turistica*, Valdivia, Chile, 2009.
- [176] Department of Energy, “PEP 2017-2040: Sectoral Plans and Roadmaps,” 2017.
- [177] A. S. Delos Santos, “Renewable Energy in the Philippines,” 2016.
- [178] “Summary of Renewable Energy Projects as of 31 May 2021,” 2021. [Online]. Available: <https://www.doe.gov.ph/national-renewable-energy-program?q=renewable-energy/summary-of-re-projects>
- [179] “Awarded Ocean Projects as of 31 May 2021,” 2021. [Online]. Available: https://www.doe.gov.ph/sites/default/files/pdf/renewable_energy/awarded_ocean_2021-05-31.pdf

Bibliography

- [180] M. L. S. Abundo, “Marine Renewable Energy for Island Micro-Grids in South East Asia,” 2016.
- [181] M. L. S. Abundo, A. Nerves, M. R. Ang, E. Paringit, L. Bernardo, M. Buhali, and M. Catanyag, “Development of TRIDEnT (Tidal Resource Investigation, Device, & Energy Tool) as a Rapid Evaluation System for Tidal In-Stream Energy Resource Assessment, Power Estimation, Energy Projection, and Technology Matching,” in *4th Regional Conference on New and Renewable Energy*, Ho Chi Minh City, 2011.
- [182] M. L. S. Abundo, M. Buhali, M. R. C. O. Ang, and A. Cayetano, “Development of an integrated multi-site & multi-device rapid evaluation tool for tidal energy planning,” in *2012 11th International Conference on Environment and Electrical Engineering*. IEEE, may 2012, pp. 612–617. [Online]. Available: <http://ieeexplore.ieee.org/document/6221449/>
- [183] I. B. O. Villalba, E. J. V. Cleofe, and D. M. Bautista, “Numerical simulation of tides for the assessment of tidal in-stream energy in selected sites in the Philippines,” *IOP Conference Series: Earth and Environmental Science*, vol. 673, no. 1, p. 012017, feb 2021. [Online]. Available: <https://iopscience.iop.org/article/10.1088/1755-1315/673/1/012017>
- [184] C. Frost, C. Morris, A. Mason-Jones, D. O’Doherty, and T. O’Doherty, “The effect of tidal flow directionality on tidal turbine performance characteristics,” *Renewable Energy*, vol. 78, pp. 609–620, jun 2015. [Online]. Available: <https://linkinghub.elsevier.com/retrieve/pii/S0960148115000713>
- [185] “IEC/TS 114 62600-200:Marine energy – Wave, tidal and other water current converters – Electricity producing tidal energy converters – Power performance assessmen,” International Electrotechnical Commission, Tech. Rep., 2013.
- [186] M. Lewis, R. O’Hara Murray, S. Fredriksson, J. Maskell, A. de Fockert, S. P. Neill, and P. E. Robins, “A standardised tidal-stream power curve, optimised for the

Bibliography

- global resource,” *Renewable Energy*, vol. 170, pp. 1308–1323, jun 2021. [Online]. Available: <https://linkinghub.elsevier.com/retrieve/pii/S0960148121001993>
- [187] A. Inoue, R. Takahashi, T. Murata, J. Tamura, M. Kimura, M.-O. Futami, and K. Ide, “A calculation method of the total efficiency of wind generators,” *Electrical Engineering in Japan*, vol. 157, no. 3, pp. 52–62, nov 2006. [Online]. Available: <https://onlinelibrary.wiley.com/doi/10.1002/ej.20426>
- [188] I. Mrcela, D. Sumina, F. Sacic, and T. Barisa, “A wind turbine two level back-to-back converter power loss study,” in *2016 IEEE International Power Electronics and Motion Control Conference (PEMC)*. IEEE, sep 2016, pp. 308–314. [Online]. Available: <http://ieeexplore.ieee.org/document/7752016/>
- [189] J. Carroll, A. McDonald, I. Dinwoodie, D. McMillan, M. Revie, and I. Lazakis, “Availability, operation and maintenance costs of offshore wind turbines with different drive train configurations,” *Wind Energy*, vol. 20, no. 2, pp. 361–378, feb 2017. [Online]. Available: <https://onlinelibrary.wiley.com/doi/10.1002/we.2011>
- [190] J. V. Lamy and I. L. Azevedo, “Do tidal stream energy projects offer more value than offshore wind farms? A case study in the United Kingdom,” *Energy Policy*, vol. 113, pp. 28–40, feb 2018. [Online]. Available: <https://linkinghub.elsevier.com/retrieve/pii/S0301421517306900>
- [191] J. Clarke, G. Connor, A. Grant, and C. Johnstone, “The impact of limiting tidal turbine capacity on the output characteristics from three complimentary tidal sites in Scotland over the lunar cycle,” in *Proceedings of the 9th World Renewable Energy Congress*, 2005.
- [192] P. Bertheau and C. Cader, “Electricity sector planning for the Philippine islands: Considering centralized and decentralized supply options,” *Applied Energy*, vol. 251, p. 113393, oct 2019. [Online]. Available: <https://linkinghub.elsevier.com/retrieve/pii/S0306261919310670>
- [193] S. Knight, “Wind Power Monthly,” 2013. [Online]. Available: <https://www.windpowermonthly.com/article/1214101/specialised-vessels-cut-costs>

Bibliography

- [194] G. Li and W. Zhu, “Tidal current energy harvesting technologies: A review of current status and life cycle assessment,” *Renewable and Sustainable Energy Reviews*, vol. 179, p. 113269, jun 2023. [Online]. Available: <https://linkinghub.elsevier.com/retrieve/pii/S1364032123001259>
- [195] G. Allan, M. Gilmartin, P. McGregor, and K. Swales, “Levelised costs of Wave and Tidal energy in the UK: Cost competitiveness and the importance of “banded” Renewables Obligation Certificates,” *Energy Policy*, vol. 39, no. 1, pp. 23–39, jan 2011. [Online]. Available: <https://linkinghub.elsevier.com/retrieve/pii/S0301421510006440>
- [196] “2016/ARP002 - The Tidal Turbine Reef (TTR) Feasibility Study,” Australian Renewable Energy Agency, Tech. Rep., 2017.
- [197] “Market Study on Ocean Energy - Final Report,” European Commission - Maritime Affairs and Fisheries, Tech. Rep., 2018.
- [198] S. Klaus, “Financial and Economic Assessment of Tidal Stream Energy—A Case Study,” *International Journal of Financial Studies*, vol. 8, no. 3, p. 48, aug 2020. [Online]. Available: <https://www.mdpi.com/2227-7072/8/3/48>
- [199] V. Buenfil Román, G. Espadas Baños, C. Quej Solís, M. Flota-Bañuelos, M. Rivero, and M. Escalante Soberanis, “Comparative study on the cost of hybrid energy and energy storage systems in remote rural communities near Yucatan, Mexico,” *Applied Energy*, vol. 308, p. 118334, feb 2022. [Online]. Available: <https://linkinghub.elsevier.com/retrieve/pii/S0306261921015841>

Appendix A

Sample Calculation on Conic Fitting for existing blade design

The general process for the conic fitting in Chapter 3 is the reversed form of the blade design methodology that applies Equations 3.6 to 3.9. This serves as a guide and sample calculation on how each conic fit was performed.

The general process for the fitting is:

1. Points of (r, θ) and (r, c) are extracted using PlotDigitizer downloadable from <http://plotdigitizer.sourceforge.net>.
2. The radial position r and chord lengths are normalised using R .
3. The value of twist and chord at the tip are subtracted to each of the segments as in Equation 3.9. This¹ gives the value of $c^*\lambda^*(r)$ for a given position.
4. $c^*\lambda^*(r)$ is further normalised by dividing using the value at the root to achieve values that are $0 \leq c^*\lambda^*(r) < 1$.
5. The values of $\lambda(r)$ and Γ are solved numerically using the GRG Non-linear solver in MS Excel.
6. The resulting $\lambda(r)$ and Γ are checked by graphing to verify the conic fit.

Below is a sample calculation using the blade designed by Xudong [112].

¹Change c to θ for twist.

Appendix A: Sample Calculation on Conic Fitting

Table A.2: Values after normalising using R_{tip}

R norm	twist	R norm	c norm
0.185378	13.21573	0.186127	0.072168
0.250664	11.5625	0.250461	0.073762
0.31595	10.11089	0.316104	0.070826
0.381237	8.477822	0.381302	0.067571
0.446079	7.076613	0.445607	0.063089
0.511365	5.997984	0.51124	0.057914
0.576207	5.100806	0.576429	0.052527
0.641494	4.22379	0.641176	0.047779
0.70678	3.296371	0.706373	0.04431
0.772066	2.34879	0.772018	0.041747
0.837353	1.471774	0.836775	0.038864
0.891536	0.826613	0.890881	0.035289
0.934172	0.403226	0.934336	0.030969
0.977696	0.100806	0.977314	0.019347
1.000791	0	1.000772	0.007725

Table A.1: Captured data points using PlotDigitizer

R	twist	R	c
11.67879	13.21573	11.72602	4.546563
15.79183	11.5625	15.77903	4.647029
19.90487	10.11089	19.91456	4.462064
24.01791	8.477822	24.02204	4.256952
28.10297	7.076613	28.07327	3.974612
32.216	5.997984	32.20814	3.648612
36.30106	5.100806	36.315	3.309182
40.4141	4.22379	40.3941	3.01005
44.52714	3.296371	44.50153	2.791506
48.64018	2.34879	48.63717	2.630046
52.75322	1.471774	52.71681	2.448443
56.16676	0.826613	56.12549	2.22323
58.85283	0.403226	58.86319	1.951052
61.59485	0.100806	61.57079	1.218834
63.04981	0	63.04866	0.4867

The radial positions and the chord lengths are normalised using the correspond R_{tip} . The values of R from θ and c has a small variation due to the precision of the PlotDigitizer tool.

Appendix A: Sample Calculation on Conic Fitting

Each of the data points are then normalised by subtracting the value at the tip $R \approx 63$. These are the values of $c^*\lambda^*(r)$.

Table A.3: Values after subtracted twist and chord values at the tip

R norm	twist model	R norm	c model
0.185378	13.21573	0.186127	0.064442
0.250664	11.5625	0.250461	0.066037
0.31595	10.11089	0.316104	0.063101
0.381237	8.477822	0.381302	0.059845
0.446079	7.076613	0.445607	0.055364
0.511365	5.997984	0.51124	0.050189
0.576207	5.100806	0.576429	0.044801
0.641494	4.22379	0.641176	0.040053
0.70678	3.296371	0.706373	0.036584
0.772066	2.34879	0.772018	0.034021
0.837353	1.471774	0.836775	0.031139
0.891536	0.826613	0.890881	0.027564
0.934172	0.403226	0.934336	0.023244
0.977696	0.100806	0.977314	0.011621
1.000791	0	1.000772	0

The points are then normalised to allow for easier calculation in MS Excel.

Table A.4: Values after normalising using the twist and chord values at the root

twist model	twist model norm	c model	c model norm
13.21573	1		
11.5625	0.874905	0.066037	1
10.11089	0.765065	0.063101	0.955541
8.477822	0.641495	0.059845	0.906239
7.076613	0.535469	0.055364	0.838374
5.997984	0.453852	0.050189	0.760015
5.100806	0.385965	0.044801	0.678428
4.22379	0.319603	0.040053	0.606526
3.296371	0.249428	0.036584	0.553996
2.34879	0.177727	0.034021	0.515187
1.471774	0.111365	0.031139	0.471535
0.826613	0.062548	0.027564	0.417402
0.403226	0.030511	0.023244	0.35198
0.100806	0.007628	0.011621	0.17598
0	0	0	0

Appendix A: Sample Calculation on Conic Fitting

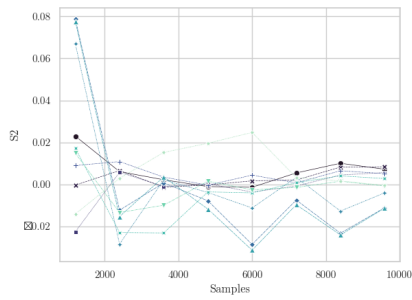
Table A.5: Computed λ_{root} and Γ after using MS Excel GRG Nonlinear solver. The function value is written as $r^2 + \Gamma r \lambda(r) + \lambda(r)^2$ where r is the normalised radial position.

Γ	4.186722				
λ_{root}	0.660786				
twist model	twist model norm	λ_r	func val	err	fitted
13.21573	1	0.660786	1	8.98E-24	13.3691
11.5625	0.874905	0.578125	1	4.76E-24	11.5282
10.11089	0.765065	0.505544	1	9.65E-24	9.903174
8.477822	0.641495	0.423891	1	1.05E-23	8.46464
7.076613	0.535469	0.35383	1	1.66E-24	7.192853
5.997984	0.453852	0.299899	1	1.64E-24	6.045371
5.100806	0.385965	0.25504	1	9.04E-25	5.016343
4.22379	0.319603	0.211189	1	3.05E-26	4.073381
3.296371	0.249428	0.164818	1	3.85E-25	3.208585
2.34879	0.177727	0.117439	1	3E-24	2.409344
1.471774	0.111365	0.073589	1	2.08E-24	1.665302
0.826613	0.062548	0.041331	1	3.4E-24	1.083577
0.403226	0.030511	0.020161	1	3.03E-27	0.645752
0.100806	0.007628	0.00504	1	7.59E-26	0.214958
0	0	0	1.001582	2.5E-06	0
Total error				2.5E-06	

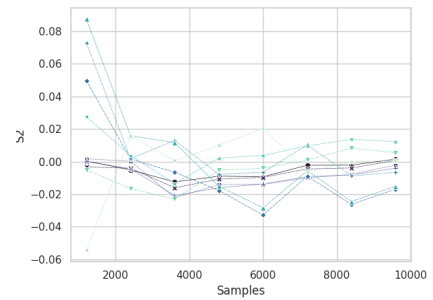
Graphs are then shown in Section 4.1.1.

Appendix B

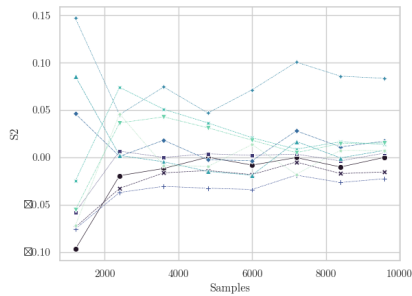
Second Order Sobol Indices



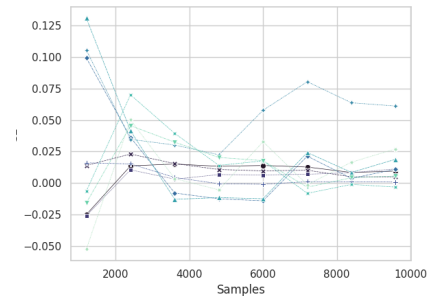
(a) S2 Indices for $C_{P_{\max}}$



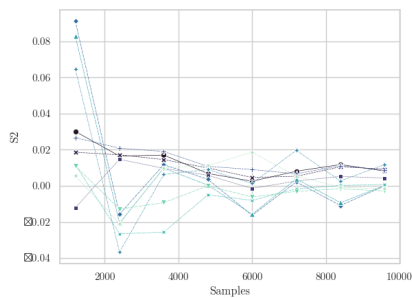
(d) S2 Indices for $C_{P_{\max}}$



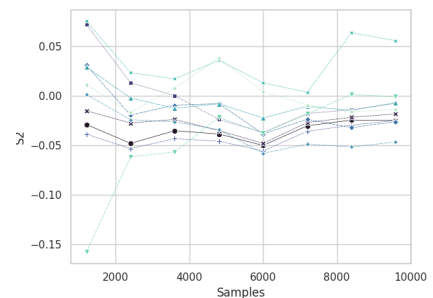
(b) S2 Indices for $TSR_{C_{P_{\max}}}$



(e) S2 Indices for $TSR_{C_{P_{\max}}}$



(c) S2 Indices for corresponding C_T



(f) S2 Indices for corresponding C_T

Figure B.1: Second Sobol Significance indices for NACA (left) and Wortmann (right)

Appendix B: Second Order Sobol Indices

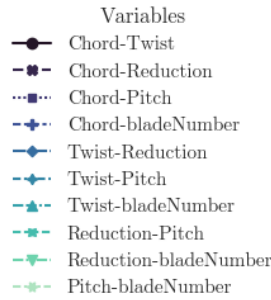


Figure B.2: Legend for Second Order Sobol Indices for one aerofoil. This is put in a separate figure for readability



Figure B.3: Legend for First and Total Order Sobol Indices including aerofoil. This is put in a separate figure for readability

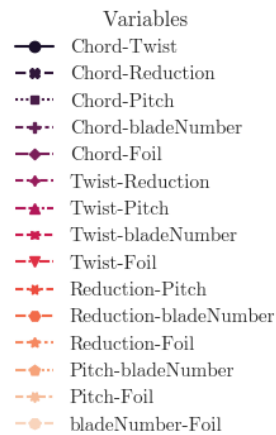


Figure B.4: Legend for Second Order Sobol Indices including. This is put in a separate figure for readability

Appendix B: Second Order Sobol Indices

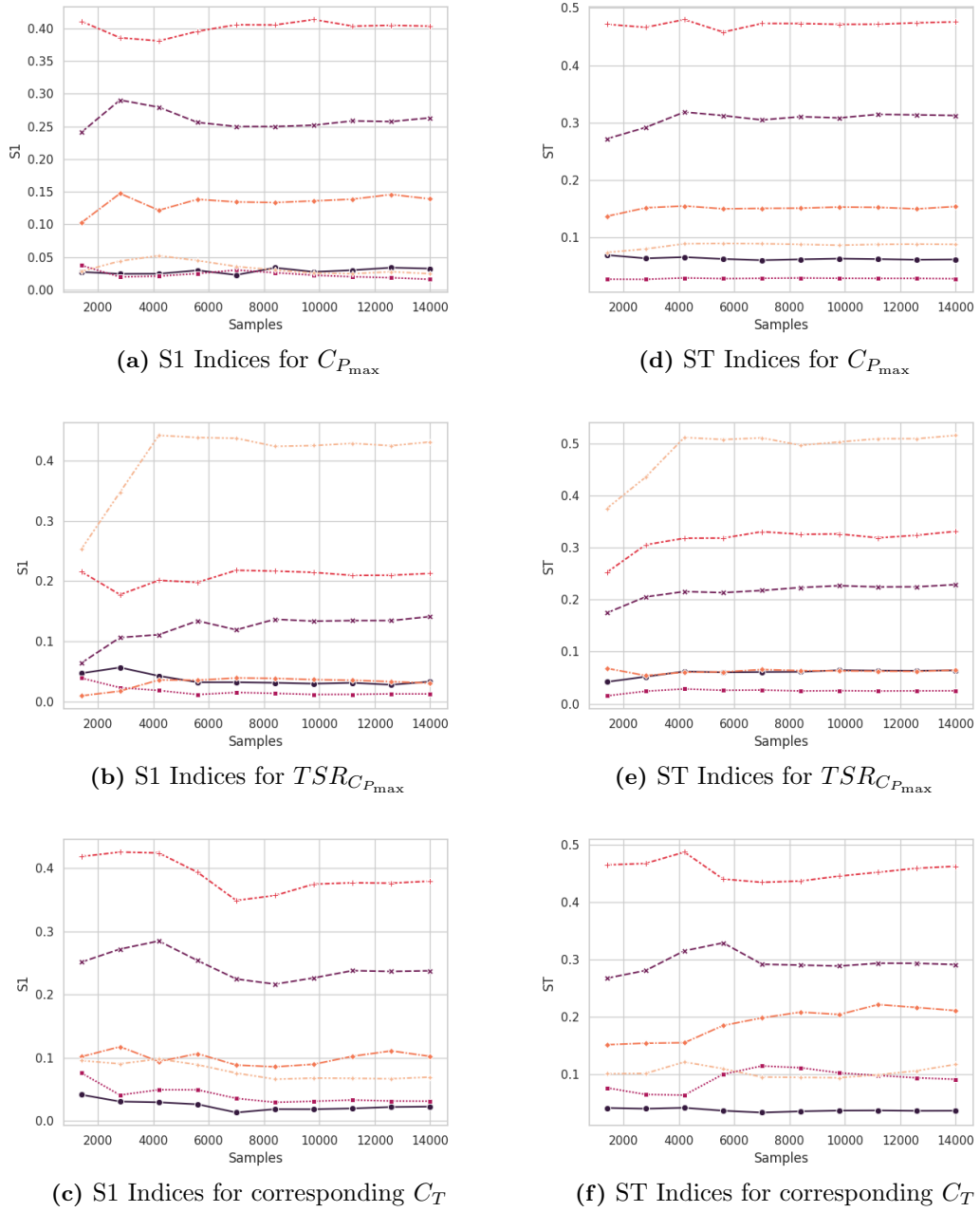
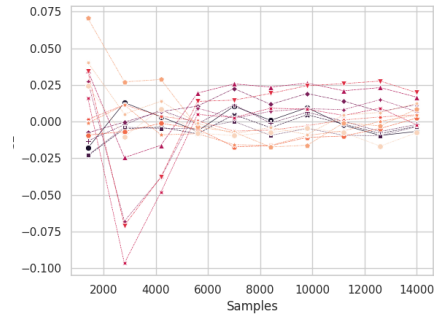
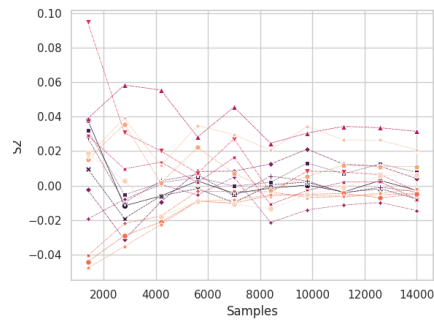


Figure B.5: First and Total Order Sobol Significance indices including aerofoil as a parameter

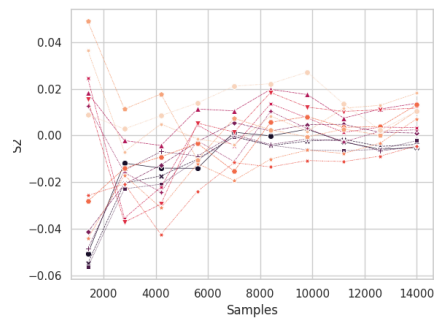
Appendix B: Second Order Sobol Indices



(a) S2 Indices for $C_{P_{max}}$



(b) S2 Indices for $TSR_{C_{P_{max}}}$



(c) S2 Indices for corresponding C_T

Figure B.6: Second Order Sobol Significance indices including aerofoil as a parameter

Appendix C

PDFs of Wortmann FX63-137

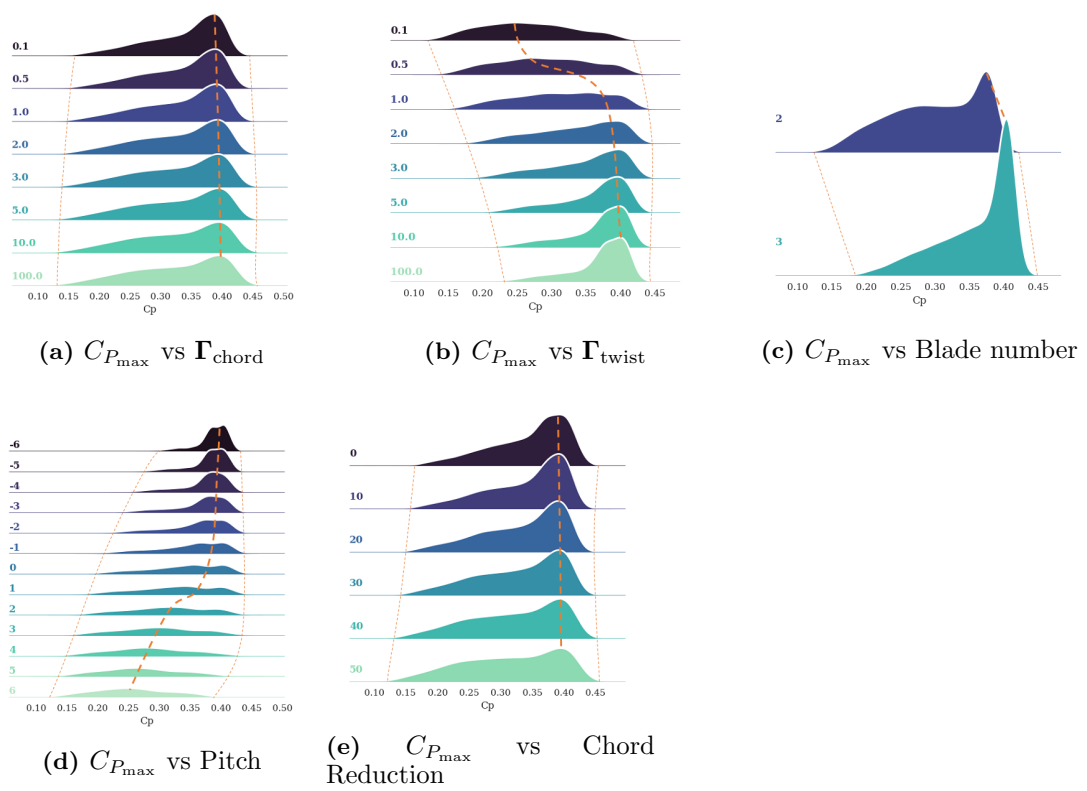


Figure C.1: Probability Distribution for Wortmann $C_{P_{\max}}$ according to different design variables

Appendix C: PDFs of Wortmann FX63-137

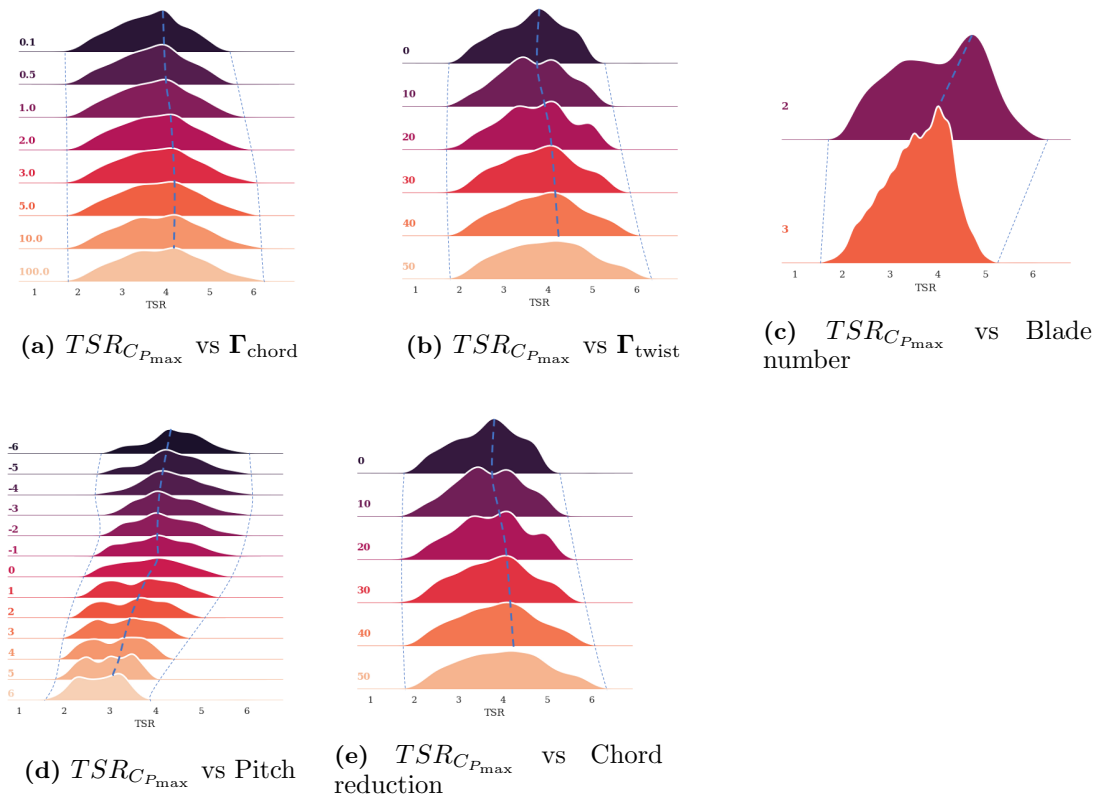


Figure C.2: Probability Distribution for Wortmann $TSR_{C_{P_{max}}}$ according to different design variables

Appendix D

Complete Statistical Results for Velocity Profile Fitting

Table D.1: Descriptive Statistics for U_o , α , and β for Philippines: Unfiltered and complete dataset

Variable	Orth	Angle	N	Mean	SE Mean	StDev	Min	Q1	Median	Q3	Max
U_o	FF	≤ 30	93	0.11076	0.00854	0.08232	0	0.03197	0.1089	0.1765	0.31344
	CC	> 150	67	0.04707	0.00558	0.04569	0	0.00641	0.03362	0.08166	0.19781
	PERP	$60 < x \leq 120$	734	0.30943	0.00761	0.20615	0	0.15304	0.27086	0.45632	0.98125
	DIAG+	$30 < x \leq 60$	83	0.2163	0.0188	0.1713	0	0.1127	0.1957	0.3105	0.7492
	DIAG-	$120 < x \leq 150$	70	0.05264	0.00869	0.0727	0	0	0.02714	0.09011	0.38577
α	FF	≤ 30	93	20.2	20.8	200.9	-73.5	0	1	2.3	1933.8
	CC	> 150	67	1.05	1.88	15.38	-75	-1.38	1	1	54.64
	PERP	$60 < x \leq 120$	734	30.2	42.7	1157.9	-4371.3	-7.5	-4	-2.3	31001.5
	DIAG+	$30 < x \leq 60$	83	-9.05	8.62	78.54	-710.48	-4.3	1	2.82	30.66
	DIAG-	$120 < x \leq 150$	70	-3.3	2.24	18.73	-148.87	-3.39	-1	1	28.19
β	FF	≤ 30	93	0.7843	0.023	0.2219	0	0.7366	0.8327	0.9173	1
	CC	> 150	67	0.8143	0.0348	0.2845	0	0.832	0.907	0.9908	1
	PERP	$60 < x \leq 120$	734	0.44466	0.00704	0.19078	0	0.36134	0.39388	0.43674	1
	DIAG+	$30 < x \leq 60$	83	0.645	0.027	0.246	0	0.4303	0.68	0.8292	1
	DIAG-	$120 < x \leq 150$	70	0.6795	0.0424	0.3544	0	0.3529	0.8785	1	1

Table D.2: Descriptive Statistics for U_o , α , and β for Philippines: Filtered for $\alpha < |10|$

Variable	Orth	Angle	N	Mean	SE Mean	StDev	Min	Q1	Median	Q3	Max
U_o	FF	≤ 30	81	0.10928	0.00954	0.08588	0	0.02623	0.10452	0.17854	0.31344
	CC	> 150	57	0.04371	0.00567	0.0428	0	0.00001	0.03287	0.08138	0.13804
	PERP	$60 < x \leq 120$	540	0.26949	0.00805	0.18696	0	0.13179	0.22886	0.40639	0.98125
	DIAG+	$30 < x \leq 60$	69	0.1857	0.0171	0.1416	0	0.1047	0.1829	0.2838	0.7317
	DIAG-	$120 < x \leq 150$	66	0.04968	0.00894	0.07259	0	0	0.01479	0.08579	0.38577
α	FF	≤ 30	81	1.003	0.326	2.934	-9.925	1	1	1.999	9.507
	CC	> 150	57	0.277	0.391	2.954	-6.953	-1.066	1	1	7.611
	PERP	$60 < x \leq 120$	540	-3.425	0.146	3.389	-9.971	-5.264	-3.572	-2.436	9.046
	DIAG+	$30 < x \leq 60$	69	0.503	0.471	3.909	-8.002	-1.13	1	2.533	7.754
	DIAG-	$120 < x \leq 150$	66	-0.893	0.343	2.783	-7.974	-2.847	0	1	7.469
β	FF	≤ 30	81	0.7777	0.0257	0.2311	0	0.7366	0.8237	0.9173	1
	CC	> 150	57	0.7997	0.0404	0.3052	0	0.837	0.9177	1	1
	PERP	$60 < x \leq 120$	540	0.42377	0.00832	0.19328	0	0.3375	0.38731	0.42548	1
	DIAG+	$30 < x \leq 60$	69	0.6577	0.0299	0.2488	0	0.5445	0.6915	0.833	1
	DIAG-	$120 < x \leq 150$	66	0.6677	0.0444	0.361	0	0.3339	0.8419	1	1
DIAG-	$120 < x \leq 150$	70	0.6795	0.0424	0.3544	0	0.3529	0.8785	1	1	

Appendix D: Complete Statistical Results for Velocity Profile Fitting

Table D.3: Descriptive Statistics for U_o , α , and β for Mexico Transect A

Variable	Region	N	Mean	SE Mean	StDev	Min	Q1	Median	Q3	Max
U_o	1	10	0.97423	0.000586	0.00185	0.97002	0.97368	0.97457	0.97522	0.97641
	2	12	0.96027	0.00518	0.01793	0.92841	0.93878	0.97123	0.97218	0.97533
	3	8	0.9487	0.0137	0.0388	0.8772	0.9129	0.9668	0.9726	0.9742
α	1	10	-11.895	0.114	0.361	-12.683	-11.977	-11.847	-11.714	-11.459
	2	12	-17.98	3.16	10.93	-44.92	-25.67	-12.32	-11.69	-10.16
	3	8	8.9	14.6	41.3	-13.9	-13.5	-12.2	38.4	92.6
β	1	10	0.33069	0.000638	0.00202	0.32848	0.32921	0.32934	0.33304	0.33311
	2	12	0.32698	0.00127	0.00441	0.31882	0.32304	0.32782	0.33101	0.33219
	3	8	0.32091	0.00599	0.01693	0.29343	0.30235	0.32828	0.3316	0.33245

Table D.4: Descriptive Statistics for U_o , α , and β for Mexico Transect B

Variable	Region	N	Mean	SE Mean	StDev	Min	Q1	Median	Q3	Max
U_o	1	9	0.7945	0.0302	0.0906	0.6073	0.723	0.848	0.8503	0.854
	2	9	0.7164	0.0421	0.1263	0.4207	0.6704	0.7434	0.8166	0.8266
	3	10	0.8191	0.0105	0.0331	0.7595	0.7867	0.8381	0.8453	0.848
α	1	9	3.383	0.346	1.039	1.456	2.374	3.973	4.035	4.253
	2	9	2.629	0.315	0.945	1.422	1.605	2.593	3.53	3.702
	3	10	3.405	0.194	0.612	2.404	2.731	3.755	3.885	3.98
β	1	9	0.3267	0.0115	0.0345	0.3057	0.3064	0.307	0.3497	0.4008
	2	9	0.3504	0.0126	0.0379	0.3129	0.3153	0.3472	0.3837	0.4199
	3	10	0.31582	0.00339	0.01072	0.30711	0.30789	0.30965	0.3233	0.33791

Table D.5: Descriptive Statistics for U_o , α , and β for Mexico Transect C

Variable	Region	N	Mean	SE Mean	StDev	Min	Q1	Median	Q3	Max
U_o	1	9	0.797	0.0188	0.0565	0.6917	0.7444	0.8264	0.8407	0.8452
	2	7	0.7	0.0291	0.0769	0.6133	0.6316	0.6744	0.7918	0.7945
	3	8	0.785	0.0302	0.0853	0.59	0.7641	0.8217	0.8392	0.8401
α	1	9	153	165	496	-40	-35	4	15	1475
	2	7	8.41	2.85	7.53	2.53	3.19	3.67	17.57	20.46
	3	8	-12.8	10.3	29	-42.4	-39.8	-16.5	11.4	28.4
β	1	9	0.32648	0.00308	0.00923	0.31932	0.32016	0.32191	0.33366	0.34595
	2	7	0.34962	0.00906	0.02397	0.32	0.32311	0.35403	0.36857	0.38176
	3	8	0.33085	0.0076	0.0215	0.32034	0.3207	0.32187	0.32937	0.38329

Table D.6: Descriptive Statistics for U_o , α , and β for Mexico Transect D

Variable	Region	N	Mean	SE Mean	StDev	Min	Q1	Median	Q3	Max
U_o	1	8	0.76023	0.00822	0.02324	0.71132	0.74699	0.76871	0.77749	0.7778
	2	9	0.6782	0.0544	0.1631	0.3769	0.5282	0.7683	0.7962	0.8045
	3	8	0.6887	0.0384	0.1085	0.5328	0.5696	0.7091	0.7882	0.8123
α	1	8	8.085	0.696	1.968	4.426	6.727	8.6	9.784	9.946
	2	9	12.2	6.23	18.7	-3.3	2.54	7.48	13.2	59.94
	3	8	6.91	1.87	5.28	2.32	3.1	5.44	10.4	17.74
β	1	8	0.33061	0.00219	0.00618	0.32587	0.32606	0.32828	0.33418	0.34363
	2	9	0.3537	0.0152	0.0456	0.3193	0.3209	0.328	0.3932	0.4431
	3	8	0.353	0.0118	0.0334	0.3169	0.3229	0.3467	0.3877	0.4046

Appendix E

Sample Calculation for LCOE

LCOE values in Chapter 8 are calculated using percentages derived from Segura *et al.* [95]. Equations on calculating submarine cable cost from Segura *et al.* are also applied.

E.1 CAPEX

The following percentages are applied:

- 13.50% - Generator/PTO
- 15.75% - Foundations
- 02.25% - Rotor
- 12.75% - Nacelle and Systems
- 20.00% - Installation
- 05.00% - Concept

Generator cost is calculated using the cost model. This constitutes 13.50% of the total cost and is used as a base for all other cost calculation. In this example, a 10m NACA TSR9.75 operating at 2m/s is used.

The generator cost is at **1286.82 EUR/kW**. Additional reference for the Wortmann TSR3.75 is provided since this will be the basis for some cost calculations:
 $C_{\text{generator}} = 3549.05\text{EUR/kW}$.

E.1.1 Foundations

Foundation cost uses the lowest TSR rotor as a reference and all other values are scaled to according to the average load value ratio of the calculated blade over the reference blade. The load values considered are the thrust values calculated in Chapter 7. For example:

$$K_{\text{thrust}} = \frac{Fn_{\text{blade}}}{Fn_{\text{reference}}} = \frac{5848.55N}{6832.97N} = 0.856$$

This is used to get the $C_{\text{foundation}}$

$$C_{\text{foundation}} = \frac{\%Foundation}{\%Generator} \times C_{\text{generator, Wortmann TSR3.75}} \times K_{\text{thrust}}$$

$$C_{\text{foundation}} = \frac{15.75\%}{13.50\%} \times 3549.05\text{EUR} \times 0.856 = 3544.03\text{EUR}$$

E.1.2 Rotor

The rotor cost used is the value of the reference Wortmann TSR3.75.

$$C_{\text{rotor}} = \frac{\%Rotor}{\%Generator} \times C_{\text{generator, Wortmann TSR3.75}}$$

$$C_{\text{rotor}} = \frac{2.25\%}{13.50\%} \times 3549.05\text{EUR} = 591.51\text{EUR}$$

E.1.3 Nacelle and Systems

The cost for systems used is the value of the reference Wortmann TSR3.75.

$$C_{\text{systems}} = \frac{\%Systems}{\%Generator} \times C_{\text{generator, Wortmann TSR3.75}}$$

$$C_{\text{systems}} = \frac{12.75\%}{13.50\%} \times 3549.05\text{EUR} = 3910.53\text{EUR}$$

E.1.4 Cabling

Cabling is calculated using Equations of Segura using the following parameters:

Appendix E: Sample Calculation for LCOE

Nacelle and device cables

- Protection Switch - 250000EUR/MW
- Submarine Connector - 25EUR/kg @ 300kg

Transformer Platform

- Rectifier - 100000EUR/MW
- Inverter - 100000EUR/MW
- Electrical Boxes - 20000EUR/MW
- Transformers - 40000EUR/MW
- Transformation Platform - 1300EUR

Electric connections at the base of the turbine

- Submarine Connector - 300EUR/kg @ 12kg
- Internal Wiring - 150EUR/kg @ 12kg
- Connection Box - 150EUR/kg @ 12kg

Umbilical, Submarine, and Ground connection

- Umbilical Cables - 75EUR/m @ 75m
- Submarine Cables - 350EUR/kg @ 500m
- Connection Box - 350EUR/kg @ 100m

The resulting value of 297905.40EUR is divided by the total power output of 129.97kW to get 2292.26EUR/kW.

E.1.5 Installation

65% of the installation cost is reduced by 63% due to the use of smaller vessels. At this point, 75% of the total cost is already calculated (20% installation and 5% concept remaining)

$$C_{\text{aggregate}} = C_{\text{generator}} + C_{\text{foundations}} + C_{\text{rotor}} + C_{\text{systems}} + C_{\text{cabling}}$$
$$C_{\text{installation}} = \frac{C_{\text{aggregate}}}{0.75} (20\%) (63\%) (65\%) + \frac{C_{\text{aggregate}}}{0.75} (20\%) (1 - 63\%) = 2416\text{EUR}$$

E.1.6 Concept

At this point, 95% of the total cost is already calculated.

$$C_{\text{concept}} = \frac{C_{\text{aggregate}} + C_{\text{installation}}}{95\%} \times 5\% = 739.03\text{EUR}$$

E.2 OPEX

The 4% OPEX case is a straightforward calculation. However, the 6.25%+ OPEX case includes the rotor cost for the Wortmann TSR3.75 and a third of the calculated installation cost.

$$C_{6.25\%+\text{OPEX}} = 4\% \text{CAPEX} + C_{\text{rotor}} + \frac{1}{3} C_{\text{installation}} = 1988.29\text{EUR}$$

E.3 LCOE

The LCOE is a simple sum of the OPEX divided by 8760hrs, and the sum of CAPEX and Cost of money divided by the annual energy production multiplied by the number of years of useful life (20 years).

The cost of money is calculated using the PMT function of MS Excel to get the annual payments multiplied by 20 with the CAPEX subtracted. The CAPEX needs to be subtracted since MS Excel includes the CAPEX in the final result. CAPEX is

Appendix E: Sample Calculation for LCOE

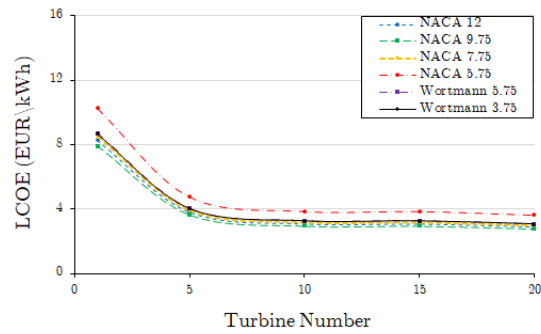
added back again after getting the cost of money. This is just a way to differentiate between CAPEX and COM.

- The cost of money for the 10m NACA TSR9.75 operating at 2m/s is 19941.96EUR.
- The CAPEX for the 10m NACA TSR9.75 operating at 2m/s is 14780.66EUR.
- The 6.25%+ OPEX for the 10m NACA TSR9.75 operating at 2m/s is 1988.29 EUR.
- The Annual Energy Production multiplied by 20 years for the 10m NACA TSR9.75 operating at 2m/s is 22769.25MWh

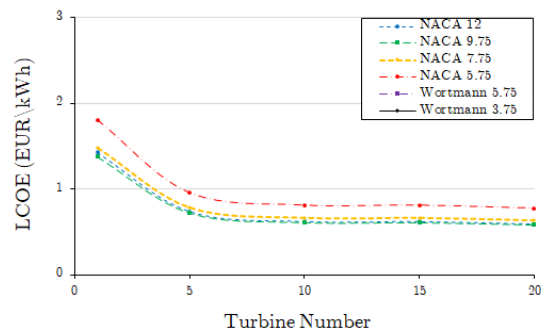
$$LCOE = \frac{CAPEX + COM + OPEX}{20 \times AEP} = 0.303\text{EUR/kWh}$$

Appendix F

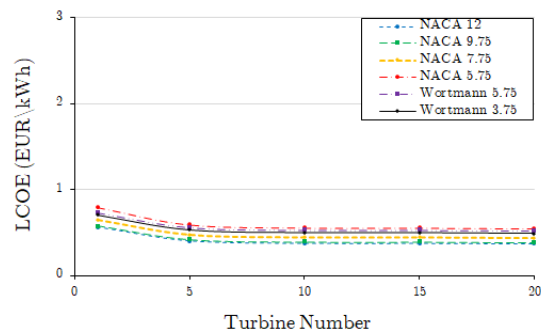
LCOE Sensitivity for 4% OPEX



(a) D=2m



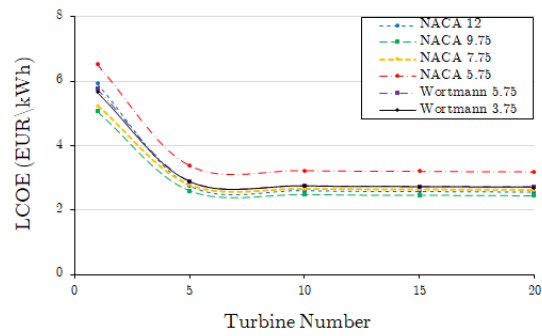
(b) D=5m



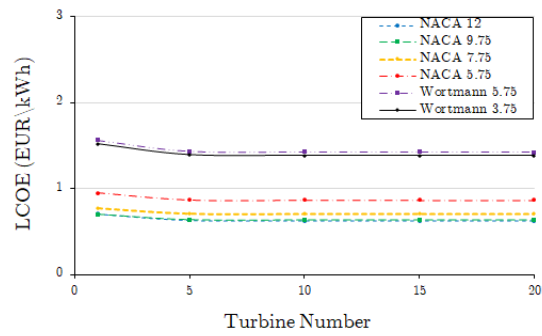
(c) D=10m

Figure F.1: Sensitivity of LCOE for varying turbine number for arrays operating at 1.0m/s

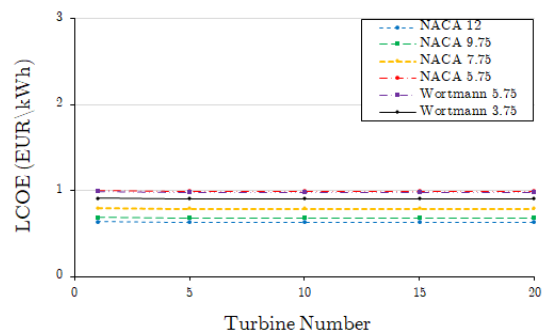
Appendix F: LCOE Sensitivity for 4% OPEX



(a) D=2m



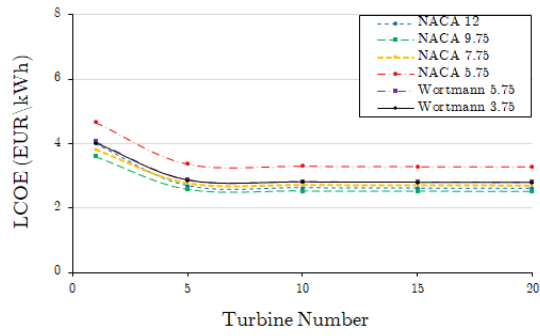
(b) D=5m



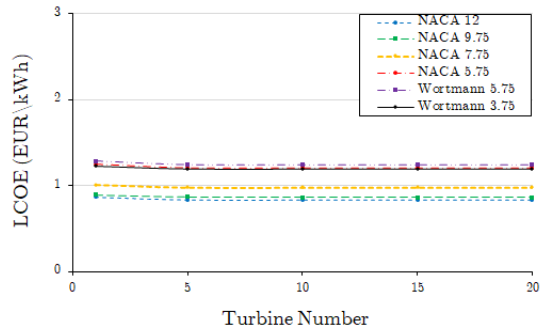
(c) D=10m

Figure F.2: Sensitivity of LCOE for varying turbine number for arrays operating at 1.5m/s

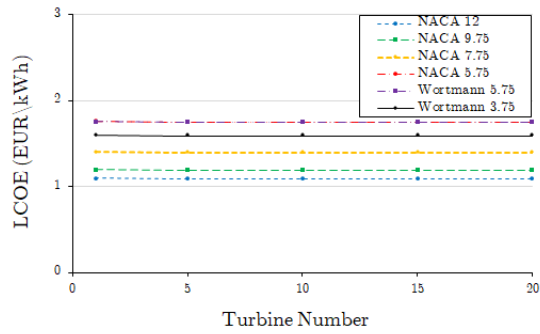
Appendix F: LCOE Sensitivity for 4% OPEX



(a) D=2m



(b) D=5m



(c) D=10m

Figure F.3: Sensitivity of LCOE for varying turbine number for arrays operating at 2.0m/s

Appendix G

AEP Calculation

Bin	Freq. Distrib.	Depth Adjusted Velocity m/s
1	0.02%	0.18
2	0.23%	0.33
3	0.76%	0.48
4	5.88%	0.63
5	13.31%	0.78
6	26.90%	0.93
7	36.24%	1.08
8	10.77%	1.23
9	4.54%	1.38
10	1.02%	1.53
11	0.25%	1.68
12	0.07%	1.8
13	0.01%	2.0

Set values for NACA TSR12:

- $C_P = 0.346$
- $D = 2\text{m}$
- V_R (Rated Velocity) = 1.5m/s
- V_S (Cut-in Velocity) = 0.45m/s
- Availability = 95%
- $\eta_{\text{electrical conversion}} = 98\%$
- $\eta_{\text{mechanical conversion}} = 80\%$

Appendix G: AEP Calculation

$$P_{\text{rated}} = \frac{1}{2} \times V_R^3 \times 1025 \frac{\text{kg}}{\text{m}^3} \times \frac{1\text{kW}}{1000\text{W}} \quad (\text{G.1})$$

$$P_{\text{fluid, bin}} = \frac{1}{2} \times U_{\infty, \text{bin}}^3 \times 1025 \frac{\text{kg}}{\text{m}^3} \times \frac{1\text{kW}}{1000\text{W}} \quad (\text{G.2})$$

$$P_{\text{rotor, bin}} = C_P \times P_{\text{fluid, bin}} \quad (\text{G.3})$$

$$P_{\text{elec, bin}} = P_{\text{rotor, bin}} \times (95\%)(98\%) \quad (\text{G.4})$$

If $V_S < U_{\infty, \text{bin}}^3$ and $V_R > U_{\infty, \text{bin}}^3$

$$AEP_{\text{bin}} = \text{Freq. Distrib}_{\text{bin}} \times P_{\text{elec, bin}} \quad (\text{G.5})$$

If $V_S > U_{\infty, \text{bin}}^3$

$$AEP_{\text{bin}} = 0 \quad (\text{G.6})$$

If $V_R < U_{\infty, \text{bin}}^3$

$$AEP_{\text{bin}} = \text{Freq. Distrib}_{\text{bin}} \times P_{\text{rated}} \quad (\text{G.7})$$

$$\mathbf{AEP} = \sum \mathbf{AEP}_{\text{bins}} \quad (\text{G.8})$$

Appendix H

Single Blade Loading under Waves

Note: Outliers in the data are not included in Figures 7.13 to 7.16

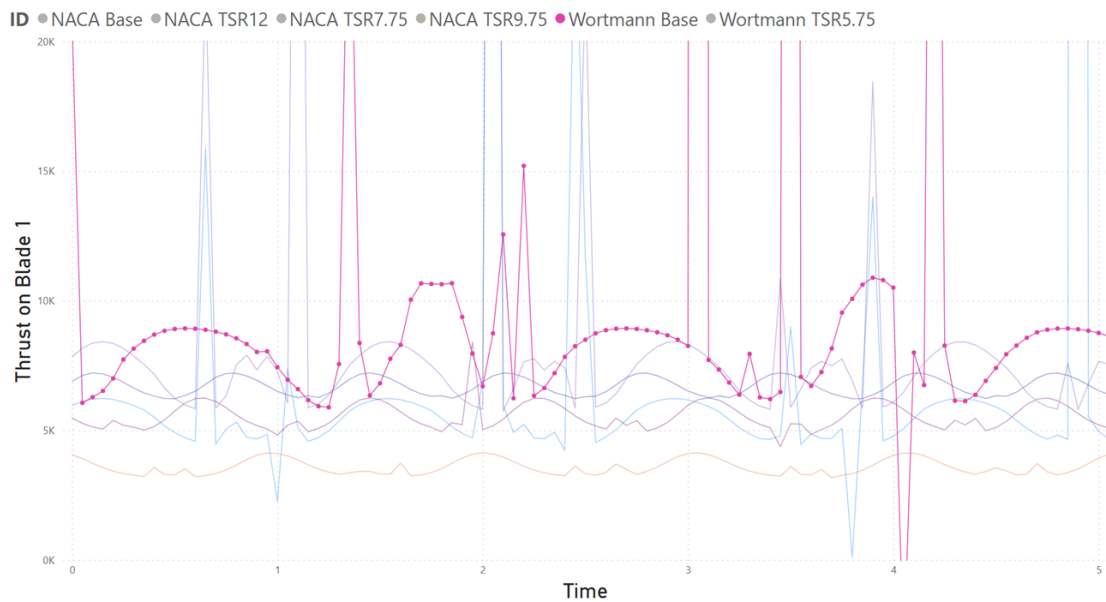


Figure H.1: Thrust Variation for the Wortmann Base Rotor (TSR = 3.75)

Appendix H: Single Blade Loading under Waves

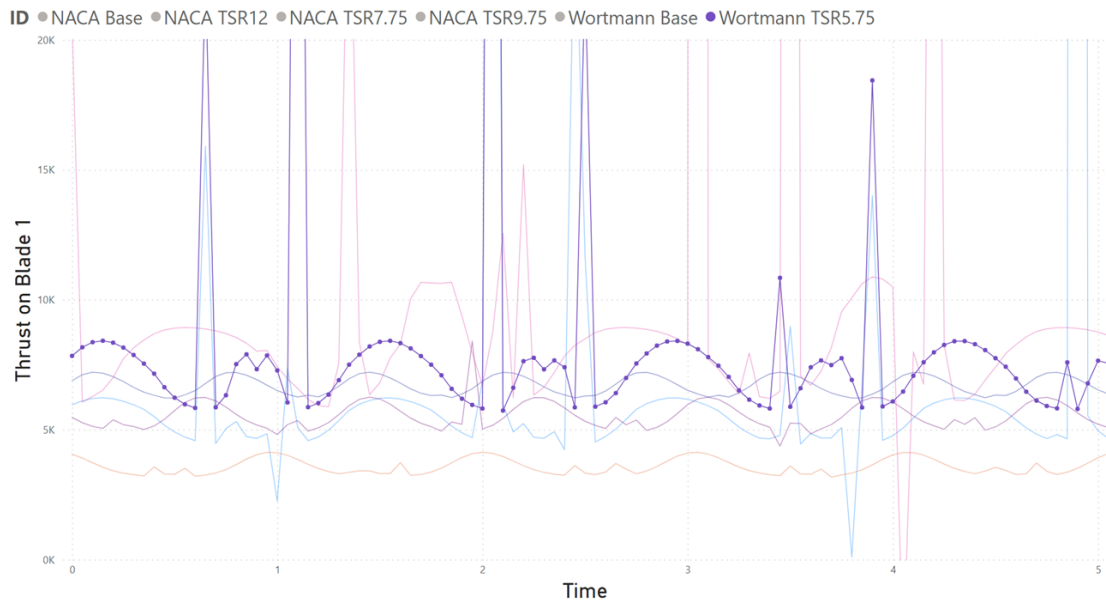


Figure H.2: Thrust Variation for the Wortmann TSR5.75 Rotor

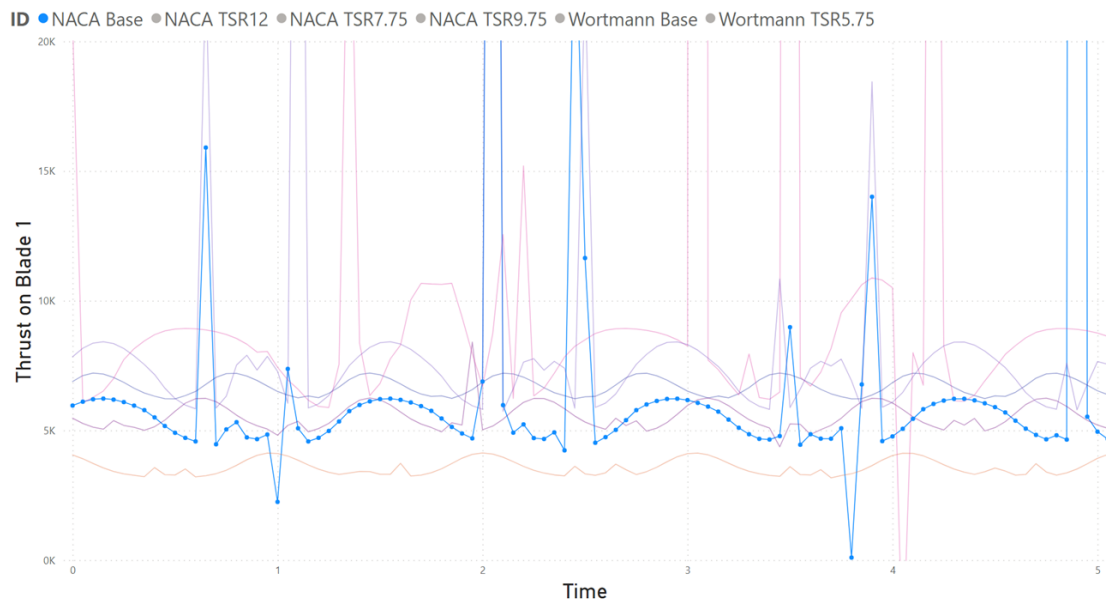


Figure H.3: Thrust Variation for the NACA Base Rotor (TSR = 5.75)

Appendix H: Single Blade Loading under Waves

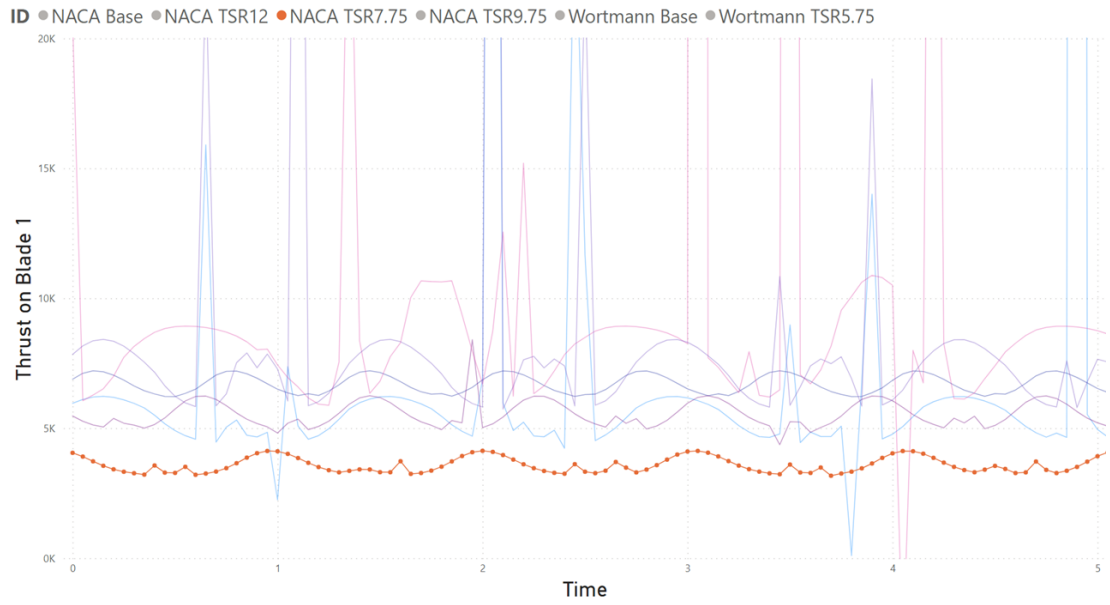


Figure H.4: Thrust Variation for the NACA TSR7.75 Rotor

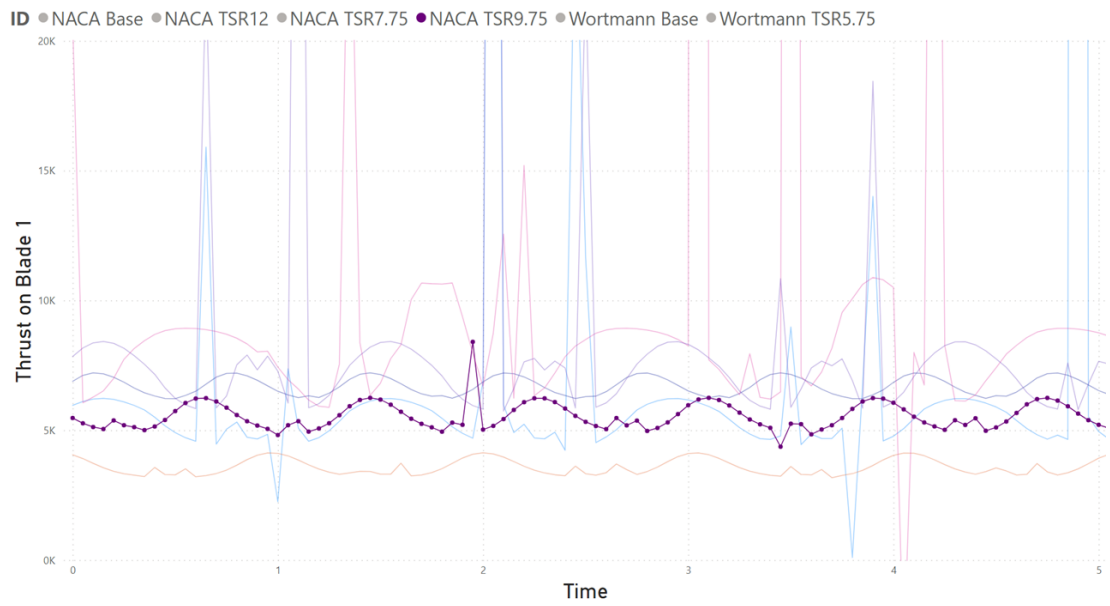


Figure H.5: Thrust Variation for the NACA TSR9.75 Rotor

Appendix H: Single Blade Loading under Waves

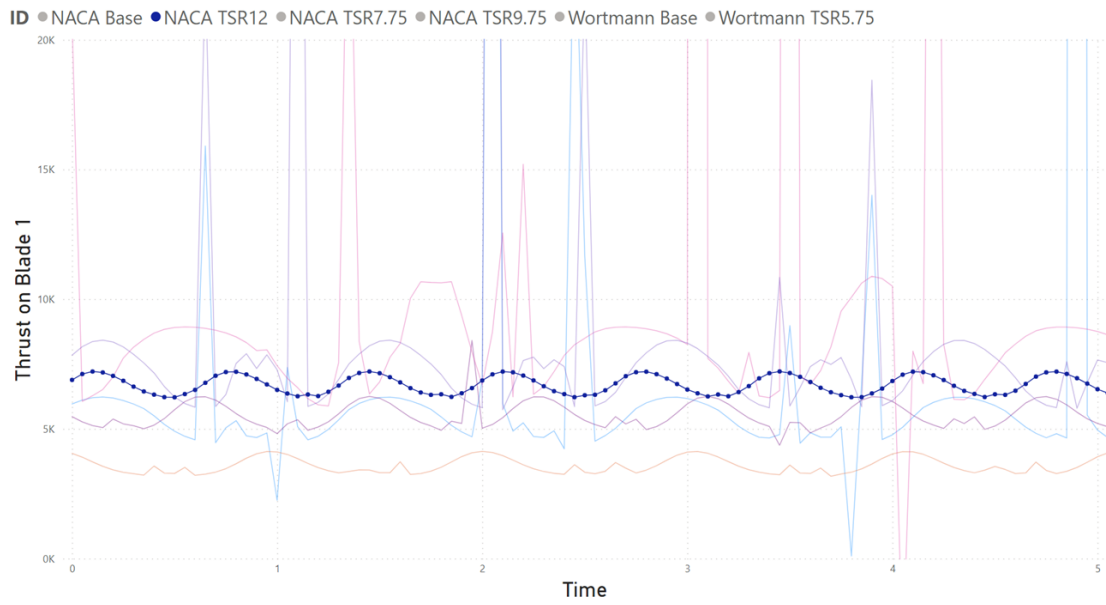


Figure H.6: Thrust Variation for the NACA TSR12 Rotor

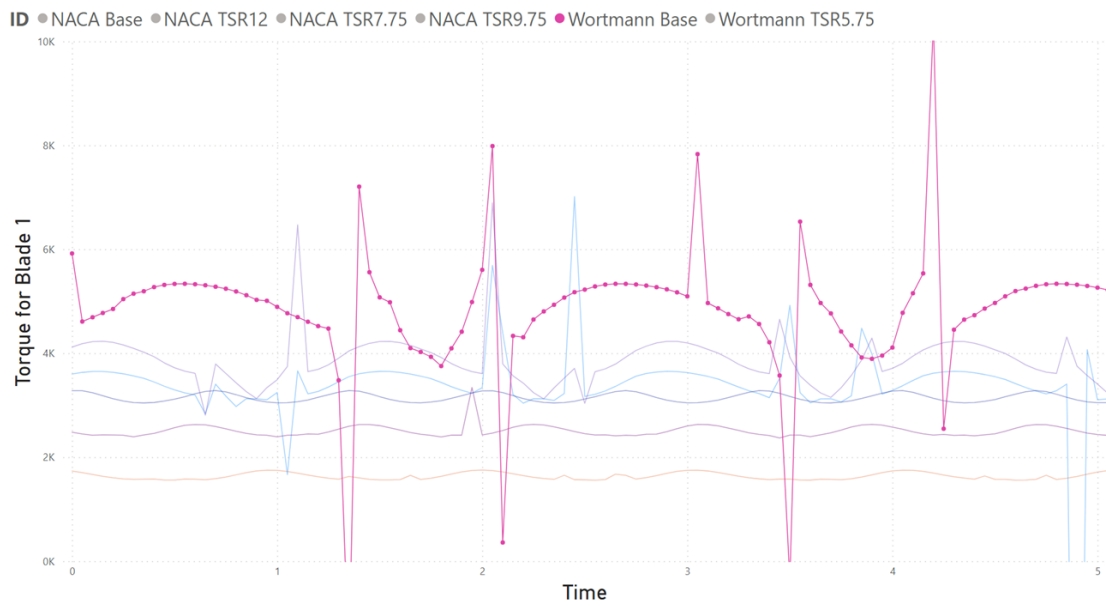


Figure H.7: Torque Variation for the Wortmann Base Rotor (TSR = 3.75)

Appendix H: Single Blade Loading under Waves

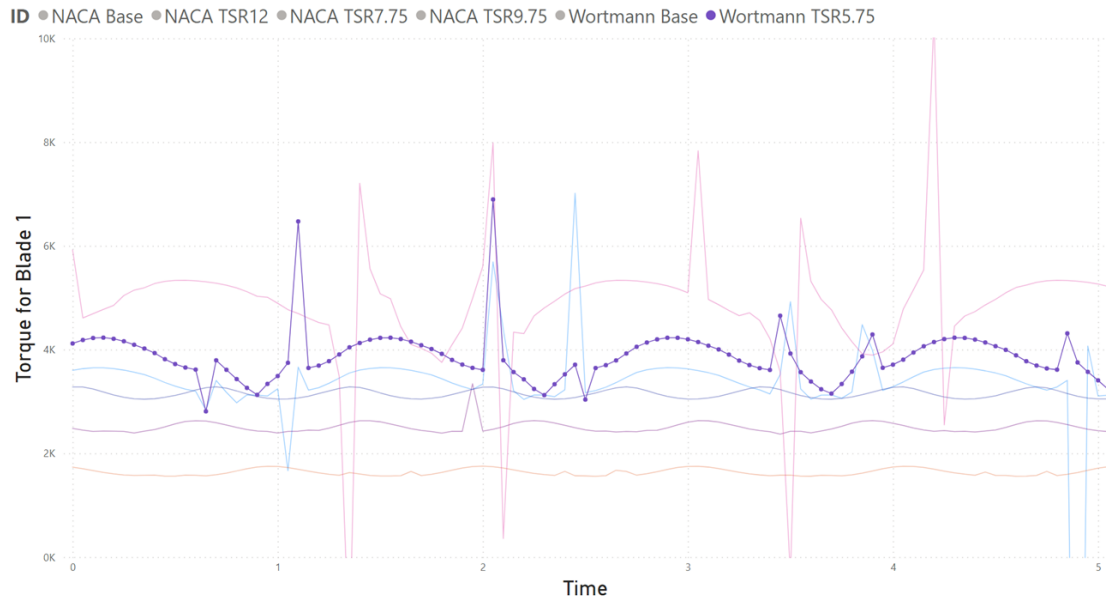


Figure H.8: Torque Variation for the Wortmann TSR5.75 Rotor

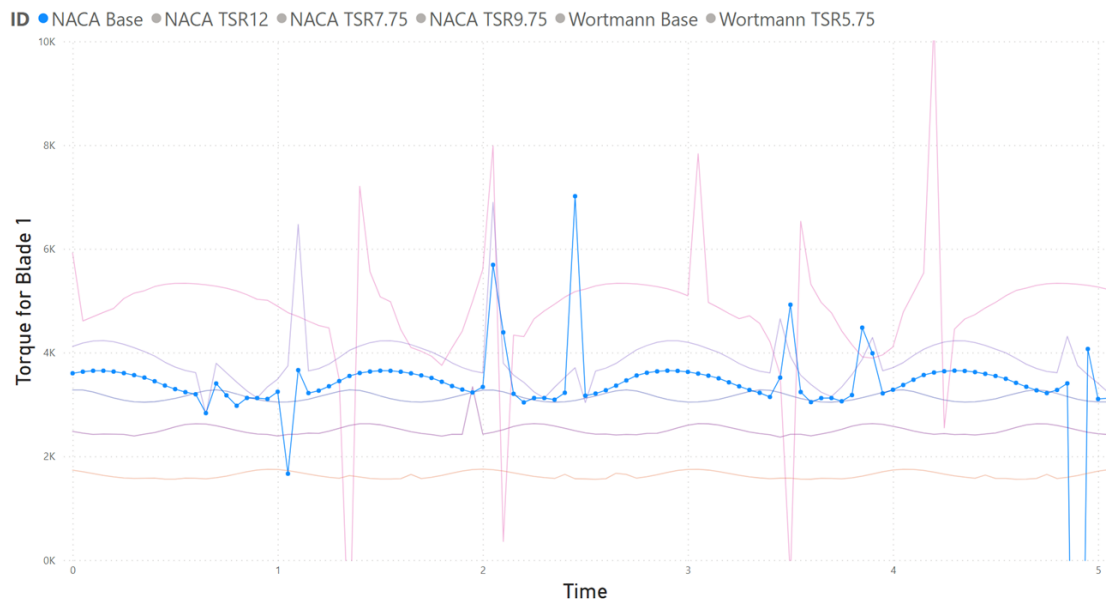


Figure H.9: Torque Variation for the NACA Base Rotor (TSR = 5.75)

Appendix H: Single Blade Loading under Waves

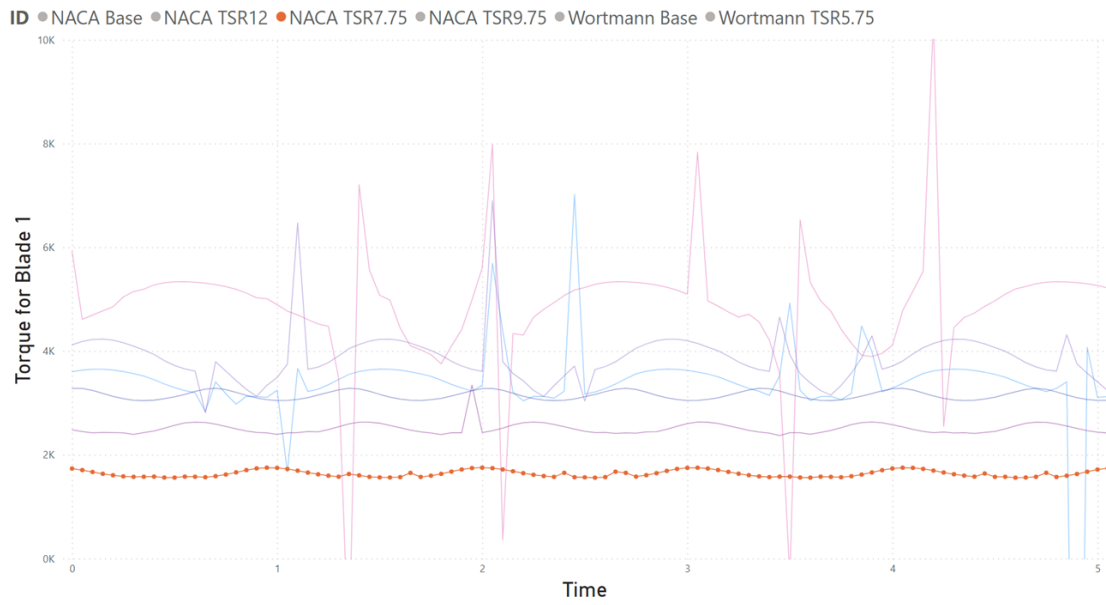


Figure H.10: Torque Variation for the NACA TSR7.75 Rotor

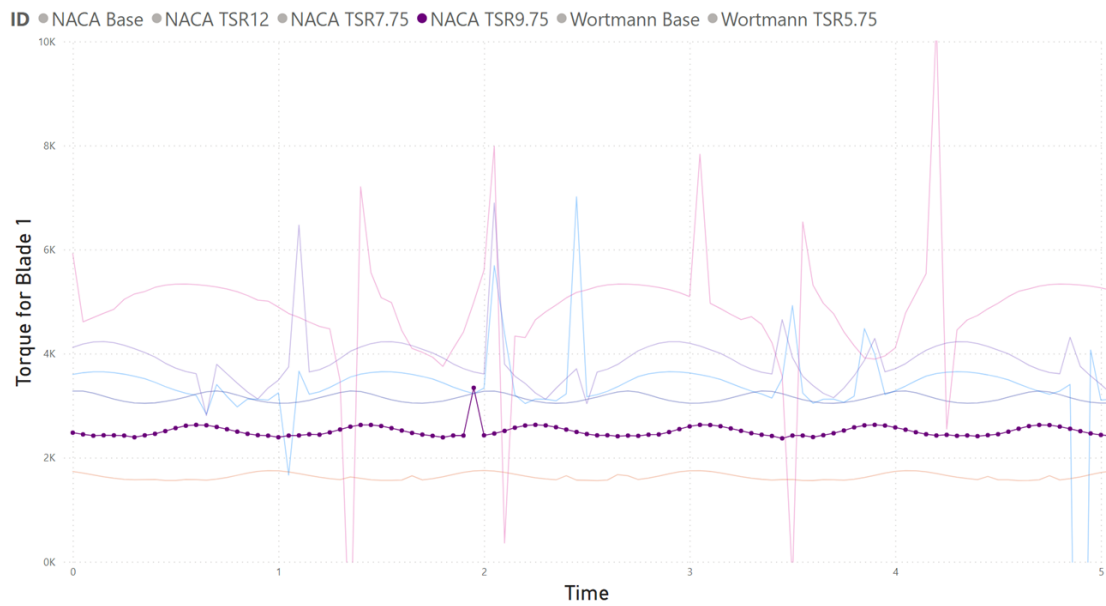


Figure H.11: Torque Variation for the NACA TSR9.75 Rotor

Appendix H: Single Blade Loading under Waves

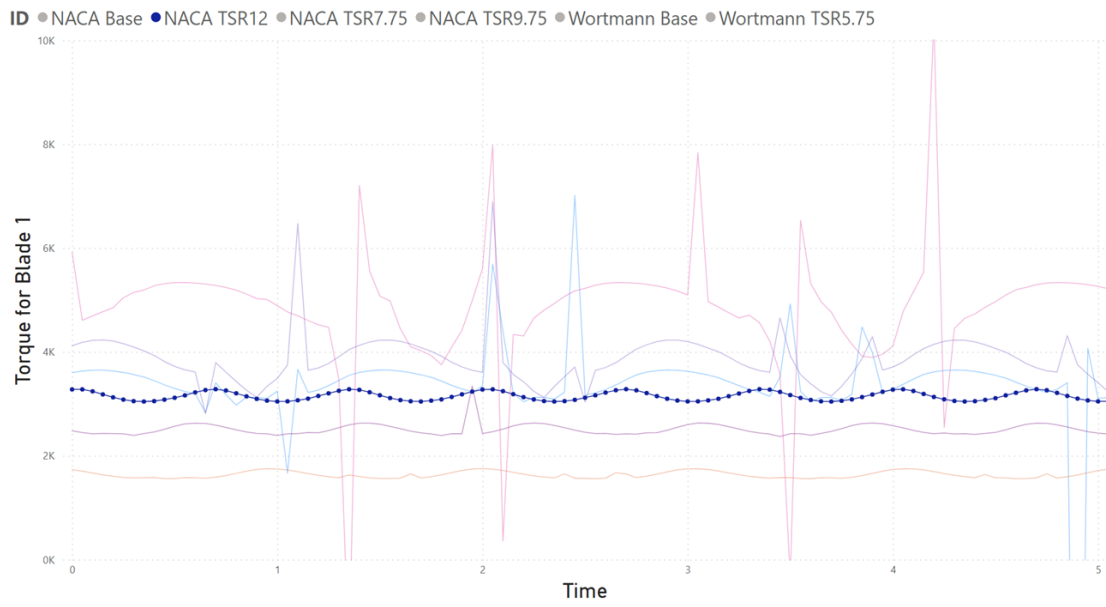


Figure H.12: Torque Variation for the NACA TSR12 Rotor